Rapid prototyping of injection moulded microfluidics with in-built sensing

By

Neil Convery

Submitted in fulfilment of the requirements for the degree of Doctor of Philosophy in Biomedical Engineering. May 2023

James Watt School of Engineering
College of Science and Engineering
University of Glasgow, UK

Acknowledgements

Firstly, I would like to thank Nikolaj for giving me opportunity to work on this project, and for all the supervision and advise that you offered along the way. I would also like to thank the various members of the BIG group who helped me with experiments, offered advice, or just listened to me complaining about things over the years. This work would have been a lot tougher without the guidance of Johnny, Paul, Andy, Rachel, and Marie who got me going in the lab at the beginning, and Alex, Iliyana, and Jack who assisted with some of the experiments later on. A special thanks goes to Duarte for his work running countless simulations for me. I greatly enjoyed my time in the BIG group, and it was a shame that many of the best aspects of working there were cut so short.

Thanks also must go to Stefan and Gareth at the University of Oslo. I learnt a lot, and thoroughly enjoyed my time in your labs (although I think I enjoyed the trip to Lofoten even more!).

I would also like to thank Lisa for providing the necessary motivation to write up and finish this thesis.

Finally, I would like to thank Styli, Alex, and Chris with whom I enjoyed (probably too many) lunches and drinks when such things were permitted.

Abstract

Microfluidics have been utilised over the past few decades to realise a wide range of academic research. These fluidic devices carry several advantages over classical analytical techniques such as lower reagent consumption, more rapid reactions, and increased sensitivity. However, while many of the currently used fabrication techniques allow for the rapid prototyping of microfluidic structures, these methods, and the design rules associated with them, do not translate well into mass-producible devices. For example, devices can be manufactured rapidly using soft lithography methods however, this requires access to specialist clean-room facilities and the through-put is limited to only a handful of devices per day.

To address this, the work in this thesis focuses on developing a manufacturing platform that allows for the rapid prototyping of microfluidic devices using injection moulding. This process not only allows for the fabrication of hundreds of devices per day, but also allows for the use of materials such as polystyrene which have material properties that are better suited for applications such as cell culture. To achieve this, 3D printed inlays were evaluated for use in an industrial injection moulding machine and it was found that channels as small as 100 x 200 µm could be reliably manufactured.

To complement this manufacturing platform, an oxygen sensor was also demonstrated that could be rapidly incorporated into the microfluidic devices without the requirement of clean-room facilities. This sensor could detect oxygen with high enough spatial and temporal resolution for most cell culture applications. Alongside this, steps towards making a device for measuring cell barrier integrity were also made. This work showed how functional elements such as electrodes and membranes could be rapidly incorporated into the injection moulded devices. However, a full demonstration of working trans-epithelial/endothelial-resistance measurements was not achieved.

Overall this work demonstrates a novel manufacturing platform that should enable a more seamless transition from prototype, to mass-produced microfluidic devices in the future.

Impact of the Covid-19 pandemic

The SARS-Cov-2 (Covid-19) pandemic resulted in the closure of all the lab facilities at the university of Glasgow from March 2021. This time coincided with what would have been the final year of this work. Most of the time out of the lab was spent preparing for future experiments and writing up what I could of this thesis.

However, once the lab began to open again in August 2021, it became apparent that it would not be possible to do the experimental work as initially planned. While a 6-month extension was granted as a result of the lab closures, regulations around numbers in the lab, and social distancing meant that for the last year spent working on this project, the lab time was limited to 3 hrs per day until spring 2022, and then only slightly more until the project finished in October. These limitations were especially apparent around the cell culture areas where access was limited severely. As such, the extension did not cover all the time that was lost at a critical point of the project.

Author declarations

The work presented in this thesis is original and my own unless otherwise stated. Some results presented here have been published in a peer reviewed journal and are detailed below.

Publications

Convery, N. *et al.* 3D Printed Tooling for Injection Molded Microfluidics. *Macromol. Mater. Eng.* **306**, 2100464 (2021).

Poster presentations

Convery, N *et al.* 3D Printed Tooling for Injection Molded Microfluidics. Poster presented at: μTAS 2021, Palm Springs, California, October 10-14.

Table of contents

Table of Figures

Table of tables

Nomenclature

Abbreviations and symbols presented in order of appearance

TEER	Trans epi/endothelial resistance
PADs	Paper analytical devices
μTAS	Miniaturised total analysis system
UV	Ultraviolet
PDMS	Poly(dimethylsiloxane)
PS	Polystyrene
CD	Compact disc
CNC	Computer numerical control
LIGA	Lithographie, glavanoformung, abformung (lithography, electroplating, moulding)
PTFE	polytetrafluoroethylene
T_g	Glass transition temperature
OoaC	Organ-on-a-chip
CYP450s	Cytochrome p-450 genes
PtOEPK	Platinum(II) octaethylporphinketone
S_0	Relaxed state of photosensitive molecule
S_0^*	Excited state of photosensitive molecule

$S_0\|_K$	Limited excited state in the presence of quencher
h	Plank's constant
f_{ex}	Excitation frequency
GI	Gastrointestinal
ZO-1	Zonula occludin-1
ZO-2	Zonula occludin-2
FITC	Fluorescein isothiocyanate
DC	Direct current
AC	Alternating current
V	Voltage
I	Current
V_0	Peak voltage
I_0	Peak current
t	Time
φ	Phase shift
Z	Impedance
j	Imaginary unit
M	Membrane area
ToaC	TEER-on-a-chip

CAD	Computer aided design
SLA	Stereolithography
SEM	Scanning electron microscope
PEEK	Polyether ether ketone
FDM	Fused deposition modelling
Ra	Average roughness
Rq	Root mean square roughness
Rz	Absolute roughness
lp	Line pairs
MDCK	Madin-Darby canine kidney
TPU	Thermoplastic polyurethane
COC	Cyclic olefin copolymer
PC	Polycarbonate
PMP	Polymethylpentene
PtTFPP	platinum tetra (pentafluorophenyl) porphyrin
PSP	Pressure sensitive paint
DMEM	Dulbeco's modified eagle media
FBS	Foetal bovine serum
LED	Light emitting diode

I_f	Intensity of light
I_f^0	Intensity of light with no quencher
k_q	Quench rate coefficient
τ_0	Lifetime of excited state
Q	Concentration of quencher
L	Maximum value of logistic function
c	Constant of logistic curve
x_0	Value of logistic curve midpoint
PMMA	Poly methyl methacrylate
PET	Polyethylene terephthalate
ITO	Indium tin oxide
ITO PET	Indium tin oxide coated polyethylene terephthalate
PBS	Phosphate buffered saline
DAPI	4′,6-diamidino-2-phenylindole
BSA	Bovine serum albumin
SAN	Styrene-acrylonitril copolymer
PLA	Poly-lactic acid
D	Distance separating electrodes
k	Electrical conductivity

A	Area
X	Imaginary component of impedance
ϕ	Phase of impedance

Chapter 1 – Introduction

1.1 Microfluidics

Over the past three decades, microfluidics has evolved from a fledgling field, to a mainstream area of interest in life science research and industry[1]. Defined as systems with a characteristic dimension between 0.1 and 100 μm [2], microfluidic devices have been demonstrated as outperforming classical analytical techniques as well as facilitating the study of new phenomena. These advantages are due to several physical phenomena that become apparent at this small length scale and have led to the creation of devices with a wide diversity of functions and applications across the chemical and biological sectors. One such application is the field of organ-on-a-chip, which aims to mimic human organ function on microfluidic chips with the aim of creating more physiologically relevant drug screening assays to expedite and improve the drug development pathway. These devices range in complexity from simple flow cells containing one cell type, to complex chips capable of mechanically stimulating the cells as well as having built-in sensing capabilities. This Chapter details the key benefits of microfluidics and explains the physics behind them. It also describes how these advantages have been leveraged to give researchers more control over the micro-physiological environment the cells in a device are subject to. It also explains how sensors have been incorporated into microfluidic devices to allow for real-time, non-invasive monitoring of cells and their micro-physiological environment. This section focuses on the detection of dissolved oxygen and how this can be controlled in devices to better mimic human physiology in certain organs such as the liver. Furthermore, the Chapter details how electrodes and membranes have been incorporated into microfluidic chips and how their inclusion gives rise to a whole new range of functionalities and measurements. A particular focus is given to trans-epithelial/endothelial resistance (TEER) measurements for the non-invasive, real time monitoring of call barrier integrity and permeability. Finally, the Chapter explains what the gaps in the current literature are, and identifies the key areas where further work is needed. This forms the aims of the project which are also listed. The Chapter also provides an overview of the structure of this thesis.

1.1.1 Physics of microfluidics

Microfluidics offer many advantages over classical analytical techniques due to certain physical factors dominating at small length scales. First, when we consider the ratio of inertial to viscous forces in a fluid (described by Reynolds' number[3]), the viscous forces dominate as the characteristic dimensions of the system are reduced. As Reynolds number decreases (Re >> 1), the system enters what is known as the laminar flow regime, or Stokes regime which carries several differences over turbulent flow (Re > 4000). Firstly, laminar flow is highly predictable meaning mathematical modelling of these systems is less intensive. Additionally, molecular transport in the laminar regime differs from the turbulent as there is no convective mixing, only diffusion, which again leads to highly predictable kinetics. In microfluidic systems, Re is almost always in the laminar flow regime. In addition to the Reynolds number, the Péclet number describes the ratio of advective to diffusive mixing in a fluidic system and shows that by reducing the dimensions of a system, the diffusive mixing dominated the advective[2]. As with the Reynolds Number, this means that the kinetics of a system are more predictable. Moreover, the behaviour of a fluid's surface differs between the macro- and the microscale. Surface tension describes a fluid's affinity to modify its surface to air interface to reduce its free energy. Interfacial tension describes the same phenomena but in two immiscible fluids, for example, oil in water. This phenomenon has been utilised to great effect in the field of droplet microfluidics [4]. On the microscale, these forces dominate with respect to gravity (the dominant force on the macro-scale) and can be used as a method to drive fluids without the need for pumps. Additionally, capillary forces also begin to dominate gravitational forces as the characteristic dimensions are reduced. Capillary forces describe the force on a fluid that allows it to travel through a porous material or narrow capillary. Again, at the microscale, this dominates over gravity and has led to the development of many analytical devices such as blood glucose meters[5], cheap pregnancy tests[6], and Covid-19 antigen tests[7], as well as the development of paper analytical devices (PADs)[8]. Finally, reaction times in microfluidic systems are much quicker than conventional devices. This is due to the smaller dimensions of the systems leading to a shorter diffusion time for any given molecule[2]. This becomes increasingly important when larger molecules with a lower coefficient of diffusion such as DNA, are considered.

With the above physical characteristics in mind, Manz et al. coined the term "Miniaturised Total Analysis System" (μTAS) and detailed how the physical advantages of fluids at the microscale could be harnessed to create faster, more efficient analytical devices[9]. In this seminal, the key tenets for microscale analysis devices were laid out which would provide guidelines for how the field progressed in the subsequent decades. In summary, all μTAS devices should be capable of all the functions required for the analysis of a sample. That is the sampling, transport, preparation, and detection should all be performed on the one device and carried out automatically. However, fabricating devices with characteristic dimensions small enough to benefit from the aforementioned phenomena requires manufacturing methods that differ from classical fabrication techniques. These processes are described in the following section.

1.1.2 Materials for microfluidic device fabrication

By definition, microfluidic devices require high resolution manufacturing techniques to fabricate the 0.1 to 100 μm channels[10]. As such, researchers looked to the photolithography protocols used within the semiconductor industry to realise these small geometries. During this process, a photoactive compound (known as a photoresist) is spun onto a silicon wafer before heating to remove any solvents (Figure 1.1A). The resist is then irradiated with ultra violet (UV) light through a mask which patterns the light in a predetermined design into the resist (1.1B). The resist is then developed to remove any non-irradiated material in the case of positive tone resists while the opposite is true for negative tone (1.1C). This pattern of resist can then be transferred into the wafer through an etching process which removes any exposed silicon (1.1D showing the wafer before (top) and after (bottom) the resist has been removed). To remove the reliance on etching processes and streamline the fabrication further, researchers developed the SU-8 series resist (a negative tone resist developed by IBM) which were mechanically and chemically stable enough to create devices without the need for any etching[11]. This resist also allowed for the deposition of thicker layers than standard photoresists (up to 1.2 mm thick) which could be used directly as microfluidic devices[12].

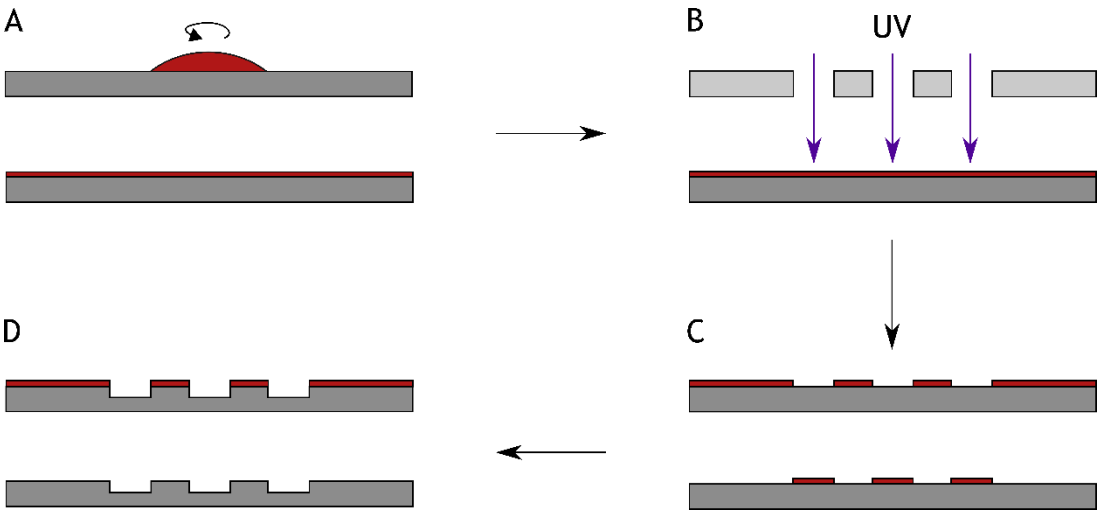

Figure 1.1– Typical photolithography and dry etch process. Photoresist shown in red with the silicon wafer shown in dark grey A shows the photoresist spinning process prior to and after spinning (top an bottom respectively) while B shows the exposure of the resist with UV light through a mask (light grey). Only the areas uncovered by the mask interact with the UV light transferring the pattern from the mask into the resist. Once exposed, the resist is developed (C) and depending on the tone of the resist, either the exposed material is removed (positive, (top)), or the unexposed material is removed (negative, (bottom)) by the solvent. Finally, the pattern in the resit can be transferred into the silicon through an etching process (shown in D) wherein the silicon is removed in the areas not protected by the resist. D shows this process before and after the initial resist has been stripped with the bottom schematic showing the final patterned silicon.

However, this direct approach to manufacturing means devices are expensive and cannot be manufactured rapidly. This becomes an issue as many copies of a device are required for biological research experiments. As such, it is often preferable to create a master structure using the advanced manufacturing techniques then replicate that structure in another, cheaper material. Hence, poly(dimethylsiloxane) (PDMS) casting is the most common material/fabrication protocol used in microfluidics today[13].

1.1.2.1 Poly(dimethylsiloxane) for microfluidic device fabrication

Since its demonstration in the late 20th century by George Whitesides, PDMS is the most popular material choice for microfluid devices due to a number of factors. Firstly, PDMS was much cheaper and quicker to manufacture when compared to silicon and glass that had been used previously. As PDMS can simply be cast from a master structure (prepared through silicon micromachining or otherwise) multiple copies of the same device can be made. This casting process can faithfully replicate features with sub 0.1 μm dimensions[14]. Furthermore, PDMS can be bonded to other materials with relative ease with the most common methods involving sealing against itself or against a glass cover slide.

This can be done due to the elastic nature of PDMS meaning it conforms to a surface and provides a moderate seal[13]. This sealing can be enhanced by treating the elastomer with O_2 plasma prior to bonding when higher pressures are required[15]. As such, PDMS has been used to create microfluidic devices capable of biochemical assays[16], genomics[17], chemical reactions[18], biological detection[19], and live cell studies[20] with the work on live cells made possible by PDMS's permeability to gases. These applications have been aided by the ability to "rapidly prototype" a device in PDMS meaning chips can be designed manufactured and redesigned before a final configuration is settled upon[21].

However, as widely used as PDMS is within engineering circles, it suffers from several drawbacks that hinder its uptake within biological and life sciences communities[22]. Firstly, it absorbs small, hydrophobic molecules[23,24]. As most drugs fall into this category, when a PDMS device is used for drug testing applications it becomes impossible to predict the quantity of substance actually reaching the tissue. Secondly, evaporation through the material can make it impossible to accurately predict the concentration of a solution within the device again detracting from its use in biological studies[25]. Furthermore, the elastic nature of PDMS can lead to a deformation of the devices under perfusion, making it impossible to calculate flow rates and shear in the channels[26]. Finally, PDMS can also leach uncured polymer into the analyte[27] and any surface treatments (such as increasing its hydrophilicity with oxygen plasma) are transient so devices cannot be stored and shipped[28]. This is increasingly becoming an issue as identical devices cannot be shared between research groups leading to little uptake in biology labs that lack the infrastructure to manufacture their own devices. A such, other materials have been considered for microfluidic applications.

1.1.2.2 Polystyrene as a material for microfluidic device fabrication

When compared to PDMS, thermoplastic materials (such as polystyrene (PS)) offers several advantages. PS has material properties that means it does not suffer from the same drawbacks as PDMS. In brief, polystyrene is a transparent thermoplastic polymer which shows good chemical resistance to alcohols meaning it can be sterilised easily. The rate of molecule diffusion into the bulk material is much lower than in PDMS and there is less leaching of the bulk

material into the flow. Moreover, PS (Young's modulus = 2.3 – 3.3 GPa[29]) is much stiffer than PDMS (Young's modulus 0.57 – 3.7 MPa depending on the ratio of base to crosslinker[30]) so channels are not deformed under high pressures and the lower degree of hydrophilic recovery means that devices can be stored for much longer before shipping to consumers. Additionally, as PS is the standard tissue culture plastic that has been used in biology labs and industry and as such, almost all knowledge of cell behaviour has been based on PS surfaces[22]. This heavy reliance of PS is due to the wealth of standard equipment in biological and life sciences research (culture flasks, petri dishes, well plates, etc.). This standardisation means that many identical parts are required and thus manufacturing methods that allow for an economy of scale can be utilised. However, for smaller production runs required for rapid prototyping of microfluidic devices, these protocols are often too expensive and time consuming to be worthwhile. The following section describes the fabrication of microfluidic device though injection moulding – the gold standard for high throughput fabrication.

1.1.3 Fabrication of microfluidic chips through injection moulding

First described in 1872, injection moulding represents the gold standard in polymer replication[31]. This process involves the injection of a molten polymer into a cavity that allows for the manufacture of many identical parts. This technology was then rapidly expanded during World War II where the need for mass produced, affordable parts was increased. This culminated with the development of the first screw driven injection moulding machine which allowed for a greater control of the injection of the plastic and hence more precision and reproducibility in the parts. Towards the latter half of the 20th century, injection moulding has become an extremely efficient way to manufacture parts on an industrial scale with the market for injection moulding plastics predicted to reach a value of $476 billion by the year 2028[32]. Currently, injection moulding of nano-scale features is most commonly associated with the manufacture of CDs and Blu-ray discs where feature sizes as small as 140 nm can be achieved, although smaller features have been achieved in research settings[33]. Injection moulding has one main advantage over techniques such as hot embossing or thermal compression moulding as a replication method. That is, the heating of the polymer melt and the cooling of the part are kept separate. This means that

when compared to embossing, the polymer does not need to be heated and cooled for every replication so the cycle time is reduced dramatically.

Additionally, the shear thinning behaviour of most thermoplastics also provides an additional advantage to the injection moulding process. As the viscosity of the polymer is reduced under shear, the polymer entering the mould cavity has a lower viscosity, and thus it is easier for the polymer to flow into and around features in the mould cavity[34].

1.1.3.1 Injection moulding process

In commercial injection moulding machines, the overall process is the same - molten plastic is injected into a mould where it is then solidified and the part can be released. In brief, a plastic is heated to above its melt temperature where the screw not only moves the molten material towards the mould cavity, but also mixes and homogenises the plastic melt. The material that is injected into the mould is known as the "shot" which typically consists of enough material to fill the mould once shrinkage during cooling has been accounted for plus a small quantity of material to allow for the transmission of pressure from the driving screw into the mould and stop the screw from bottoming out. The plastic then cools in the mould, with the material in the gate being the first to solidify. This means that no more material can enter the cavity so the screw retracts and prepares the shot for the next part. Once the plastic in the mould has been cooled to such an extent that it is dimensionally stable, the part is ejected and the process can begin again. This entire process is completely automated, and can be run without supervision hence why it is such an attractive technique for the high throughput production of parts from the previously mentioned CDs and Blu-ray discs, to much larger components such as bodywork for automobiles. This process is summarised in Figure 1.2 with 1.2A showing a photograph of an injection moulding machine, and B showing an exploded view of the tooling and the inlays (discussed in more detail section 1.1.3.2) while 1.2C shows a schematic of the whole tool with the heating of the plastic on the right, and the mould on the left.

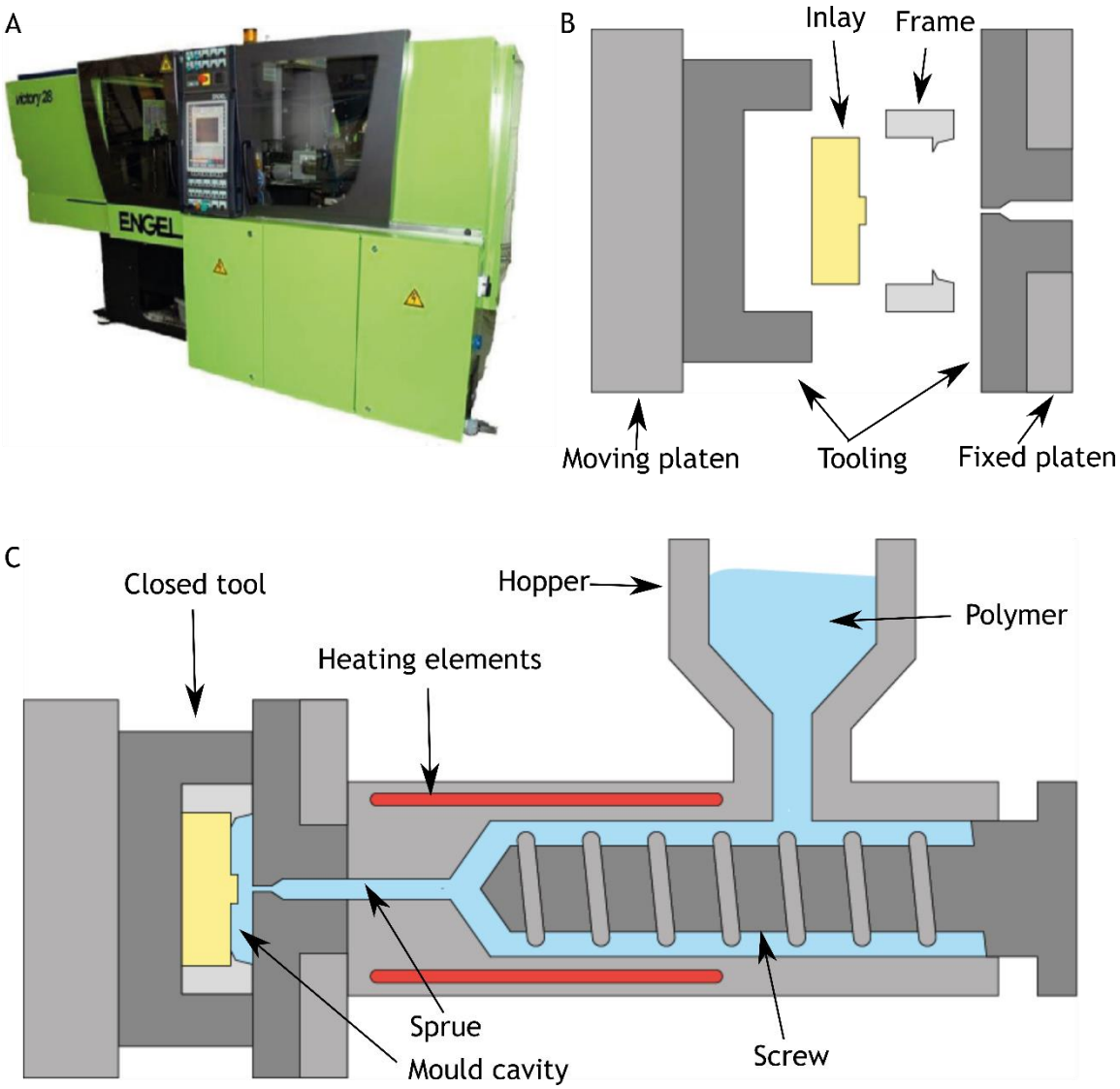

Figure 1.2 – Injection moulding machine anatomy. A photograph of the injection moulder used in this project is shown in A with the plastic heating on the right-hand side of the control panel, and the tooling on the left. B shows an exploded view of the tooling showing how patterned inlays can be incorporated into the mould. C shows a schematic overview of the whole injection moulder with the hopper filled with polymer, the heaters to melt the polymer, the screw to drive the melt into the mould, and the closed.

1.1.3.2 Fabrication of master moulds for injection moulding

As previously mentioned, injection moulding allows for the rapid production of thousands of identical parts from the one master mould[22] and as such, the master structure is perhaps the most important factor to consider. For the manufacture of planar devices and patterns, parts are often moulded against inlays which are held in place inside the tool (Figure 1.2B). These inlays are planar structures which contain relief patterns of the final configuration desired on the part. The tool must be designed to fit these inlays and hold them in place throughout the moulding process. Traditionally, these inserts have been manufactured by CNC milling of metals and this can be adapted to produce features on the microscale[35-37]. However, CNC milling suffers from shortcomings

such as high surface roughness and a large feature size limit. To address this, researchers have also shown a variety of means of fabricating these shims that can act as a bridge between the high-resolution manufacturing of photolithography and the high throughput technique of injection moulding. Examples of the materials and methods that have been used are LIGA (Lithographie, Galvanoformung, Abformung (German for Lithography, Electroplating, Moulding, a photolithography and etch process where the silicon wafer is electroplated in nickel which is then used as a master structure))[38], etched quartz[39], etched silicon[40,41], polytetrafluoroethylene (PTFE) backed nickel[42], SU-8 photoresist on nickel[43], UV curable polyurethane resins[44], bulk metallic glasses[45], and SU-8 on polyamide sheets[46]. However, when the smaller production runs required for the rapid prototyping approach of microfluidics are considered, the expense of a high-quality milled or LIGA inserts cannot be spread over thousands of parts. This means that injection moulding, and thus PS, is not often considered for microfluidics. For PS to be a viable material for chip production in research settings, inlays must be fabricated through another means that those described above.

Alongside injection moulding, hot embossing has been shown as a viable means of replicating microstructures in thermoplastic materials. In short, a thermoplastic substrate is heated to 40-50°C above its glass transition temperature (T_g). Next, a stamp containing the relief of the desired pattern is pressed into the substrate and the part is cooled. Once cooled, the part is then released from the stamp. Vinyl records are an example of how this process has been used to mass produce parts in an industrial setting. In more research orientated settings, gratings[47] and features as small as 25 nm[48] have been realised though this fabrication method. Furthermore, as there is little flow of polymer, the final parts have low thermal stresses[49]. With this in mind, hot embossing has been utilised for the fabrication of an assortment of microfluidic devices[50–53]. However, while hot embossing can be automated the time associated with heating and cooling the substrate and tool is too long for high throughput fabrication so this fabrication technique is rarely used in both microfluidics research and industry. Furthermore, hot embossing still relies on the fabrication of a master structure such as those used in injection moulding meaning it too is less suited to small production runs.

1.1.3.3 Sealing of thermoplastic microfluidic devices

As discussed above, there are many potential benefits to fabricating microfluidic devices from thermoplastic materials. However, the sealing of these devices is not as trivial as the sealing of parts made with PDMS which conforms to surfaces due to its elastomeric nature. As such, there have been many approaches to seal microfluidic channels fabricated from thermoplastic materials. The main approaches for this are detailed below.

Firstly, and most simply, adhesives have been used to seal microfluidic channels. These approaches can be split into using glue[54], or double sided adhesives[55] to bond the open microfluidic structures against a sealing surface. However, glue leads to issues with clogging where excess adhesive can block channels during sealing. Also, there are issues with both glue and double sided adhesive leaching molecules into the flow. Another similar approach to this is the use of pressure sensitive adhesives (PSAs). PSAs work in a similar way to tape, however the adhesive compound is only activated by the application of pressure to the device meaning that areas of the tape covering the channels should not have any activated adhesive compounds on their surfaces[56]. This means that prototype device can be fabricated and tested quickly but these prototype devices often do not resemble production ready devices. The issue with leaching adhesives into the flow also persists with PSAs.

Thermal fusion bonding is another approach that is commonly used to seal microfluidic devices[57]. In this process, the two parts are held together under pressure and heated to above their glass transition temperatures (T_g). This leads to a bond between the two parts without having to include any adhesives which carry drawbacks discussed above. This approach can give strong bonds between the parts however, un-optimised bonding conditions can lead to deformation and collapse of channels[57]. The main issue with thermal bonding is the cycle time, with bonding typically taking a few minutes, meaning it is often not compatible with a fabrication process such as injection moulding where parts are created every few seconds.

To address this, there are methods such as solvent and UV or plasma assisted thermal bonding can be used to significantly reduce the time and temperature

requirements of thermal fusion bonding[58]. In the case of solvent bonding, the T_g of the polymer is lowered by the addition of a solvent to the bonding surface. The application of the solvent causes a physical change in the polymer at the surface which means that there is more polymer chain interfusion when the parts are heated and held under pressure. This means that devices can be bonded at temperatures up to 30°C below their T_g[59]. However, there have been reported issues with solvents impacting the geometry of the channels[60,61]. While this approach can be quicker than thermal bonding, the time requirements are still above what would be compatible with injection moulding so this approach is rarely used in industrial applications.

In the instance of UV or plasma assisted thermal bonding, UV light, or plasma is used to photodegrade the polymer such that the T_g is lowered only at the surfaces that are intended to be bonded[62–64]. As the polymer is not required to heat up as much, the thermal bonding process can take less time, and thus this bonding method is higher throughput than standard thermal bonding. This process has been used to produced microfluidic devices with strong bonds that can withstand high pressures[65]. UV assisted thermal bonding also shows low deformation of small micro-channels meaning that complex geometries can be consereved[66].

Finally, ultrasonic welding is another approach that has been demonstrated for the sealing of microfluidic devices. This technique involves using ultrasonic energy to melt the plastic at the interface of two parts under pressure. Typically, weld seams (or energy directors) are included to localise the energy to specific areas of the chip. These structures are usually triangular in profile and act to concentrate the energy and provide enough material to melt, flow, and create a seal between the parts. This process has been used to assemble complex devices such as piezo pumps[66]. While this process is very fast however (with the entire process taking place in a few seconds), the requirement on energy directors means that there is often an added height to the microfluidic channels that has the potential to change the flow characteristics of the device. To combat this, a tongue-in-groove approach was demonstrated by Kistrup *et al.* which eliminates the issue of the added height[67].

1.2 Microfluidic organ-on-a-chip devices for pharmacological studies

As mentioned in section 1.1, microfluidics have been applied to a wide range of problems within the chemistry and life science fields with one of the areas of great interest being drug discovery. As the cost of developing new drugs is predicted to double every nine years, there is need for new models to replace the most costly aspects of drug development[68]. This is shown by "Eroom's Law" in Figure 1.3A with the traditional model for drug development is shown in Figure 1.3B with the preclinical development and the phase 1 trials representing the steps at which most candidates fail. This failure is often down to the fact that the animal models used in pre-clinical trials (usually rat and mice models which make up 95% of all laboratory animals[69]) are not accurate enough to predict human physiology[70] and the standard current *in vitro* models are not reliable enough for use in industry. Furthermore, these two steps also represent the greatest cost in drug development as companies have to recoup the losses for all the failed compounds. As such, in recent years, there has been a great deal of work in more physiologically relevant *in vitro* models termed "organ-on-a-chip" (OoaC) that aim to recapitulate organ level function and organisation from human cells in microfluidic devices[71]. Early research focussed on looking at single perfused chambers with one cell type however, more complicated systems consisting of multiple cell types have been developed to recreate the interfaces between cells and tissues seen *in vivo*. The ability to couple microfluidics and microfabrication with cell culture also comes with a plethora of other advantages: The physics of microfluidics mean that researchers can have more control over the flow of fluid in devices. The laminar flow in microchannel has been used to create concentration gradients in chemicals to monitor cell migration and differentiation amongst other behaviours. By capturing the multicellular construction, mechanical and chemical stimulation, and blood supply of living organisms, OoaC devices offer much greater accuracy as models for the body compared to conventional two- and three-dimensional cultures[72]. As such, OoaC devices have been utilised as assays to study the function of living tissues within the greater context of organs and organ systems. Furthermore, due to the increased accuracy of OoaC devices, it is hypothesised that these

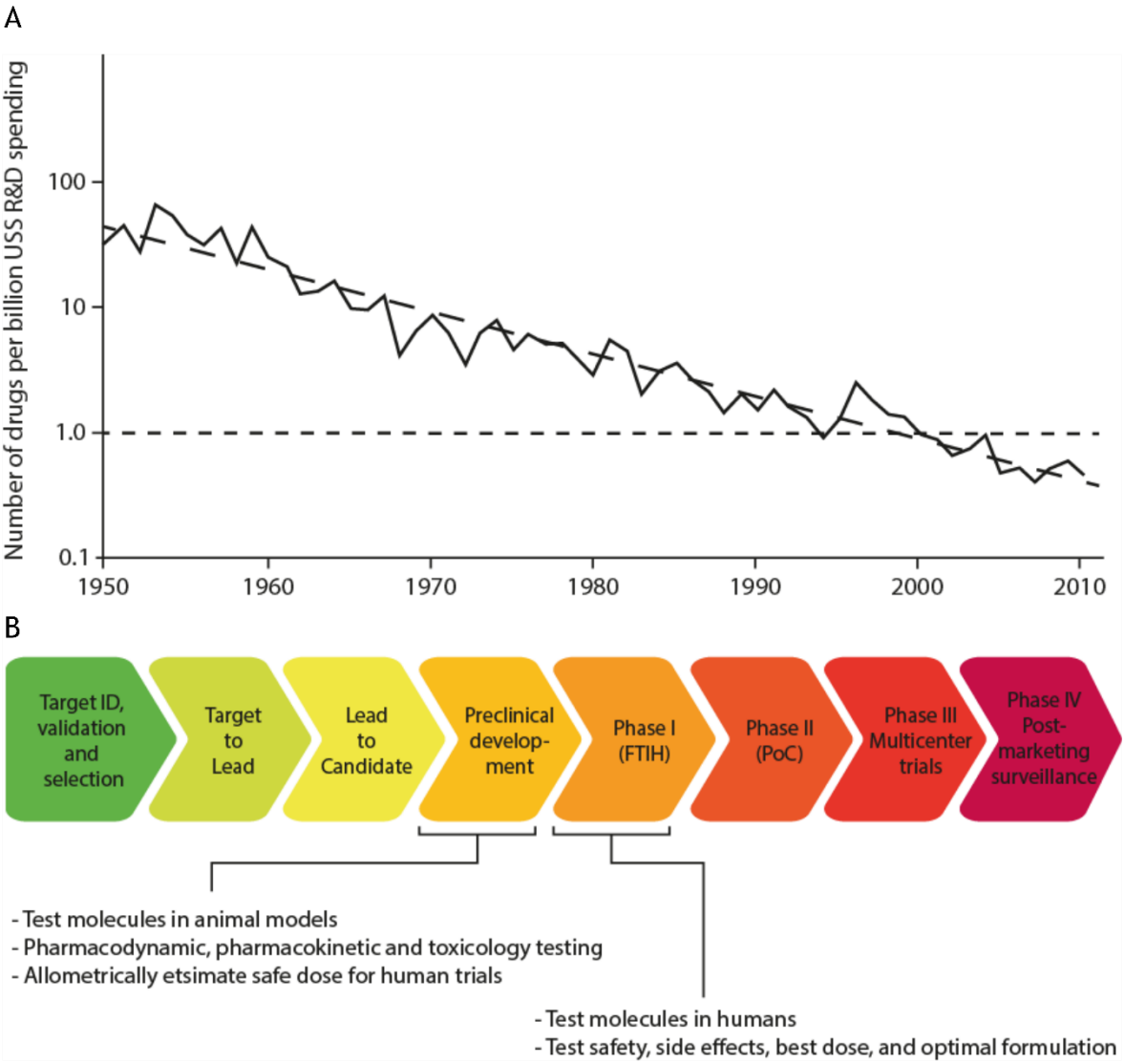

Figure 1.3 – Drug development pathway and bottleneck. A shows Eroom's law (inverse Moore's law) showing how an increasing amount is being spent to bring every new drug to the market (adapted from reference 68). The traditional drug development pathway is shown in B. Preclinical development and phase I (first time in humans) represent the areas where most compounds fail due to poor drug screening and inadequacy of animal and in vitro models.

chips will reduce the reliance on animal (in compliance with the 3R´s (replace, reduce, and refine[73])) and human tests that come with a great deal of cost and ethical issues. These devices have thus become of great interest within the pharmaceutical industry[74].

With the above advantages in mind, a great deal of devices have already been demonstrated covering a variety of tissues such as muscle[75], bone[76], blood vessels[77], lung[78], gut[79] , brain[80], fat, liver, and heart[81]. It is also possible to couple multiple organ types together to create an organ system that is more representative of the human body[82,83].

Currently, much of the OoaC work is conducted using polydimethylsiloxane (PDMS) devices due to the advantages discussed previously. However, as small, hydrophobic molecules are absorbed into the material and as most metabolic drugs fall into this category, PDMS is not ideal when drug screening applications are considered. Thus, if devices could be rapidly and cheaply manufactured from PS, research in the field could be accelerated while avoiding the pitfalls of PDMS[23]. Additionally, the current microfabrication techniques require a vast amount of engineering knowledge and facilities that put this technology out of reach for many researchers. That being said, with all the potential benefits of organ-on-a-chip, it is imaginable that these devices could replace animal assays in the thus lowering the time and costs associated with drug trials. However, in order for OoaC devices to replace existing models, chips must be capable of replicating the micro-physiological environment of a given organ. This can involve the introduction of various chemical and/or mechanical stimuli to better mimic the human body. An important chemical stimulus in the human body is oxygen which plays an important role in cell metabolism among a wide range of other processes. The following section describes how oxygen concentrations measured and controlled within OoaC to create micro-physiological environments more relevant to the human body and model various pathologies.

1.2.1 Creating a physiologically relevant oxygen micro-environment in microfluidics

As mentioned above, the main aim of organ-on-a-chip systems is to create as physiologically relevant a system as possible. This can include mimicking mechanical stresses, recapitulating the 3D nature of human physiology, or by recreating the chemical environment found within the body. For example, maintaining oxygen (O_2) concentrations within microfluidics chips at physiologically relevant levels is important. Not only is O_2 important for general cell metabolism, the gas plays a vital role in the regulation of cell function. As such, normoxic cell culture (~12% dissolved O_2) is used to maintain the function and health of cells in vitro [84]. It has also been shown that hypoxic conditions can lead to cell death[85] and that any changes to the O_2 concentration can lead to an increase in stress of the cells, or a change in functionality[86]. This change in functionality is especially important in certain organs, such as the liver, where it has been demonstrated that an oxygen gradient (along with other molecules)

drives the differentiation of hepatocytes towards different functionalities[87]. While control over the O_2 concentration inside microfluidics chips is considered to be simpler in PDMS as the gas permeability means that gas can diffuse from the incubator into the media in the channels. In PS chips however, control over the oxygen concentration is thought to be more difficult as there is little to no diffusion of gas through the chip. The following sections detail how oxygen can be controlled and measured within microfluidic devices.

1.2.1.1 Control of oxygen in organ-on-a-chip systems

Due to the importance of oxygen within the body and its roles in cell differentiation and metabolism, researchers have sought to control the gradients of O_2 within microfluidic devices. With respect to organs such as the liver, these gradients can lead to a difference in cell function better mimicking in vivo physiology. In its simplest form, cells are cultured in a perfused chamber and as cells near the inlet use up the oxygen and nutrients, cells further down the chamber are subject to a hypoxic environment. Allen *et al*. used this type of device to culture rat cells and showed that cells in the lower O_2 environment had a greater expression of cytochrome p-450 genes (CYP450s) and thus a greater susceptibility to acetaminophen toxification as per *in vivo*[88]. In another publication, the same group showed how the hepatocytes in the high O_2 (zone 1) showed increased phosphoenolpyruvate carboxkinase activity and the cells in zone 3 (low O_2) showed increased CYP540 activity which correlates to observations made *in vivo*[89]. Similary, Lee-Monteil *et al*. observed increased phosphorylation and albumin and urea production in zone 1 and increased glycolysis, α-1-anti-trypisin production, CYP450 activity and increased acetaminophen toxicity in zone 3[90]. In a similar approach, Tomlinson *et al*. studied rat hepatocytes at different locations in a bioreactor and used a mathematical model to predict the O_2 concentrations in the chamber and thus the areas that would best represent the three zones[91]. Again, they saw increased expression of zone specific markers.

The permeability of PDMS to gasses has also been used as a means of setting up oxygen gradients in microfluidic devices. Tonon *et al*. differentiated human pre-hepatocytes in a chamber with a O_2 channel running alongside it creating a continuous oxygen gradient similar to that seen *in vivo*[92]. Through this, they saw

zonated glycogen storage as well as increased CYP450 activity in zone 3. Sato *et al*. used a similar device and also observed different gene expressions in the peri-portal and peri-venous regions[93]. Finally, microfluidic gradient generators have also been used to set up gradients across liver cells. One such approach created gradients in nitrogen, carbohydrate and xenobiotics showing the flexibility of this technique compared to the aforementioned ones[94]. Through this, they were able to observe a zonal toxic response that resembled human liver tissue. Similarly, Bulutoglu *et al*. were able to model non-alcoholic fatty liver disease by creating gradients of free fatty acids and showed an increase in fibrosis in areas under high fatty acid concentration[95]. Furthermore, they observed an increase in lipid storage on low O_2 environments emulating *in vivo* studies. The above section highlights the importance of control over the chemical environment and how this affects the function of an OoaC.

However, while the gas permeability of PDMS has been leveraged to create O_2 gradients in microfluidic devices, this can also lead to some problems. As the bulk of the material is PDMS, any O_2 gradient is subject to gasses moving into the channel through the bulk material thus any cells in the channel, may not be under the predicted oxygen conditions.

Furthermore, most of the work done on oxygen sensors has so far been on point based detection and thus cannot be applied to monitor the gradients being constructed in microfluidic devices. While spatial detection of O_2 concentration has been demonstrated[96], the high cost and expertise required hinders the use of this technique for many applications.

1.2.1.2 Detection of oxygen in organ-on-a-chip systems

Alongside the control of O_2 in microfluidic systems, there have been many attempts at setting up lab-on-a-chip systems with integrated oxygen sensors to measure and visualise the changes in oxygen concentrations. These devices fall under two main categories: amperometric detection, and optical detection. Amperometric sensing has been utilised in a range of microfluidic devices[97–99] and have been shown to display the high sensitivity needed to detect oxygen at physiologically relevant concentrations. However, there are a few main drawbacks to using electrochemical sensing in lab on a chip devices. Firstly, the

lifetime of the sensor is limited as the membrane surrounding the electrodes can be fouled. This becomes an increasing problem in cell culture media which can contain a cocktail of proteins and salts. Furthermore, oxidation of the electrodes can result in discrepancies between the measured concentrations and the actual concentrations. Moreover, the Clarke electrode configuration works by reducing O_2 at the electrode to produce a current, and as such, readings have been shown to have a strong dependency on flow rate as the reduced species move downstream[100]. Furthermore, the reliance on nanofabrication techniques and the need to integrate several electrodes into one devices further detracts from the attractiveness of using amperometric sensors in microfluidic devices.

Optical oxygen sensing offers an alternative that again has high enough sensitivity to measure oxygen at physiologically relevant concentrations. Optical oxygen sensors fall into two main categories: organic luminescent, and organometallic[101]. The working principle for these compounds is the same and is based on fluorescent quenching where a fluorophore is excited by incoming light, and then emits light as it returns to its relaxed state[102]. This is summed up by the following realtionships[103]:

$$S_0 + hf_{ex} \rightarrow S^* \qquad (1.1)$$

where S_0 and S^* are the relaxed and excited states of the fluorophore respectively, h is Plank's constant and f_{ex} is the frequency of the incoming light. This shows the fluorophore in the excititaion stage. The following equation shows the emission phase:

$$S^* \rightarrow hf_{em} + S_0 \qquad (1.2)$$

where f_{em} is the frequency of the emitted light. Finally, in the presence of some quenching molecule (in this case, O_2), the emission equation looks like:

$$S^* + O_2 \rightarrow S_0|_K \qquad (1.3)$$

where $S_0|_K$ is the limited excited state in the presence of O_2.

As with the amperometric sensors, there has been a great deal of work in developing LOC systems with integrated optical sensors. These fall into two main categories: leaving the dyes in solution[104–106], and immobilising the dyes on the surface of the substrate[86,107–110]. For many microfluidic applications, immobilising the dye has the advantage of using less material, and thus less cost. An example of one such molecule, platinum(II) octaethylporphyinketone (PtOEPK) has been used in many devices due to good optical properties, availability and can be integrated into a variety of materials. Furthermore, the optical stability of the molecule means that under constant illumination, the intensity of the emission only drops by 12%[101] which is much less when other molecules are considered[100]. Full reviews on such techniques and molecules can be found elsewhere[111–113] with the rest of this section summarising the fabrication, and integration of such sensors into microfluidic devices.

Despite being easier to fabricate when compared to amperometric sensors, the patterning of optical sensors can prove problematic with many protocols consisting of multi-step procedures requiring a high degree of user expertise as well as access to clean-room facilities thus detracting from their use in many organ-on-a-chip applications. There are many commercially available fluorescence based oxygen sensors that can easily be incorporated into devices, but the cost of these sensors is often high when compared to something that can be integrated directly into devices[114]. As such, many approaches have been developed to incorporate molecules such as PtOEPK into microfluidic devices. The sensing molecule can be mixed into thermoplastics by dissolving the plastic in a solvent. This solution can then be used to produce a plastic film that contains the sensor[108,115,116]. Additionally, the luminescent molecules can be mixed directly with PDMS before it is moulded and cured. This approach has been used to make membranes with built in oxygen sensing capabilities[117]. However, there remains very few efforts to make the fabrication and integration of oxygen sensing molecules into microfluidic chips cheaper, and quicker. One such approach injected a solution of O_2 indicator beads into a microchannel where the beads were adsorbed onto the surface[118]. As such, there is a need for a technique that allows for the integration of a luminescent oxygen sensor, into thermostatic microfluidic devices, at timescales and a throughput compatible with injection moulding.

1.3 Cell barrier models in drug discovery

Alongside oxygen detection however, there are a wealth of other technologies that have been applied on microfluidic chips with the goal of mimicking the micro-physiological environment and measuring certain aspects of the biological systems. In OoaC devices, the devices generally try to capture human physiology so that the models better predict drug efficacy *in vitro*. While this is of interest to the pharmaceutical industry to lower the cost of drug development, it is not the only consideration that needs to be made when studying a new compound. The delivery method of a drug needs to be taken into account and also how the drug enters the tissue of interest. For orally taken drugs, the compounds must survive the chemical insult of the stomach before it is absorbed through the intestines to enter the bloodstream. This barrier between the gut and the bloodstream is referred to as the epithelium while barriers between the blood stream and organs (such as the blood-brain barrier) are known as endothelium. Epithelia not only function for the protection for other cells, but also to act as a selective diffusion barrier between the lumen of organs and the blood stream. To understand the functionality of the epithelia, their anatomy is discussed below.

1.3.1 Anatomy of the epithelium

In brief, the epithelium is composed of a single layer of cells which are supported and articulated by different structures depending on the organ of interest. Individual cells are joined together by tight junctions which act to firmly hold the cells together and allow the epithelium to act as a relatively impermeable membrane. The spatial organisation of the epithelium can also influence organ function. In the case of the gut, these structures are arranged to form villi which act to vastly increase the surface area of the gut to increase absorption. Furthermore, the epithelial cells undergo constant renewal (every 4-5 days) with new cells being formed in the crypts between villi and old ones shed from the top. The epithelial cells on the villi also contain micro-villi which act to further increase the surface area of the gut. The combination of the villi and microvilli along with folds in the intestine allow the surface to be 600 times greater than that of a cylindrical tube[119]. The anatomy of these villi is shown in Figure 1.4 A.

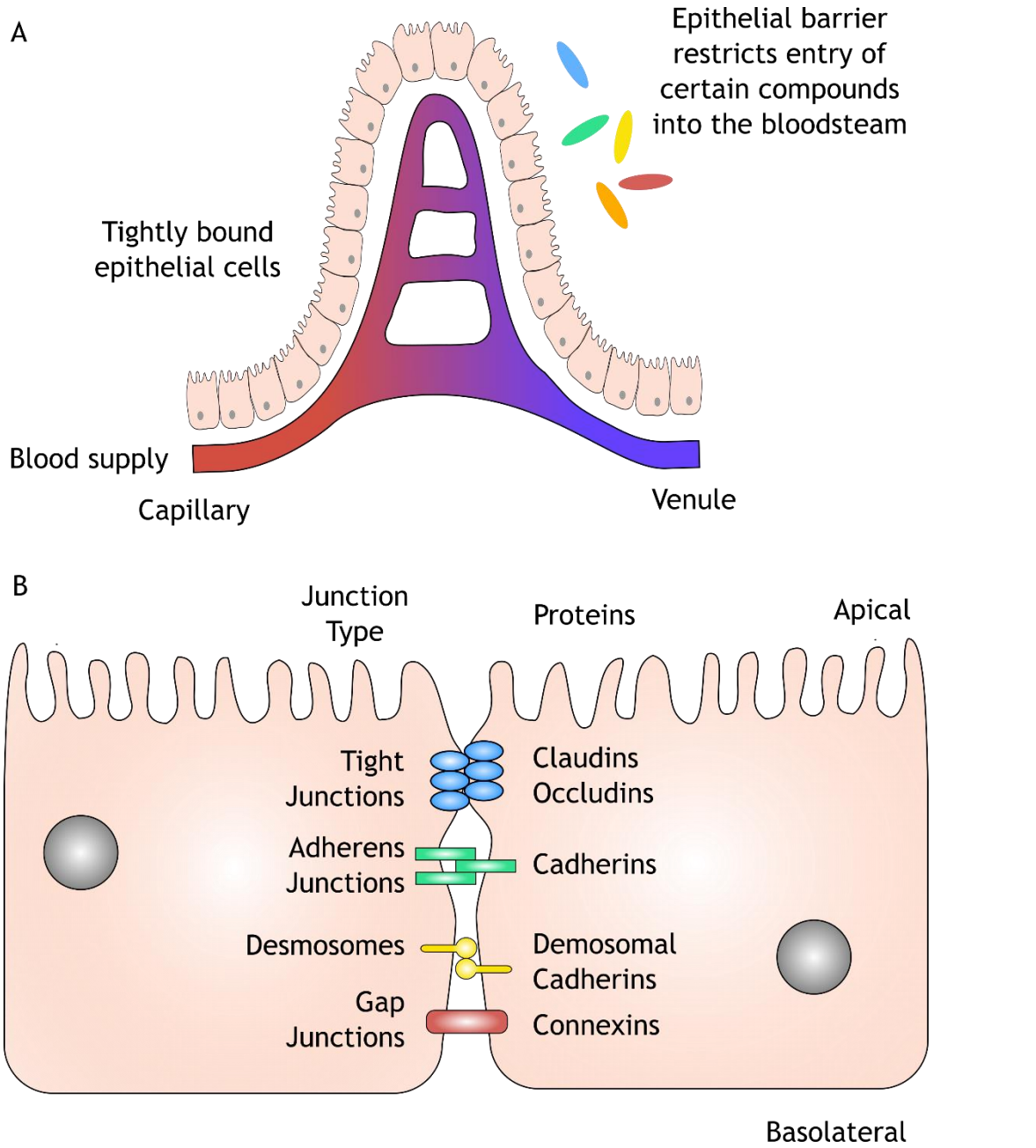

Figure 1.4 – Anatomy of epithelial cell junctions. A shows the micro-anatomy of the epithelia of the gut where cells form structures called villi which are supplied with blood (red) through vessels that extend up into the villi and drain into venules (blue). The cells act as a barrier to prevent certain molecules and pathogens from entering the bloodstream. B shows the junctions present in epithelial cells. Hair-like micro-villi appear on the apical side of the barrier (top). The junction name is on the left of the structures while the protein type is on the right. Gap junctions (shown in red) form channels for the passage of small molecules. Desmosones (yellow) connect cells leaving a gap of ~30nm. Adherens junctions (green) link cells and play a role in cell migration. Finally, tight junctions (blue) form an almost impermeable continuous structure linking cells.

1.3.1.2 Cellular junctions

As mentioned previously, tight junctions act to firmly hold the epithelial cells together and form an almost impermeable membrane between the lumen on the gut, and the blood stream. However, these are not the only junctions present on the epithelium. Figure 1.4B shows a schematic of the epithelium with all the

major junction types. These include gap junctions which bring the cells within 2 nm of each other. These junctions form a channel which allows for the passage of various small molecules and ions to pass between the two cells. Desmosomes also act to bind the cells together and for a link by binding the cytoskeletons of adjacent cells. Desmomsones leave a gap of 30 nm between the cells while adherens junctions are also present. These play a role in linking adjacent cells as well as in cell migration and in the formation of other junction complexes. Finally, tight junctions are perhaps the most important junction of the intestinal epithelium[120]. These junctions are formed of complexes of proteins from the occludin and claudin families (although they are made up of about 35 different proteins) and form a continuous structure that surrounds cells. The extracellular components of these junctions form a tight seal however, this seal can be modified by the cells to provide selective paracellular transport that is, transport around rather than through individual cells). These are dynamic structures that have been shown to adapt to different physiological challenges while also allowing for the passage of small ions and water-soluble solutes while blocking antigens, micro-organisms and toxins from entering the blood stream[121-123]. As these junctions form a tight, almost impermeable barrier, the transport of orally taken drugs through these membranes must be considered when developing a new drug, even if the target organ is far away from the gastro intestinal (GI) tract.

1.3.1.3 Modulation of barrier integrity

As previously mentioned, epithelial permeability is an issue when the oral delivery of a drug is concerned. During development, many compounds are discarded at an early stage due to their poor permeability and thus low efficacy in clinical trials. Furthermore, whole groups of large, hydrophobic molecules with increased complexity exhibit increased safety when compared to smaller, more hydrophilic molecules that readily cross the epithelium[124]. However, these drugs are often not considered viable as their poor transport over the barrier leads to an increase in dose being required, and thus increase in cost. However, with the inclusion of permeation enhancers (molecules reversibly disrupt the epithelia) these larger molecules could become more viable when oral delivery is considered. Permeation enhancers fall into two main categories: paracellular (which disrupt the junctions between cells[125,126]) and transcellular (which disrupt

the cell membranes and allow molecules to pass through the cells[127-130]). However, there is a lack of data preventing the uptake of permeation enhancers in the clinic. Issues surrounding solubility, absorption, distribution, metabolism excretion, and stability are still left unaddressed when PEs are considered. Furthermore, it has been suggested that a dual approach in early drug development addressing the issues above as well as the efficacy is highly important, however, a lack of proven technologies to do this remains a hindrance[124].

Alongside permeation enhancers, there are many pathologies that lead to a disruption of the epithelia and endothelia in the body. One of the main hallmarks of an ischemic stroke, is the breakdown of the tight junctions in the blood-brain-barrier[131]. Also, as the skin is composed of epithelial cells, any laceration or injury to the skin results in an opening of the epithelia which then closes again with time[132]. With this in mind, there is a great deal of interest in studying how the tight junctions in the epithelia and endothelia close up again after insult. As such, a host of technologies have been developed to measure and analyse barrier function *in vitro*.

1.3.2 Barrier integrity measurement techniques

As the study of cellular barriers within the body is of great importance to understanding drug delivery methods and other pathologies, many techniques have been developed in order to visualise and measure barrier function[130]. Here, some of the main techniques are described as well as their advantages and disadvantages when applications for drug development are considered.

Immunostaining represents the most basic analytical tool for the qualitative analysis of tight junctions and barrier properties. In short, membranes are grown, fixed, permeabilised and stained for various proteins so they can then be visualised better through microscopy. For the analysis of tight junctions, the proteins zonula occludin-1 and 2 (ZO-1, and ZO-2) are often used as these proteins occur abundantly in tight junctions[133]. Although a simple assay to run, immunostaining represents and end point measurement and requires killing of the cells and as such real-time measurements cannot be taken. This becomes an

issue when the dynamic nature of the tight junctions is considered as it is impossible to monitor this behaviour through this method.

Freeze fracture microscopy has been used for the study of membranes. In this technique, a sample is frozen rapidly and snapped to reveal the cross-sectional structure of the cells. These structures can then be immunostained to give a qualitative analysis of junction properties. Although this can reveal high resolution images and viewing angles that are impossible to achieve through regular microscopic techniques, freeze fracture microscopy is again an end point measurement. Furthermore, the complex protocols required for this technique mean that it is not high throughput enough for large scale drug screening applications.

Another commonly used assay to determine barrier functionality is the use of labelled tracer compounds[121,123,134]. Here, cells are grown on a membrane separating two areas of media. The compounds are then added to one of the areas and after a specified amount of time the presence of the compounds in the other area of media is measured. In the past, radio labelled sucrose has been used[135] however, the availability of radio labelled molecules and he reliance of expensive detection equipment has meant that researchers have sought other means of labelling the compounds. Horibe *et al* labelled dextrans with Fluorescein isothiocyanate (FITC) which meant that a standard fluorescent plate reader was capable of measuring the diffusion through the membrane[136]. Furthermore, the use of dextrans meant that molecules of different molecular weights could be used while keeping the chemistry of the marker molecules the same. By including a variety of short, medium and long dextran molecules, more information about the structure of the barrier can be obtained with little additional effort. In addition to radio and fluorescent molecules, a simple colorimetric technique can be used as demonstrated by Duffy and Murphy[137]. Again, a labelled protein is added to one side of a membrane, and the passage through the barrier is measured. All three of these techniques (radio, fluorescent, and colorimetric labelled proteins) do not require killing of the cells in order to take the measurement, however, the experiments are often laborious if different conditions are required. Although the use of labelled markers gives quantitiative information about the membrane integrity, this technique again does not give any real-time data on what is happening to the tight junctions.

Additionally, both fluorescent and colorimetric tracers lack the sensitivity of radio tracers while radio tracers have a whole range of issues associated with the storage and disposal of radioactive compounds.

Finally, another commonly employed technique for the analysis of cellular barriers is trans epithelial/endothelial resistance (TEER). In short, the electrical resistance of a monolayer of cells is measured to give non-invasive, real time analysis the barrier properties. The details of this technique are discussed in their own section below.

1.3.3 Barrier integrity study by trans-epi/endo-thelial resistance measurement

In its simplest form, the measurement of TEER involves modelling the cell barrier layer as a direct current (DC) circuit, where the resistance of the system (including the electrodes, media and membrane resistances) is in series with the TEER[138]. This is shown in Figure 1.5A. Typically; these measurements are carried out on transwell systems – inserts that allow for the partitioning of the a well plate into an apical and basolateral compartment separated by a monolayer of cells (Figure 1.5B). Electrodes (often termed "Chop-stick electrodes") are then placed into either side and the resistance of the system can be measured in accordance with Ohm's law (equation 1.4).

$$R = \frac{V}{I} \qquad (1.4)$$

where R is the resistance of the whole circuit, V is the voltage, and I is the current. However, the downside to measuring TEER in such a way, is that by applying a DC current, the electrodes and the cell layer can become damaged due to overcharging. Furthermore, the use of a DC current leads to water splitting meaning that this approach is rarely, if ever used. To overcome these issues, systems have been developed using an AC square wave to dissipate the charging effect and give more reliable results[139]. This is the approach used in the commercially available EVOM2 device[140]. Although better than a simple set up, this arrangement still leads to variabilities in the TEER measurements as the manual positioning of the electrodes can lead to inhomogeneity in the current

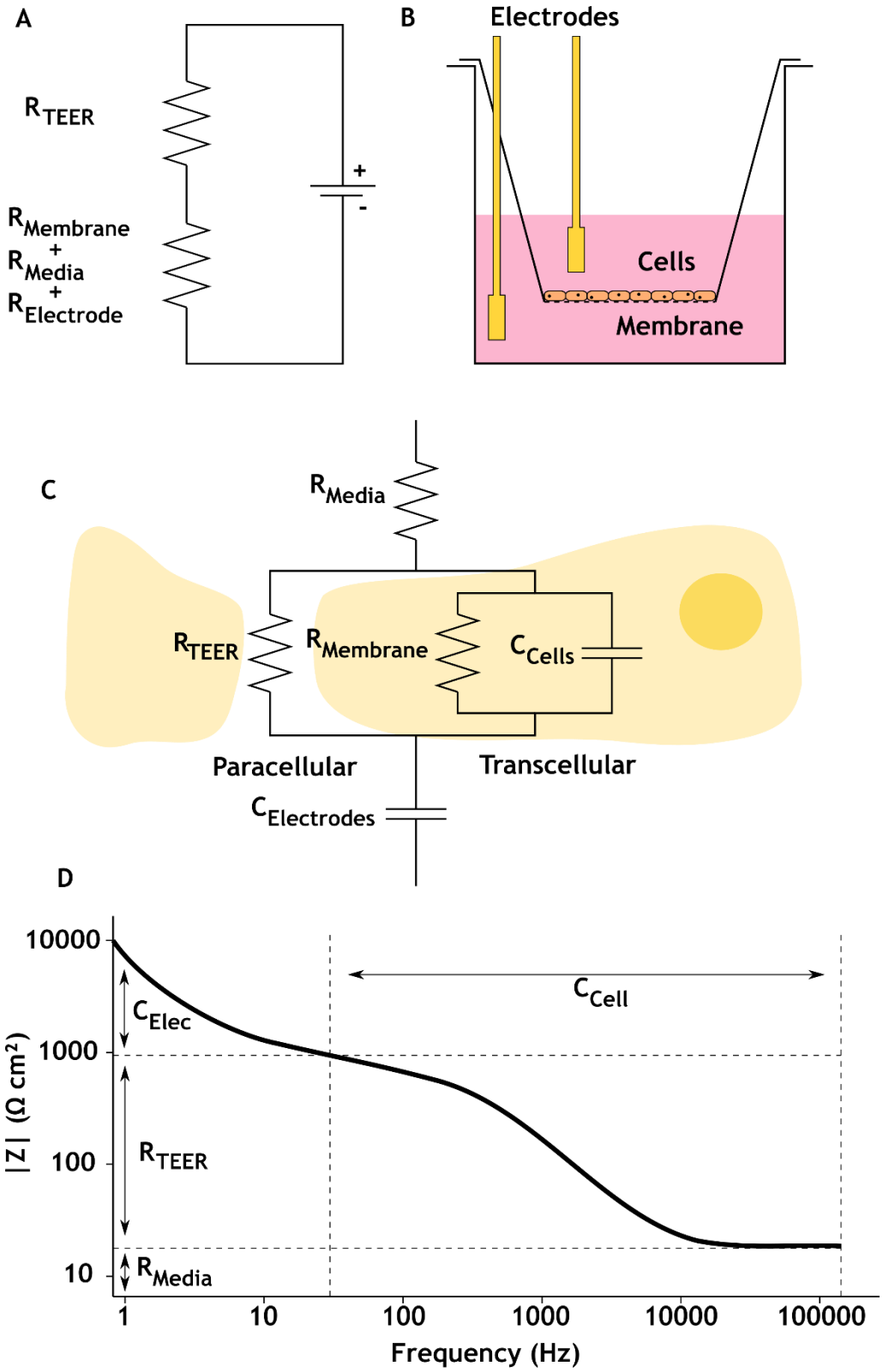

Figure 1.5 – Principles of TEER measurements. A shows an equivalent circuit when DC signal is applied. R_{TEER} is the resistance of the layer of cells while $R_{Membrane}$ is the resistance of the semi-permeable membrane used, R_{Media} is the resistance of the cell media and $R_{Electrode}$ is the resistance of the measurement electrodes. A standard trans-well set up is shown in B with the chop-stick electrodes being used. C shows the equivalent circuit for a cell layer when AC current is considered. Here, $C_{electrode}$ and C_{Cell} are the capacitances of the electrodes and the cells respectively. This also shows how the different components of the circuit split the current path into a paracellular and transcellular pathway. D shows a typical impedance spectrum for TEER measurements and how each of the components affect the shape of the curve.

density, and this variability in the results when compared with other

permeability assays[141]. As such, there have been a great deal of chips developed that contain integrated electrodes to counteract the error introduced by their positioning[142–149]. These chips are discussed in more detail in section 1.3.3.1.

Furthermore, by taking measurements from arrange of frequencies instead of just the 12.5 Hz used by the EVOM2 system[139], more information can be implied from the readout. Similar to the simple DC circuit, an equivalent circuit diagram can be seen in Figure 1.5C. Here, the circuit accounts for the capacitance of the cells (C_{cell} caused by the phospholipid bilayers) and the capacitance of the electrodes (C_{elec}). By measuring not only the amplitude of the resistance of the system, but the phase shift at a variety of frequencies, values can be given to the various components of the circuit through fitting to appropriate mathematical models, thus giving a much more accurate readout of TEER. The impedances are given in equations 1.5 and 1.6.

$$Z = \frac{V(t)}{I(t)} = \frac{V_0 \sin\theta}{I_0 \sin(2\pi f t + \varphi)} \qquad (1.5)$$

$$Z = Z_R + jZ_I \qquad (1.6)$$

where V_0 and I_0 are the peak voltage and current, f is t frequency, φ the phase shift between the voltage-time and current-time functions. Z is a complex function that can be described by the modulus $|Z|$ and the phase shift φ or by a real part Z_R and an imaginary part Z_I.

Because the total impedance of the circuit shown in Figure 1.5C is measured, the impedance Z_{tissue} is often reported as:

$$Z_{tissue} = Z_{total} - Z_{blank} \qquad (1.7)$$

for a given frequency. Where Z_{total} is the impedance of the full setup, and Z_{blank} is the impedance of the setup with no cells, just media (these measurements are taken before the cells are seeded). As various systems vary in their dimensions, and as:

$$Z_{tissue} \propto \frac{1}{M_{area}} \qquad (1.8)$$

where M_{area} is the area of the membrane in cm^2, the actual TEER value is often reported as:

$$TEER = Z_{tissue}\, M_{area} \qquad (1.9)$$

to give a value of Ωcm^2.

An example of how the magnitude of the impedance ($|Z|$) varies with frequency is shown in Figure 1.5D[150]. In this plot, the current can take one of two paths – the transcellular, or the paracellular (through the tight junctions). Both these paths are shown in 1.5C. When low frequencies are considered, the capacitance of the electrodes dominates and so $|Z|$ is influenced most by this. At high frequencies, both C_{elec} and C_{cell} become increasingly conductive so $|Z|$ is dominated by the resistance of the medium. Finally, at mid-range frequencies, the $TEER$ and C_{cell} contribute equally to $|Z|$ giving rise to the overall shape of the plot in Figure 1.5D.

With these advantages over other barrier functionality measurements in mind, TEER measurements have been used to study a wide range of phenomena. Firstly, TEER has been used widely as a means of measuring cell growth and proliferation. Hoheisel *et al.* showed that by adding hydrocortisone to cells, the TEER values after 40 hours were increased two-fold compared to cultures without the glucocorticoid[151]. Wegener *et al.* and Weidenfeller *et al.* reported similar findings showing how the TEER measurements can be used as means of drug testing[152,153]. Taking these findings one step further, Kröll *et al.* not only showed that glucocorticoids lead to an increase in TEER, but also that in the inclusion of astrocytes and pericytes lead to an increase as well[154]. This demonstrates that the tight junctions of the cells are regulated by other cell types – as well as by in inclusion of drugs into the media. Similar to the measure of cell growth, TEER measurements have also been utilised to measure wound healing, and cell migration[155]. In this work, the barrier was damaged through scratching the cell layer and measuring the TEER as the cells began to repopulate. Finally, TEER assays have also been used to show that immune cells

penetrate endothelial barriers by crossing the transcellular pathways as opposed to the paracellular. Wedel-Parlow and Galla showed that although immune cells were migrating from the apical to the basolateral areas of the assay, there was no disruption to the TEER indicating that the tight junctions remained un-touched [156]. These findings were backed up with microscopy data[157].

1.3.3.1 Trans-epi/endo-thelial-resistance measurement on a chip

As previously mentioned, some work has been done to create TEER-on-a-chip devices to take advantage of both the real-time, non-invasive measurement of barrier integrity as well as the advantages associated with microfluidics. One of the first of these chips, described by van der Helm *et al.* showed how platinum wires could be inserted horizontally into microfluidic channels and sealed in place using glue, negating the need for clean room fabrication[147]. Another chip, described by Henry *et al.*, uses polycarbonate plates with evaporated gold electrodes sandwiching 3 layers of PDMS with two containing the microfluidic channels, and one forming the membrane separating them[144]. With this, they demonstrated how the TEER value increased over time as the cells grew on the membrane, and how the barrier integrity recovered after chemical insult. This work was expanded on by Moaz *et al.* to include a multi electrode array capable of measuring the electrical activity of cells, as well as the TEER[145]. This chip was also used by van der Helm *et al.* to show how impedance spectroscopy could be used to isolate the resistive and capacitive elements of a caco-2 cell culture, and show how the impedance was dependant on the flow of media over the cells[146]. Bossink *et al.*, further expanded on the work by van der Helm *et al.* to vertically incorporate platinum wires into chips reducing the obstruction of the membrane associated with the horizontal channels[149]. In short, platinum wire was placed through the PDMS chips into the channels on either side of a membrane. However, all the devices detailed above rely on using PDMS as a means of creating the channels and membranes. While this approach means that chips can be sealed around electrodes and membranes with ease, all the chips suffer from the aforementioned drawbacks of PDMS. While some work has been done to de-skill the fabrication, many biology labs do not have the facilities to make their own PDMS chips and as such, TEER-on-a-chip remains an academic research tool for specialist lab. Chips made in PS material however, would go some way into solving these problems, and mean that chips could be shipped and

shared between research groups, leading to a broader uptake of the technology within life science communities.

1.4 Summary

This Chapter has introduced the concept and fabrication of microfluidics and how they can be applied and utilised to produce organ-on-chip devices. In short, fabrication of PDMS devices was described and the advantages and disadvantages of soft lithography were discussed. PDMS allows for quick, cheap, and simple fabrication of microfluidics devices, however, material properties such as small molecule absorption, leaching of monomer into cell cultures and low throughput fabrication mean that alternative materials and manufacture methods must be considered if microfluidic devices are to be commercially successful. Injection moulding was highlighted as a fabrication method allowing for the high throughput manufacture of microfluidic devices in a variety of thermoplastic materials. However, when the rapid prototyping approach favoured in most research settings is considered, the cost of injection moulding tooling prohibits the uptake of this technology in the wider chemistry and life science communities.

Alongside the fabrication of the microfluidic channels, the incorporation of sensors into chips has been discussed. With regards to oxygen sensing, both potentiometric sensing and fluorescent quenching systems were detailed as well as how these technologies have been incorporated into microfluidic chips already. However, as with the chip fabrication, none of the sensor manufacturing technologies align with the high throughput manufacture of injection moulding. This means that more work is needed in developing an oxygen sensor that can be included in microfluidic chips without the requirement of highly skilled fabrication. This fabrication must also cut down on the time and cost currently associated with microfluidic chip manufacture.

Finally, bio-sensing with regards to tissue integrity (in this case, epithelial barrier function) was discussed. The anatomy of the epithelia was described detailing how tight junctions play a key role in controlling the diffusion of molecules from the gut in to the bloodstream. Different measurement techniques for inspecting barrier function were discussed, with TEER being the

most useful, both in terms of giving a real-time measurement of barrier integrity while also being non-invasive. Efforts to create TEER-on-a-chip systems have also been discussed however, as with the oxygen sensors, none of the fabrication protocols allow for high throughput, low skill manufacture. With TEER being such a ubiquitous technique in life science labs around the world, it is thought that creating an injection moulded TEER-on-a-chip platform would assist biological research, while also allowing for TEER systems to take full advantage of the benefits of microfluidics (low reagent consumption, more physiologically relevant flow etc.).

1.4.1 Aims

The areas that are believed to be lacking in the current microfluidics literature have been described above. It is believed that finding solutions to these problems will lead to a further uptake in microfluidics across the chemistry and life sciences fields while also making the fabrication of microfluidic devices more commercially viable. As such, the specific aims of this project are as follows:

- Develop a platform for the cheap and reliable fabrication of microfluidic devices. This platform should revolve around injection moulding to take advantage of the high throughput capabilities, while also allowing the fabrication of devices in thermoplastic materials to overcome some of the disadvantages associated with PDMS devices.

- Demonstrate how dissolved oxygen concentration can be controlled in PS microfluidic devices and develop a sensor that gives real-time and spatial information on the distribution of oxygen within a device. This sensor should be able to be rapidly incorporated into a microchannel to align with the high throughput manufacture associated with injection moulding. The performance in terms of sensitivity and the temporal resolution should also be determined.

- Demonstrate a barrier on a chip model with integrated TEER measurements for use in modelling barrier permeability. Again, this chip should be assembled rapidly to align with the injection moulding process.

Work on the chip will focus on two areas. First, the assembly of a microfluidic chip including a membrane separating two channels. This assembly should produce a water tight seal while also being quick enough to align with the injection moulding process. Secondly, the electrode material and how the electrodes are incorporated into the device should be investigated to determine the best solution in terms of sealing and electrode performance.

1.4.2 Structure of thesis

With these aims in mind, this thesis is structured accordingly: Chapter 1 discussed the background and motivation for the project. Following that are three chapters documenting the development of techniques and results relating to the aims of this thesis. The first of these (Chapter 2) focusses on the limitations of current tooling fabrication and details how a new approach using 3D printing has been developed. The performance of the 3D printed tooling is discussed in detail. Chapter 3 describes how dissolved oxygen concentration can be controlled within injection moulded PS chips and how that can be applied to better mimic human physiology. This Chapter also documents the development of a novel paint based oxygen sensor and how it can be used to monitor the real-time distribution of oxygen within a microfluidic device. The performance of the oxygen sensor is also discussed in detail. The final results Chapter (Chapter 4) documents the development of a TEER-on-a-chip system for measuring the barrier integrity of various systems. Here, the sealing of an injection moulded PS chip with an integrated membrane separating two chambers is discussed, as well as an investigation into the electrode materials. Furthermore, different means of incorporating the electrodes into the devices are evaluated and the trouble-shooting to better understand the functionality of the device is discussed in detail. In this thesis, the materials and methods are specific to each Chapter with little common techniques and analysis. As such, the materials and methods for the work presented in each section are described at the beginning of each chapter. The final Chapter (Chapter 5) is dedicated to the conclusions drawn from this work and outlook for the techniques and results discussed therein.

Chapter 2 – Development of 3D printed inlays for injection moulded microfluidics

The following Chapter is adapted from Convery et al., *Macromolecular Engineering*, **2021**, 306.

2.1 Introduction and aims

As discussed in Chapter 1, microfluidics offers an improvement of classical analytical techniques such as biochemical assays[16], genomics[17], and live cell studies[20]. Furthermore, microfluidics have also been allowed for the study of new phenomena that were elusive to macro-scale protocols[1,158,159]. These advantages over standard laboratory procedures are largely driven by the physics of fluids on the microscale, where viscous effects dominate inertial effects leading to predictable fluid kinematics[2]. Furthermore, by virtue of the small channel size (100 nm to 100 μm [10]), microfluidic devices allow for much smaller volumes of reagents to be used, as well as faster reaction times[2].

To realise the small architectures required for microfluidic devices, chips were initially fabricated using silicon micromachining process borrowed from the microelectronics industry. These processes such as photo lithography allowed for the fabrication for micro- and nano-channels with dimensions from a few nm, up to several mm [160] and allowed for the creation of the first microfluidics devices[161,162]. However, as microfluidics became more of a mainstream research discipline, a means of fabrication to reduce the reliance on clean rooms with expensive equipment and highly skilled operators became more required.

2.1.1 Problems with existing fabrication methods

As mentioned in Chapter 1, PDMS was used as a means of reducing the complexity of microfluidic device fabrication. While a master structure was still required to be fabricated using photolithographic processes, multiple replicas of the master could be produced quickly with little expertise. The properties of PDMS meant that it was able to replicate nanoscale features[14]. Furthermore,

PDMS is also optically transparent making it more suitable to biological assays than silicon as it is compatible with standard microscopy techniques. In addition to this, PDMS is also permeable to gases making it idea for live cell studies as gas can be exchanged from the cell media and their surrounding environment. This property is discussed in more detail in Chapter 3. PDMS suffers from several limitations that have hindered its use in OoaC and other microfluidic devices. These are small molecule absorption[23,24], deformation under flow[26], leaching of uncured material into the cells [27], the transient nature of any surface treatments[28]. Perhaps the biggest drawback, however is that it is very difficult to scale PDMS fabrication into a commercially viable means of chip production. As PDMS takes time to cure, the throughput of device manufacture is limited to the ~2 hrs curing time per device. Although the fabrication can be multiplexed, the throughput is still limited.

To tackle the material concerns associated with PDMS, researches have sought to fabricate microfluidic devices out of thermoplastic polymers such as cyclic olefin copolymers[163], polystyrene[164], polymethyl methacrylate[165], and polycarbonate[166]. In general, thermoplastic polymers offer lower small molecule absorption; good optical properties for biological assays; and can be manufactured in the dimensions required for microfluidics. Furthermore, almost all tissue culture plastic is polystyrene meaning the behaviour of cells on this material is already well understood, so lends itself to microfluidic applications. However, despite these properties, thermoplastic microfluidics devices are still not readily used in life sciences applications as the fabrication of devices in these materials is more complicated and less suited to small scale, rapid prototyping fabrication than that of PDMS devices. However, a range of techniques have been established to allow for small scale fabrication.

One such approach for the fabrication of polymer microfluidics devices involves the stacking of laser cut layers[167]. In short, the microfluidic channels are cut through thin plastic sheets which are then sandwiched between thicker slabs. This approach means that microfluidics chips can be made and assembled quickly, but also allows for multilayer channels to be assembled with ease. Alongside laser cutting, hot embossing has also been utilised to produce microfluidic chips[50–53]. Here a polymer slab is heated above its glass transition temperature and a stamp is pressed into the parts to transfer the pattern.

Typically, parts are sealed either with tape, or through thermal bonding whereby the parts are again heated to above the glass transition temperature, and held in contact under pressure to form a seal. Similar to the laser cut sheets, channels have also been fabricated by using a laser to engrave structures into the devices[168]. Again, as with hot embossing, this leaves open channels that still require sealing. However, despite all these approaches allowing for the rapid and simple fabrication of small batches of microfluidic devices, when it comes to scaling up the manufacture, they fall short in terms of throughput with the devices requiring upwards of 20 mins to fabricate, seal and package. This detracts from these protocols when commercial scale manufacture is considered. For commercial scale manufacture, injection moulding is considered to be the gold standard both in terms of throughput, and replication quality of microstructures and as such, has been used to industrially produce DVDs and BluRay discs. However, despite the superior throughput compared to other thermoplastic fabrication techniques, injection moulding is seldom used for microfluidic fabrication in the lab. This is due to the fact that the master structures for injection moulding are expensive (costing on the order of £1000s for a LIGA inlay). This means that it becomes increasingly expensive to injection mould microfluidics for the small production runs often required during the prototyping phase. Efforts have been made to fabricate master structures out of other material in a bid to lower the cost (etched quartz[39], etched silicon[40,41], polytetrafluoroethylene (PTFE) backed nickel[42], SU-8 photoresist on nickel[43], UV curable polyurethane resins[44], bulk metallic glasses[45], and SU-8 on polyamide sheets[46]), however, all of these efforts fall short in terms of time required for fabrication and cost when a "fail-fast-and-often" approach for microfluidic development is employed.

Alongside the physical fabrication of the microchannels, an area of equal importance is the sealing of the chips. Despite this, there has been very little effort put into optimising this for microfluidic devices. As PDMS forms a conformal seal with flat substrates, the sealing becomes a large issue when transferring from prototype devices into large scale production. As mentioned above, thermal bonding is often used to seal thermoplastic devices. While this approach means that the devices can also be sealed to a flat substrate such as in PDMS, the time taken to form a seal is often very long (up to 30 mins per device) making it less suitable for high throughput fabrication. As such, the sealing and

the fabrication for microchannels needs to be considered holistically to come up with a process that allows for cheap, as well as rapid microfluidic device manufacture. As such, the aims of this Chapter are detailed below:

2.1.2 Aims

- Find an alternative to the above-mentioned inlay fabrication techniques for injection moulding of PS. The solution will be simpler than existing techniques or, at least, not add any complexity to the fabrication protocol.
- Determine the limitations of said solution in terms of resolution, minimum/maximum feature sizes, a replication quality of moulded parts.
- Implement a rapid sealing process to complement the injection moulding fabrication and determine the limitations and design requirements of such a protocol.
- Fabricate and demonstrate a functional, injection moulded, microfluidic device.
- Quantify and document successes and failures in meeting these aims.

2.1.3 Overview of chapter

This Chapter documents the development of a 3D printed tooling solution which can produce microfluidic devices through injection moulding. Firstly, the materials and methods used for this work are documented. Also detailed are the considerations concerning the choice of 3D printing material, the orientation of the inlay during the printing process, and the design of the microchannel such that devices with a predefined geometry can be achieved. Also discussed is the durability of the 3D printed inlays and how polishing the inlays can produce devices with greater optical clarity high enough for imaging cells. Analysis into the robustness of the sealing of the chips through both ultrasonic welding, and lamination is given as well as a discussion of and how the design of the weld seams can be optimised to reduce any changes to channel geometry. These two sealing methods are also compared to thermal bonding to highlight the advantages and disadvantages of each approach. Furthermore, the fabrication of devices through 3D printed inlays and ultrasonic welding is compared to existing

fabrication protocols. Finally, a functional microfluidic device is demonstrated capable of maintaining a liver organoid culture for as long as 7 days.

2.2 Materials and methods

As mentioned above, this project concerns the fabrication of fluidic chips with integrated functionalities such as in-built sensors. However, before any additional functionalities can be incorporated into the chips, the chips themselves must be fabricated in a robust manner. This section describes the processes by which basic chips are fabricated through injection moulding.

2.2.1 Inlay fabrication

The inlays used as master structures in the injection moulding machine are designed to fit into existing tooling. This tooling allows for interchangeable inlays to be inserted into the machine so that a variety of different channel geometries can be moulded without having to invest in new tooling each time. As discussed in Chapter 1, the cost and time associated with producing master structures for injection moulding is prohibitive to its use in applications outside of mass production. In this work, inlays are fabricated through stereolithography (SLA) 3D printing. Details of this process are given below.

Inlays were designed using Solidworks computer aided design (CAD) software (Dassault Systèmes, France) and printed using a Form2 or Form3 printer (Formlabs, US) in both Clear and High Temp resins (Formlabs proprietary resin formulations). This system uses a stereolithography (SLA) process in which a photocurable resin is selectively patterned by a laser for each subsequent layer. After each layer is defined, the build plate of the printer is raised leaving a gap between the previous layer and the bottom of the build tank for the subsequent layer to be cured in. Post printing, parts are removed from the build plate and any un-cured resin is removed by washing in isopropyl alcohol whilst agitating for 10 mins (Form Wash, Formlabs). Finally, all parts were allowed to dry under a stream of nitrogen (using a nitrogen spray gun) before the clear resin was cured using a Form Cure (Formlabs) for 30 mins at 60^{o}C, and the high temp resin was cured under the same conditions for 60 mins. This process uses 405 nm light from LEDs to fully cure the resin. This is in accordance with the datasheets for

both the resins[169,170]. However, in some instances. The cure time on the high temp resin was cut to 30 mins in an attempt to produce an inlay that was less brittle, and thus less susceptible to cracking in the injection moulding machine. All inlays were printed with a layer height of 25 µm which was the minimum layer height possible on both the Form2 and Form3 printers. Injection moulding inlays were designed with dimensions of 24.7 x 24.7 x 8 or 27.7 x 77. 7 x 5 mm to fit into the existing injection moulding tooling. How the tooling fits into the injection moulding process is shown in Figure 1.2.

2.2.2 Annealing of inlays

As mentioned above, attempts were made to fabricate inlays from the high temp resin that were less brittle. This was due to the fact that despite the high temp resin having a working temperature that was more suited to the injection moulding process, the material proved too brittle to withstand the high pressure (350 bar) inside the injection moulding machine. In an attempt to increase the toughness of the inlay, the parts were fabricated as above however, prior to moulding, the high temp resin inlays were placed into an oven at 250^{o}C for 2 hrs before being allowed to cool.

2.2.2 Inlay and moulded part characterisation

Once the inlays had been fabricated, multiple approaches were used to characterise the in terms of their surface roughness, optical clarity, and the dimensional fidelity of the 3D printing process. Details of these characterisations are given in the subsequent sections.

2.3.2.1 Surface characterisation

The surface roughness of a fluidic channel is an important factor when considering its performance. Any roughness on the surface of a microfluidic device can disrupt the laminar flow along the channel and lead to unwanted mixing within the device. The roughness is also an important factor when considering the pressure drop in a fluid flow. Furthermore, roughness can also affect the optical properties of a device with an increase in the roughness likely to distort light as it passes through leading to a reduction in the resolution of

images that can be taken in the chips. To determine the surface roughness, an Alicona Infinite Focus G4 optical microscope (Bruker, US) using a 10x objective (Olympus, Japan) was used to take 3D scans of the surface of blank inlay, that is, an inlay with no fluidic or sealing features present on it. As optical profiling relies on light being reflected from the surface of the device, the blank inlays were sputter coated with a mixture of gold and palladium to increase the reflectivity of the surface. Images taken from microscope were analysed and surface roughness measurements obtained from Vision 64 Map Software (Bruker). Figure 2.1A shows how the surface features on a sample are defined.

2.2.2.2 Optical clarity

Although surface roughness is a useful metric for comparing the quality of microfluidic devices, its surface roughness can be misleading as an indicator of optical clarity. As can be seen in 2.1A, there are multiple components that make up the roughness of a surface. In the case of 3D printing, the roughness is dominated by the waviness created by the lay of the laser. This means that any roughness measurements must be able to capture these large-scale undulations in the surface of a part. If the waviness is not considered, the surface measurements will only show the roughness which does not give a good indication of optical clarity. As mentioned above, the roughness of a surface can lead to the distortion of light as it passes through the sample. This mean that small objects in the microchannels (such as cells which range in size between 10 and 100 μm) will appear distorted on micrographs. Although surface roughness gives an indication of this, it is often better to measure the optical clarity directly. This was done with the use of a 1951 USAF wheel pattern test target (Thorlabs, Germany). This target it illustrated in 2.1B. The target was placed on top of the PS chips moulded from 3D printed inlays and imaged with an EVOS 7000 (Thermo Fisher, US) microscope with a 10x objective (Olympus, Japan). The optical quality (in terms of line pairs/mm (lp/mm)) was determined by seeing what the smallest group 3 lines that could be made out as separate objects were on the target. Using group and element number (as defined by the target), the resolution could be calculated with equation 2.1.

$$Resolution = group\ number + \frac{element\ number - 1}{6} \tag{3.1}$$

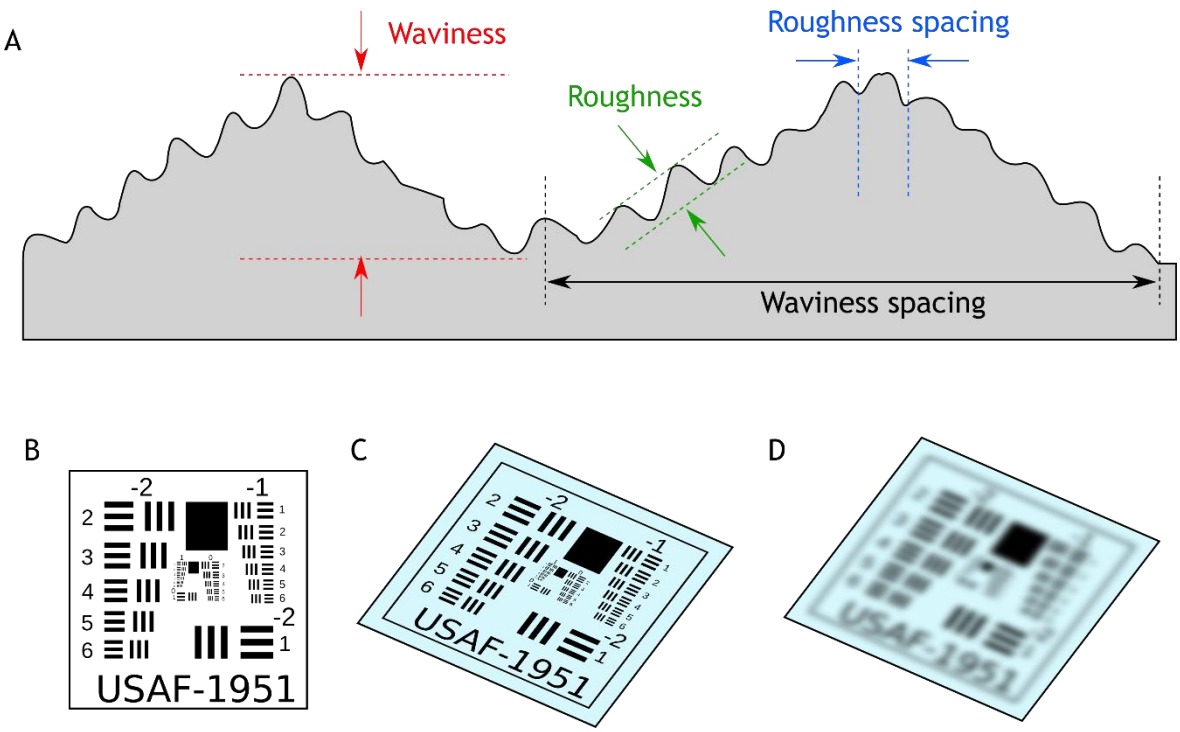

Figure 2.1 – Surface roughness vs. optical clarity. A shows how the various components of surface roughness are defined. These include the waviness (red), roughness (green), roughness spacing (blue), and the waviness spacing (black). B shows an image of a USAF-1951 optical clarity target while C shows the target as seen through an optically clear sample. D shows the blurred image of the target as would be seen through a non-optically clear sample.

To improve optical quality, the inlays were polished using Brasso (Reckitt Beckiser, UK) and a microfiber cloth. This was done by hand polishing the surface of the microchannel for ~1 min. This was done prior to moulding so that the polished surface was replicated in the PS chips. Schematics of the optical clarity target imaged through clear, and rough samples are shown in Figure 2.1C and D respectively.

2.2.2.3 Feature Dimensions

Alongside the surface roughness and optical clarity, the feature size of the 3D printed inlays is also an important factor in determining the performance of microfluidic devices. As discussed in Chapter 1, the feature size of microfluidics leads to a prevalence of laminar flow (in accordance with the Reynold's number [3]), the dominance of diffusive mixing over advective (Peclet number[2]), and shorter reaction times. The characteristic dimension of the channel plays an important role in determining the flow properties as per these equations. The characteristic dimension is often described as the smallest dimension that characterises a channel. As such, the ability of the 3D printer to accurately and

precisely realise features of a pre-defined geometry is important when it comes to making master structures for injection moulded microfluidics. Details on how this dimensional fidelity was measured are given below.

Firstly, the ability of the printer to accurately print structures of a given height was determined. Inlays were printed with a series of rectangular cross-section channels ranging from 100 x 600 µm tall, and either 200, 400 or 600 µm wide. Once printed and cured, the inlays were sawed most of the way through from the back and then snapped so that a clean cross-section of the channels could be imaged. The parts were then sputtered with gold/palladium before cross-sectional images were captured using a Hitachi S4700 scanning electron microscope (SEM) (Japan) at 100x magnification. Figure 2.2A shows a representative image of the cross-section of a feature on a 3D printed inlay. Images were adjusted for contrast and the background was removed using ImageJ (National Institutes of Health and the Laboratory for Optical and Computational Instrumentation, US) (2.2B) before the cross-sections of the channels were analysed and measured using a Python script. This script took each image and looked for the pixels with the highest pixel value (which corresponded to the areas at the edges of the part after the contrast was adjusted). The script then looked for the white with the highest position in each pixel column. Once this had been repeated for every column in the image, a trace of the microchannel could be obtained. This trace is shown in Figure 2.2C. From here, the height was defined as the distance between the max value of the trace, and the lowest (2.2D).

The width of each channel was more difficult to define however. Although the channels were designed with a rectangular profile, the SLA printing process meant that the features present on the inlay had a more trapezoidal cross-section with rounded corners. To account for this, and reduce the effect of error that any corner radius would have on the measurement of the width at either the base or the top of the feature, the width was defined as the measured with at 50% of the maximum height (shown in 2.2D). In order to characterise the feature widths, the printer was capable of reproducing, features were printed with widths ranging from 100 – 600 µm and at heights of either 200, 400 and 600 µm. Parts were cleaved, sputter coated and imaged as described above.

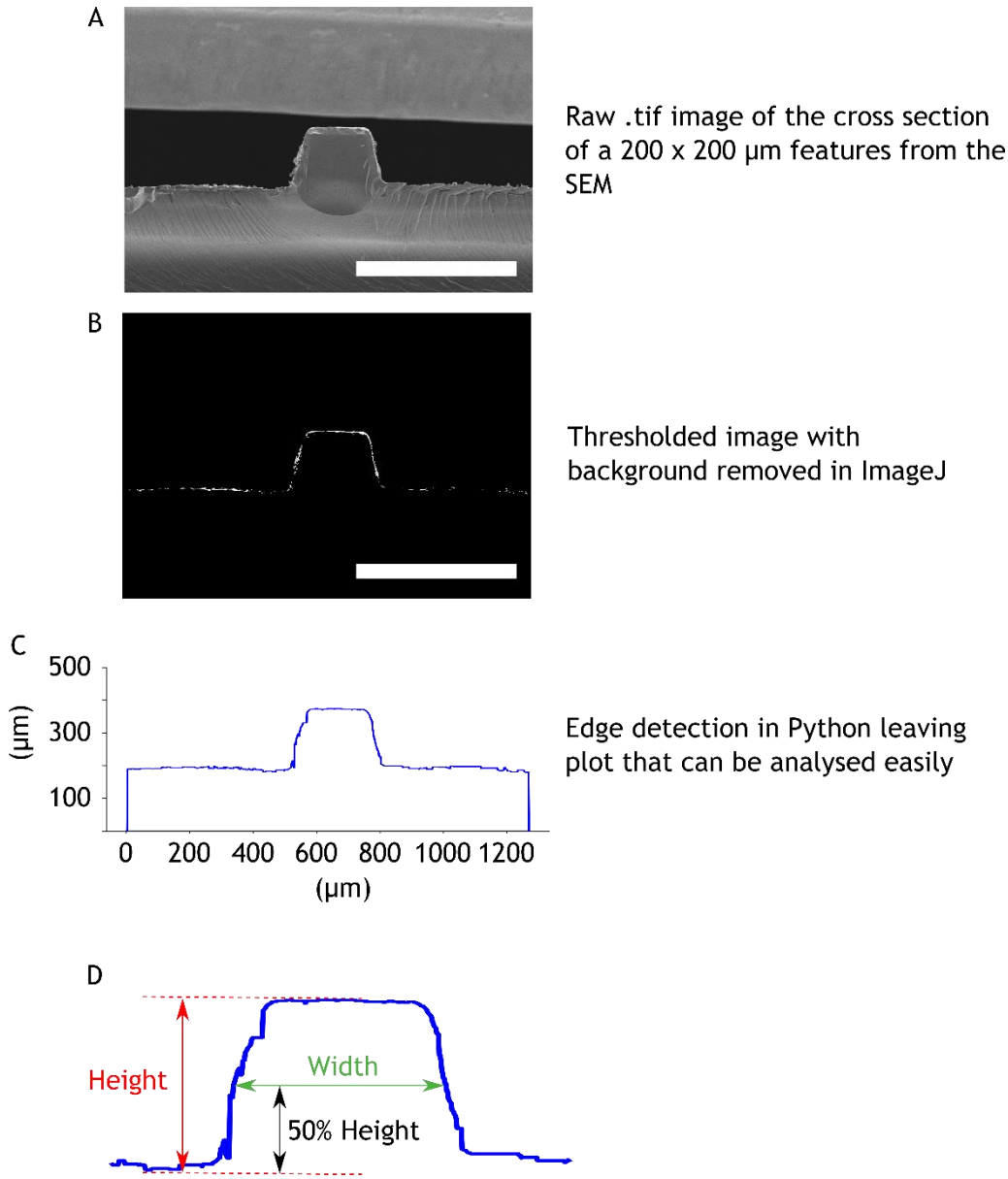

Figure 2.2 – Cross-section analysis using Python. A shows an SEM micrograph of a 200 x 200 µm feature on a 3D printed inlay. This image is then thresholded to leave only the bright pixels (which correspond to the feature edges and the background in removed in ImageJ (B). These images are then analysed in a python scrip which create a trace of the outline of the feature (shown in C). The height (red) and width (green) are defined in D. Scale bars = 500 µm.

The resolution of the printer is also in important factor when it comes to characterising the fabrication processes. The resolution here is defined as the closest that two features can be placed on the inlay without merging into each other. This was determined by printing features with different spacings between them. The height of the features was then measured with the resolution being defined as the minimum spacing between the features such that the full height of the feature was realised. The resolution is important as it defines the density at which features can be placed on the inlay.

The dimensional characterisation of the PS injection moulded parts was done in exactly the same way, with the only difference being that the parts were dipped in liquid nitrogen after they were sawed most of the way through. This ensured a cleaner snap on the parts leading to a cleaner cross-section that could be imaged.

2.2.3 Injection moulding

To fabricate the PS chips form the 3D printed inlays, an injection moulding process was used. An injection moulding machine works by heating a polymer in the barrel above its melt temperature. A screw inside the barrel drives the polymer from the back where the hopper enters, towards the nozzle. As the polymer travels through the barrel, it is heated by series of heating elements that get progressively hotter to heat to the polymer to its final injection temperature. The screw also acts to mix and homogenise the polymer melt. A non-return valve located at the end of the screw allows for plasticised polymer to fill the nozzle cavity, however, when the cavity is full, the valve closes preventing the polymer from moving back down the barrel. This also allows for the plasticised polymer to be injected into the mould cavity under pressure when the injection cylinder is activated. A schematic of the moulder is shown in Figure 1.2.

On the other side of the nozzle sits the tooling. The tooling for this project resembles that shown in Figure 1.2. It is here that the 3D printed inlay sits held into place in the tooling by a steel frame. The printed inlays are designed to the dimensions detailed in section 2.2.1 in such a way that they fit snuggly in the frame with the use of a 12 mm thick backplate. Once the inlay is in place inside the tool, and the tool close, the polymer can be forced from the nozzle cavity into the mould cavity created by the inlay, the frame and the tooling. The polymer is then allowed to cool, before the tool is opened and the part is injected. This whole process typically takes under a minute.

In this project, polymer replicas were fabricated in polystyrene (PS) (1810 crystal polystyrene, Total Petrochemical and Refining, Belgium) using a Victory 28 injection moulding machine (Engel, Austria). PS was chosen as it is the primary material used for tissue culture devices in life-sciences[22]. The Engel

injection moulding machine used here is what would typically be used in industry to create parts in a similar size to those made in this work. Given that injection moulding allows for the rapid and efficient production of parts, the use of an industry standard Injection moulding machine meant that all the fabrication here could easily be translated to a mass-production without having to alter the process to account for the differences between industrial injection moulding machines and benchtop machines commonly seen in research settings. Table 2.1 shows the exact parameters used for moulding in PS throughout the injection moulding work conducted in this project.

Parameter	Value
Melt temperature (°C)	260
Shot volume (cm^3)	4.0
Injection speed (cm^3/s)	1
Holding pressure (bar)	350
Initial cooling time (s)	35
Secondary cooling time (s)	10

Table 2.1 – Injection moulding parameters

A melt temperature of 260°C was used as this was hot enough to allow for all the PS to melt and flow freely into the mould cavity, while not being hot enough for the PS to burn. As the cured resin used here is less thermally conductive than traditional injection moulding master materials (metals), a relatively long cooling time (35 s) was required to ensure the parts cooled below the glass transition temperature (90°C for PS) in the mould. After the part had been cooled sufficiently, the tool was opened slightly (5 mm) for 10 s to ensure the part was cooled further before releasing from the mould to avoid warping. This prevents any deformation that can occur when the part cools after it is ejected from the tool. After this time, the tool opened completely, and the part was ejected. The lack of thermal conductivity from the inlays also means that a lower injection speed can be used (1 cm^3/s) as the polymer is less likely to cool

in the mould before it has completely filled. This lower injection speed results in a lower injection pressure which helps to prolong the life of the 3D printed inlay. A relatively low holding pressure when compared to other work (350 bar) was used to prevent the inlay from deforming. Too low a holding pressure can result in defect where the part shrinks in the mould however, defects such as these were not observed in this work.

Once the parts are ejected from the injection moulding machine, they still contain the gate and the sprue. The sprue is the piece of plastic that cools and solidifies in the injection nozzle of the injection moulding machine. The gate is a structure on the tooling that allows the injected polymer to spread out before reaching the mould cavity and ensures even filling of the mould and it is this structure where the molten plastic cools and solidifies first. This means that nor more plastic can enter the mould, so the screw retracts and prepares the shot for the next part. The gate and the sprue parts can be snapped away from the moulded chips once they have been ejected from the mould cavity, or cut off using scissors.

After the parts had had their gates and sprues removed, inlet and outlet holes were drilled in the device. These were drilled using a 0.7 mm drill bit and drilling speed of 100 rpm. This low drilling speed was used as it was found that the parts melted as a result of the friction when higher speeds were used. The inlets and outlets were drilled so that after sealing, it was possible for fluid to flow into and out of the devices.

2.2.4 Plasma treatment

Once the PS chips have been injection moulded, certain steps need to be taken in order to tailor the surface of the channels towards more attractive properties depending on the application. PS is naturally a hydrophobic material, and it is widely known that cells require a hydrophilic surface to attach to, grow, and divide. To make the surface of the PS hydrophilic, parts were subject to an oxygen plasma to break the carbon-hydrogen bonds on the surface and replace them with hydroxyl groups which increase the surface energy of the PS thus making it more hydrophilic. It should be noted however, that the nature of these hydrophilic treatments is transient. Thermoplastics such as PMMA have been

shown to recover its hydrophobic properties over a number of hours[171], while PDMS has been shows to have a hydrophobic recovery time on the order of minutes[172]. Possible causes for this hydrophobic recovery are reorientation of the polymer chains in the material due to the thermodynamically unstable high energy surface[173], or contamination from materials such as hydrocarbons or moisture[174]. With this in mind, parts were kept as clean as possible between their plasma treatment, sealing, and eventual use in cell culture experiments.

To treat the samples in this work, the PS chips were placed in a plasma chamber (Plasmafab) for 1 min at 80 W. By increasing the surface energy of the parts, the capillary force is also increased which allows fluids to wick through the channels without any external fluid drive. This aided in the sealing tests as any leaks were easy to spot as the fluid quickly spread from the channel throughout the whole chip.

2.2.5 Sealing

As mentioned above, and discussed in Chapter 1, the bonding of PDMS devices is trivial as the elastic nature of the material means that it creates a conformal contact with a given substrate. This means that PDMS can simply be pressed against a blank substrate in order to seal the channel and create a microfluidic device. However, as thermoplastics such as PS are stiffer (characterised by their higher Young's Modulus), they do not form such a conformal bond when held into contact with other materials. As such, other means of bonding the parts and sealing the channels need to be utilised. Two such means of sealing injection moulded PS fluidic chips are given below.

2.2.5.1 Ultrasonic welding

Ultrasonic welding is a process commonly used in industrial settings to bond two thermoplastic parts. During ultrasonic welding, parts are joined by vibrating the interface between them. This friction melts the polymer and the parts fuse together. Using energy directors (referred to as weld-seams) the energy is localised to predefined regions, reducing heating and warping of the overall part. As such, triangular weld seams of varying dimensions were incorporated round the edge of the channel during the design. The process of ultrasonic welding typically takes <5 s so was seen as an attractive means of sealing

injection moulded parts. As the injection moulding machine can produce multiple parts per minute, the sealing of the chips also had to be as quick in order to not slow the production of the devices down too much. Furthermore, ultrasonic welding creates a hermetic seal between the parts without the need for any extra adhesives which may block channels or interfere with any biological systems inside the chips. A detailed description of the welding process is given below.

Prior to sealing, parts were plasma treated in O_2 (80 W, 1 min) to increase their hydrophilicity. Channels were placed against against a moulded PS blank under the sonitrode of a Standard 3000 welder (Rinco Ultrasonics, Switzerland). Tape (Scotch, 3M, US) was used to secure the parts to the base of the welder and prevent them from moving as a result of the vibrations of the welding process. In this work, either differential mode (which controls the welding by moving the sonitrode a set distance), and energy mode (which controls the welding by transferring a set energy into the device) was used to weld the devices while a hold time of 2 s was used throughout to allow the welds to cool before the parts were removed from the tool. Successful sealing of the channels was determined by filling the channel with food colouring and examining for leaks. A part with no apparent leaks after fluid had been in the channel for 10 mins was deemed as a successful weld. Details on how this process was optimised for the welding of chips moulded from 3D printed inlays are discussed in Chapter 3. To fully characterise the effects that the UW process had on the geometry of the channel, the chips were then cleaved and sputter coated (as per section 2.1.2.3) and their cross sections imaged by SEM.

2.2.5.2 Lamination

Alongside ultrasonic welding, lamination was also explored as a means of sealing the chips. As it was found that the weld seams required for ultrasonic welding left a small gap between the parts once bonded, another sealing process was required in instances where that added height to the channel was unacceptable for the performance of the chip. For the sealing by lamination, plasma treated chips containing no weld seams were placed in a lamination pouch (either woven fiberglass, Kapton film, or brass plates) along with a plasma treated 100 µm thick PS foil for the chip to seal to. A thin PS film was used to ensure an efficient

heat transfer to the interface between the layers of the device. The chips were then passed through an Armoured660 Heavy Duty A3 Office Laminator (Swordfish, UK) at temperatures ranging from 90 – 170°C and with the number of passes ranging from 1 – 4. Sealing success was again determined by filling the channels with dye and examining for leaks as detailed above.

2.2.6 Fluidic connections

As mentioned previously, inlet and outlet holes were drilled into the chip prior to sealing in order for the fluid to have a pathway into and out of the sealed devices. However, in order to connect the chips with pumps to drive the flow of fluids, connections need to be made on the chips in order to connect tubing to. This section describes the two forms of fluidic connections used for the chips described in this project.

3.2.6.1 Flanged PEEK tubing connectors

In order to connect tubing to the chips with a minimal dead volume and without the need for glues or adhesives, a method using flanged polyether ether ketone (PEEK) tubing was used to connect tubing to the chips. This was done by 3D printing a connector out of polycarbonate (Ultimaker, US). Polycarbonate was used as the connector had to be tough enough to withstand the clamping force, as well as being able to be cleaned by autoclave use in cell culture experiments. These connectors consisted of two flat plates with hole through which an M3 bolt could be inserted to clamp the two parts together. The top piece contained an M6 threaded hole in the middle through which a PEEK fitting could be screwed (Vici Jour, Switzerland). These fittings contained a hole through which a flanged length of PEEK tubing could be inserted. The tubing was flanged with an Easy Flange Kit (Vici Jour). Once the connector was assembled, the 3D printed parts were placed either side of the microfluidic chip such that the flanged tubing lined up with the drilled holes. The threaded PEEK fitting could then be screwed down which pressed the flanged end of the tubing against the PS chip. The fitting was screwed down such that there were no leaks when fluid was flowed through. The flanged fluidic connectors are shown schematically in Figure 2.3A.

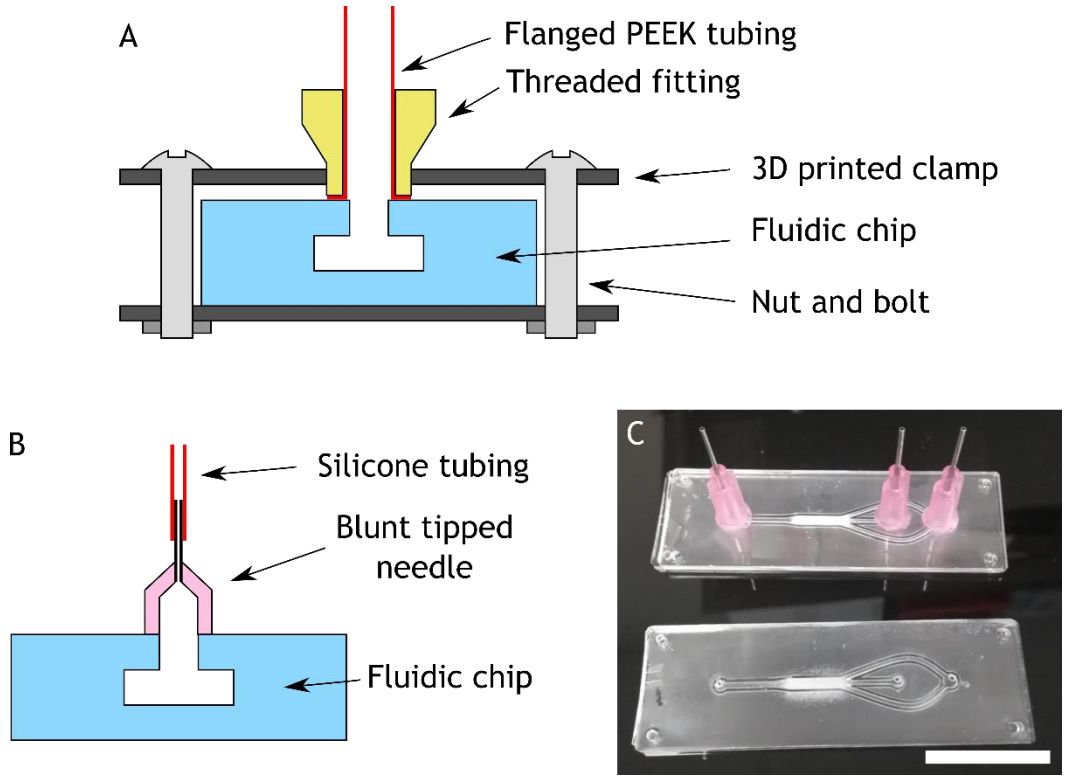

Figure 2.3 – Fluidic connectors. A shows a cross-section schematic of the flanged PEEK connectors using a 3D printed clamp and a threaded PEEK fitting. B shows a cross section schematic of the blunt tipped needle connectors which are glued to the chip. C shows a photography of a chip before (bottom) and after (top) the needles have been glued on. Scale bar = 25 mm.

Despite the fact this this connector required no glue and had a minimum dead volume, it proved unreliable with the connectors prone to slipping during experiments. A such, a method using glue and blunt tipped needles was also used to connect the chips to tubing.

2.2.6.2 Blunt tipped needle connectors

To solve the reliability issues associated with the flanged PEEK tubing connectors, an alternative solution using needle tips was also used. Here, 18 g blunt tipped needles (Metcal, US) were simply glued to the device using UV curable glue (Loctite, Germany). To do this, and reduce the risk of blocking the flow path, a small quantity of glue was dispensed onto a clean surface. The base of the needle was then dipped into the glue ensuring that there was an even coat surrounding the entire way around the base. The needle was then placed onto the chip before the glue was cured with a 405 nm laser pen (Amazon, US). Once the initial layer of glue was cured, additional glue was added to the outside of the needle base to increase the strength of the bond. The chip with connectors was then placed into the Form cure under UV for 10 mins to cure completely. Once the glue had set, tubing could simply be slipped over the

needle to connect it to a pump. Again, a schematic of this connector is shown in 2.3B with a photo of a device both prior to adding the connectors (C, bottom) and with the connectors (top).

2.3 – Organoid culture and staining

Liver organoids were generated by Sean Harrison and Gareth Sullivan at the University of Oslo according to previously described protocols [175,176]. Once the organoids had been grown, they were pipetted into 50 ml tubes along with 25 ml of media (see section 2.2.1.1). The tubes could then be packaged with heat packs and shipped to the lab in Glasgow.

Once the organoids had arrived, they were placed in conical flasks and incubated at 37°C with 5% CO_2. In the incubator, the organoids were constantly agitated by a shaker plate (100 rpm) to prevent the individual organoids from merging together. The media was changed every 48 hrs by removing the flasks from the incubator and placing the flasks on an uneven surface such that one side of the base of the flask was higher than the other. The flasks were left like this for 10 mins to ensure all the organoids had fallen to the bottom most part of the flask. The old media could then be removed, and 25 ml of fresh media added before the flask was placed back in the incubator.

For the OoaC experiments, the flasks were removed from the incubator and organoids were pipetted from the flasks. These were then pipetted into the channels before the flanged PEEK connectors (section 2.2.6.1) were added so that the media could be flowed through (Aladdin Syringe pumps, WPI, UK). Media was either flowed though at a rate of 100 µl/hr or left without flow. After 1, 3, or 7 days, the cells, the fluidic connections were removed from the chip so that the cells could be stained. This was done by first pipetting PBS through the chips to wash any media off of the organoids, taking care to only pipette the media in the direction of media flow so that the organoids would not be moved from their location at the trap in the device. Once washed, a live dead stain (LIVE/DEAD Viability/Cytotoxicity Kit, for mammalian cells, Invitrogen, US) (2 µM Calcein AM, and 4 µM ethidium homodimer in PBS) was pipetted into the chip. Calcein AM works as a stain for live cells, as it does not fluoresce until it is transported though the lipid membranes and converted in calcein by live cells.

Eithidium homodimer cannot travel through the membrane of cells unless they are damaged hence it's use in staining dead cells. The chip was then incubated for 15 mins as per the viability kit instructions before it was imaged on a Zeiss LSM700 confocal microscope using Zen capture software.

2.3.1 Organoid media recipe

To make 600 ml or organoid media, 483.5 ml of L-15 Medium Leibovitz (Sigma Aldrich) was mixed with 50 ml fetal bovine serum (Biowest, France), 50 ml tryptose phosphate broth (Sigma Aldrich), 6 ml 100x GlutaMAX-I supplement (Thermofisher, US), 6 ml Penicillin streptomycin (Thermofisher), and 3.5 ml 100x Insulin-Transferin-Selenium (Thermofisher). Also added was 1 ml of 30 mg/ml (w/v) sodium L-ascorbate (Sigma Aldrich) in PBS, 6 ml of 1 mM hydrocortisone-21-hemisuccinate sodium salt (Sigma Aldrich) in PBS, 60 µl of 1 mM dexamethasone (Sigma Aldrich) in Dimethyl Sulfoxide (DMSO, Sigma Aldrich), and 60 µl of 1 mM N-hexanoic-Tyr, Ile-(6) aminohexanic amide (dihexa, Sigma Aldrich) in DMSO. All the components were placed in a corning vacuum filter and filtered before the media was kept in the fridge until needed.

2.4 Fabrication of 3D printed inlays for injection moulding

To realise the aims of this chapter, a fabrication protocol was required that allowed for the manufacture of micro-scale features while also being able to withstand the pressure and temperatures of a typical PS injection moulding cycles (>350 bar and 250^{o}C respectively). Furthermore, any such protocol should be simple to follow and require minimal expensive equipment or expertise.

3D printing is a rapidly evolving fabrication technique that while requiring little in the way of technical expertise, is also capable of realising features in the order of 100 µm. As such, 3D printing has been utilised as a means of direct fabrication for a wide range of micro- and milli-fluidic devices[177]. However, despite all 3D printers relying on a sequential stacking of 2D layers, there is two main printer types that are used to achieve this: Fused deposition modelling (FDM) and stereolithography (SLA). FDM is the method by which most affordable 3D printers operate and in this technique, thermoplastic polymers are heated to above their glass transition temperature (Tg) and extruded through a nozzle in a

pre-determined pattern onto a build-stage. This staged is moved down after every layer has been patterned so the subsequent layer can be deposited on top. This process is shown in Figure 2.4A. As this process requires the melting of polymers, only thermoplastic polymers can be used in this process. This means that many FDM parts cannot be used in injection moulding applications as the glass transition temperatures of such materials are often close to the processing temperatures of injection moulding polymers which would lead to deformation of any printed tooling.

On the other hand, SLA cures a photoactive polymer by irradiating with a high energy laser. Here, a build platform is submerged into a tank filled with resin leaving a gap at the bottom which defines the layer height of a print. A laser is then scanned across the bottom of the tank in a predetermined pattern before the build plate is raised with the cured layer attached and the subsequent layer can be cured (Figure 2.4B). After the full part has been defined, the piece often needs to be washed to remove any excess solvent and then further cured so that the maximum mechanical properties can be reached. Through this process, 3D printed parts can be realised in thermoset polymers thus avoiding the issue of deformation due to the high heat and pressure in the injection moulder. Furthermore, Formlabs, makers of the Form family of SLA printers have developed a wide range of materials for SLA printing including a high temperature version for parts that are to be used in hot environments. Additionally, SLA systems, while more expensive than their FDM counterparts, are still relatively affordable with many systems available for under £1000. Thus, SLA was considered as the superior technology for printing injection moulding inlays and results pertaining to the different form materials are discussed in the next section.

2.4.1 High temp vs. Standard resin for 3D printing injection moulding inlays

As mentioned above, Formlabs have designed a wide variety of materials for SLA printing with one such material being the High Temp Resin. The properties of this resin as well as the Standard Clear Resin are detailed in table 2.2.

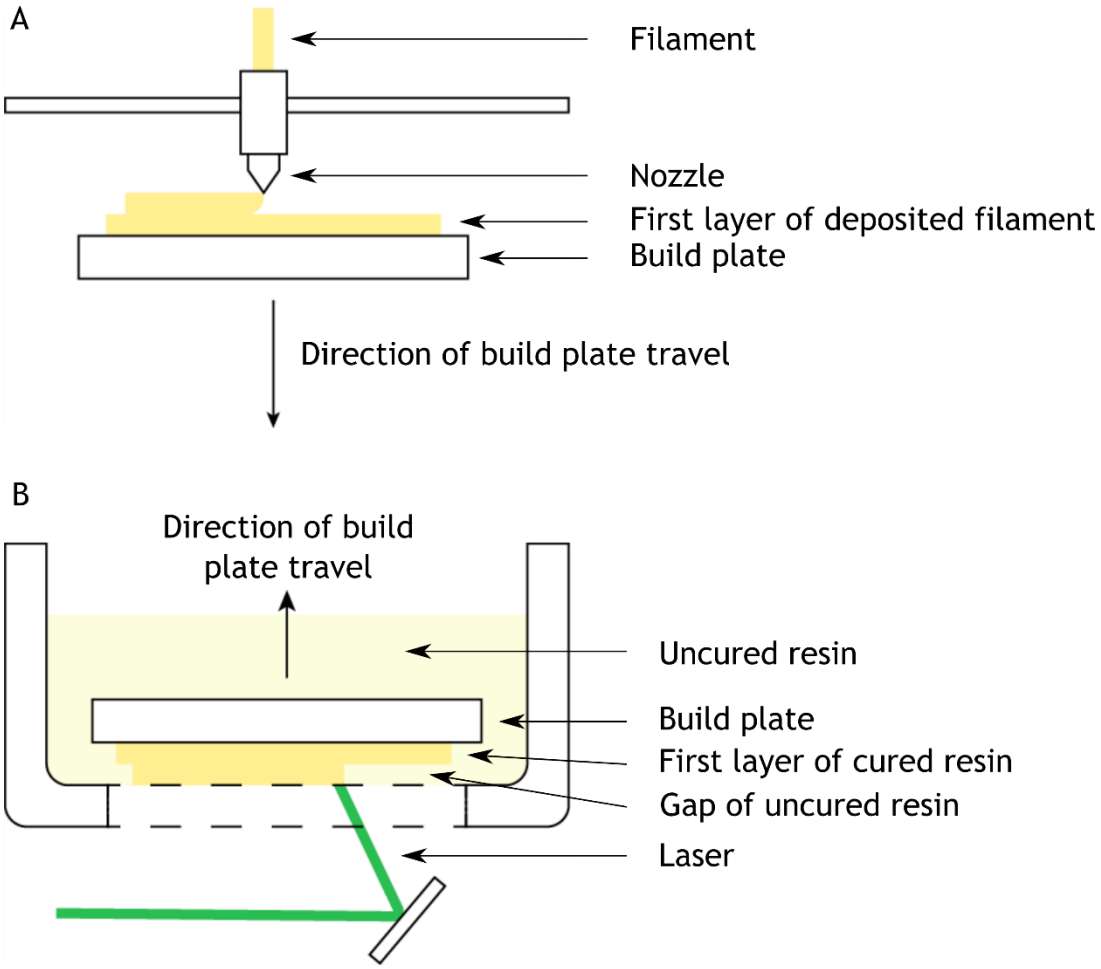

Figure 2.4 – SLA and FDM printing processes. A shows the FMD process where filament is extruded through a nozzle onto the build plate. B shows the SLA printing process whereby subsequent layers of photoactive resin are cured by a laser.

Both resins used here are proprietary materials manufactured by Formlabs and as such, there is very little information regarding their make-up. The chemical SDS however, reveal both resins to be made up of a mixture of methacrylates and photo initiators[178]. However, despite the proprietary nature of the resins, the Formlabs materials were preferred as they removed any variability between printers and resins that can occur when non-commercially available systems are used. Due to the superior heat deflection temperature, which was assumed would increase the durability of the material during the injection moulding cycle, the High Temp Resin was initially considered for inlay fabrication. All inlays were printed at 25 µm layer height and post-processed according to the Formlabs data sheets for maximum mechanical properties. Initially, inlays were moulded without any consideration to dimensions so as to confirm whether they would be suitable candidates for injection moulding or not. However, during these initial tests it was found that the high pressure in the mould cavity during the injection of the polymer was causing a mechanical failure of the inlay resulting in cracks in the part. An image of such an inlay after moulding is shown

in Figure 2.5A with the cracks clearly visible. From this, it was hypothesised that the High Temp Resin was not tough enough for injection moulding applications so in order to improve the mechanical properties, a couple of different approaches were used. Namely, subjecting the part to only half the recommended cure time and annealing the part after curing, leading to a less brittle final part. Images of inlays are shown in Figure 2.5B and C respectively.

Curing the inlay for half the recommended time was thought to increase the toughness of the part making it less brittle and more likely to withstand the pressure inside the injection moulding machine. Table 2.2 shows the pre- and post-cured values for the material properties with the toughness (specifically, Notched IZOD, which indicates the energy required to initiate a fracture) higher for the pre-cured version of the resin thus, it was thought that only curing for half the recommend time would lead to tougher material. However, as can be seen in Figure 2.5B, after 20 shots, the inlay failed showing that the reduced curing time did not increase the toughness enough. Figure 2.5C shows that the inlay burnt during the annealing process. It was thought that by annealing the inlay, the internal stresses would be reduced leading to a tougher part capable of withstanding the high stresses of the injection moulding cycle. However, after annealing it can be seen that the inlay is discoloured compared to the unannealed parts, and that the surface of the inlay is covered in small cracks and there are large cavities inside the inlay presumable caused by small pockets of trapped air expanding in the oven. To combat this, the material properties of the Formlabs resins were consulted further to identify a tougher material that could still withstand the pressures inside the mould cavity.

From examination of table 2.2, it is apparent that while the High Temp Resin has favourable thermal properties, its toughness is lower than that of the clear resin (shown by the lower elongation to failure). Therefore, it was decided that the clear resin would be trialled as a material for inlay fabrication. Using the same design as the inlays seen in Figure 2.5, Figure 2.6A shows an inlay fabricated from the standard clear resin after moulding. Although apparent that the inlay has failed during the moulding process, the mode of failure differs from that seen in the High Temp inlays. While the High temp inlays cracked through the bulk material, the clear inlays failed around the features. This was hypothesised as being down to the polymer “grabbing” the inlay upon cooling and then

	High Temp Resin[170]		Standard Clear Resin[169]	
	Pre-cure	Post-cure	Pre-cure	Post-cure
Tensile Properties				
Ultimate Tensile Strength (MPa)	20.9	58.3	38	65
Young's Modulus (GPa)	14	3.3	1.6	2.8
Elongation to Failure (%)	0.75	2.8	12	6.2
Flexural Properties				
Flexural Modulus (GPa)	0.7	2.6	1.25	2.2
Impact Properties				
Notched IZOD (J/m)	32.8	18.2	16	25
Temperature Properties				
Heat deflection Temp @ 264 psi (°C)	49	120	42.7	58.4
Heat deflection Temp @ 66 psi (°C)	44	78	49.7	73.1

Table 2.2 – 3D printer resin properties

removing this material upon ejection of the part. To test this, a series of parts were imaged with parts 1, 10 and 25 shown in Figure 2.6B-D respectively. Here it can be seen that while initial parts look good coming off the inlay, the damage caused by subsequent shots causing further defects for the ensuing parts.

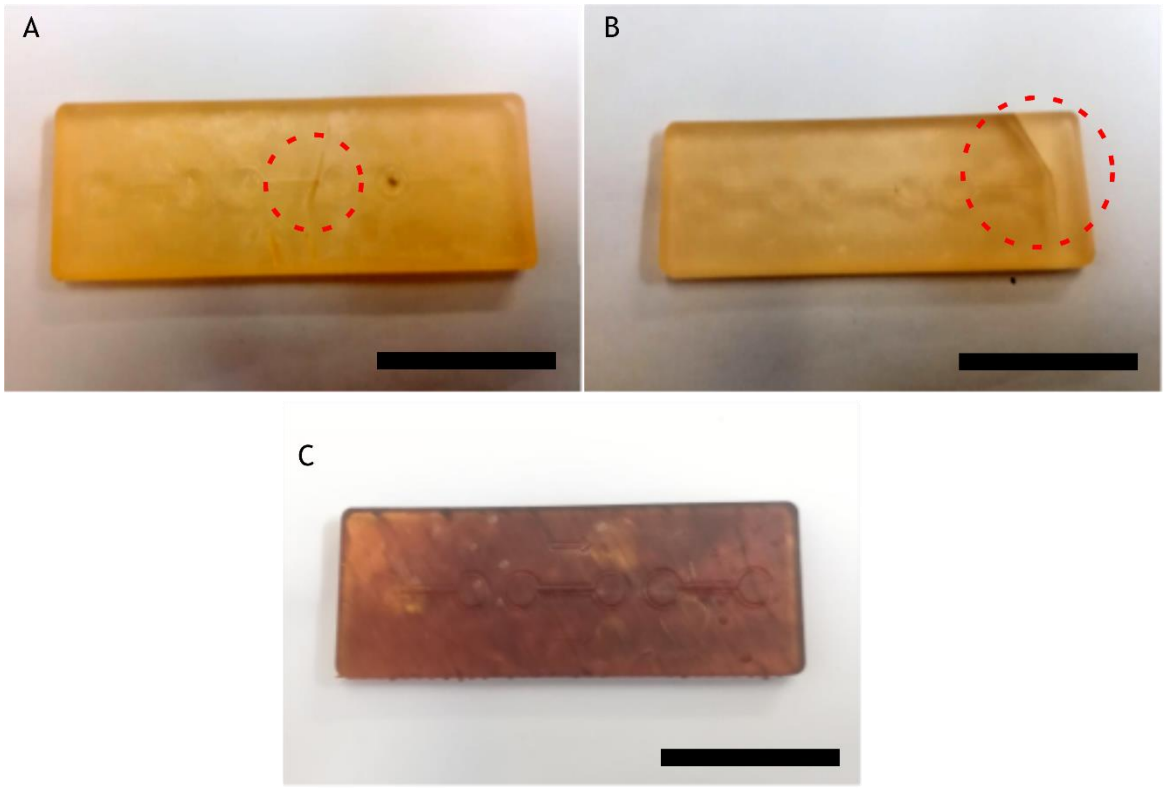

Figure 2.5 – Damage to High Temp resin inlays. A shows a high temp resin inlay after the recommended standard full cure. Cracks can be seen there the bulk of the material has failed under the high pressure of the moulding process (highlighted in the red circle). B shows an inlay with half the recommended cure however, cracks are still present after moulding – again shown in the red circle. C shows an annealed inlay. The material has burnt and cracked during the annealing process so this inlay was not moulded. Scale bars = 25 mm

From the above, it was determined that the thermal properties of 3D printed resins were not as important as the toughness when it comes to injection moulding. This may be due to the fact that the inlay is only momentarily subject to high temperatures during an injection moulding cycle. Furthermore, the stresses on the inlay during the injection of an injection moulded part are very high. In addition to the injection of the polymer, the ejection of the part also causes strain on the inlay so the master must be tough enough to not break under this force either.

The thermal conductivity of the 3D printed inlays may also have an advantage over the use of metal moulds when it comes to the fabrication of small features. Table 2.3 summarises the thermal conductivities of commonly used mould materials

Table 2.3 shows that the more traditional mould materials (steel and nickel) have a much higher thermal conductivity when compared to the 3D printer resin used in this work. This means that when the molten plastic enters the cavity, it

	High conductivity tool steel	Nickel	Formlabs Clear Resin
Thermal conductivity (W/mK)	66[179]	97.5[180]	0.28[181]

Table 2.3 – Thermal conductivity of mould materials

will take longer to completely cool and solidify on the 3D printed inlay. This has the advantage that small features should be able to be made without the plastic solidifying before it has flowed into the mould completely. However, the lower thermal conductivity means that a longer cycle time is required to allow the parts to cool completely before ejection. As such, a relatively long cooling time of 35 s was used for all parts made from 3D printed inlays.

2.4.2 Effect of draft angles on damage during demoulding

As mentioned above, the ejection of the parts causes strain that can lead to a failure of the inlay. To combat this, it was thought that including a draft angle into the channel design would aid in the demoulding. The concept of a draft angle is well documented as being beneficial to all injection moulding and is thus advised to include angles greater than 0.5° into the tooling design[182]. The concept is illustrated in Figure 2.7A. Here, the draft angle reduces the friction between the part and the inlay during injection, resulting in less strain on the inlay and thus a lower chance of failure. Figure 2.7B illustrates this by showing a photograph of an inlay with a designed draft angle of 20° after moulding 100 parts with the inlay showing no visible damage, in contrast to the damaged inlay shown in Figure 2.6A. A more in-depth study into the draft angles and inlay durability is discussed in sections 2.4.3.2, and 2.5. From the data presented here however, it was concluded that the clear resin was a suitable candidate for injection moulding inlays and merited a more thorough investigation into its suitability for injection moulding microfluidics.

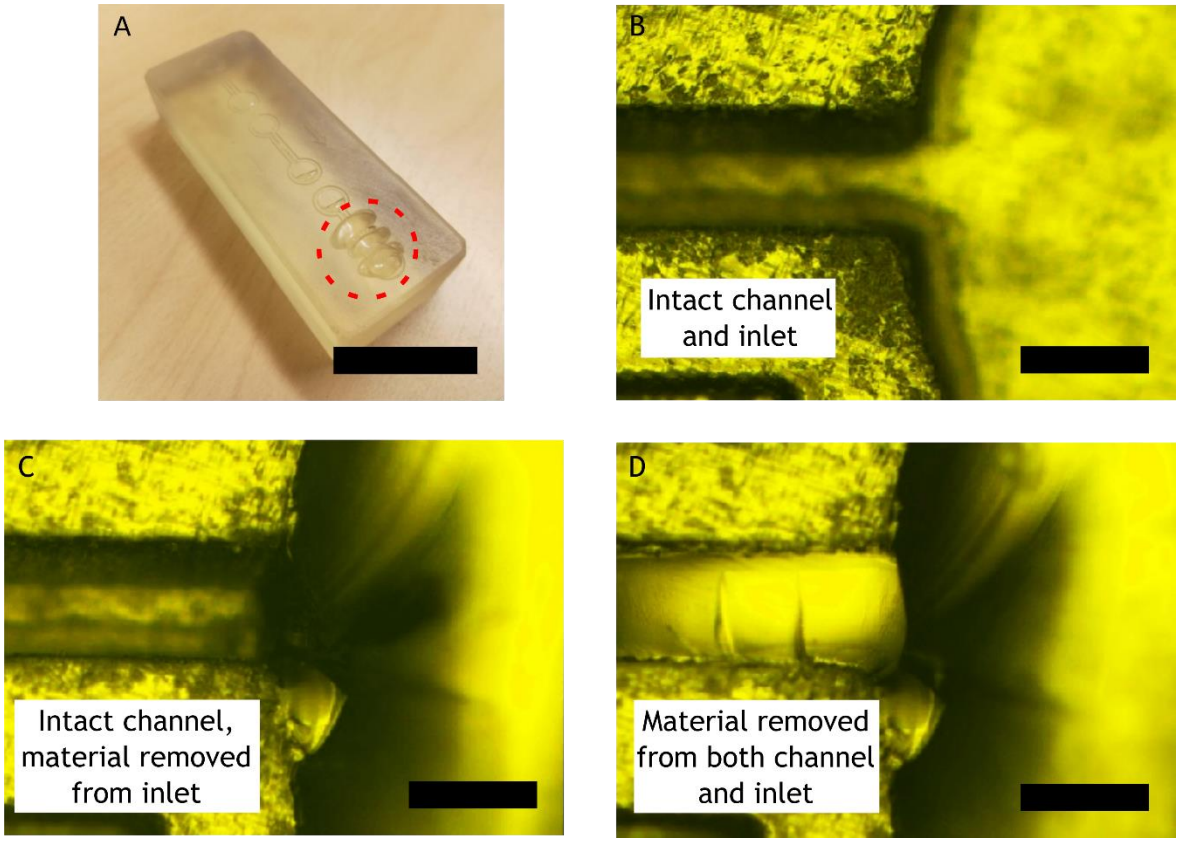

Figure 2.6 – Images of Clear inlay after moulding. A shows a clear inlay after moulding 25 shots. Although the mould has failed, it has not failed in the same manner as with the high temp inlay but through the removal of material from the surface of the inlay shown in the red circle. 3.3B-D show micrographs of parts 1, 10 and 25 respectively with more damage being seen in the parts later in the production run. Scale bar = 25 mm in A, and 300 µm in B-D.

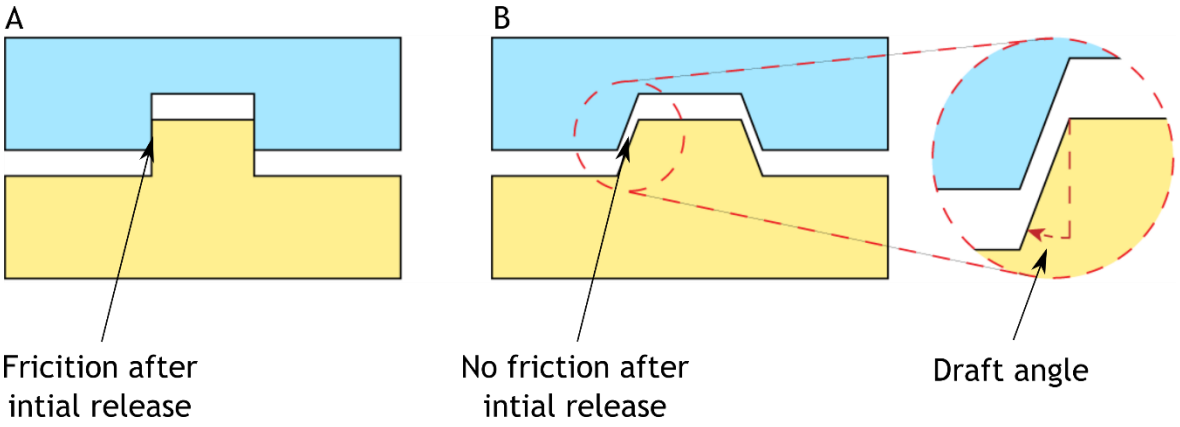

Figure 2.7 – Concept of draft angles. A shows the release from a mould with no draft angle while B shows how adding a draft angle reduces friction after the initial release. Inset in B shows how the draft angle is defined.

2.4.3 Optimisation of 3D printing for injection moulding master fabrication

As discussed above, Formlabs Clear resin was shown to be a viable candidate for use as an injection moulding master. However, for microfluidic applications, the resolution and fidelity of the 3D printing process is as important as the durability

of the inlay. As the behaviour of fluids at the microscale rely so heavily on the dimensions of the channel, it is important to determine the most reliable process for printing microchannel in terms of orientation within the printer, the feature size offset, the resolution, and the surface quality of the inlays. The following sections document the studies into each of these areas and give means of improving the quality of the prints over the base printer settings if need be.

2.4.3.1 Effect of print orientation on feature geometry

For microfluidic applications, it is important for any fabrication process to give features of a predictable cross sections and thus predictable fluid kinematics under flow. However, the default printer settings meant the inlay was printed at a different angle with each subsequent print, leading to variation in the profile and dimensions of the ridge. To address this, we printed straight ridges at a range of angles rotating in the θ (around the face of the inlay) and φ (around the side of the inlay so that the features face towards the print bed) directions as defined by Figure 2.8 where SEM images of the cross sections of these features can be seen. Here, the ridge printed at 0^o in both the θ and φ directions have a symmetrical profile however, channels not running in the build direction will have a profile of that at $\theta = 90^o$ and $\varphi = 0^o$. This means this orientation is only useful for linear microfluidic channels. To address this, ridges printed facedown ($\varphi = 90^o$) exhibit a symmetrical profile and steep sidewalls and the profile is not influenced by the orientation of the channel on the part. The supports and base are added by the slicing software used by the printer to create a normalised build plane on the build plate so that the exact position of the build plate is not required for the printing of each part and to ensure that the resin can easily flow around the part and prevent a build-up of resin which can be cured by scattered light on areas of the inlay during printing. However, it was found that by printing devices directly on the build plate, without the raft and supports that are the default setting for the printer not only cut down on print time but the parts were also more reproducible as there was no influence from the random generation of the support structures which position the part at different heights from the build plate. Additionally, the lack of supports meant that these did not need to be removed before moulding thus cutting fabrication time even further.

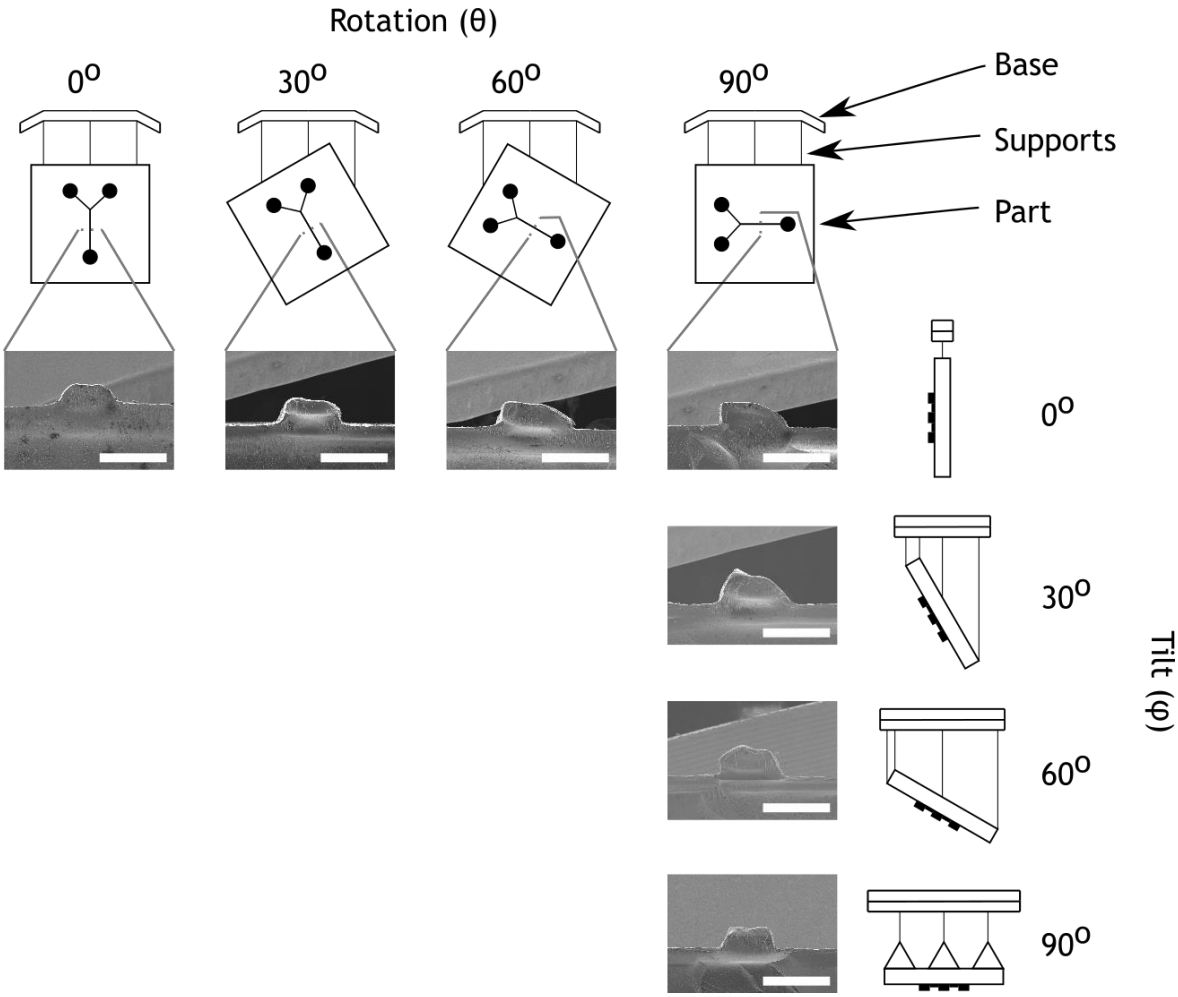

Figure 2.8 – Channel profile vs. print orientation. Figure 2.8 shows how the orientation of the print affects the cross-sectional profiles of printed ridges. Printing facedown will give the most consistent profile for all channels printed on the inlay. Scale bars = 300 µm

2.4.3.2 Accuracy of the 3D printing process

In addition to predictable profiles, accurate fabrication of channels with well-defined widths and heights is also important when manufacturing microfluidic devices to predict fluid kinematics in the final device. In order to incorporate a draft angle into the design, but still have parts of predictable geometry, a series of channels of varying heights (600 µm designed width) were printed and their cross-sections measured to see if the draft angle had any effect on the printed dimensions. As can be seen in Figure 2.9A, printing with a 0° draft angle leads to a widening of the feature, the magnitude of which differs depending on the height of the feature. This is thought to be down to scattered light from the laser interacting with and curing uncured resin that has stuck to the part on a previous layer. This process is shown in Figure 2.9B (ideal case) and 2.9C showing the real case and showing the widening of the beam and final part respectively. However, this discrepancy in printed width for features of different

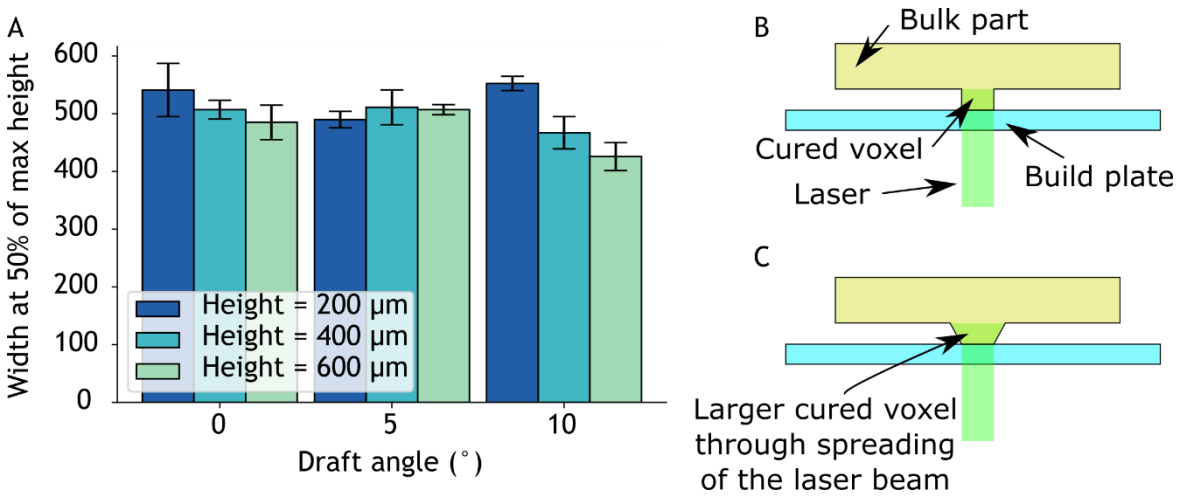

Figure 2.9 – Effect of draft angle on dimensions. A shows how the measured width at 50% of the height of a channel depends the draft angle included into the design. All channels were designed to have 500 µm widths with heights of 200, 400 and 600 µm (dark blue, light blue, and green respectively). B shows the ideal 3D SLA printing process, while C shows what happens in reality when the beam spreads leading to a larger exposed area.

heights is much less when a 5° draft angle is included in the design (Figure 2.9A). When the draft angle is increased to 10° however, this discrepancy in widths returns so was decided that all parts should be designed with a 5° draft angle to make the final geometries of the features more predictable. It is worth noting that through photolithography, these draft angles cannot be realised and in fact, when thick resists such as SU-8 are used, the profile of the sidewall is actually a slight negative draft angle. This results in an overhang which is a geometry that is impossible to mould due to the part not being able to be ejected.

To better gain an understanding of the capabilities of the printer when it comes to printing features of a desired design, ridges of varying heights and widths were designed and printed with a 5° chamfer and SEMs were acquired and the cross sections. These cross sections were then measured and compared to the designed dimensions. The heights and widths of the channels were defined as per Figure 2.2. The measurements for the heights of the ridges are shown in Figure 2.10A-C showing the heights of features 200, 300, and 400 µm wide respectively. This shows that, for a range of widths of the ridges, the heights are offset by a mean value of -59 ± 1.7 µm. This decrease in the height of a feature is likely down to an over-exposure of the resin to increase the confidence in the adhesion of the layers to one another. The slope of the best fit lines (least squares regression) shows that this systematic error can be compensated for by including this offset into the design of the feature. The measured widths of the

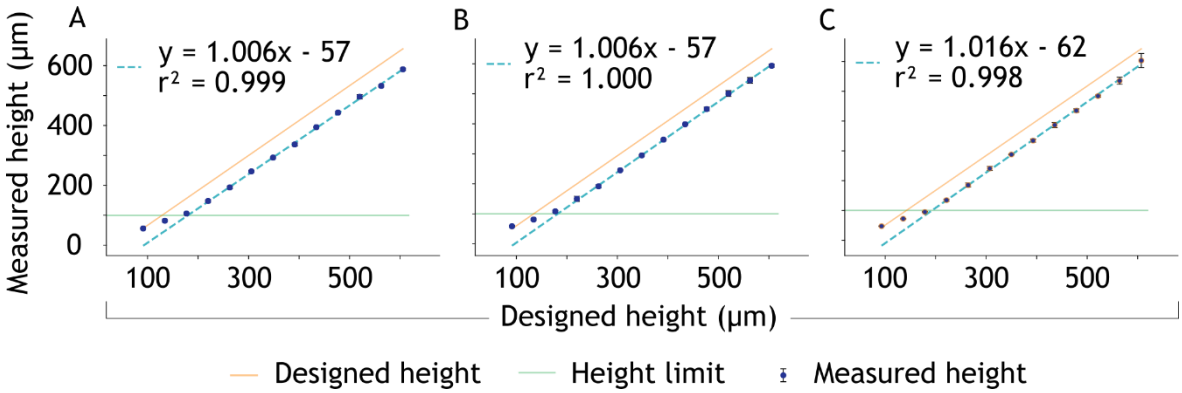

Figure 2.10 – Measured vs. designed heights of printed features. A-C shows the measured heights vs designed heights for features 200, 300, and 400 µm wide respectively. It can be seen that the measured heights flatten out as the designed height drops below 200 µm giving a lower height limit above 100 µm. Only points above this limit were used to determine the best fit lines (linear regression, green dashed lines) which give an indication of the offset (y-intercept of straight line) required to print features of a designed geometry. The gradient close to 1 shows that only an offset is required. Orange lines shows measured height = designed height.

features printed at heights of 200, 300, and 400 µm vs. their designed widths are presented in Figure 2.11A-C respectively. Again, similar to the heights discussed above, the best fit lines of the lines regions of the plots show r^2 values ~1 and an offset of 66 ± 3.2 µm. This discrepancy in the measured vs. designed widths comes from the fact that as each subsequent layers are cured by the laser in the printer, this light is scattered and any uncured resin that is coating features in previous layers is cured. Hence the features are wider at the bottom than the top. Combining this with the offset acquired from the height data above, a general rule for printing ridges is to overcompensate for the height by 59 µm and undercompensate for the width by 66 µm. This was found to give accurate and reproducible features for all subsequent experiments and devices. It is also worth mentioning that within the range of widths and heights studied here, aspect ratio had no effect on the measured dimensions of the features highlighting that the printing process is not limited by the aspect ratio.

2.4.3.3 The resolution of the 3D printing process

To further characterise the capabilities of this fabrication process, ridges were printed at different spacings to determine the resolution of the printer – that is, the minimum distance between two features that still give two distinct features of the designed height, with no material filling in the gap between them. This was done by measuring the heights of the features placed with different spacings with a ridge of full, designed height indicating a fully resolved feature. This data

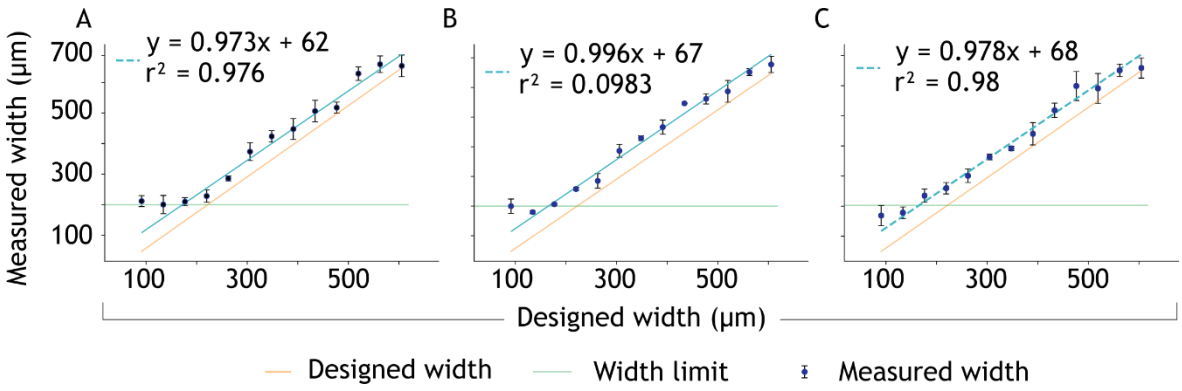

Figure 2.11 – Measured vs. designed widths for printed features. A-C shows the measured widths vs designed widths for features 200, 300, and 400 µm wide respectively. Best fit lines were taken from all points above 200 µm (taken to be the lower limit for width of a feature) and again the y-intercepts indicate the offsets required to fabricate ridges of a designed geometry.

is shown in Figure 2.12A-C showing the heights of features of various heights, normalised to their designed height, at widths 200, 400, and 600 µm respectively with the orange areas illustrating the distances for which the ridges were fully resolved (greater than 400 µm for the 200 and 400 µm wide features and greater than 600 µm for the 600 µm wide features).

2.4.3.4 Analysis of the surface roughness of 3D printed inlays

Finally, to completely characterise the features that could be realised by the printer, surface roughness measurements were taken of 3D printed inlays with no features on their surface. Surface roughness affects the transparency of the final devices so should ideally be as low as possible. Surface roughnesses of Ra = 0.81 ± 0.02 µm, Rq = 1.07 ± 0.10 µm, and Rz = 4.97 ± 0.49 µm were obtained (mean ± standard deviation, n = 3) which is an order of magnitude smaller than similar 3D printed tooling for embossing described previously[50]. This is shown in Figure 2.13A.

2.4.3.5 Analysis of the optical clarity of parts moulded from 3D printed inlays

However, as surface roughness can be misleading as in indicator of optical clarity, a resolution target was used to better understand the optical quality. Using this, chips were able to resolve 0.28 line pairs/mm (lp/mm) however, by polishing the inlay prior to moulding, the chips could then resolve 128 lp/mm.

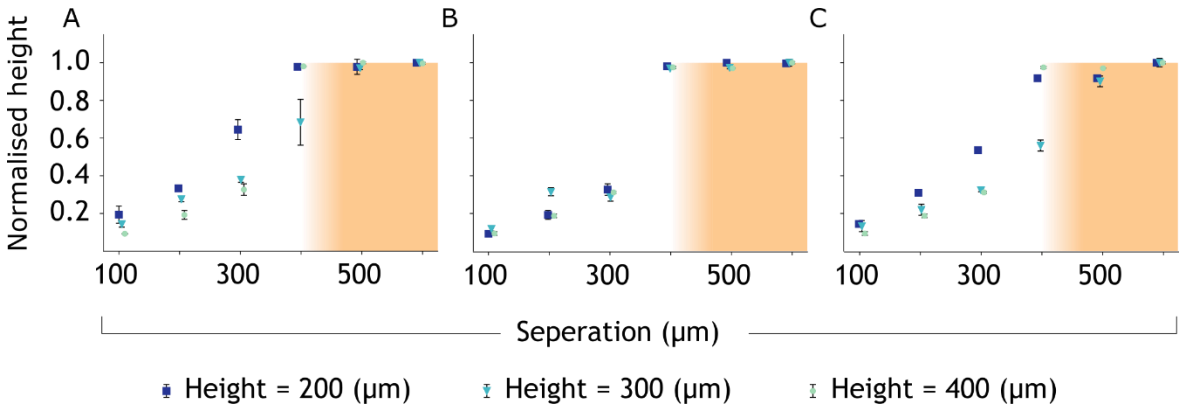

Figure 2.12 – Resolution of the printing process. A-C show features (200, 400, and 600 µm wide respectively) printed at different spacings. In all cases, features 100, 200, and 300 µm tall (taking into the account the above-mentioned offsets) were printed at different separations and the heights measured and normalised to the designed height. A value less than 1 here illustrates that the area between two features has filled in with resin this this separation is below the resolution limit for this printer. In all cases, the resolution limit lay somewhere above 400 µm (shown by the orange region the plots). A spacing of 500 µm was used for all future designs

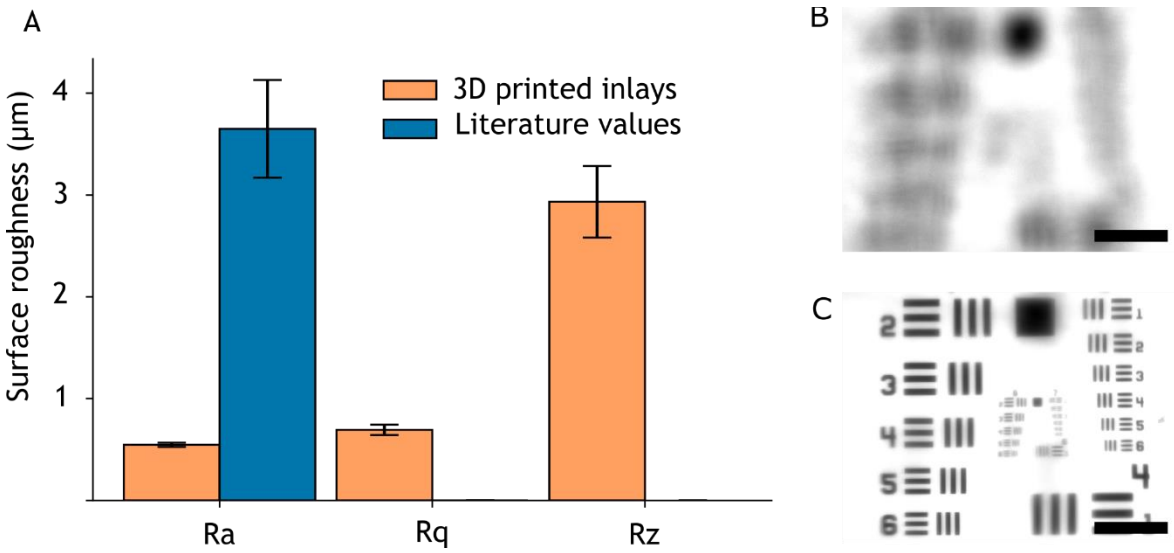

Figure 2.13 – Surface quality of chips moulded from 3D printed inlays. A shows how the roughness values are different to that of similar chips described in literature (reference 12). B shows the optical clarity of the chip, while C shows how this can be improved through polishing the inlay. Scale bars = 100 µm

Images of the target's smallest features through the unpolished chip is shown in Figure 2.13B and the polished chip in 2.13C

2.4.3.6 Summary of 3D printing process

In summary:

- Inlays should be printed face down to give the best channel profile in all directions.

- Parts should be printed with a 5° draft angle as that gives the most consistent channel geometries over a range of dimensions.
- Parts should be designed 59 µm taller than required.
- Parts should be designed 66 µm narrower than required.
- Microchannels should be placed no closer than 400 µm to each other.
- Channels should be polished to improve optical clarity.

2.5 Durability of 3D printed inlays

The injection moulding process involves high temperatures and pressures (260°C and 800 bar) which can lead to wear and damage to inlays used for moulding. As such, it was important to test the accuracy and reproducibility of micro-channels moulded from our 3D printed inlays as well as the durability of the inlays themselves. A series of ridges of varying width, height and aspect ratio were printed at desired dimensions accounting for the offsets and spacings determined above. The height and width of the channels formed on the plastic replicas were then measured and compared to the designed dimensions. Figure 2.14A and B show the replication of the height and width varies over 50 shots respectively. Here it can be seen that shallower channels show very good reproducibility over the full production run while the taller channels, particularly those over 500 µm showed a reduction in height of 30 µm with subsequent shots. That is, the height of the shallower channels remained stable over the course of the run, while the depth of the deeper ones reduced with the reduction being most noticeable in the deepest channels. It was thought that the aspect ratio of the channels would have an effect with regards to their dimensional stability over the whole production run, with the lower aspect ratio channels showing a lower reduction in height over the course of the experiment. However, when the 600 x 600 µm channels (aspect ratio = 1) are compared to the 600 x 100 µm (aspect ratio = 6), the reduction in height from the first shot to the 50th remains the same (~30 µm) showing that it is the absolute depth of the channels, not the aspect ratio that has the largest effect on feature reproducibility. This also demonstrates the suitability of using 3D printed inlays for injection moulding high aspect ratio structures.

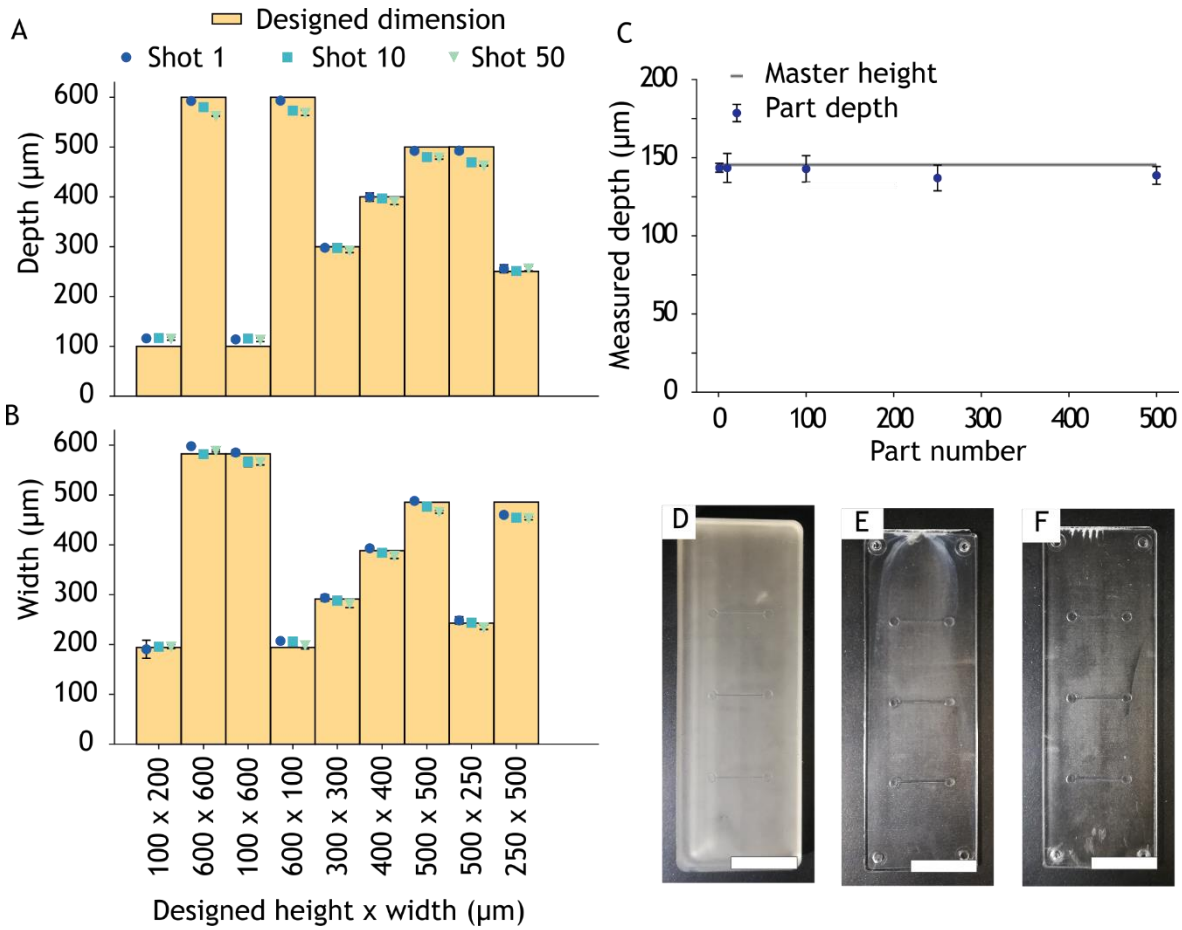

Figure 2.14 – Durability of 3D printed inlays. A shows how well the depth of channels is preserved with subsequent shots while B shows the same for the widths. C shows how the depth of a 146 x 200 µm channel varies over 500 injection parts while D-F shows photographs of the master, the 1st shot (still containing some polypropylene) and the 500th shot respectively.

In terms of the widths, a small reduction in the width of the channels can be observed over most of the designs with each shot, however, this is most apparent in the higher aspect ratio channels with the shorter and lower aspect ratio channels showing excellent reproducibility over the production run. Over 500 parts have been moulded from a 3D printed inlay with no visible signs of wear on the inlay or any of the parts, further highlighting the suitability of these inlays for mass production applications.

To further validate this, an inlay was printed with channels 146 µm deep and 500 parts were moulded from it. The 1st, 10th, 100th, 250th and 500th part were measured and this data is shown in Figure 2.14C. Here it can be seen that even after 500 parts have been moulded, the channel height is still within error of the master dimensions showing that 3D printed inlays are durable for at least 500 parts. Photographs of the master, the 1st part and the 500th part are shown in 2.14D, E, and F respectively.

As discussed in the preceding sections, 3D printed inlays can be used to reliably injection mould microfluidic channels as long as the steps detailed in section 2.4.3.6 are followed, and the absolute depth of the channels is kept below 500 µm. In terms of minimum channel size, the injection moulding process was able to reliably reproduce even the smallest of the channels that the printer could realise showing that the fabrication is limited by the 3D printing process which is likely to improve in the years to come. The reduction in the depth of the channels is likely due to the softening of the 3D printed inlay in the heat of the moulder and could likely be improved through more specialist resin design. Indeed, since this study was conducted, Formlabs made a specific injection moulding resin, but its resolution is limited compared to that of the clear making it currently unsuitable for microfluidics.

2.6 Impact of ultrasonic welding on 3D design

In the case of PDMS, bonding to other materials can be achieved with relative ease with the most common methods involving sealing against itself or against a glass substrate. This can be done due to the elastic nature of PDMS meaning it conforms to a surface and provides a moderate seal[13]. This sealing can be enhanced by first plasma treating the elastomer when higher pressures are required[15]. However, bonding of thermoplastics is not so trivial. Thermal-sealing involved heating the two parts and holding them together under pressure allow the parts to fuse together. However, the need for a long cooling stage means that this method is not viable for high throughput applications. Furthermore, the fact that the whole part needs to be heated can lead to deformation within the channels. A such, an alternative sealing method was sought for the injection moulded parts.

2.6.1 Ultrasonic Welding for the sealing of microfluidic chips

Ultrasonic welding is one of the most common thermoplastic bonding process used in industry due to its rapid, easy to automate, and cheap nature and the fact it required no additional materials for the fusion of parts. As such, ultrasonic welding complements injection moulding processes for high-throughout, rapid manufacture of devices. During ultrasonic welding, it is

beneficial to use energy directors (referred to as weld seams). These structures act to focus the welding energy to a small, localised region of the device and prevent excessive deformation to the parts due to heating. Once in contact, the sonistrode exerts pressure and ultrasonic vibrations onto the two parts which heats and melts the weld seam, thus fusing the two parts together. By having the seam encircle the channel, a hermetic seal is formed during the fusion of the parts. Typically, these weld seams need to have a triangular profile which is difficult to fabricate with traditional silicon micromachining protocols. However, with 3D printing, complex 3D shapes can be incorporated into the device with ease thus reducing the fabrication time while simultaneously allowing for geometries that would be impossible to manufacture using traditional advanced manufacturing methods. Furthermore, the time taken to ultrasonically weld parts is on the order of a few seconds meaning it aligns with well with an injection moulding process which can produce several parts per minute. However, as ultrasonic welding necessitates the inclusion of weld seams, it is important to optimise the design of these as well as the welding parameters that lead to microfluidic devices with the best geometry. To do this, master for weld seams were printed (that is, inverse channels) to determine the minimum dimensions that the printer was capable of fabricating. An investigation in how to achieve as close to a triangular structure as possible was also conducted before a range of sealing parameters were analysed to find the process with the least impact on microfluidic geometry. The following sections detail this work.

2.6.1.1 Optimisation of weld seam design for 3D printing

Firstly, it was important to determine the smallest weld seam structures that could be achieved through 3D printing. Smaller weld seams will have a smaller effect on the geometry and the performance of a microchannel however if they are too small, and there will not enough material to seal the chip. The lower weld seam size limit was determined by printing a series of troughs (that would become ridges in the moulded part) of different depths (100 and 200 μm) and widths (200 – 700 μm) (defined in Figure 2.15A, with the sidewall angle defined in B, and an ideal trough shown in C), cleaving the part and imaging the cross section before measuring and comparing to the designed geometries. For narrower channels, the printer was not able to realise the designed shape as the resolution was not high enough. This resulted in features filling in which can be

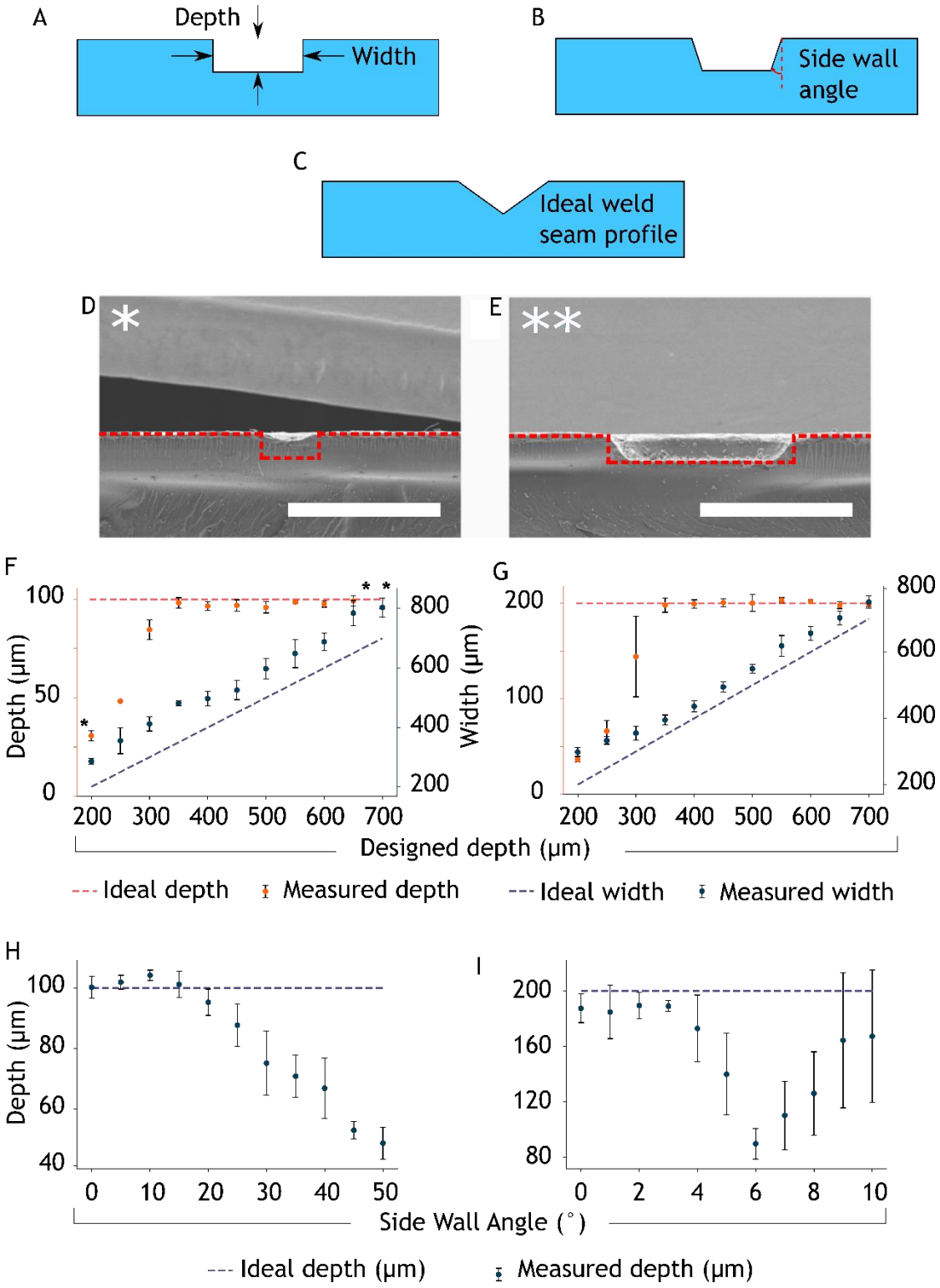

Figure 2.15 – Design of weld seams in 3D printed parts. A shows how the depth and width of the master structures for moulding weld seams from 3D printed masters. B and show how the side wall angle of the feature is defined, while C shows the ideal weld seam profile. D and E show printed trough with designed dimensions of 200 x 100 µm (width x depth) and 700 x 200 µm respectively. Red dotted lines show the designed shape of the trough. Filling in of the feature can be observed in the smaller channel, while the larger one is better realised. F and G show how the designed and the measured dimensions of these features differed from one another for features 100 µm and 200 µm deep respectively. With the full depth of the features only being realised once the width is above 350 µm. The effect on the sidewall angle on the depth of the channels in shown in H shows how the side wall angle of these features affects the depth of a 100 µm through. I shows the same as F but for a 200 µm trough. Scale bars = 500 µm. All points = mean ± standard deviation with n = 3.

seen in Figure 2.15D. however, for wider features, this filling in was less of an

issue and the troughs were able to be printed (Figure 2.15E). By measuring and comparing the widths and heights of these troughs to the designed dimensions, the lower feature size limit can be determined. Figure 2.15D and E show the widths and depths of features 100 and 200 µm deep respectively. These results show that the narrowest trough feature that can be reliably printed is one designed to be 350 µm wide.

Next, in order to achieve the desired triangular shape of the features, a series of troughs was printed with a range of sidewall angles. This was done in order to determine the most triangular channel that could be printed. The shape of these features with the side wall angle is shown in 2.15B with the ideal profile shown in 2.15C Figure 3.12F and G show the measured depths of troughs designed to be 350 µm wide and 100 and 200 µm deep respectively. This illustrates that for 100 µm deep troughs, the side wall angle can be increased to 15° while it can only be increased to 2° for the 200 µm deep ones. When the side-wall angles were increased above these values, the channels filled in during printing meaning that they were no longer the designed depth. The 15 and 2° for the 100 and 200 µm channels respectively were the angles that led to the most sloped side walls while still allowing for the channel to have its full height. This is important in ultrasonic welding as it means the seam will have the tallest, pointiest profile possible which leads to efficient energy transfer and a more reliable seal. Considering the design requirements set out above, channels were designed to have weld seams encircling them with dimension of either height = 100 µm, width = 350 µm, and sidewall = 15° or height = 200 µm, width = 350 µm, and sidewall = 2°. These parts were then moulded and plasma treated before inlet/outlet holes were drilled.

2.6.1.2 Optimisation of the welding process to minimise added height

As discussed above, the optimum weld seam dimensions were found. However, in order to fully optimise the welding process, the welding parameters were also investigated. To determine the optimum welding parameters for these weld seams, two different operation modes on the ultrasonic welding machine were considered: travel differential, and energy mode. In travel differential mode, the sonistrode moves a predefined distance while vibrating to fuse the parts, while in energy mode, the sonistrode vibrates until a certain energy has been

transferred to the parts. Using a travel differential of 20, 40, 60, 80 and 100% of the weld seam height, 10 chips were sealed at each setting and the sealing success was determined by filling the channels with dye and examining for leaks. The same was done in energy mode using energies of 5, 10, 15, 20 and 25 Ws. The sealing success was determined by filling the channels with dye and examining for leaks. As the parts had been plasma treated prior to sealing, any leaks meant that fluid would readily flow out of the channel and be easily detected by eye. Figure 2.16A and B show a schematic of the welding process prior to and after welding respectively while the sealing success of the 2 weld seam designs is shown in Figure 2.16C. Here it can be seen that the 200 µm seams sealed more reliably than the 100 µm ones, and that energy mode was far more successful in sealing the chips than travel differential. No 100 µm seams sealed in travel differential mode with energy mode having a 100% success rate for the 200 µm seams at energies over 10 Ws. However, the 100 µm seams could reliably seal in energy mode at 25 Ws. There are two possible mechanisms as to why the 100 µm weld seams did not seal reliably. Firstly, there may not be enough material in the seams to melt form a stable bond between the two parts. Secondly, the 100 µm seams are shallower, and thus less pointed that the 200 µm seams. This means that the energy transfer into the seams takes place over a larger area and is thus less efficient which may result in less of the material melting and forming a seal. However, in order to investigate this fully, a higher resolution printer would be required to print weld small weld seams with the same aspect ratio as the larger ones and is outwith the scope of this thesis.

As ultrasonic welding involves the melting of weld seams, the process does mean that the resulting microchannel has added height due to these structures. As such, it was important to determine how much height is added so that this can be compensated for in the design. Chips were sealed using the parameters described above before being cleaved and their cross sections imaged and measured. Added height was defined as the height from the bulk of the chip material to the foil used to seal. Figure 2.16D shows the added heights for all the weld seam design/ welding parameters that gave a sealing rate of above 90%. This shows that, for the 200 µm seams, the more energy used to weld, the less added height in the final channel. It was though that using a smaller weld seam would result in less overall added height however, the 100 µm seam gave an added height of 50 µm compared to 28 µm for the 200 µm ones. It is thought

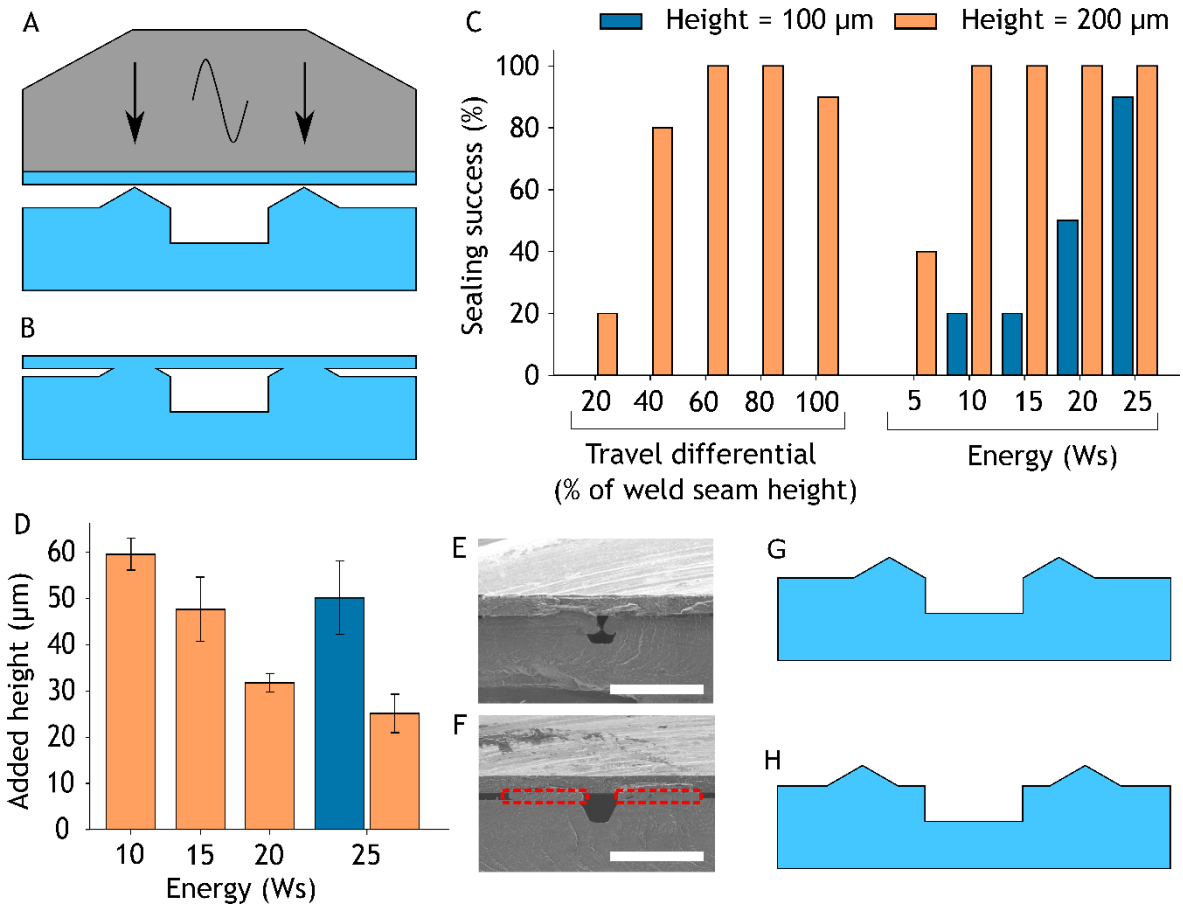

Figure 2.16 – Sealing success of weld seams. A shows a schematic of the welding process with e final welded part shown in B. The sealing success of different welding parameters and weld seam designs is shown in C and the added heights of the successfully sealed channels shown in D. Finally, E and F show cross sectional images of sealed channels where the weld seams were placed adjacent to the channels, and offset by 150 µm respectively. Red dotted boxes show the weld seams and how they fit in the final channel in F. G shows a schematic the weld seams adjacent to the channel while H shows the weld seams with a designed offset (as in F). Scale bars in E and F = 500 µm

that, as mentioned before, the profile of the 200 µm seam is more pointed which allowing for a more efficient transfer of energy, and more of the plastic melting and fusing.

It was also noted during this experiment that the weld seams were flowing into the microchannels during welding (Figure 2.16E). Finally, it was hypothesised that by placing the seams adjacent to the channels would give the best channel profile once sealed but this was not the case 2.16F. However, these defects could be compensated for, by moving the weld seams 150 µm back from the edge of the channel (2.16F) (designs for the adjacent weld seams and the offset seams are shown in Figure 2.16G and H respectively).

Despite the weld seam designs a sealing process being optimised here, there are still several areas of ultrasonic welding that would merit further study to

completely characterise the process. Perhaps the biggest limitation is that all the chips sealed here were the same design – that is a small channel with inlet/outlets at each end. As the ultrasonic welding process relies on transferring energy from the sonistode to the parts, it follows that a longer channel, and thus longer weld seam will require more energy to seal. As such, to fully characterise the process, a relationship needs to be found between the length of the weld seam, and the sealing energy. In addition to this, the devices here were single layered sealing to a blank sheet of PS. In reality, many more interesting microfluidic devices (such as the TEER chips discussed in Chapter 4) rely on multi-layer architectures. As such, the process needs to be optimised for sealing 2 parts, both with weld to understand this fully. Furthermore, the method used here to determine the sealing of the chips is rudimentary. While the seal on the chips may be watertight, it may not in fact be airtight which would be a requirement for most microfluidic applications. To investigate this, the chips should be pressurised with air, and the air pressure recorded over time to make sure it does not drop which would indicate a leak in the chips. Finally, the design of the chips could be improved to ensure the welding process was as simple as possible while maintaining the geometry of the channels. Firstly, a tongue-in-groove style seam should be used to eliminate the issue of added height and material overflow from the sealing process[67]. This would also have the added benefit of aligning the chips prior to the welding thus eliminating the need for any manual alignment that may otherwise need done.

2.6.2 Sealing of microfluidic devices through lamination

As discussed above, ultrasonic welding of the chips provides a robust means of sealing chips. However, the main drawback is the addition of the weld seam that lead to extra height added to the chip and distort the initial designed shape of the channel. To address this, lamination was investigated as a means of sealing the chips. In this process, a standard heavy-duty paper laminator was used to head and bond a thin polystyrene foil onto the chips. This process is shown in Figure 2.17A. To determine the optimum lamination parameters, chips were sealed at different temperatures, using a different number of passes through the rollers, and using different pouch materials. The purpose of the pouch is to provide a non-stick coating that stops the polymer adhering to the rollers during the process while also allowing for the conduction of heat from the rollers to the

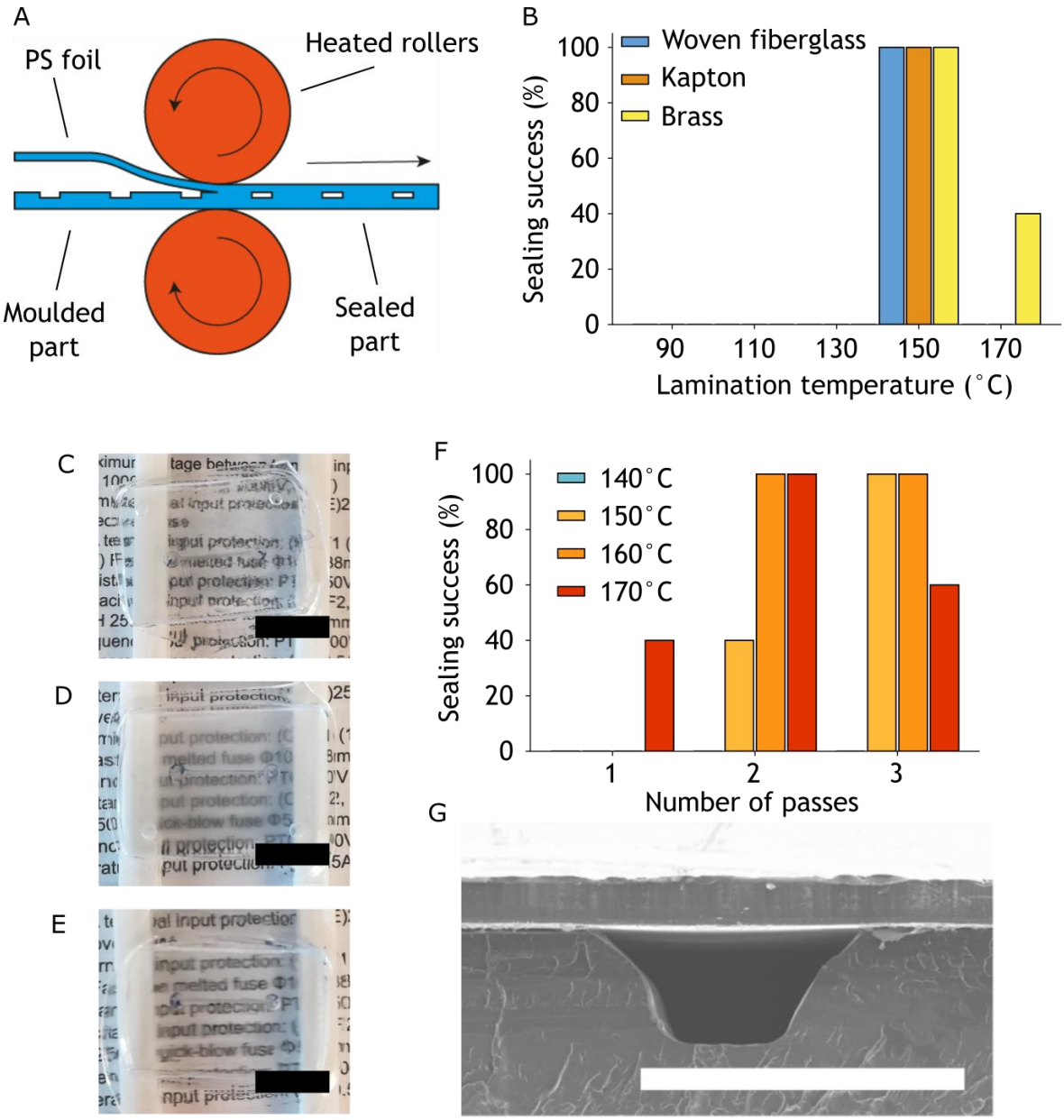

Figure 2.17 – Sealing of chips by lamination. A shows a schematic of the lamination process. B shows the sealing success of the chips when different temperatures and different pouch materials. 4 passes through the laminator for all pouch materials. C-E shows the optical clarity for the fibreglass pouch, Kapton, and brass shims in C – E respectively. F shows sealing success of the lamination process using just the Kapton pouch at a narrower range of temperatures and different numbers of passes through the laminator. G shows an SEM of a sealed channel. Scale bar = 10 mm in C-E and 500 µm in G.

polymer. A plot showing the sealing success of the chips after laminating in each of the three pouches at different temperatures is shown in 2.17B. Each chip was subject to four passes to ensure that the chips sealed properly. This process was refined and will be discussed later. 2.17B shows that the only temperature that the chips sealed successfully at was 150ºC although there was some success at 170ºC using the brass shims. Although there was success in bonding the two layers of plastic at 170ºC using the Kapton and the pouch, the high temperatures lead to deformation of the part which result in the channels being unfillable and thus unusable so these chips were deemed to have sealed unsuccessfully.

With no real indication as to what the best pouch material in terms of bonding success, there was a difference in the appearance of the chips after lamination. 2.17C-E shows photographs of the chips after sealing which give an indication of the optical clarity (with C, D and E showing chips sealed in the pouch, Kapton, and brass respectively). Here it can be seen that the texture of the pouch has transferred to the chip distorting the image of the text below. Although initially, the brass produced clear parts, the brass was imprinted with the outline of the chip after 10 runs so this pattern was then transferred to the chip resulting in the distortion shown in E. The Kapton on the other hand, did not distort the chip and led to parts that did not distort the image of the text even after multiple laminations. As such, Kapton was chosen as the optimum pouch material for lamination.

To optimise this process further, chips were sealed using a Kapton pouch at a narrower range of temperatures than in 3.18B and by using a different number of passes to determine the lowest number, and thus quickest means of sealing the devices. This data is shown in 2.17F. Here it can be seen that none of the chips seal at 140ºC, and that a minimum of 3 passes are required at 150 ºC. However, as little as 2 passes resulted in 100% successful sealing at 160 and 170ºC while 3 passes at 170ºC resulted in damaged chips. From this it was determined that the quickest, and most robust means of sealing the chips was to use 2 passes at 160ºC using a Kapton pouch.

Finally, a cross-sectional SEM of a chip sealed at 160ºC with 2 passes is shown in 3.17G. This shows how the profile of the channel is superior compared to the ultrasonically welded channels shown in Figure 3.17. Here the channels have little to no added height because of no extra material required for sealing. This also means that the designed geometry of channel sealed with lamination is preserved resulting in more predictable fluid kinematics when compared to channels sealed via ultrasonic welding.

However, despite the creation of sealed microfluidic channels with good geometries, there are still several limitations to this process. Firstly, the process is slow compared to ultrasonic welding meaning that it aligns less well with fabrication through injection moulding, and also require more hands-on time than thermal bonding which can be left unattended for most of the sealing time.

Secondly, the process likely induces high thermal stresses into the parts meaning they are more likely to warp and the foil delaminate form the part. Finally, the lamination process is limited to foils as the heat needs to transfer from the rollers all the way to the sealing surface in a much shorter time than thermal bonding. This becomes an issue when multi layered parts (such as the TEER chips discussed in Chapter 4) are considered.

2.6.3 Ultrasonic welding vs. lamination vs. thermal bonding for the sealing of microfluidic devices

In this section, two different means of sealing injection moulded polystyrene chips have been discussed. Although they achieve the same goal, the two different methods have different properties that offer different advantages and disadvantages depending on the application. These considerations are detailed in table 2.3 with another commonly used sealing method (thermal bonding) included for comparison. From table 3.2, the different sealing methods have different advantages and disadvantages. Ultrasonic welding proved the fastest seal, but at the cost of channel geometry. Lamination also provides a rapid seal, but the high temperatures required limit the applications when certain surface treatments and coatings are considered. Meanwhile, thermal bonding leaves channels with excellently preserved channel geometries, but at 20 mins per chip, may not be useful for high throughput manufacture. Additionally, thermal bonding also requires the whole sample to be treated (albeit to a lower temperature than in lamination) so certain bio-functionalisations may be denatured. As such, it is important to consider the final application of a device before deciding on a sealing protocol.

2.7 Organoid culture in an injection moulded microfluidic device

As discussed above, 3D injection moulding from 3D printed inlays allows for the creation of fluidic devices with channel dimensions on the order of 100s of micrometers. While this is larger than silicon micromachining process, this increase in size allows for the incorporation of organoid systems that would otherwise be too large for silicon micromachining. Organoids are 3D structures

	Ultrasonic welding	Lamination	Thermal bonding
Design	Features have to be designed into the master structure and not to interfere with the fluidic channels	No extra design other than the channels themselves	No extra design other than the channels themselves
Channel geometry	Extra weld seam material leads to added height in the channel distorting the designed geometry	High temperatures are used so increased risk of thermal deformation	No change in designed channel geometry
Time per chip	30 s	1 min	20 mins
Surface treatments	Weld seams can puncture through surface treatments and still for a seal	Surface treatments must be restricted to the channels as will not allow the plastic to fuse together – also, must be able to withstand high temperatures	Surface treatments must be restricted to the channels as will not allow the plastic to fuse together. Must be able to withstand moderate temperatures.

Small features/ Bio-functionalisation	Energy is localised to the weld seams so nano-features/bio-functional coatings in the channels are not distorted/denatured by excess heat	Whole sample is heated so nano-features/bio-functional coatings will be distorted/ denatured	Whole sample is heated so nano-features/bio-functional coatings will be distorted/ denatured

Table 2.4 – comparison of ultrasonic welding, lamination, and thermal bonding for the sealing of microfluidic devices

of cells composed of the different cell types required to make up an organ. In the case of liver cells, the organoids were composed of hepatocytes, cholangiocytes, stellate cells, kupffer cells and endothelial cells. Organoids are organotypic *in vitro* models that capture the complexity and physiology of the organ and organ systems within the body and are thus an area of great interest within the OoaC community.

As discussed in Chapter 1, the spatial organisation of cells within a tissue play an important role in determining the function of said tissue. Organoids are cellular systems that rely on the innate self-assembly of cells during embryogenesis to create complex tissue architectures that better capture human physiology. Defined as "a collection of organ-specific cell types that develops from stem cells or organ progenitors and self-organises through cell sorting and spatially restricted lineage commitment in a manner similar to *in vivo*", organoids represent a new model systems for biological research[183]. In short, through aggregation of stems cell which are then guided down specific differentiation pathways with the introduction of specific growth factors, the cells grow in a manner that mimics growth during embryogenesis. As such, the cells organise and continue to differentiate as they would in an embryo and self-assemble into 3D structures that resemble organs during early organogenesis. These organoids can then provide a more complex *in vitro* tool that acts as a link between monocultures of cell lines that lack the tissue-tissue interactions seen in the

body, and animal models that, while complex, often fail to capture physiology that is unique to humans[70,184]. Additionally, organoids provide a human specific means of studying organ development *in vitro*. Furthermore, as organoids can be derived from adult stem cells, they can be manufactured to contain patient specific mutations that allow for patient specific toxicology and drug screening[185]. This was demonstrated by Hans Clevers who took adult stem cells from a cystic fibrosis patient with a rare mutation and was able to test the drug Kalydeco on gut organoids derived from these cells[186]. Upon seeing that the drug was effective in treating the symptoms of this rare mutation *in vitro*, the drug was given to the patient whose symptoms have alleviated highlighting the power of organoids for personalised medicine. It has also been shown that through CRISPR-CAS9 gene editing, organoids with specific mutation can be corrected for, further demonstrating their potential as a model for disease and therapy testing[187]. Due to the enormous potential of organoids as a model system, various tissue specific organs have been demonstrated such as the intestine[188], brain[189], kidney[190], liver[191], and retina[192].

Alongside organoids, OoaC devices are chips that better mimic human physiology compared to traditional 2D cell culture techniques. As such, it is thought that by integrating the two technologies a more accurate drug screening model compared to standard cell culture techniques can be created, thus alleviating the current bottle-neck in the drug development pathway. As organoids represent more physiological relevant cell systems by coupling them with microfluidic systems mimicking nutrient supply, concentration gradients, and fluid flow, organoid-on-a-chip systems can be made with the potential to better replicate human physiology than static 2D and 3D culture techniques. These more accurate devices could then be used to screen compounds during pre-clinical development in a more efficient manner than the current drug development process.

Despite being such a nascent field, several attempts have been made at creating organoid-on-a-chip devices. Zbinden *et al*. created a hydrodynamic flow trapping device which allowed for the trapping of discrete pancreatic islets[193]. Once the organoids were trapped, the response to glucose stimulation was studied proving a pancreas-on-a-chip model for diabetes research. Achberger *et al*. also coupled microfluidic technologies and organoids however, this time using a membrane to

separate a culture of retinal pigment epithelium and retinal organoids from the media flow and nutrient supply and provide vasculature like perfusion of nutrients[194]. With this model, the side effects of certain drugs were reproduced highlighting the power of organoid-on-a-chip systems for drug screening. Homan *et al.* also created an organoid-on-a-chip device however, they cultured kidney organoids on a 3D printed microfluidic chip. This allowed for vascularisation similar to that seen in embryonic development showing how these chips can create accurate models of human physiology. However, as is the issue with other microfluidic technologies, the reliance on PDMS, or similar silicone elastomers as a material for these chips come with the aforementioned issues of small hydrophobic molecule absorption meaning it is impossible to predict the quantities of a compound actually making it into the tissue. Furthermore, the size of organoids also presents an issue when trying to couple them with existing microfabrication techniques.

With the size of organoids ranging from ~10s to 100 µm in diameter, any devices manufactured have to also be on this length scale. While fluidic devices have been made to accommodate these larger cell constructs[193], they often require complex multistep photolithography procedures which are not then amenable to mass manufacture. However, with injection moulding from 3D printed inlays channels with depths of 100s of micrometres can easily be fabricated and produced in bulk. To demonstrate the use of 3D printed inlays for organoid-on-a-chip applications, a simple 300 x 300 µm fluidic channel connecting an inlet and an outlet were fabricated. However, the channel had a constriction at one end lowering the depth of the channel to 100 µm. This constriction meant that organoids got trapped and held in the chip, but media was still able to flow around the cells to supply nutrients. Again, this complex 2.5D geometry would be very difficult to fabricate using other manufacturing methods (this requires at least two photolithography steps), but with 3D printing, it is a simple, 1-step process. Furthermore, the incorporation of this 2.5D geometry with the 3D geometry of the weld seams is something that only 3D printing can fully capture in a single fabrication step. A schematic the chip made here is shown in Figure 2.18A. Once the organoids were loaded into the chips, tubing was connected and media was supplied to the chips from a syringe pump at a rate of 100 µl/hr. Cells in different chips were stained after 1, 3, and 7 days with an additional chip stained with a live dead stain after 1 day but with no media (no flow) supply

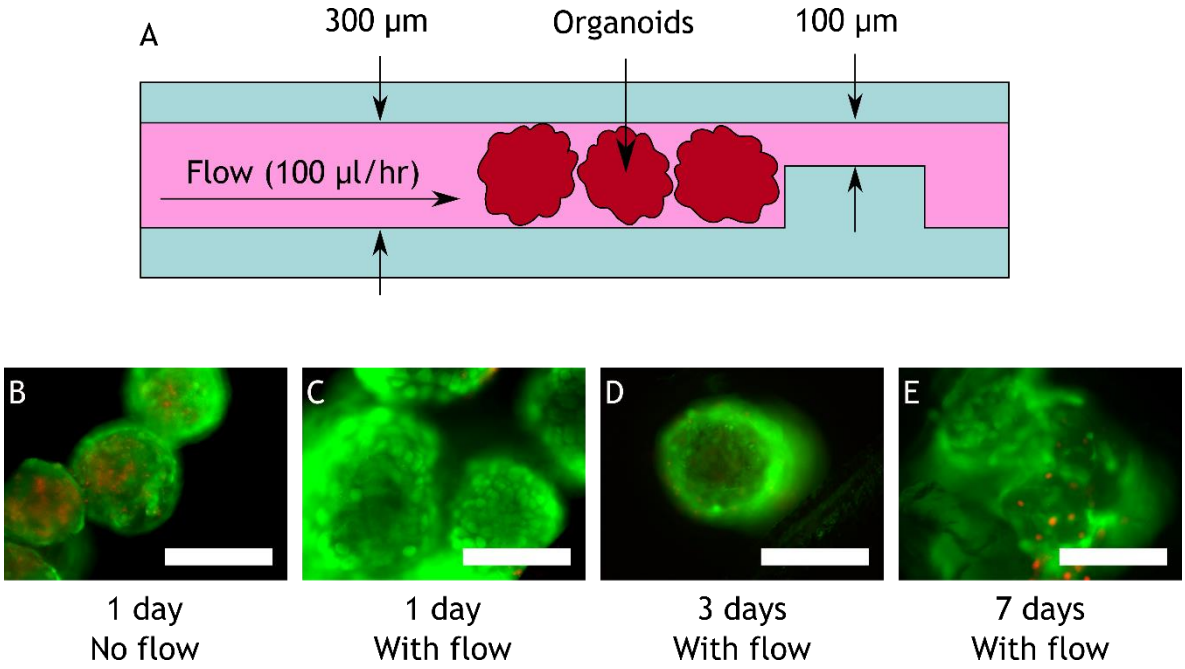

Figure 2.18 – Liver organoid-on-a-chip. A shows a schematic of the device consisting of a 300 x 300 µm channel, with a 100 µm contraction. B shows the viability of the organoids (calcein = green, propidium iodide = red) after 1 day with no media flow. C to E respectively shows the organoids after 1, 3, and 7 days with media flowing at a rate of 100 µl/hr. Scale bars = 300 µm

acting as a negative control. These fluorescent images can be seen in Figure 2.18C-E showing the organoids after 1 day with no flow, 1, 3 and 7 days with flow respectively. Here it can be seen that after one day with no flow of media, the cells in the organoids are predominantly alive however, there is a higher number of dead cells compared to the others. The organoids supplied with flowing media showed a minimal number of dead cells, showing that the organoids stayed healthy after seven days in the chip. This ability to maintain cell viability for prolonged periods of time highlights the attractiveness of polystyrene microfluidic chips, and the fact that such a chip was simple and cost effective to manufacture at the length scales required, show a usable example of microfluidic chips moulded from 3D printed inlays.

2.8 Conclusions

In this chapter, a new method of fabricating injection moulded microfluidic devices has been developed. It was found that the standard clear resin was more suited towards an industrial injection moulding process than the high temp resin when using a commercially available Form2 printer. With this process, features as small as 100 x 200 µm could be realised with a minimum spacing of 500 µm. Although these features are relatively large compared to most microfluidic

devices however, the dimensions are limited by the 3D printing and not the injection moulding process so can be expected to be lowered as printers become more capable. Furthermore, it was shown that the fidelity of the features remained good for a 500 part production run when shallower channels were considered. When deeper channels (larger than 400 µm) were moulded, there was a reduction in height with subsequent parts showing some limitations of this process. It was also shown that the roughness of parts moulded directly from the 3D printed inlays meant that their optical clarity was insufficient when microscopy of cell cultures was considered. This optical quality could be improved vastly however, by simply polishing the inlay prior to moulding.

Post-injection moulding, ultrasonic welding was utilised to seal parts and create functional microfluidic devices. It was shown that weld seams – structures difficult to fabricate with traditional manufacturing techniques – could easily be incorporated into the design of the chips. The design of energy directors for ultrasonic welding was optimised showing that features as small as 350 x 100 µm could be printed and used to seal the device, however, more reliable sealing was seen with larger energy directors (350 x 200 µm) while the ultrasonic welder was in energy mode. Lamination as a means of sealing was also investigated and it was discovered that sealing could be achieved using as little as 2 passes through the laminator. Different lamination pouches were also considered with Kapton performing best in terms of optical clarity. In addition, devices were fabricated with the aim of maintaining an organoid culture under flow of media. These chips consisted of channels with differing depths and dimensions which would have been difficult to fabricate through other methods.

Furthermore, the time frame of this fabrication process is also an important point of discussion. CAD modelling of the device takes approximately 1 hr, and a typical inlay takes 2.5 hrs to print, wash, and cure. To prepare the injection moulder and run 50 parts takes a further 2 hrs, while an additional 30 mins is required to drill inlets/outlets and seal the chips. Thus, a total time of 6 hrs is needed to completely fabricate a large number of chips from scratch, meaning that devices can be designed, manufactured, and tested within one working day. As such, multiple iterations of a device can be tested rapidly in line with the rapid prototyping approach often used in microfluidics research. While techniques such as soft-lithography also allow for the rapid turnaround of

microfluidic devices, the reliance on PDMS means that devices have unwanted properties such as small molecule absorption, deformation under flow, or a short shelf life. Moreover, the translation of PDMS chip into mass-producible devices is difficult due to the differences in the fabrication protocols. For example, the conformal sealing of PDMS devices means that the bonding of materials is often overlooked in the prototyping phase. The use of PS in the injection moulded chips eliminates these drawbacks while also allowing prototypes to more closely resemble the final product. Furthermore, as 500 parts can be made from a single mould, this technique technique can be used in semi-industrial applications.

In addition to the throughput and material considerations, the increased dimensions of the 3D printed inlays means that devices are better suited to organoid cultures where channels with larger cross-sectional areas are required. The fact that complex biological structures can be maintained in these devices illustrates how such chips can be used for OoaC research and pharmacological applications.

With the above considerations in mind, injection moulded microfluidic chips moulded from 3D printed masters and sealed through ultrasonic welding were used for the future microfluidic experiments in this work.

In summary, injection moulding of microfluidics using 3D printed inlays combines low cost, rapid-prototyping with high-throughput, industrial scale manufacture in a manner that is unparalleled by existing processes.

Chapter 3 - Oxygen Detection and Control in Microfluidic Devices

3.1 Introduction

As mentioned Chapter 1, microfluidics have been implemented to supply nutrients and remove waste from *in vitro* cultures to better mimic the blood supply *in vivo*. However, this supply of nutrients and removal of waste are not the only factors that need to be captured for a microfluidic device to emulate human physiology. Firstly, the complex structure of human tissue needs to be replicated with tissues composed of the multiple cell types capable of carrying out all the functions of a human organ. For example, the human liver consists of not only hepatocyte cells that carry out the main functions of the liver, but also cholangiocytes, stellate cells, kupffer cells and endothelial cells which support the main function of the liver as well as providing structures for the transport of nutrients, nervous support, and waste removal.

However, alongside this biological complexity, the microchemical environment must also be recapitulated if any organ-on-a-chip device has a chance of fully capturing human *in vivo* conditions. The supply of specific nutrients and hormones to specific regions of the body inform organ development and cell phenotype as well as genotype during organ development. For example, different Wnt expression and signalling within the developing spinal cord are thought to drive the development of the brain as well as further development of the spinal cord itself. With this in mind, many studies have been conducted using differing concentrations signalling molecules to drive the differentiation of cells into more functional units. With this in mind, it is beneficial for OoaC devices to not only capture the diversity of cell types found within an organ, but also the chemical environment they are subject to in the body. As such, there has been a great deal of research showing how these gradients can be formed, and maintained by the low Reynolds/peclet number flows found within microfluidic devices. As mentioned in Chapter 1, oxygen is of particular interest in the life sciences, not just for the maintenance of metabolic function within living cells, but oxygen is also thought to drive the differentiation of cells towards different functionalities in organs such as the liver[195]. As such, various approaches have

been taken to create microfluidic devices that subject cells to gradients in oxygen concentration. A summary of these devices is given below:

Perhaps the in their simplest form, microfluidic devices that subject cells to oxygen gradients consist of a cell culture chamber, an inlet and an outlet. Cells located nearer the inlet experience higher concentrations of oxygen and other nutrients than those nearer the outlet – mimicking the physiology of that of the liver. This approach has been used by a variety of researchers, mainly with a focus on liver zonation[88–91]. The permeability of PDMS to gasses has also been used as a means of setting up oxygen gradients in microfluidic devices. In one approach, a channel carrying O_2 gas is run alongside the cell culture area and the O_2 diffused through the PDMS and into the cell culture chamber creating a gradient of increasing oxygen concertation with increasing proximity to the gas channel. With this approach, researchers have differentiated human pre-hepatocytes in a chamber with a O2 channel running alongside it creating a continuous oxygen gradient similar to that seen *in vivo*[92,93]. Finally, microfluidic gradient generators have also been used to set up gradients across liver cells. These chips utilise many layers of mixing from two discrete inlets to generate a smooth gradient in the cell culture chamber. This approach has been used in the modelling of non-alcholoic fatty liver disease where gradients of both oxygen as well as other molecules were generated[95]. This generation of gradients in molecules other than oxygen shows the flexibility of this technique when compared to those mentioned above. The above devices highlight the importance of control over dissolved oxygen concentration within microfluidic devices however, all the approaches mentioned above suffer from one of two drawbacks. Firstly is their reliance on PDMS meaning they cannot be used for drug screening application due to the issues discussed in Chapter 1, and secondly is that there is no verification of the oxygen concentration in the device other than simulations or analytical mathematical models which may not be representative of the true distribution of oxygen within a device.

With regards to the first point, culture in microfluidic chips other than PDMS has been avoided due to perceived issues with gas permeability. That is, without oxygen diffusing into the chips through the material, normoxic conditions cannot be maintained leading to cells being cultured under non-ideal conditions. So far, there has been few documented studies into the distribution of oxygen within

thermoplastic microfluidic devices other than the development of oxygenation chips to allow for gasses to diffuse into the flowing media prior to it entering the main cell culture device[196]. This lack of understanding about oxygen in thermoplastic microfluidic devices acts to hinder their uptake in the life sciences.

3.1.1 Existing O_2 sensors

In order to fully understand how oxygen is distributed throughout microfluidic devices however, sensors capable of spatial detection of oxygen must be incorporated into the device so that a true readout of O_2 concentration can be obtained and then used to verify results from simulations. As with control of oxygen, there have been a variety of attempts to create oxygen sensors compatible with microfluidic technologies. These range from commercially available options[197] to those presented by researchers such as the platinum based sensor described by Volker Nock *et al.*[96]. However, such sensors rely on complicated fabrication protocols that do not align with the injection moulding procedure described in Chapter 2. As injection moulding produces a part every 30s, there is a need for an oxygen sensor that can be integrated into a microfluidic device rapidly so that the manufacture of such devices remains fast. Furthermore, as most options for oxygen sensing are point based, they are limited in detecting the gradients that drive many processes in the body.

3.1.2 Aims

As discussed above, the ability to measure and control the O_2 concentration inside microfluidic devices is beneficial to many areas of life science research. Current means of doing this however, are not compatible with a high throughput injection moulding process as they take too long and require specialist clean room fabrication techniques. As such, the aims of this Chapter are detailed below:

- Demonstrate the difference in O_2 concentrations within PDMS and PS microfluidic devices and how this concentration can be leveraged to provide ample supply of O_2 to the cells

- Development of an O_2 sensor capable of resolving spatial information of O_2 concentration in PS microfluidic chips. Fabrication of such a sensor should be fast enough to align with the manufacture of chips by injection moulding (one part every 30s) while still providing sensitive detection of oxygen at concentration relevant to human physiology (0-20%).
- Analyse the performance of the oxygen sensor for the spatial detection of oxygen within PS microfluidic chips. Conduct further analysis showing the temporal resolution of the sensor with the aim of providing real time, spatial readouts of oxygen concentration.
- Compare the performance of the oxygen sensor to those previously described in the literature.

3.1.1 Overview of chapter

This Chapter documents the analysis of oxygen concentrations within PDMS and PS microfluidic devices. It also describes how the properties of the PS devices can be leveraged to provide enough supply of nutrients to the cells while also allowing for control over the dissolved oxygen concentration within the chips. Firstly, it documents the materials and methods used for this work, as well as details on the development of a new oxygen sensor (based on pressure sensitive paint (PSP) used in the aerospace industry). Analysis of the sensitivity of the paint as an oxygen sensor is presented, as well as experimental data showing how the PSP can be used to provide spatial information of the oxygen within a PS microfluidic device. This experimental data is also compared to simulated data to further validate the usefulness of the PSP oxygen sensor. The temporal resolution of the PSP with regards to oxygen sensing has also been shown and the performance and fabrication protocol of the PSP oxygen sensor is compared to previously described oxygen sensors. Parallel to this, the Chapter also details the development of the hardware required for optical sensing using the PSP. This includes a bench top set up based on a microscope that allows for both spectroscopic data.

3.2 Materials and methods

As discussed in Chapter 1, determining the oxygen concentration inside a microfluidic chip is important when creating OoaC devices to mimic organs such

as the liver. To accomplish this, an oxygen sensor that could be rapidly incorporated into injection moulded fluidic chips was developed. Details on how the sensor was integrated into the chips and how this was used to measure the oxygen concentration are given here. Also given are details on how a commercially available oxygen sensor was used to calibrate the newly fabricated one as well as details on how the gas permeability of PS vs PDMS chips was demonstrated. The oxygen gradients within the chips were also simulated and details on how this was done are also given.

3.2.1 Measurement of gas permeability of PDMS and PS

As discussed in Chapter 1, a perceived issue with the use of PS fluidic chips for OoaC applications is the lack of gas permeability when compared to materials such as PDMS. To illustrate this, PS and PDMS chips were fabricated with the same geometry and Presens dots (Presens, Norway) were included into the chips prior to sealing. Madin-Darby canine kidney (MDCK) cells were seeded into the chips at a density of 2,500 cells/cm^2. The inlets and outlets to the chips were then sealed using parafilm to ensure that only gasses diffusing through the bulk material were able to reach the media. The O_2 concentration was measured daily for 5 days.

To try and improve the oxygenation in the PS chips, an oxygenator chip was fabricated. This consisted of an injection moulded microfluidic chip, only instead of welding to a blank PS slide to seal it, it was welded to a PS foil (Goodfellow, UK) which had been laser cut to provide a hole over which a 0.4 µm (Steriltech, UK) pore size, hydrophobic PET membrane was glued. The principle here is that the pores are small enough for liquid to not pass through but large enough to allow for the free diffusion of gases. This is shown in Figure 3.6. Blunt tipped needle connectors were then added to the chip so that it could be connected in series before a cell culture chip. Again, MDCK cells were seeded at a density of 2,500 cells/cm^2 before media was flowed through the chips at a rate of 100 µl/hr. The oxygen concentration was measured daily. Chips were also set up without an oxygenator, and also without cells to act as controls.

3.2.2 Sensor fabrication

The oxygen sensor developed in this work is based on pressure sensitive paint (PSP) (Innovative Scientific Solutions, Inc, US). This paint consists of the fluorescent molecule, platinum tetra (pentafluorophenyl) porphyrin (PtTFPP) immobilised in a range of solvents (full details are discussed in section 3.4.2)[198]. This PtTFPP molecule fluoresces (excitation = 405 nm, emission = 650 nm) however this fluorescence is quenched in the presence of oxygen (as per equations 1.5, 1.6, and 1.7). The PSP comes in a spray can meaning that application of the paint to the chips is fairly quick and simple. To apply the paint, the chips were masked leaving only the area to be coated exposed. The chips were masked using either a laser cut 200 µm thick PS foil (Goodfellow, UK), or using masking tape that had been cut with a scalpel to expose the area of interest (3M, US). The paint was then sprayed onto the chip taking care to allow the paint to spray for a few second prior to covering the chips to ensure an even coat free of any particulate that built up around the nozzle when the paint was not in use. The can was held ~20 cm from the chips and the spray was passed over the chips 3 times. This ensured that every part of the unmasked area was coated. Once painted, the chips were allowed to dry at room temp for 10 mins before the masks were removed. The chips were then baked at 80°C for 2 hrs to remove the solvents ensuring a more stable sensor. The benefits of the baking process is discussed in more detail in section 3.4.2.1. Once the chips were cool, they were ultrasonically welded to a blank PS slide and had fluidic connectors added (blunt tipped needles).

3.2.3 PDMS chip fabrication

Alongside the injection moulded PS microfluidic chips, PDMS chips were also created with the purpose of highlighting the difference in the permeability to gases between the two materials. To fabricate the PDMS chips, master structures were 3D printed, washed and cured according to section 2.2.1. Meanwhile, PDMS (Sylgard 184, Dow Corning, US) was mixed at a ratio of 10:1 (*w*/*w*, bulk:curing agent) and placed under vacuum to degas. This meant that all the bubbles were removed from the mixture which could lead to defects in the final part. Once all the bubbles had disappeared, the mixture was removed from the vacuum and poured over the master structures before being placed back in

the vacuum to degas once more. Once all the bubbles had been removed, the parts were placed in an 80°C oven for 2 hrs to allow the PDMS to cure completely. After the curing, the PDMS was carefully peeled from the 3D printed master before inlet and outlet holes were cut with a 0.5 mm biopsy punch. Once the holes had been cut, the parts were placed under an O_2 corona and in order to increase the surface energy of the material and thus increase the strength of the bond. The PDMS was then pressed firmly against a plasma treated injection moulded PS blank slide to create the device. A schematic of this process is shown in Figure 3.1.

3.2.4 MDCK cell culture

MDCK cells were used for experiments as they are easy to handle and, with a doubling time of 24 hrs, would allow for rapid biocompatibility experiments. MDCK cells were cultured in a media composed of Dulbecco's Modified Eagle Media (DMEM), + glucose, pyruvate, and glutamine (Thermofisher), along with 10% (v/v) FBS and 1% penicillin streptomycin. The cells were grown in T25 flasks until almost confluent before they were passaged and seeded at a lower confluence, or used in experiments. Suspended cells were pipetted into the chips and allowed to attach to the surface for at least 2 hrs before any flow was introduced. This prevented the cells from being washed away before they had a change to attach. For experiments in well plates, cells were simply pipetted into the well along with the desired volume of media. The seeding density varied between experiments and is stated where appropriate.

To image the cells, phase contrast micrographs were taken using an EVOS FL1 imaging system (Thermofisher) with either 10x, or 20x objectives. Cells were not stained for the work in this section.

3.2.3 Readings from the PSP sensor

To measure the emmitance of the PSP and thus the oxygen concentration of a solution, a Nikon microscope was altered in order to contain the light source necessary for the 405 nm excitation, as well as having all the filter necessary to protect the user from this high energy light. A schematic and a photograph of

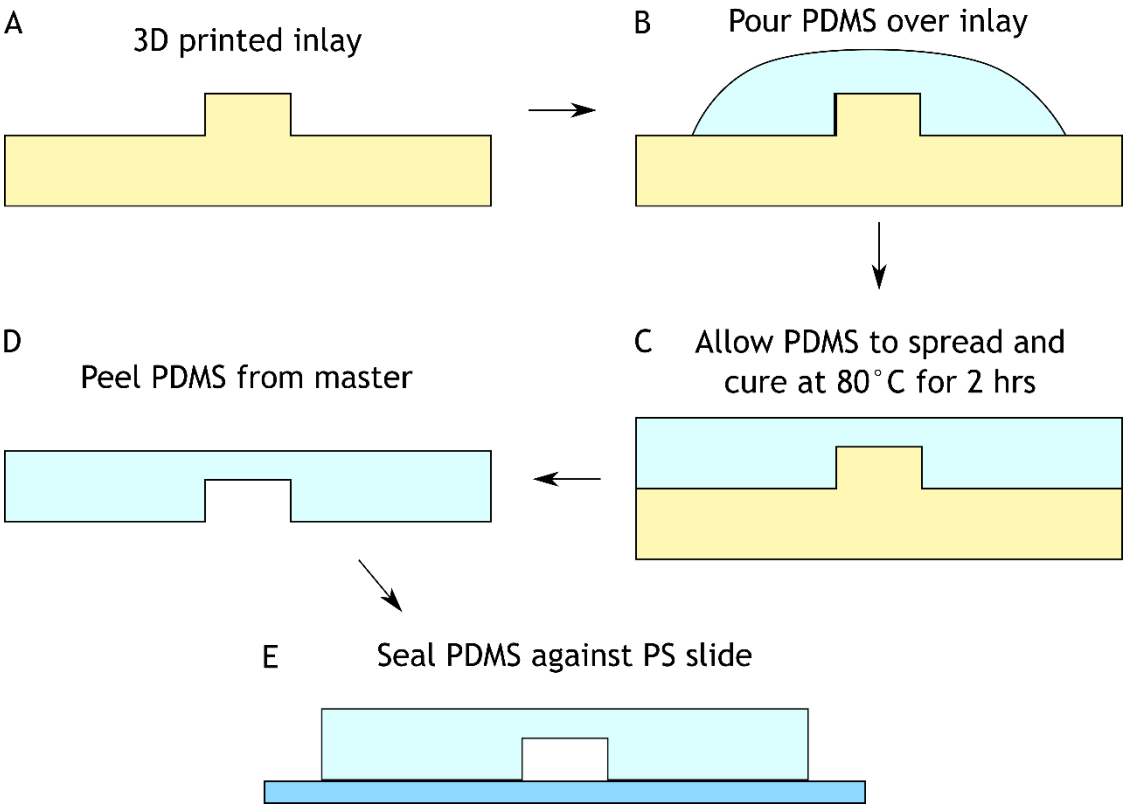

Figure 3.1 – Soft lithography process. A shows a schematic of a 3D printed master (yellow) with a relief pattern of the desired structure. B shows how the PDMS (blue) is poured over the inlay while C shows how the PDM spreads over the part and is cured at 80°C for 2 hrs. Once cured the PDMS is peeled from the master (D), before being sealed against a blank PS slide (E).

this set up are given in Figure 3.2A and B respectively, while a list of the components required are given in table 3.1.

The 405 nm LED was included to provide the excitation light for the PSP and the condenser lens was used to focus the LED light onto the sample. The mirror diverted the LED light up and into the existing light path of the microscope. The 3D printed mirror mount was designed to hold the mirror mount in place above the existing light path of the microscope. This part is shown in 3.2C. A 2.5x objective (Microplan, UK) was used to image the chip while a long pass filter was added above the objective in order to prevent any harmful 405 nm light from reaching the eyepiece of the set up and to filter this out so that only the 650 nm light was being imaged. This filter was held in place in a custom-made filter mount (3.2D) which fitted into the existing filter cube mounts on the microscope (3.2E). For spectral analysis, the spectrometer was used, whereas the eyepiece camera (controlled using Spinnaker software (FLIR, US)) was used to obtain images of the chip.

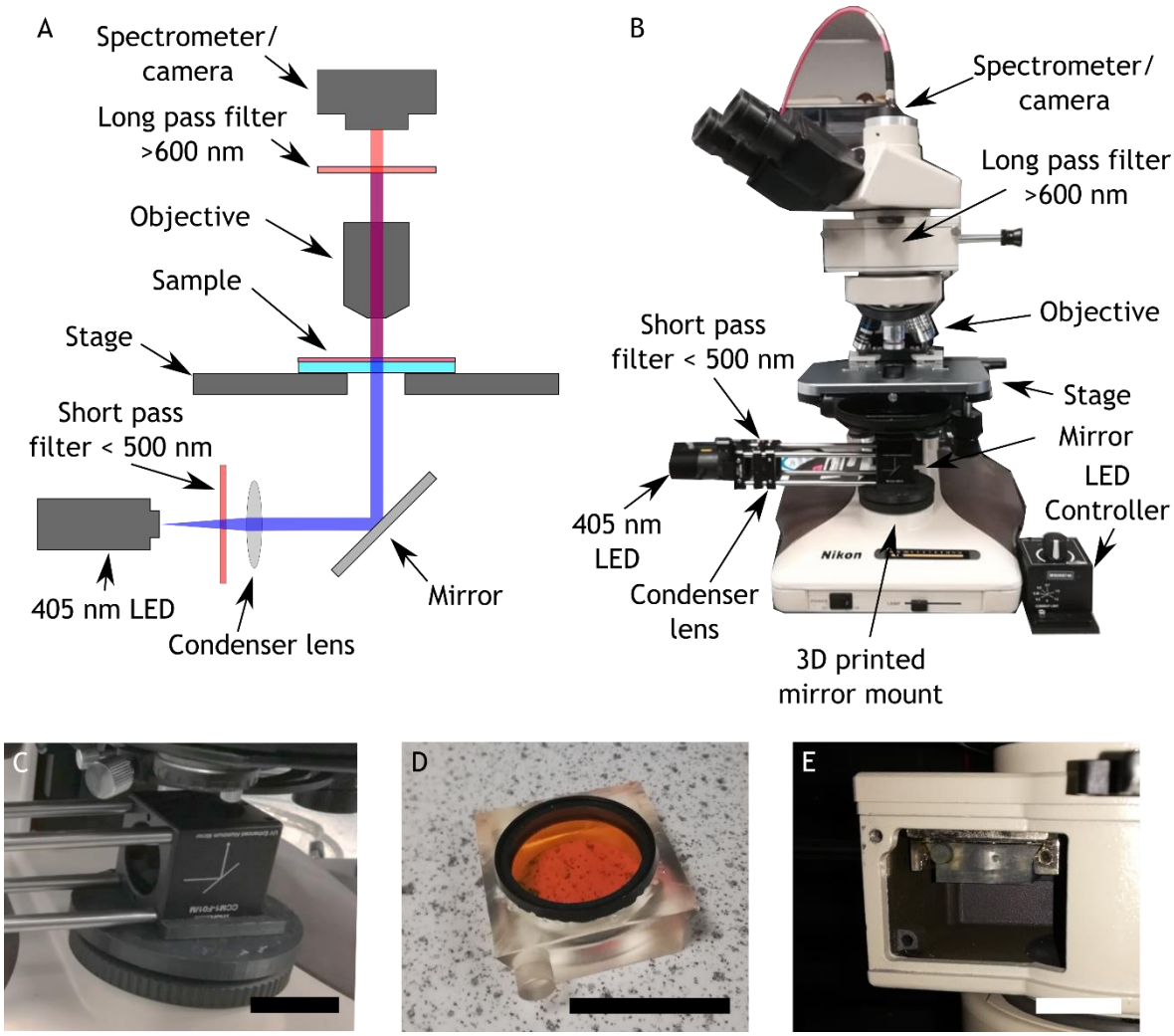

Figure 3.2 - ***Microscope setup for PSP based oxygen sensing. A shows a schematic of the light path with all the various components while B shows a photograph of the setup. C shows the 3D printed filter cube mount. D Shows a photograph of the long pass filter in the custom filter mount, while E shows this mount installed in the exisiting filter cube holders on the microscope. Scale bars = 30 mm in C, and 25 mm in D and E.***

3.2.3.1 Calibration of the PSP sensor

To calibrate the fluorescence intensity measurements from the PSP with respect to oxygen concentration, the spectrometer readings from the PSP at a range of oxygen concentrations were compared to the readings from a commercially available sensor. To do this, a plastic petri dish was sprayed with a 1 cm^2 region of PSP on its base. A Presens dot (SP-PSt3-NAU-D5-YOP, Presens, Norway) was also stuck to the base of the dish. Nitrogenated water was created by bubbling Nitrogen through DI water for 5 mins. Once the water was added to the dish, an emission spectrum from the PSP was recorded as well as the oxygen concentration measured from the presens dot using a Fibox 4 meter (Presens). Over time, oxygen from the air diffused into the water, slowly increasing the oxygen concentration. To expedite this process, air was bubbled

Part name	Supplier	Part number (if applicable)
Microscope	Nikon	
405 nm mounted LED	Thorlabs	M405L4
Ø1" Shortpass Filter, Cut-Off Wavelength: 500 nm	Thorlabs	FES0500
Ø1" Longpass Filter, Cut-On Wavelength: 600 nm	Thorlabs	FEL0600
SM1-Threaded 30 mm Cage Plate, 0.35" Thick, 2 Retaining rings, M4 Tap	Thorlabs	CP33/M
30 mm Cage Cube-mounted UV-Enhanced Aluminium Turning Mirror, 8-32	Thorlabs	CCM1-FO1/M
Blackfly S	FLIR	BFS-U3-32S4M
Lens	Thorlabs	
Spectrometer	Ocean Optics	
3D printed mirror mount	Custom	
3D printed lens holder	Custom	

Table 3.1 – ***Required items for PSP oxygen sensing hardware. Supplier = custom indicates that parts were designed and 3D printed in-house***

through the water using a Pasteur pipette. A schematic of this set up is shown in Figure 3.3. Readings were taken every minute until the oxygen concentration was observed to plateaux. The photon count measured at 650 nm for each of the oxygen concentrations was plotted against the readings from the Presens meter to create a calibration curve.

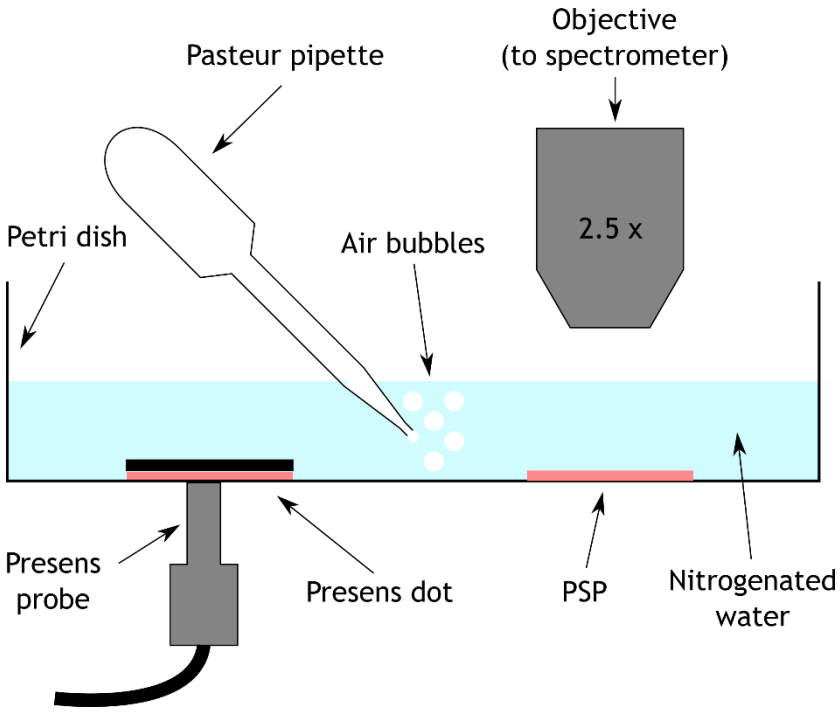

Figure 3.3 – Experimental details of PSP oxygen sensor calibration. Figure 4.2 Shows a schematic of the calibration of the PSP O_2 sensor. A petri dish with a PSP dot and a region of PSP on the bottom was filled with nitrogenated water. Readings were taken simultaneously from the Presens meter and the spectrometer reading the PSP as air was bubbled through the water to slowly increase its dissolved oxygen concentration.

3.2.3.2 Spatial analysis of dissolved oxygen

To demonstrate the ability of PSP to resolve the spatial distribution of oxygen within a microfluidic chip, a Y-channel design (shown in Figure 3.4A) was made with a region of PSP just after the union of the two inlet channels. One inlet of the chip was supplied with water at a flow rate of 200 µl/hr that had been allowed to sit uncovered to ensure the O_2 concentration was at atmospheric levels, while the other inlet contained water with 0.13% w/v Na_2SO_4 and 13 µMol $Co(NO_3)_2$ to scavenge the dissolved oxygen and give a solution close to 0% (also at a flow rate of 200 µl/hr). This reaction is commonly used to create a low O_2 solution[95]. The concentrations of the two solutions used were verified with the Presens sensor to calibrate the measurements from the PSP. The eyepiece camera was then used to take an image of the chip. The flow rate in the low oxygen channel was then increased to 400 µl/hr and left to equilibrate for 5 mins before another image was taken This was repeated for flow rates of 600, 800 and 1000 µl/hr in the 0% O_2 inlet. The 0% channel was then turned off, and the chip was allowed to fill with just fluid from the high O_2 channel and an image of the PSP under these conditions was taken to subtract from the other images to remove the background. The mean grey values of the images were

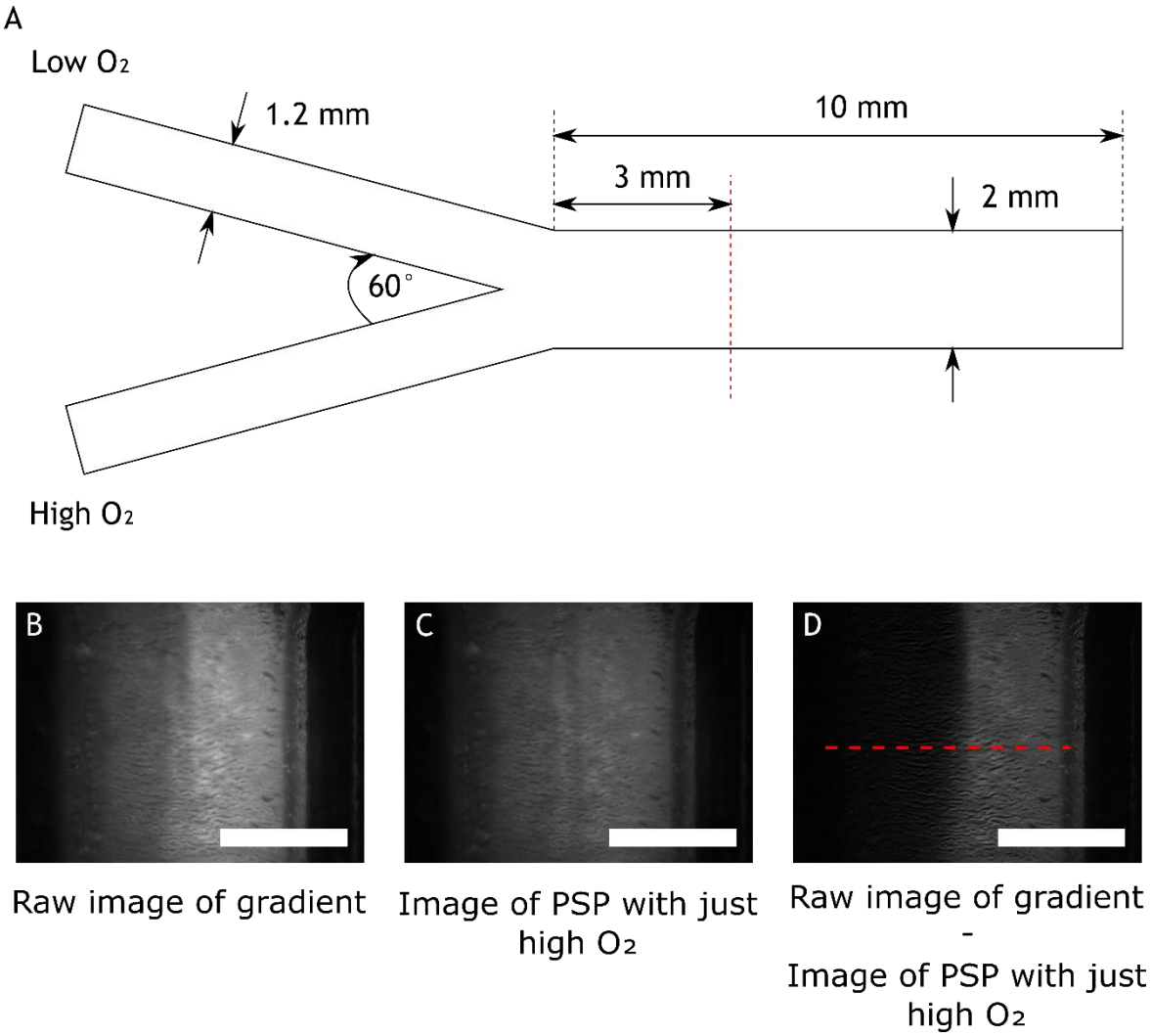

Figure 3.4 – Experimental details of the spatial analysis of oxygen using PSP. A shows the geometry of the chip used for these experiments with the red dotted line indicating where the mean grey values were recorded from. B and C show the raw images from the eyepiece camera of the channel with a gradient and with just the high O_2 solution respectively. D shows an image of the gradient image minus the high O_2 image so that the effects of uneven illumination are eliminated from the analysis of the PSP. The red dotted line corresponds to the red dotted line in A and shows where the mean grey values were measured from. Scale bars = 1 mm.

plotted with respect to their location in the x-direction to give a plot of the oxygen gradient. This analysis process is summarised in 3.4B, C, and D.

3.2.3.3 Temporal analysis of dissolved oxygen

Alongside the spatial resolution of the PSP, the temporal resolution is also important when it comes to monitoring how the oxygen concentration changes with respect to time. To analyse this, the same Y-channel design as used for the spatial analysis (Figure 4.3) was used. In this instance however, the channel was first filled with a 0% O_2 solution and a video of the chip was recorded with no flow. After 10 s, the high O_2 solution was forced into the chip before the video was stopped after 40s. The same image analysis as used for the spatial analysis

of the PSP was used here on each frame of the video. The mean grey value of the PSP was then plotted with respect to time. The response time was calculated by measuring the time from when the high O_2 solution was forced into the chip to the point at which fluorescent intensity from the PSP reached its peak value. Curve fitting was done using a least squares regression on Python.

3.2.5 COMSOL simulations

COMSOL simulations (carried out by Pedro Duarte Menezes) were conducted to give an analytical basis for what the gradient inside the fluidic chips should look like. The simulations were created using COMSOL's computational fluid dynamics (CFD) module. This utilises the Navier-Stokes equation for the conservation of mass and momentum. COMSOL's Transport of Diluted Species modules was used to model the diffusion of molecules in accordance to Fick's law. The simulated channels were created to have the same geometry as the chips used for the experimental readings with the flow rate at both inlets set to provide a constant flow rate with the walls being impermeable and having a no-slip boundary condition. The fluid was defined as water (dynamic viscosity = 0.6965 mPas, density = 993.30 kg/m^3)[199] with a dissolved oxygen concentration of 20% in the left channel, and 0% in the right. The diluted species simulated as O_2 with a diffusion coefficient of 3.35 $x10^{-9}$ m^2/s[200]. Full details of how the simulations were carried out have been described by Menezes *et al.*[201].

3.3 Permeability of polystyrene vs PDMS

As mentioned previously, the cells behave differently when introduced to environments with different levels of O2. As such it is important to know what the O2 concentration within a given microfluidic device is so that the cells are not subject to increased or decreased O2 levels that could cause undue harm or stress to them. As stated above, one of the concerns with using PS devices instead of PDMS is the lack of permeability to gas. As PDMS has a much higher gas permeability than PS (~2000 $\mu m^2/s$[202] in PDMS compared to ~2 $\mu m^2/s$[203] for PS) PS is thought to be an unsuitable material for microfluidic chips as the oxygen required for healthy metabolism will not be able to diffuse into the chip, and waste gases (CO_2) will not be able to diffuse out. To illustrate this, identical chips manufactured in both PS and PDMS were fabricated. In brief, the PS chips

were fabricated according to the protocol described in Chapter 2 wherein a 3D printed inlay is used for injection moulding. A Presens dot was then stuck to the roof of the channels before the devices were sealed through ultrasonic welding to a plasma treated, injection moulded blank PS slide. The PDMS chips were made using a soft lithography processes. PDMS devices were fabricated as per section 3.2.3. A schematic of this experimental setup is shown in Figure 3.5A. Once assembled, devices were then seeded with MDCK cells before then the inlets and outlets were sealed using parafilm. This was done so that the cells would not be supplied with any O_2 that was dissolved in any media supply, just the O_2 that was able to penetrate the chips. As described previously, PDMS has a much higher gas permeability compared to PS so the PDMS chips should be able to maintain a more normoxic environment for longer. After the inlet/outlet were sealed, the oxygen concentration was measured every day over the course of 4 days and this data is shown in 3.5B.

Here it can be seen that although both chips start out with a similar O2 concentration, after day one, the concentration in the PS chip begins to drop where it settles around day 2. After this time, it was thought that the cells died from a lack of nutrients and thus did not use up any more of the oxygen in the media in the chip. Meanwhile, the oxygen concentration stayed stable for all 4 days in the PDMS chip indicating that the cells were receiving O2 not just from what was already dissolved in the media, but were also receiving oxygen that had diffused through the PDMS. This highlights the previously held fears that without the diffusion of gases through the bulk material, PS devices cannot maintain a normoxic environment for cells to grow in.

However, it should also be noted that in this experiment, the devices were not removed from the incubator before the oxygen concentration measurements were taken. Assuming that the time between opening the incubator door and measuring the oxygen concentration was not long enough for the media in the PDMS device to equilibrate to atmospheric oxygen concentrations (~21%), then it would be expected that the oxygen concentration in the devices should only be as high as the oxygen concentration in the incubator (when using 5% CO_2, the oxygen concentration is around 18.6%[204]). However, as seen in 3.5B, the measured oxygen concentration in the devices is as high as 23% in some instances which is not only higher than what would be expected from media in

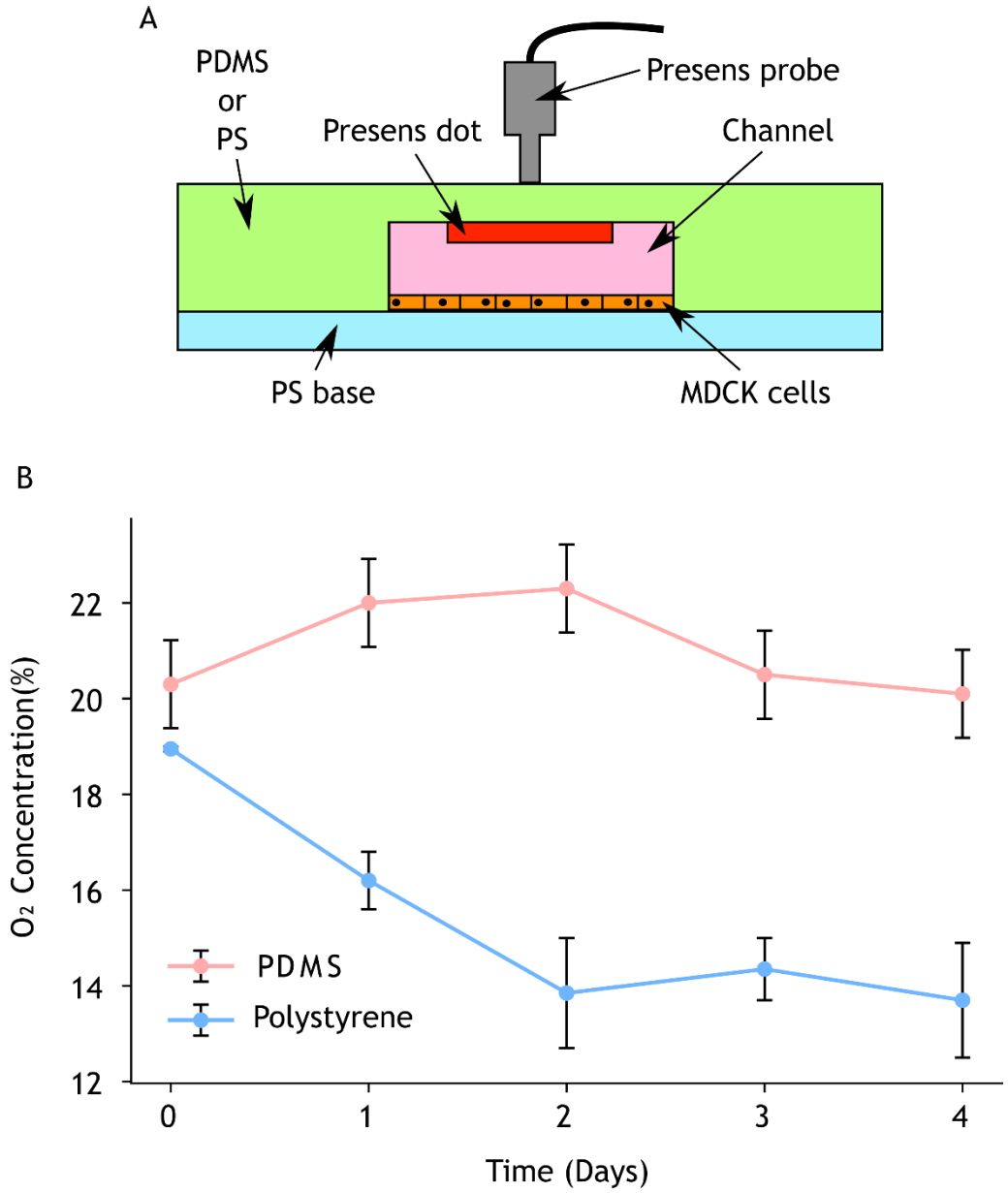

Figure 3.5 – Oxygenation of PDMS and PS microfluidic devices. 4.1A shows an experimental schematic of the PDMS or PS devices used in the experiments. The chips were the same geometries and both included a Presens dot on the roof of the cell culture chamber in order to determine the oxygen concentration of the media. B shows how the oxygen concentration changes with time in completely sealed PDMS (orange) and PS (blue) chips. Error bars = max/min values with n= 2.

an incubator, but higher than we would expect from media in normal atmospheric conditions. This spurious data points to there being something wrong with the experimental setup when these experiments were conducted and that valid conclusions cannot be drawn. The possible causes are discussed below.

Firstly, it could be the case that there was an issue with the CO_2 supply to the incubator. If there was no CO_2 to displace the oxygen, then it could be expected that the oxygen concentration would be higher in the incubator, and thus higher in the cell media. However, the incubator used for in these experiments has an alarm that warns the user when the CO_2 level is outside of normal conditions, so

it is unlikely that the oxygen concentration would have been higher than 20% in the incubator for as long as 5 days. Also, in the absence of CO_2, the oxygen concentration would only reach atmospheric oxygen concentration, and not the 22% O_2 that was observed.

Another cause is improper measurement of the O_2 concentration. As mentioned in Section 3.2.1, a Presens sensing system was used to measure the O_2 concentration in the devices. It could have been the case that the sensing dots were not properly attached to the cell culture devices meaning that there could have been an error introduced into the measurements. Furthermore, the Presens meter uses a polymer optical fibre as a sensing probe. Damage to this fibre, or damage to the tip that interfaces with the device could also provide a source of error into the measurements. Finally, as Presens offers a variety of different sensing "dots" that could be placed inside the device, it may have been the case that the sensor was expecting a different dot, to the one that was used in these experiments which in turn, could have led to the results seen in figure 3.5.

3.3.1 Further analysis of O_2 concentrations in PS devices

As PS has been reported to be an unsuitable material for microfluidic cell culture application due to its lack of O_2 permeability which results in the creation for a harmful environment for the cells, a study was conducted to better understand the oxygenation of PS devices. Here a commonly used strategy to overcome the issues associated with a perceived lack of oxygenation was utilised. The same PS chips as those used in section 3.3 were seeded with MDCK cells however, in this instance, the inlet/outlet was not blocked and media was supplied to the chips at a constant flow rate of 100 µl/hr. For the chips with the oxygenation devices, another chip composed of chamber sealed by a semi permeable membrane was included upstream from the cell culture chamber. A schematic of this is shown in 3.6A. The working principle of this device is that oxygen can diffuse through the membrane and into the media before it reaches the cells meaning that normoxic media is supplied to the cells. 3.6B shows the configuration of the cell culture chip connected to the oxygenator chip. A final set of chips was set up no cells, but with media flowing through them to act as a control. Again, the oxygen concentrations for all the chips (control, with oxygenator, without oxygenator) were measured daily over the course of 4 days. However, this data affected by

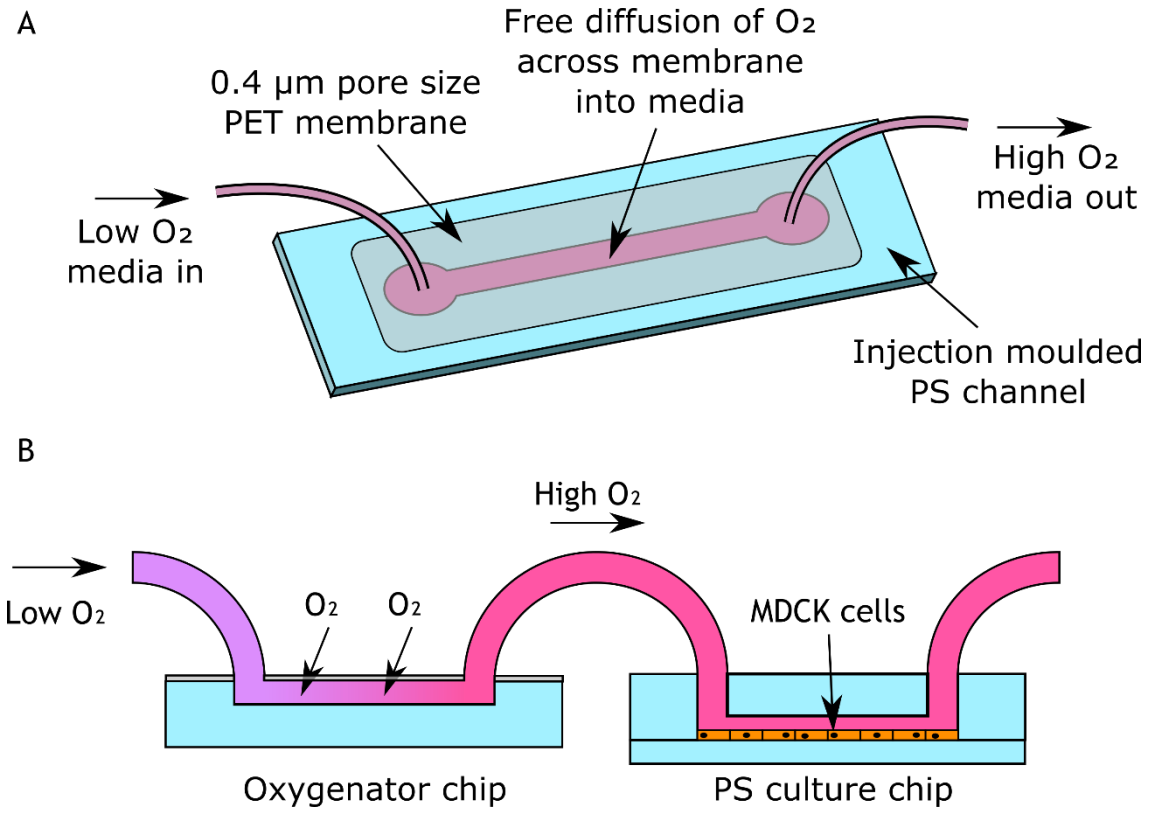

Figure 3.6 – Oxygenation of PS chips. A shows the working principle of the microfluidic oxygenator whereby a semi-permeable membrane allows for the transport of O2 into the media. B shows how such a chip can be included in line with a cell culture chip to better oxygenate cells.

the same issues that was present in the data shown in Figure 3.5. That is, the measured oxygen concentration in the PDMS controls were much higher than the expected levels in the incubator. In this instance, the O_2 concentration was measured as high as 24% which is much higher than any accurate measurement should be. Again, this means that no valid conclusions can be drawn from this experiment. That being said, the relative permeability of PS when compared to PDMS is a well understood issue and there are many reported and well understood methods in the literature that overcome this. These techniques are discussed below.

These oxygenator chips generally consist of a fluidic channel designed to maximise the contact area between the media flow and the air, and a semipermeable membrane which allows for gas to pass through, but not liquid. In some cases, the membrane is left open to the atmosphere however, in others a secondary network of channels above the membrane means that gases other than air can be flowed through to better control the dissolved gas concentration in the media. Examples of such devices include that described by Leclerc *et al.*[205]. Here PDMS layers are stacked in such a way that media is flowed through

micro-channels separated from oxygen flowing in adjacent channels. Due to the gas permeability of PDMS, oxygen can freely diffuse from the gas channel into the media, thus increasing the dissolved O_2 concentration of the media reaching the cells. Higgins *et al.* used a similar PDMS to create a device to allow them to study sickle cell vasoocclusion[206] while Lachaux *et al.* made a device to study endothelialisation[207]. Femmer *et al.* Showed that the transfer of oxygen into the media could be increased by adding in herring-bone like structures into the media channels to increase mixing[208]. Like the design shown by Leclerc *et al.*, Vollmer *et al*[108]. used a network of PDMS micro-channels either side of a thin PDMS membrane. Nock *et al.* and Lo *et al.* used a similar device however O_2 or N_2 (or low O_2 gas in the case of Lo *et al.)* were flowed through the gas channels to create oxygenated, or hypoxic media[96,209]. This approach was also used by Adler *et al.*, who used a computer controlled mixer for the incoming gas to produce oxygen gradients of any arbitrary shape[210]. Lam *et al.* and Polinkovsky *et al.* also used the permeability of PDMS to generate oxygen gradients, however in this instance, the gradients were created by running the inlet gas through a standard microfluidic gradient generator[211,212]. This created channels with discrete, and different oxygen concentrations which were then allowed to diffuse through the PDMS and into the media creating a chip capable of studying cell growth at different concentrations.

Alongside the PDMS devices listed above, researchers have also created oxygenation devices in thermoplastic materials that would be more suited to mass manufacture. The most common way of constructing such chips is to use a similar approach to the PDMS chips described above, there a gas channel or chamber is separated from the media by a semi-permeable membrane. This approach was utilised by Ameri *et al.* who created channels in PMMA, and then separated the gas from the media using a 25 µm thick thermoplastic polturethane (TPU) membrane[213]. Barsukova also showed a similar device, but used cyclic olefin copolymer (COC) for the channels, and PTFE for the membrane[214]. Sønstevold *et al.* also used a gas permeable thermoplastic (polymethylepentene (PMP)) to create films to cover a polycarbonate (PC) fluidic chamber. The oxygenation was achieved through the free exchange of gas through the PMP[215]. Ochs *et al.* created an entirely injection moulded device using PMP. Using this gas permeable thermoplastic material, they were able to show that there was little to performance difference between the PMP and PDMS

when culturing endothelial cells[200]. This paves the way for mass-manufactured thermoplastic devices that have can perform as good as, if not better than PDMS devices. Is addition to the diffusion of oxygen through thin films, or permeable materials, alternative techniques for controlling oxygenation in microfluidic devices include incorporating a series of electrodes to control oxygen concentration via electrolysis[216].

As discussed above, the use and fabrication of oxygenators for microfluidic cell culture is well understood. Although it had been hoped to study this in this project, the issues discussed in section 3.3 meant that no valid conclusions could be drawn from the data that was gathered. While this means that the first aim of this chapter has not been met by the data presented here, the wealth of literature on this topic goes a long way in showing how the perceived issues with the lack of O_2 permeability in thermoplastic devices can be dealt with. In fact, there has been research that suggests that the gas permeability of PDMS devices may be too high for a lot of OoaC research and that better control of oxygenation can be achieved in non-permeable chips thus highlighting the benefits of a thermoplastic chip, with some form of oxygen control as described above[217].

3.4 Detection of O_2

As discussed by Bussooa *et al.*[217], there is scope for controlling the oxygenation within PS devices to a higher degree than in PDMS. This becomes increasingly important when biological applications involving control over oxygen concentration are considered. As previously mentioned, attempts have been made to control the oxygen gradient within a microfluidic device for the purposes of mimicking the physiology of the liver. As physiological oxygen concentration ranges between 3-12% depending on the proximity to the portal vein[90], recapitulation of this gradient on a microfluidic chip will lead to more physiologically relevant OoaC devices. Furthermore, control over the oxygen microenvironment is important for the study of pathologies such as ischemia[218], and for other models such as fat[219]. However, for such applications, control over the oxygen concentration in the devices cannot be fully achieved without a direct measurement of the O_2 concentration within the microchannel.

3.4.1 Existing microfluidic oxygen sensors

As mentioned in section 3.1, a wide variety of oxygen sensors exist, ranging from the commercially available ones used for the experiments in section 3.3, to amperometric and optical detection approaches (described in section 1.2.1.2). However, despite the high sensitivity of reported microfluidic amperopmetric sensors, their drawbacks include complicated fabrication processes relying heavily on clean room manufacturing protocols for the patterning of conductive metals onto the surface of the chip, and issues with the lifetime of the sensors associated with membrane fouling. Optical methods, on the other hand, also offers sensitive oxygen detection and are based on the fluorescent quenching phenomenon described in section 1.2.1.2. For most microfluidic applications, these fluorescent molecules are immobilised onto the surface of the chip however, this process is often laborious requiring complex protocols for the mixing of the dyes with a matrix to ensure it binds properly to the microfluidic channels, and then often a photolithography process to pattern the sensor onto the region of interest. A summary of the fabrication process for two of these sensors is shown in Figure 3.7.

Here, the sensor fabrication approached described by Vollmer *et al.*[108] (3.7A), and Nock *et al.*[96] (3.7B) are described. While both methods rely on photolithography, their approaches differ slightly. Vollmer uses AZ 4260 resist to leave exposed areas on a glass substrate to which platinum (II) octaethylporphyrin ketone (PtOEPK) dye is applied directly. The PtOEPK molecule is a fluorescent molecule whereby the fluorescence is quenched in the presence of oxygen. This, means that when PtOEPK is included in a device, the intensity of the fluorescence can be equated to the oxygen concentration inside the chip. The resist is them removed by washing in acetone leaving only the patterned dye. However, according to Nock, acetone can damage the PtOEPK films so should not be used during the process of oxygen sensor fabrication. As such a photolithography process was used to define a master structure from which a PDMS stamp can be made. This stamp then acts as a mask to protect certain regions of the sensor from a plasma etching process that removes the unprotected PtOEPK dye and thus leaving defined regions of sensor on the glass substrate. Also, when considering an approach to pattern oxygen sensors onto injection moulded parts, the time taken for each of these approaches is an

A

Vollmer

1. Fabricate AZ 4260 mask on glass

- Spin and bake resist
- Expose resist through mask
- Develop to reveal exposed areas of glass

- Time ~ 1 hrs

2. Pattern sensor onto glass

- Etch glass with dilute HCL to reomove material and increase roughness for increased bonding
- Pipeete PtOEPK/PS/toluene solution onto exposed areas and wait for solvent to evaporate
- Reomve mask with acetone

- Time ~ 2.5 hrs

3. Incorperate into microfluidic device

- Plasma bond to PDMS channels

- Time ~ 0.5 hrs

Total time ~ 4 hrs

B

Nock

1. Fabricate SU-8 master structure on silicon

- Spin and bake resist
- Expose resist through mask
- Post exposure bake and develop

- Time ~ 2 hrs

2. Cast PDMS stamp from SU-8 master

- Mix and de-gas PDMS
- Pour onto master and cure

- Time ~ 2.5 hrs

3. Pattern the sensor onto glass

- Mix PtOEPK/PS/toluene solution
- Spin onto glass and bake to remove solvent
- Stamp with PDMS and oxygen plasma etch to remove unwanted sesor material

- Time ~ 1 hr

4. Incorperate into microfluidic device

- Plasma bond to PDMS channels

- Time ~ 0.5 hrs

Total time ~ 6 hrs

Figure 3.7 – Fabrication of existing sensor technologies. A shows the fabrication process described by Vollmer et al. (reference 16) showing the various steps and estimated times associated with each one. B shows the sensor described by Nock (reference 11) utilising a PDMS stamp as a means of patterning the sensor.

important factor. As injection moulded parts can be fabricated as fast as 1 every 10 s, any approach to incorporating sensors into such devices should also be just as quick. As can be seen above, the requirement for manually placing a stamp on each device and running it through a plasma etching process not only requires expensive, specialist equipment, but can also take several hours per chip. Furthermore, in the process detailed by Vollmer, each chip must be spin coated with resist, exposed, developed and etched, again taking several hours.

In addition to concerns about the timescale of sensor fabrication, both the processes described above rely on spinning of either the sensor material (Nock) or the resist (Vollmer). While this method has been shown to produce very uniform layers of a substance, it is only suitable for patterning flat substrates. As

described in Chapter 3, the injection moulded microfluidics not only contain micro-channels that can affect the spinning process, but can also contain weld seams which are likely to cause further issues. As such, there is a need for an oxygen sensor that can be rapidly incorporated onto 3D PS substrates. The full requirements for such a sensor a detailed in full below.

3.4.1.1 O_2 sensors requirements

As mentioned above, existing methods for incorporating O_2 sensors into microfluidic are lacking when fabrication time and substrate geometry are considered. As such, the requirements for any new O_2 sensors are:

1. Able to coat any surface, with any feature geometry
    - Compatible with microfluidic devices with deep channels, and weld seams
2. Have a fabrication time that complements injection moulding
    - Patterning of an individual device must not take longer than ~10 s per chip to align with manufacture of devices through injection moulding
3. Thinner than commercially available options
    - The Presens dots used in section 4.2 are 5 mm in diameter and 500 µm thick. This is too large for incorporation into microfluidic channels, and the thickness of the dots is likely to disrupt the flow around it

3.4.2 Proof of concept of a pressure sensitive paint O_2 sensor

With the above requirements in mind, a pressure sensitive paint (PSP) (Innovative Scientific Solutions Inc., USA) was considered. PSP was designed for use in the aerospace industry where a model could be sprayed with the paint and put in an air tunnel[220]. Under high pressure, fluorescent molecules within the paint would be quenched by increased oxygen at the surface thus leading to a lower intensity of light. As such, the model could be imaged and then information about the air pressure at different areas could be inferred. The working principles and chemical constituents of the PSP are detailed below.

In terms of oxygen sensing, PSP uses platinum tetra (pentafluorophenyl) porphyrin (PtTFPP) as an oxygen sensitive molecule. The chemical structure of this molecule is shown in Figure 3.8A. It works through the quenching of a fluorescence process (described in section 1.2.1.2) whereby the intensity of emitted light (in the case of PtTFPP, 650 nm, with an excitation of 400 nm) is reduced in the presence of oxygen[221]. In the case of PSP, the PtTFPP is suspended in a matrix of acetone, methyl methacrylate, n-butyl methacrylate and toluene (in decreasing order of abundancy within the paint)[198]. The presence of the solvents acts to keep the paint in solution, while the methacrylates act as a binder to immobilise the PtTFPP on the surface or the substrate.

Figure 3.8B[222] shows the expected spectra of the PSP with both the excitation peak (blue) and the emitted peak (red) shown. Although developed for pressure sensing in the aerospace industry, it was hypothesised the PSP could act as a dissolved O_2 sensor in microfluidic devices. The inset shows the schematic of the paint on a substrate with both the incident 405 nm excitation light and the emitted 650 nm photons. To demonstrate that PSP was suitable for oxygen sensing applications, a channel was coated in the PSP and two solutions (one with 20% O2 (high)) and one with 15% (low)) were introduced to the channel. As can be seen in 3.8C, there is a difference in the fluorescence of the paint showing that oxygen in the solution quenches the fluorescence process. This provides a proof of concept as to how PSP can be used as an oxygen sensor in microfluidic devices. As such, the following sections detail the fabrication, biocompatibility, microscope set up and calibration of the paint for use as an integrated oxygen sensor in microfluidic devices.

3.4.2.1 Fabrication of PSP oxygen sensors

As detailed in section 3.4.1.1, any oxygen sensor for use in injection moulded microfluidic devices must be simple, and quick enough to integrate into the device, otherwise the purpose of using injection moulded devices is defeated. Despite the fact that, as detailed in Chapter 1, many luminescent based oxygen sensors have been developed, they rely on complex fabrication protocols meaning that they cannot be readily incorporated into devices. Furthermore, by relying on users fabricating their own sensors, issues with reproducibility become

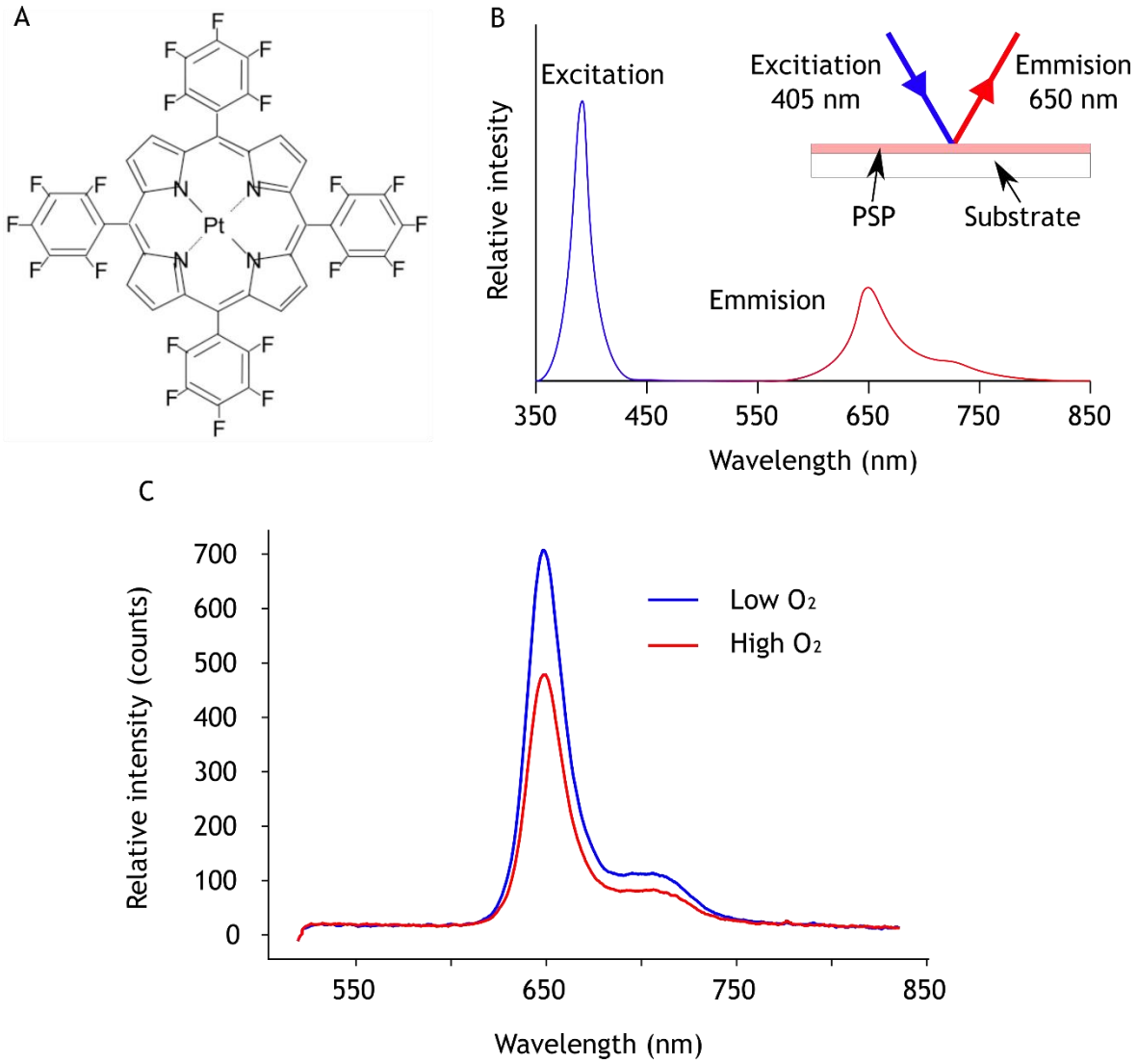

Figure 3.8 – Working principle of PSP based oxygen sensor. 4.4a shows the chemical structure of the oxygen sensitive PtTFPP molecule utilised in the PSP while b shows the typical spectra obtained from the PSP after exciting with 405 nm light (adapted from ISSI website). The inset shows a typical substrate coated with the PSP showing the incoming 405 nm, and the emitted 605 nm light. 4.4c shows the different spectra obtained when the chip was subject to both low (blue) and high (red) oxygen solutions.

more of an issue. PSP on the other hand, can be easily applied to PS microfluidic devices as shown in Figure 3.9.

Figure 3.9A-D shows a schematic of the fabrication process of the paint from the blank chip, through the application of the sensor, the annealing of the sensor and the sealing (A – D respectively). This process is far quicker and requires considerably less expertise compared to many other oxygen sensor fabrication protocols that require access to clean room facilities as well as the need to mix the sensor/binder yourself. PSP eliminates these issues by coming pre-mixed in a can that can then be simply sprayed onto a masked chip to pattern the sensor. Furthermore, the commercial availability of PSP means that much of the user

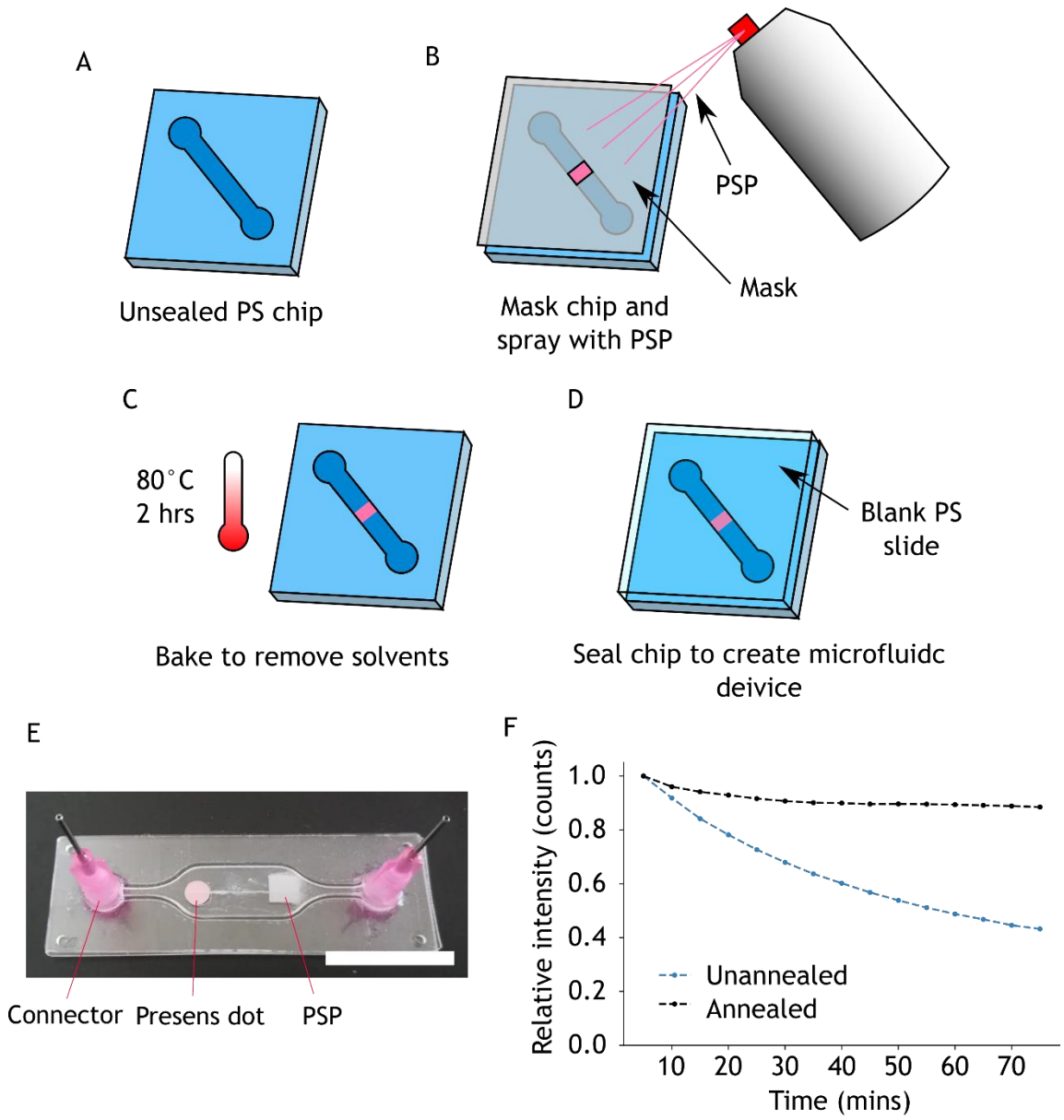

Figure 3.9 – Fabrication of PSP oxygen sensor. A shows a schematic of the fabrication process from the blank chip with a channel (i), to the masking and spraying of the PSP (ii). The chip is then annealed at 80°C for 2 hrs (iii) before the chip is sealed (iv) either through ultrasonic welding, or lamination. B shows a photograph of an ultrasonically welded chip with both a PSP sensor (right) and a Presens dot (left). C shows the difference in the stability of both an annealed (black) and un-annealed (blue) sensor over time. Scale bar = 25 mm.

error is removed from the fabrication process highlighting the advantages of such a sensor. A photograph of a sealed chip containing the sensor can be seen in Figure 3.9E with the PSP on the right, and a commercially available sensor, presens, on the left. Although not illustrated here, the presens dots come in a fixed size so cannot be integrated into channels smaller than 5 mm across, meanwhile, as the PSP is a spray, providing the channel can be masked, the PSP has been integrated into channels as small as 300 um. Finally, the stability of the PSP as an oxygen sensor is shown in 3.9F. Here, an area of the PSP was illuminated with 405 nm light constantly for the duration of the experiment, and

the photon count was taken (with respect to the original value at t = 0 min) to determine if the PSP was suitable for long term experiments. Here it can be seen that the intensity of the emitted light from the annealed sample dropped by only 10%, while the non-annealed sample dropped by almost 50%. This was thought to be due to poor adhesion of the PSP to the PS which was enhanced through the annealing process. As described above, the PSP is made up of the sensing molecule, a mixture of methacrylates that serve as a binder, and solvents that act to keep the mixture in solution. In the unannealed samples, it was thought that the solvents had not fully evaporated from the paint, leading to poor bonding of the paint and thus degradation of the paint with time (shown by the drop in the intensity in Figure 4.9F). In the annealed sample however, the solvents had been fully evaporated from the paint leading to better bonding, and a more stable sensor. Furthermore, by annealing the paint at 80^{o}C (the glass transition temperature of PS) it was thought that the bonding between the methactylates and the PS would be improved further. However, the annealed sample still showed a degradation of 9% after the first hour. Literature values for similar fluorescent based molecules are reported as low as 1% degradation per hour indicating that either the intensity of light used in these experiments is higher, or that the binding could still be improved further. It is hypothesised that this increase in the binding of the PSP to the chips could be improved by a number of means. Firstly, the baking of the chips post spraying with PSP could be optimised. The chips were baked at 80^{o}C as this was thought to be hot enough to remove all the solvents from the PSP. However, by increasing the temperature above the glass transition temperature of the PS, the sensing molecules in the PSP would bond better with the PS. The binder in the PSP is PMMA which has been shown to bond well to PS at temperatures between 110 and 125^{o}C[223]. Furthermore, by mixing the PSP in a solvent such a toluene, the solvents would dissolve the PS and leave the PSP in a matrix of PS and PMMA. Once the solvents were removed, the bonding between the PSP and the PS chip should be enhanced greatly[96].

Moreover, spraying of the chips takes approximately 1-2 s and multiple chips can be sprayed at once. Even when factoring in a 2 hr bake time, sensor fabrication with PSP still comes out quicker than previously described sensors – even if the suggested improvements to the annealing steps are considered. There are however some trade-offs when PSP is considered. Firstly, PSP results in a non-

transparent sensor area. This means that visual inspection of any areas of the chip covered in the sensor is impossible. However, this issue could be circumnavigated through pattering of an array of sensors and then interpolating the concentrations between them. Additionally, the surface roughness of the PSP is quite high which has the potential to disrupt flow.

All in all, the above highlights how PSP oxygen sensor, are simple to incorporate into injection moulded microfluidic devices. Despite having several disadvantages when compared to existing sensor fabrication techniques, the rapid incorporation of PSP into microfluidic chips makes it an attractive alternative when the mass production of oxygen sensors is considered. Furthermore, this rapid fabrication process leads to a stable sensor that is capable of distinguishing between high and low oxygen concentrations. The calibration and sensitivity of the oxygen sensor is discussed in section 3.3.2.4, however, the performance of PSP as an oxygen sensor for OoaC application hinges on its biocompatibility, so that is discussed below.

3.4.2.2 Biocompatibility of pressure sensitive paint

Alongside rapid and reliable manufacture of sensors, any material used must not affect the health of the cells in its vicinity. As such, a biocompatibility test (with MDCK cells) was conducted to test if the paint had any negative effects on cell growth. For this, wells in a standard 12 well plate were sprayed with the paint (3.10A) and the cells were seeded and allowed to grow for 3 days. On the 3rd day, the cells were imaged to determine if the paint had any effect on their viability. Figure 3.10 shows how the well plates were painted, as well as the images of the cells. 3.10A and B show MDCK cells grown in wells either containing PSP with a window (B) or in a blank well (D). From these images, the cells in both wells appear to be healthy and have formed a “cobblestone” pattern indicative of good epithelial cell health. However, as the PSP is not transparent, imaging through the sensor proved difficult (3.10C). Here, the PSP is shown in red, while cells are only partly visible through the gaps of the paint (green). As discussed previously however, this was not deemed to be too much of an issue, as the PSP can just be placed in areas of the device where there are

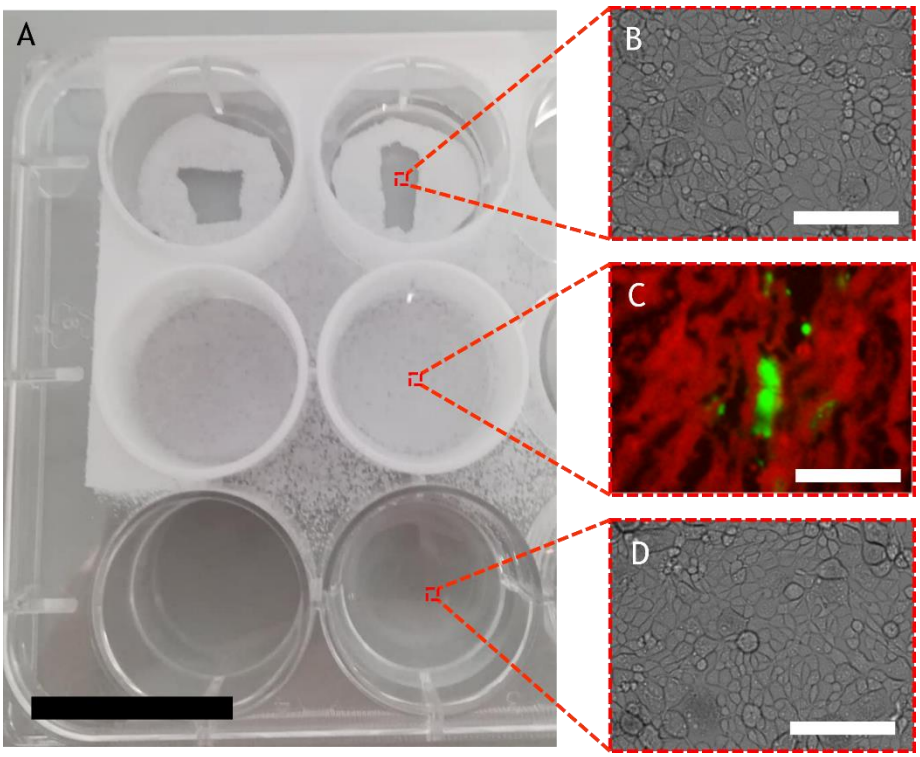

Figure 3.10 – Biocompatibility of PSP. A shows how the well plates were painted with the PSP coating the wells either completely (middle row), with a window (top row), or blank as a control (bottom row). B shows a micrograph of MDCK cells growing in wells coated with PSP while C shows a fluorescent micrograph of cells stained with calcein (green) through the PSP (red). Finally, D shows a micrograph of cells imaged in a blank well acting as a control. Scale bars = 25 mm in a, and 50 µm in B, C and D.

no cells, or, on the top surface of the device so cells could grow underneath the sensor and still be imaged.

In summary, the images in Figure 3.10 highlight that the PSP has a negligible effect on the health of cell in its vicinity thus adding to its attractiveness as a candidate for oxygen sensing *in vitro*.

3.4.2.2 Improvements in the sensing setup

Although not initially included, a further filter was added to the light path just after the LED. This was because it was found that the LED not only had a peak at 405 nm, but also a very large peak at ~690 nm which was much bigger than the 650 nm emitted peak from the PSP and was thus interfering with the results. This errant peak can be seen in Figure 3.11 (red). However, by including a low pass filter to the light path, this peak was removed leading to much less noise in the signal from the PSP (3.11, blue and green showing the spectra with no sample, and with a sample coated in PSP respectively).

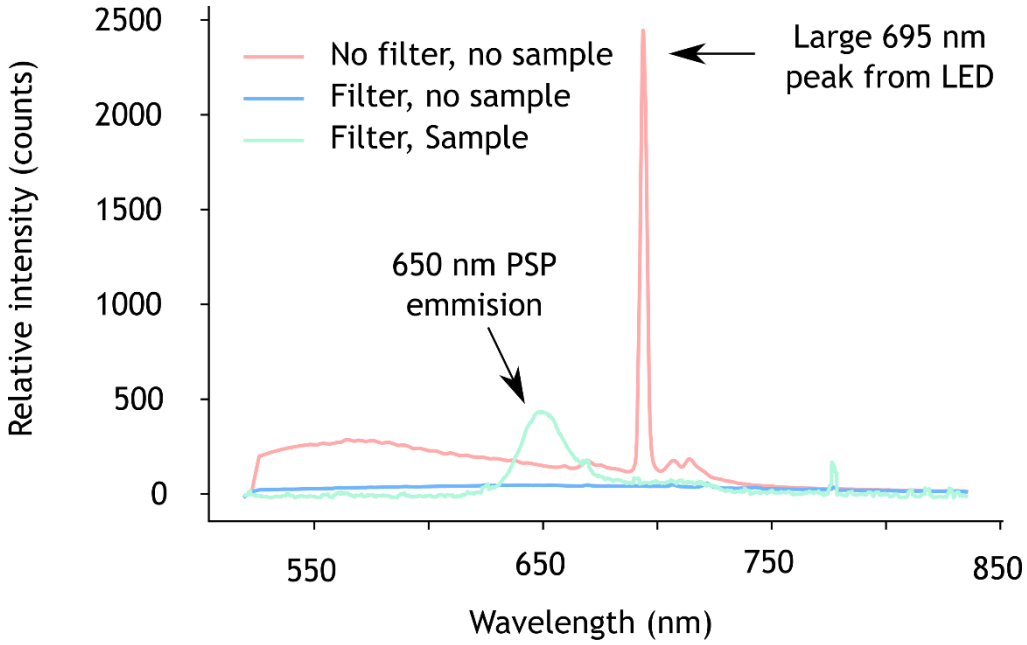

Figure 3.11 – Filters used in the light path for PSP oxygen sensing. 3.7 illustrates the need for including the low pass filter in the set up. The spectra from the LED is shown in red, while the same spectra with the filter is shown in blue. Finally, the spectra from the PSP with the filter is shown in green.

3.4.2.4 Calibration of pressure sensitive paint for dissolved O_2 sensing

As discussed in the above section, PSP offers a means of sensing between high and low oxygen solution, while also being biocompatible. However, in order to fully characterise the performance of the PSP an oxygen sensor, a calibration of the sensor must be performed. That is, the response of the sensor when subject to a wide range of oxygen concentrations must be analysed. Generally, in the case of fluorescence quenching based sensors, the reading from the sensor is compared to the Stern-Volmer equation for fluorescent quenching[224]:

$$\frac{I_f^0}{I_f} = 1 - k_q \tau_o \cdot [Q] \qquad (3.1)$$

where I_f^0 and I_f are the intensities with and without the quencher respectively, k_q is the quencher rate coefficient, τ_o is the lifetime of the excited state, and $[Q]$ is the concentration of quencher. However, in the instance of oxygen, it proved difficult to reliably and repeatedly create solutions with the same dissolved oxygen concentration to subject different sensors to run repeats of experiments. Despite a wide range of oxygen sensors reported in the literature (as discussed in section 1.2.1.2), it was not explained in great detail how the solutions with different oxygen concentrations were generated. There are a few

exceptions, however, with Nock explaining how and oxygenator similar to that described in section 4.3.1, was used with a nitrogen channel running over the top [225]. By varying the flow rate of the fluid, running past the membrane, different amounts of nitrogen would diffuse into the fluid and thus different concentrations of O_2 could be generated. However, in order for this to work, the concentration of oxygen coming from the oxygenator chip for a given flow rate must be determined either experimentally, or by comparison to a simulation. Thus, for the calibration of PSP, it was decided that the calibration of the sensor could be done simply by comparing the response from the PSP to a commercially available sensor, in this case, the Presens dots.

As previously mentioned, creating solutions with different oxygen concentrations is difficult. This is due to the fact that as soon as a solution is made, oxygen can freely diffuse in from the atmosphere and thus the oxygen concentration will always tend towards ~20% with time. The most common approach used to purge oxygen from a solution is through an oxygen scavenger reaction. This reaction is shown in equation 3.2:

$$2\,Na_2SO_3 + O_2 \rightarrow 2\,Na_2SO_4 \qquad (+Co(NO_3)_2) \tag{3.2}$$

In this reaction, sodium sulphite acts as on oxygen scavenger while the cobalt nitrate acts as a catalyst for this process. With this approach, creating a solution with 0% dissolved oxygen is trivial: 0.13% (w/v) was added to DI water along with 13 µM/l cobalt nitrate[95]. However, during initial experimentation, it proved impossible to reliably create solutions with oxygen concentrations ranging from 0 – 20 % so this methodology was not used for making the calibration solutions.

Due to the issues associated with the aforementioned protocols, a different method was used. In brief, petri dishes were coated with a region of PSP (defined by a cardboard mask) and then baked (according to section 3.4.2.1). A presens dot was then placed on the base of the dish such that the concentration could be read from the bottom. The setup described in section 3.2.3.1 was used to calibrate the readings from the PSP sensor. Once it was found that the concentration of the solution had reached a plateaux, 0.13% (w/v) of sodium sulphite and 13 µM/l cobalt nitrate were added to the water and one final

reading was taken with the oxygen concentration of the solution ~ 0%. The results from this experiment are shown in Figure 3.12.

Here it can be seen that the response from the PSP in each dish is linear (r^2 = 0.99, 0.99, and 0.98 for dishes 1-3 respectively. This indicates that the fluorescent quenching process in the PSP is linear with respect to oxygen concentration in accordance with the Stern-Volmer relationship. Furthermore, the gradients of the best fit lines fitted to the data (linear regression) are also similar (-74, -72 and -64, for dishes 1-3 respectively). However, when the y-intercept of the best fit lines in 4.12 are considered, a discrepancy in the PSP's response in each of the dishes to the oxygen concentration can be seen. This inconsistency was likely down to variations in paint thickness. As the paint was sprayed onto the samples, it was difficult to precisely control the volume of paint deposited onto each sample. This meant that the thickness between the samples varied and so there would be a difference in emitted light from each sample.

Furthermore, by calculating the average gradient of the 3 samples, the scaling factor for the calibration of any future measurements can be determined. The mean of the three gradients = -70, thus by taking one measurement at 0%, a standard curve can be drawn to determine the concentrations from a given PSP reading. For example, using a gradient of -70 and considering the data from dish 1, the following line can be used for calibration:

$$y = -70x + 2125 \qquad 3.3$$

Thus taking the reading at 15.9% O_2 (experimentally determined to be 930), eqn. 4.3 yields 1012 giving reading error of 8% in the photon count, or in terms of dissolved oxygen, an error of 1.3% when one calibration point is used. While this is high compared to commercially available sensors (the Presens dots used here have a quoted error of 0.1% at 20.9% dissolved O_2) an error of 1.3% still allows for the difference between physiologically low and high oxygen concentrations to be observed. It is rare that control over the oxygen centration in a device would need to be within an error of 1.3% as the dissolved oxygen values in an organ such as the liver range from 3 – 12%[90]. However, as mentioned above, it is thought that this error is due to the inconsistency in the thickness of the PSP between the 3 samples and it is thought that this could be improved by

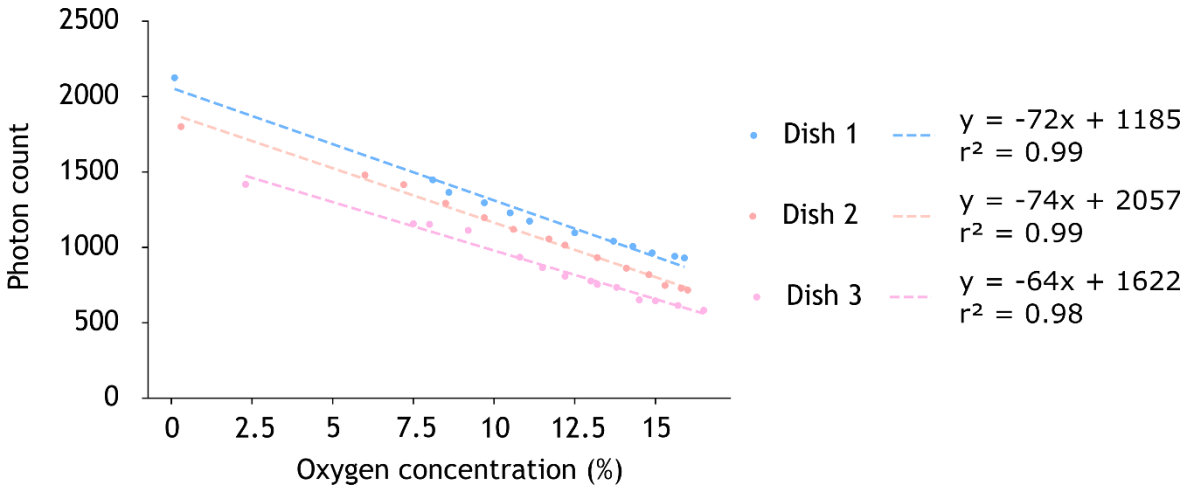

Figure 3.12 – Calibration of PSP as an oxygen sensor. Plot shoes the readout from the spectrometer against the reading from the presens dots for a solution of nitrogenated water in a petri dish. Increased oxygen concentrations were created by bubbling through air with a dropper pipette. Points show the individual readings, while dotted lines show the best fit (linear regression) for the readings from each dish (blue, orange and pink, for dishes 1, 2, and 3 respectively).

implementing a fabrication process that allowed for better control over the thickness of the deposited PSP layer. This could be achieved through a variety of means. Firstly, a stamp could be utilised to deposit a layer of the PSP onto the chips in a predetermined pattern. This technique, known as micro contact printing, has been used to pattern a variety range of materials ranging from gold[226], to proteins[227]. Furthermore, incorporating a microcontact printing process into a high throughput protocol wold not be too difficult as the stamp only needs to be in contact with the chip for a matter of seconds[227]. In addition to microcontact printing, spin coating also provides a means of generating uniform coatings of polymers. However, to pattern to PSP onto the chips would first require the deposition, exposure and development of a mask as well as the spin coating of the PSP which would be too labour intensive for a high throughput fabrication process. Furthermore, the spin coating works best on flat surfaces and the chips here have deep channels as well as tall weld seams which would prevent the PSP from forming a uniform layer during the coating and may exacerbate the error in the results.

The flexibility of the single point calibration however, is that the oxygen concentration of a solution is dependent on atmospheric conditions and thus, the concentration of a solution left open to the atmosphere cannot be known without measurement. However, as mentioned above, it is relatively trivial to create a solution of 0% O_2 using the scavenger reaction described in eqn. 4.2. Therefore, to calibrate any future sensors, all that is required is a reading from

a 0% solution. However, due to the high error that is currently introduced using a single point calibration, all future experiments conducted in this work use a two-point calibration to give more accurate readings of O_2 concentration.

In summary, with the biocompatibility data, the data presented above illustrates that PSP can be used to determine the oxygen concentration in a solution from a single calibration point. This calibration does introduce a small error into the oxygen measurements, however it is hypothesised that this error could be reduced through further optimisation of the fabrication protocol. That is, better control over the thickness of the paint layer deposited onto the sample.

However, despite the non-uniformity in the intercepts of the PSP between the dishes, the highly linear nature of the measured response from the PSP is in accordance with theoretical models for fluorescent quenching. Also, the fact that PSP uses an optical method for determining oxygen concentration, the emission can be imaged to give spatial information of the oxygen concentration in a microfluidic device. The following section demonstrates a working principle of this, and compares the results taken from the PSP to simulation to further validate the performance of PSP as an oxygen sensor.

3.4.3 Spatial analysis of O_2 using pressure sensitive paint

As previously discussed, determining the spatial distribution of oxygen within a microfluidic device is of great importance when it comes to mimicking the micro-physiological environment in OoaC devices. It has been established that in organs such as the liver, oxygen gradients drive the differentiation of cells towards different functionalities and as such, any OoaC device should provide a measurement of the oxygen in the channels to give information on the fate of the cells. As PSP relies on fluorescent quenching as a means of sensing oxygen, variation in O_2 concentration across the surface of the paint, will lead to different rates of fluorescence, and thus different intensities which can be captured by a camera.

For the spatial analysis of O_2 using PSP, the experimental setup remained largely unchanged from that used in section 3.4.2.4, but with the addition of an eyepiece camera to the microscope as opposed to the spectrometer. With this,

images of the PSP in the microchannel could be taken and the intensity of the images would linearly equate to the concentration of oxygen for each given pixel. In order to visualise a gradient, a simple Y shaped chip (two inlets, one outlet) was made and the roof of the channel was sprayed with PSP before the chip was sealed through ultrasonic welding. The chip was supplied with water that had been allowed to sit uncovered to ensure the O_2 concentration was at atmospheric levels, while the other inlet contained water with 0.13% w/v Na_2SO_4 and 13 µMol $Co(NO_3)_2$ to scavenge the dissolved oxygen and give a solution close to 0%. The concentrations of the two solutions used were verified with the Presens sensor so that the readings from the PSP could be calibrated. Different flow rates between the inlets were used to move the gradient from right to left in the chips. COMSOL simulations (carried out by Pedro Duarte Menezes) were conducted to give an analytical basis for what the gradients should be, and the experimental data was compared to the simulations.

Images showing the spatial distribution of the O_2 in the chips as determined by the simulations are shown in Figure 3.13A with simulations of the chips with 200 µl/hr in each inlet (flow ratio 1:1) and 200 (high O_2, left) and 1000 (low O_2, right) µl/hr in the inlets (flow ratio 1:5) shown in the left and right hand simulations respectively. Here it can be seen that by increasing the flow rate in the low oxygen channel, the gradient shifts from being central in the 1:1 chip, to the left-hand side in the 1:5 chip. Images of the PSP were captured with the chips subjected to a range of flow rates (1:1 to 1:5) with the 1:1 chip shown in 3.13B and the 1:5 chip shown in C. After the images were taken, an image of a chip filled with just high O_2 solution was subtracted from the gradient images to remove any background noise from the pictures. Here, the lighter parts of the image correspond to a low oxygen concentration (as the quenching of the PtTFPP means that the intensity of the light from the PSP under low O_2 will be higher) and the dark areas correspond to high oxygen concentration. Again, similar to the simulations, the gradient in the 1:1 chip (B) remains in the centre of the channel, while in the 1:5 chip (C), the gradient is shifted to the left-hand side. To better illustrate this agreement between the simulated results, and the measurements from the PSP, the mean grey value was taken from each image and converted into oxygen concentration (based on the fact that the concentrations of the high and the ow oxygen solutions had known

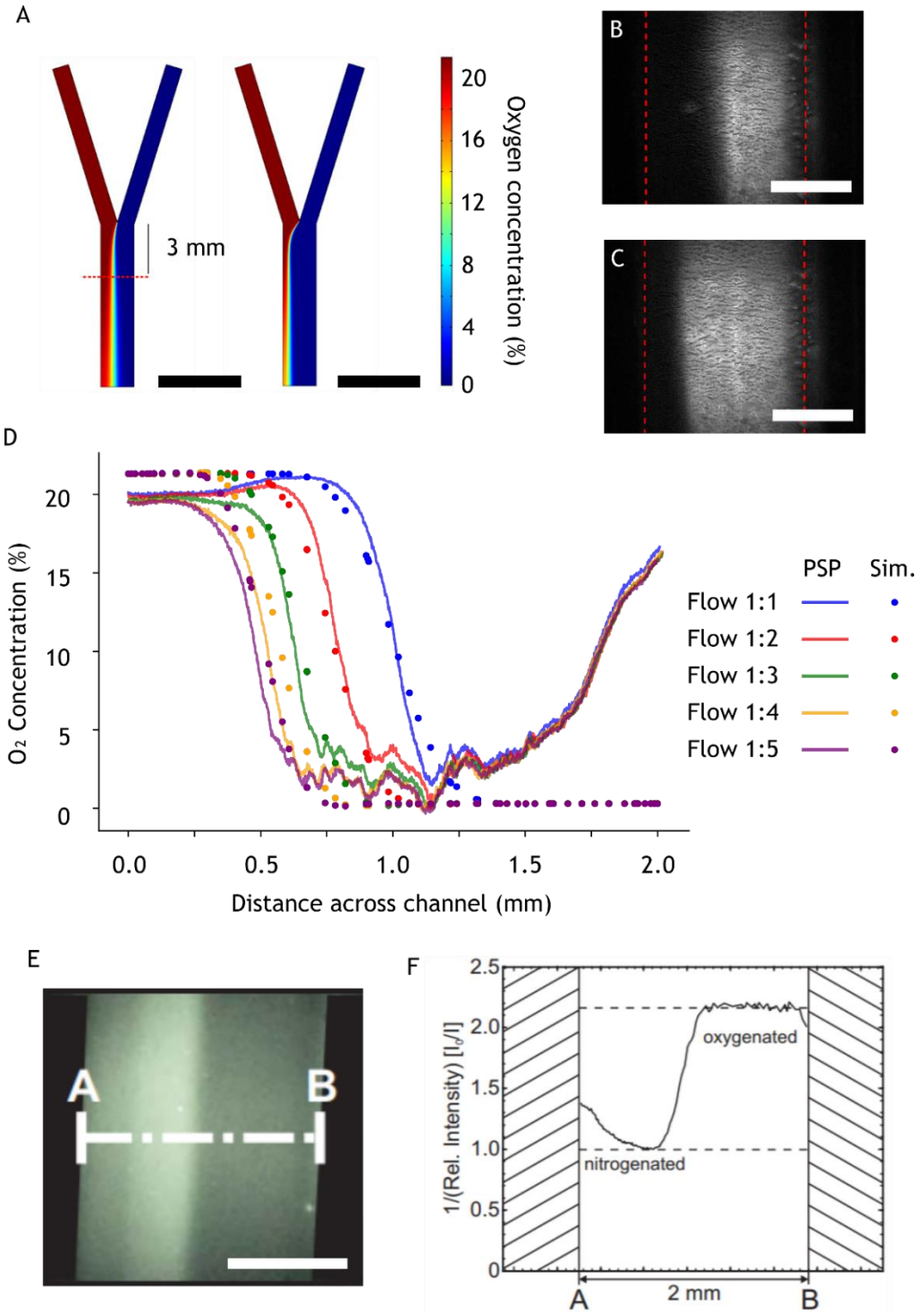

Figure 3.13 -Spatial analysis of oxygen using PSP. A (left) shows COMSOL simulations of the oxygen concentration within a Y-channel microfluidic device where the flow rates between the two inlets (high and low O_2) are equal (both 200 µl/hr). The right hand simulation shows the simulated concentration when the flow rate in the low O_2 inlet is 5 times that of the high O_2 (1000 and 200 µl/hr respectively). B shows micrograph of the channel with a flow rate of 200 µl/hr in the high O_2 inlet, and 200 µl/hr in the low O_2 inlet (flow ratio 1:1), while C shows the same channel with flow rates of 200 and 1000 µl/hr in the high and low inlets respectively (ratio 1:5). The red dotted lines indicate the edges of the channel. D shows the experimental data (solid lines) for a range of flow ratios (1:1, 1:2, 1:3, 1:4 and 1:5 shown in blue, red, green, orange, and purple respectively) plotted with the simulated data (dots, flow ratios represented by the same colours). E shows an image of the sensor described by Nock when subject to glows of oxygen and nitrogen gas while F shows the relative intensity of the sensor under the gradient. Scale bars = 5 mm in A, and 1 mm in B, C, and E.

concentrations based on measurement with the Presens sensor, and the fact that

the relationship between the intensity of light from the PSP and the oxygen concertation is linear). These oxygen concentrations were then plotted alongside the simulated oxygen concentrations in the chip for the range of flow ratios and this data is shown in Figure 4.13D.

Here it can be seen, at least for the lower ratios, that the experimental data matches up well with the simulated data, however, this relationship weakens for the higher flow ratios (1:4 and 1:5) – seen by the deviation of the experimental results from the simulated data. Also, there appears to be an increase in oxygen concentration after boundary between the two flows shown by the upwards trend in the plots. It is thought that this is not in fact due to a change in the oxygen concentration within the channels, but rather an artefact of the weld seams used to seal the channels. Excess material from the weld seams flows towards the channel during the welding process and it is thought that this excess material interferes with the light as it passes through the chip leading to a lower signal. Due to the fluorescent quenching of PSP, this lower signal means can be interpreted as higher oxygen concentration. This darker area can be seen on both the images shown in 3.13B and C. Furthermore, the similarities in experimental data for this region for all the different flow rates show that this apparent increase in O_2 concentration is not affected by flow rate so it is likely an intrinsic part of the chip geometry. Interestingly, this same upwards trend in oxygen toward the edges of channels can also be seen in other experimental data. E shows micrograph of the oxygen sensor chip described by Nock. This chip uses a similar Y-channel structure with the same 2 mm outlet channel to the chips used in this study. The base of these chips was patterned with an oxygen sensor, and gases (oxygen and nitrogen) were flowed through the chip. F shows the relative intensity of the sensor under and oxygen gradient and again, similar to the data obtained from PSP in this study, the spatial distribution of oxygen can be observed. However, there appears to be an increase in oxygen concentration towards the edge of the channel, again likely due to interference from the channel walls. It was thought that an accumulation of the paint at the corners of the channels could have an effect on the readout, but this would lead to a higher signal, and thus lower apparent O_2 concentration at the edges which is not what is observed here. However, when comparing the images in B and C, to E (the PSP sensor, to the sensor described by Nock), the sensor described by Nock appears to give better images of the O_2 gradient. This is due to the

uniformity of the coating of the fluorescent compound on the device due to the spinning process outlined in section 3.4.1. The PSP on the other hand, presents a grain like structure due from the spraying process. This grain like structure can be seen clearly in Figure 3.13B. Despite the differences in the appearance of the two sensors however, comparison of the plots in 3.13D and E show that the performance of the sensors when it comes to resolving the spatial distribution of oxygen in a microfluidic device, is largely the same. That is, both sensors can show oxygen gradients in the chips. However, in the case of PSP, the sensor can be incorporated into a device with a much quicker and simpler fabrication process. This highlights the benefits of PSP as an oxygen sensor in microfluidic devices, over previously presented technologies.

3.4.4 Temporal analysis of O_2 with PSP

Just as the spatial distribution of O_2 can play an important role in human physiology, an indication of how the oxygen concentration changes with time is also useful for studying pathologies such as ischemia. As such, a study was conducted to determine the temporal resolution of the PSP. For real time measurement of oxygen concentrations, the PSP should idealy react to changes in the oxygen concentration as quickly as possible so that the measurements of a changing oxygen concentration are as accurate as possible. In order to investigate the latency of the PSP's response to changing O_2 concentrations, a simple channel was set up containing the PSP, and was filled with a solution containing 1% w/v Na_2SO_4 and 52 µMol $Co(NO_3)_2$ to make a solution with an oxygen concentration as close to 0% as possible. After the channel was filled with the low O_2 solution, a video of the PSP was recorded using the eyepiece camera setup described in Figure 3.2. After 10 s of recording, the chip was rapidly filled with a low O_2 solution (5 ml in 1 s) by pushing a syringe as hard as possible by hand. The recording was stopped after 50 s. Once recorded, the mean grey value of each frame of the video was measured, and the intensity converted to oxygen concentration. These concentrations were then plotted against time to give an indication of the latency of the sensor. This data is presented in Figure 3.14 with the point at which the high O_2 solution was introduced to the chip taken as t = 0 s.

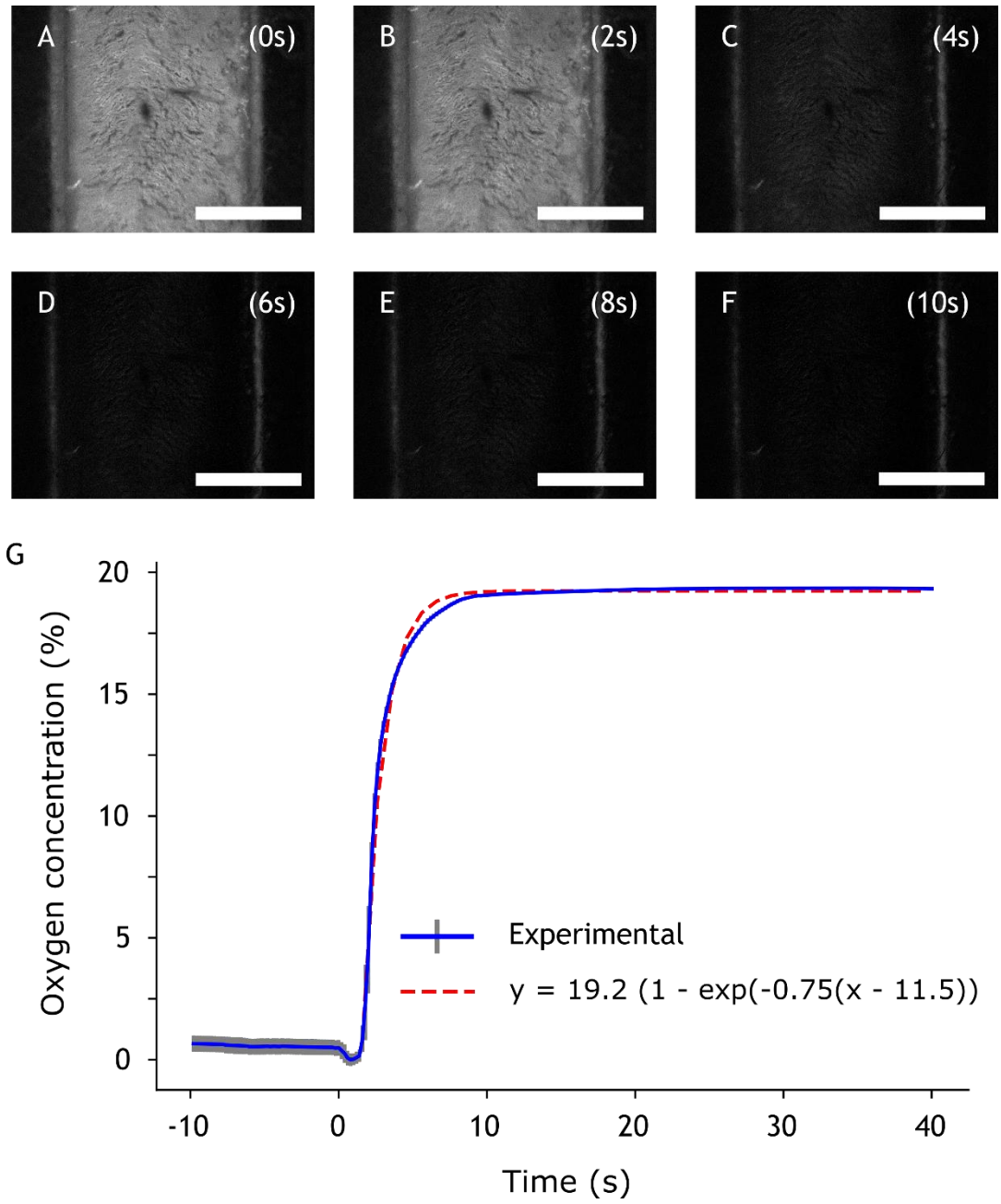

Figure 3.14 – Temporal analysis of oxygen using PSP. A(i) shows a series of images from 0 s (where the channel was filled with the low O_2 solution and the high O_2 solution was just stared to be injected). (i) – (vi) show a series of time points from 0 to 10 s after the addition of the high O_2 solution showing the 650 nm channel from the chips. B shows how the measured O_2 concentration varies with time in the chip when the low O_2 solution is replaced with the high at 0 s (shown in blue). The red dashed line shows the fitted data from which the half-time can be determined. Scale bars = 1 mm. Error bars = mean ± standard deviation with n = 3.

3.14A-F shows a series of individual frames from the recordings taken from different time points in the experiment (A = 0 s, B = 2 s, C = 4s, D = 6 s, E = 8 s, and F = 10 s). Here it can be seen that the channel begins brighter - indicating low O_2 and then after 4s, the channel begins to get darker until it appears to reach a steady brightness by 10 s. The mean grey values for the entire series of images were converted into oxygen concentrations (based on the measured concentrations of the high and low O_2 solutions form the Presens dots, and the

linear response shown previously) and this data with respect to time is shown in Figure 3.14G.

3.14G shows how the oxygen concentration varies in the channel from a series of time points from 10 s before the solutions were changed to 40 s after. Here it can be seen that the oxygen concentration in the channel is steady at just above 0% before the high O_2 solution is added at 0 s. After the high solution was injected (over a period 1 s) the pressure then drops and the measured oxygen concentration begins to rise before reaching a steady value after 10 s. Also, in 4.14G, an apparent decrease in the oxygen concentration can be seen just after the high O2 solution was added. It is though that this is not an actual decrease in O_2, but rather a pressure change in the channel caused by pushing the fluid through from the syringe.

To better understand the temporal response of the sensor, the data was fitted using a logistic function. Logistic function are used to describe growth whereby the growth starts at a rapid rate, and the rate then decreases until the system reaches a steady state value. In fact, logistic functions are often used to model the kinematics of chemical reactions[228]. As the data here represented the kinematics of chemical reaction between the PtOEPK molecule and the O_2 in the media and showed a decreasing rate of growth, the logistic function was deemed to be an appropriate means of fitting the data. The equation for logistic growth is shown in eqn. 3.4:

$$y = \frac{L}{1 + e^{-c(x - x_0)}} \tag{3.4}$$

where L is the curves maximum value, x_0 is the value at the curves midpoint, and k is a constant describing the steepness of the curve. A least squares logistic regression model was implemented in Python in order to calculate the values of L, x_0, and c. From the fitted values of this function, the half-time of the PSP response to rapidly changing oxygen concentrations is 0.75 s. The half-time for a is the time taken to reach half the final value and is often used as a means of quantifying logarithmic growth. However, the response time of the sensor is longer, taking ~ 4 s to reach 90% of the final reading. In the PSP data sheet, the response time is quoted as 750 ms, which is significantly faster than the values reported here. This is likely down to three main reasons: Firstly, it takes time

for the high O_2 solution to get into the channel so the switching of the two solutions is not instantaneous. Thus, during the transition period of the plot in 4.14G, the concentration of oxygen in the channel rises from 0 – 20% over a short period of time, thus extending the measured latency of the sensor. To mitigate this, an excess of the scavenger solution was used, and the high O_2 solution was introduced to the channel as fast as possible so that the transition from 0% to 20% oxygen was as fast as possible. Secondly, the PSP is not a monolayer on the chips and during the spraying process, multiple layers of the paint were applied. This means that it takes time for the solutions to penetrate all the layers this leading to a further lag in the latency. Finally, the quoted values on the PSP datasheets are measured using gaseous O_2, and not dissolved O_2 in solution. The diffusion time for O_2 in solution will be larger than that of a gas, and thus the measured latencies of a sensor will differ between the two phases.

Moreover, these values response time of the PSP are comparable with previously reported sensors. Nock reported a latency of ~ 2.1 s [225], which is quicker than that of the sensor reported here but again used gaseous O_2 and N_2 as the extremes, so a faster response could be expected.

In conclusion, PSP can be used as an oxygen sensor with a fast enough response time to allow for the real time measurements of oxygen within OoaC devices. Despite a slower response time compared to other sensors, the latency of PSP is still fast enough to measure the slow oxygen changes seen in physiological systems. Furthermore, it is thought that by improving the fabrication process to deposit a thinner, more uniform layer of PSP, the response time to a sudden change in dissolved oxygen concentration could be decreased. A such, along with the simplified fabrication and the ability to resolve spatial oxygen concentrations, PSP presents an attractive alternative to previously reported and commercially available oxygen sensors for microfluidic applications.

3.5 Conclusions

In this chapter, it had been hoped to study the oxygenation of media within PS microfluidic devices was compared to devices manufactured from PDMS. However, issues with the experimental setup meant that no valid conclusions could be drawn from the data that was gathered. However, a review of the

literature surrounding the oxygenation of media in microfluidic cell culture devices points to many possible solutions for increasing and controlling the oxygenation in thermoplastic microfluidic chips. The most common of these approaches uses a thin, gas permeable layer to separate the media from a gas supply. Oxygenation is achieved through the free diffusion of gases into and out of the media through the membrane. Other approaches include the manufacture of devices entirely out of gas permeable thermoplastics such as PMP. The wealth of literature on this topic suggests that the topic of oxygenation in microfluidic cell culture devices is well understood, and there are many viable solutions to either increase, or have more accurate control over the oxygenation when compared to the use of PDMS devices.

An oxygen sensor based on PSP was also described with the stability of the sensor being better after being annealed on the chips. This fluorescent quenching based sensor was shown to have a linear response to oxygen concentration meaning that calibration of the sensor was simple requiring just one data point. As solutions with 0% dissolved O_2 are easy to make repeatedly, the calibration of the sensor can be done without any extra measurements. That being said, a two-point calibration provides further accuracy and was used to calibrate the sensors that were shown in this work. Furthermore, it was shown that this sensor was biocompatible, highlighting its attractiveness for OoaC applications. Alongside this, the fabrication of this sensor was shown to be much quicker than that of previously designed technologies meaning that PSP is a suitable means of incorporating oxygen sensing into injection moulded devices. Previously described fabrication protocols rely on complicated fabrication protocols that while not only require a higher degree of expertise to carry out, can take upwards of 4 hrs per chip and are thus unsuitable for incorporating into injection moulded parts. PSP also comes pre-mixed meaning that the sensing compound is likely to be the same for every application thus further reducing the effect on handling errors on the chip fabrication. However, the method of spraying the PSP onto the chips may be causing some variability between measurements. As the thickness of the layer will affect the photon count coming from the PSP, a small change in thickness could result in an error in the oxygen concentration. Although not conducted here, strategies to improve the uniformity of the PSP coating have been discussed.

In addition to being simpler and faster to fabricate, PSP can also resolve the spatial distribution of oxygen inside a channel. This spatial measurement of oxygen was also shown to be comparable to that of other sensors which acts to show that despite its simpler fabrication, and rougher appearance, the performance of PSP is just as good as other sensing technologies. It was also illustrated that by changing the ratio of flow rates in a Y-channel microfluidic device, the distribution of oxygen could be controlled which matched up closely with simulated data. This control over the spatial distribution of oxygen in a channel highlights how OoaC devices can be created to better mimic the oxygen gradients seen in the body. Moreover, the temporal response of the PSP was also measured giving a response time of 4 s when switching between a 0 and 20% O_2 solution. Although not as fast compared to other reported sensors, this is more than quick enough for real time monitoring of oxygen *in vitro* where the oxygen concentration will likely change over a matter of minutes or hours. Also, through further optimisation of the fabrication (as discussed previously), it is hypothesised that this latency could be reduced.

The biocompatibility of the oxygen sensor was also demonstrated with the PSP having little effect on the viability of MDCK cells after 24 hrs in culture. This is important as it means that the sensor can be incorporated into microfluidic OoaC devices as a means of monitoring the oxygen in the media surrounding the cells. This becomes especially important when models for organ like the liver are considered. As discussed previously, the differentiation of cells towards different phenotypes within the liver is thought to be driven by the oxygen concentration of the blood supply. As such, when a liver-on-a-chip system is considered, it becomes increasingly important to have an accurate readout of the spatial distribution of oxygen within the device as this will have a profound effect on not only the viability of the cells, but also their functionalities. The fact that the PSP sensor is also quick to assemble and can readily be incorporated into injection moulded microfluidic devices means that PSP in PS chips offer an attractive alternative to PDMS chips for pharmacological applications where the cost of advanced *in vitro* assays is one of the main factors limiting their uptake.

In summary, this new oxygen sensor combines a low cost, rapid means of integrating the sensor into a microfluidic device while also allowing for sensing

of oxygen concentrations relevant to *in vitro* applications. This rapid fabrication means that it can be incorporated into injection moulded parts without slowing the manufacture of chips down paving the way for truly mass produced OoaC devices capable of oxygen sensing. This work demonstrate how sensors can be incorporated into mass produced microfluidic chips with little effect on the fabrication time. Furthermore, by incorporation sensors into the injection moulded PS chips, it brings them more in line with the tenets of microfluidics laid out by Manz *et al*.[9].

Chapter 4 - Towards injection moulded barrier models

4.1 Introduction

As mentioned in Chapter 1, methods of modelling drug delivery are important when it comes to understanding how a compound enters the body. When a drug is introduced to the body, it must pass at least one barrier to reach the target organ. For example, orally taken drugs must survive the chemical insult of the stomach before being absorbed through the barrier of the small intestine. This epithelial barrier is composed of tightly bound cells that form a selectively permeable barrier to compounds entering the blood stream. As such, even if a drug is super effective in treating a certain pathology, if it cannot enter the blood-stream and reach the tissue of interest, it is effectively useless. What makes the epithelial barrier in the intestine so impermeable is the presence of tight-junctions (along with other protein structures that link the cells together). These tight junctions are composed of claudin and occludin proteins and for a continuous structure around the cells [133]. This continuous structure forms an almost impermeable barrier but this seal is dynamic and can be opened to allow for the passage of larger molecules into the blood stream. As this barrier is of such importance for the transport of orally taken compounds to the tissue of interest, many methods such as immunostaining, freeze fracture microscopy, labelled tracer compounds[121,123,134,136,137] have been used as a means of studying cell barriers. This is both in terms of transport of molecules through the membrane, and protein makeup of the tight junctions. However, these approaches suffer from several drawbacks when it comes to measuring the properties of tight junctions. Namely, immunostaining and freeze fracture microscopy are end-point assays and require the sample to be killed and fixed in order for them to be imaged. This means that the dynamic nature of tight junctions cannot be measured. While the use of labelled tracer compounds allows for the measurement of barrier integrity on live cells, the experimental protocols are often laborious, and they still do not give real time data on the properties of the barrier. To combat these issues, researchers developed a technique known as trans epithelial/endothelial resistance (TEER) as a means of giving real time analysis of living cells in a barrier model.

4.1.1 Existing TEER models

As discussed in Chapter 1, TEER measures barrier integrity by measuring the impedance of a layer of cells growing on a membrane through the inclusions of electrodes into the system. The most common technique uses a measurement at a single AC frequency. This is the approach used by many commercially available systems such as the EVOM2 which measures impedance at a frequency of 12.5 Hz[139]. The advantages of using an AC over a DC signal is that AC significantly reduces the charging effect on the cells which could lead to damage to the tissue. Furthermore, the use of an AC signal allows for the impedance to be broken into the magnitude and the phase shift (as shown in Chapter 1). This gives even more detail on the integrity of the cell barrier. However, despite the experimental and analytical simplicity of measuring TEER at a single frequency, it is often beneficial to measure the impedance over a range of frequencies in a process known as impedance spectroscopy. By analysing this data, an equivalent circuit (such as the one shown in Figure 1.5C) can be reconstructed. With this circuit, the component of the impedance given by the tight junctions (the TEER) can be isolated from the capacitance of the cells' lipid bilayers as well as the impedance of the membrane and the media, as well as the capacitance of the electrodes. This means that data specific to the tight junctions can be extracted which is not possible when a single frequency measurement is considered. As a result, a more precise model of the tight junction proteins can be obtained. Furthermore, the experimental protocols associated with TEER measurements are relatively simple compared to that of freeze fracture microscopy and labelled tracer compounds so the experiments analysing tight junctions can be de-skilled, and the analysis completely automated allowing for a much higher throughput and multiplexed experimental method. In addition to this, TEER represents a completely real-time measurement of the tight junction proteins. This means that the dynamic nature of the tight junctions can be studied.

Currently, most of the research involving TEER is conducted on systems known as Transwell inserts (shown in Figure 1.5B). These systems consist of a plastic frame that keeps a membrane submerged in the media in a well plate. This creates two compartments in the well separated by a membrane on which cells are grown. As the cells grow and populate the membrane, an electrode placed on either side of the Transwell can be used to measure electrical impedance.

This technique has been used across both research and industry to study barrier integrity[229], cell invasion/migration[230] as well as to construct more complex barrier models requiring fluid/air interfaces[231]. However, these Transwell systems are not without some major drawbacks. Firstly, in Transwell systems, the electrodes have to be placed into each well prior to measurements being taken which means that it is difficult to have the electrodes in exactly the same place for every measurement which could lead to some discrepancies in the results. Also, it has been shown that cell types associated with tight junction formation show an increase in tight junction proteins (and thus TEER) when subject to fluid flow [232]. As such, researchers have created microfluidic devices capable of TEER measurements with the aims of capturing both the advantages associated with microfluidcs (such as the flow of media), and OoaC, along with the real-time, non-invasive measurements of TEER. These chips have the potential for large impact within the OoaC community where until now, the transport of molecules into the body has played a secondary role to the metabolism and efficacy of new compounds. These membrane models also become interesting when body-on-a-chip systems are considered, wherein multiple organ chips are interconnected to better mimic the human physiology as a whole, and capture the downstream effects of one organ to another[83].

However, despite the many advantages offered by TEER-on-a-chip (ToaC) systems, they are far from ubiquitous within the life sciences community. This is largely down to the fact that fabrication of TEER chips is complicated, relying on the incorporation of microfluidic channels, membranes, and electrodes into a single device. Due to this, only two variations of TEER chips have been demonstrated. A table detailing the materials and methods associated with these previously reported ToaC devices is shown in table 4.1.

From looking at the devices shown table 4.1, a few things become apparent: Firstly, as with all other microfluidic fabrication, here is a heavy reliance on PDMS to make the micro-channels on the devices. While this allows for simple direct fabrication of chips, it also means that the chips are difficult to translate into a mass producible product hindering the uptake of ToaC devices outside of all but a few specialised labs. In fact, all the devices detailed in table 4.1 come from only 2 lab groups showing how ToaC is still a specialist area and not being widely adopted in the larger life sciences

Reference(s)	Membranes	Channels	Electrodes	Sealing
Maoz *et al.*[145] Henry *et al.*[144] Van der Helm *et al.* (2019)[146]	PET sheet (0.4 µm pores)	Laser cut PDMS	Evaporated gold on glass	Conformal PMDS seal (O_2 plasma)
Bossink *et al.*[149] Van der Helm *et al.* (2016)[147]	PDMS (2 µm thick, 5 µm pores) cast from silicon master	PDMS cast from milled PMMA	Platinum wires inserted into device	Conformal PMDS seal (O_2 plasma)

Table 4.1 – ***Fabrication and materials used in previously reported TEER-on-a-chip devices***

communities. Furthermore, PDMS is permeable to small hydrophilic molecules. This increasingly becomes an issue where PDMS is intended to be used as a permeability model as material could diffuse through the bulk material thus introducing error into the experiment. Also, as previously mentioned, absorption of small molecules means that it is impossible to determine whether the drug is reaching the target tissue in the concentrations that are needed. However, the advantage of PDMS is that it forms a conformal seal with the membranes meaning that little thought needs to be put into sealing the devices. Secondly, the chips used by Moaz *et al.*[145], Henry *et al.*[144] and van der Helm *et al.* (2019)[146] all require evaporated gold electrodes which require expensive equipment and highly skilled operators for device manufacture. van der Helm (2016)[147] and Bossink *et al.*[149] sought to overcome this issue by placing platinum wires into the chips however, this approach requires the electrodes to be manually inserted into the devices manually. This can slow down manufacture and lead to differences into how the electrodes are placed resulting in variability between devices.

As such, the fabrication of existing ToaC devices means that unless researchers have access to expensive clean room facilities and the time and expertise required to manufacture the chips, this technique is out of reach. However, if a protocol could be developed that allows for the mass production of the chips, devices could be manufactured and shipped to researchers paving the way for a whole host of new research. The creation of an injection moulded ToaC device

solves both the material (PDMS vs PS) issues as well as the fabrication issues that the existing ToaC devices have. Furthermore, as TEER chips require the inclusion of multi layered micro-channels, electrodes, and membranes, creating an injection moulded device containing these shows the flexibility of this technique in creating different microfluidic chips.

4.1.2 Aims

As discussed above, TEER-on-a-chip offers presents an attractive method for monitoring barrier integrity in real time however, the current reliance on PDMS and complex fabrication techniques has meant that this technique has not reached its full potential outside of a few specialist labs. As the injection moulding protocol detailed in Chapter 2 allows for the rapid fabrication of thermoplastic microfluidic devices, the ability to make ToaC devices with this process would represent a significant step towards mass producible, functional microfluidic devices. As such, the aims of this Chapter are detailed below:

- Demonstrate a means of incorporating membranes into multi-layered, thermoplastic microfluidic devices. This process should be compatible with ultrasonic welding to allow for the rapid and high throughput manufacture of devices to align with the manufacture of devices by injection moulding.
- Demonstrate how electrodes can be incorporated into multi-layered, thermoplastic microfluidic devices. Again, this process should be rapid enough to align with the injection moulding process.
- Analyse the performance of the chip for TEER-on-a-chip applications in terms of biocompatibility, and through real time measurement of barrier integrity.

4.1.3 Overview of chapter

This Chapter documents the development of an injection moulded ToaC device. The materials and methods required to fabricate the TEER chips used in this work as well detailing how the measurements were made, and how the results were analysed. It also details the methods used to incorporate membranes and electrodes into the device while allowing for sealing through ultrasonic welding.

This includes a study into electrode materials and fabrication techniques as well as the description of a variety of methods to include membranes into the devices. The capabilities of the chip in measuring TEER are also investigated along with details of experiments troubleshooting issues with the chips. This includes investigations considering the configuration, conditioning and positioning of the electrodes. Furthermore, the membrane was also included in the troubleshooting with an experiment conducted to investigate the conditioning of the membrane layer. Although this troubleshooting led to some interesting findings however, the chips TEER performance was still not ideal. As such, this Chapter also details the further experimentation required to fully characterise the performance of thermoplastic ToaC systems which would lead to a fully functioning, injection moulded ToaC device.

4.2 Materials and methods

As mentioned above, and in Chapter 1, the ability to measure the integrity of cell membranes has been demonstrated as a powerful tool for the modelling of barriers such as the gut in the human body. Despite the fact that other researchers have already created TEER-on-a-chip devices[144–147,149], the reliance on PDMS makes these devices unsuitable for drug development applications. Furthermore, the switch from PDMS to thermoplastic materials presents a whole new set of fabrication challenges from the incorporation of membranes to the integration of sensing electrodes. This section details the principles behind TEER measurements, as well as the fabrication protocols used to build, assemble and test the performance of the injection moulded TEER chips.

4.2.1 Design and fabrication of TEER chips

As the chips required for TEER analysis consist of multiple components (channels, membranes, and electrodes), which all have an impact on the sealing of the chip, their fabrication is significantly more complex than the other devices described in this project. Furthermore, with no other injection moulded ToaC devices having been described in the literature, the processes surrounding the design and manufacture all had to be developed as part of this work. As such, the details surrounding the fabrication of the devices are given in this section.

The microfluidic channels for the chip were injection moulded using the process described in Chapter 2. The chips were designed in such a way that the top layer of the chip contained vias through to the bottom channels so that fluidic connections could be made from the top of the chip only. The chips were designed to have a circular membrane with a diameter of 5 mm. This corresponds to the area of a 96 well plate as it was hoped that by making the membrane a standard size, it would allow for easier comparisons between well-plate and on-chip experiments. The membranes used were 12 μm thick, track etched hydrophilic PETE membranes with a pore size of 3 μm and $6x10^5$ pores/cm^2 (Steriltech, US). Depending on the chip, these membranes were either directly put in the chips, or glued onto a carrier layer consisting of a 200 μm thick laser cut PS foil (Goodfellow, UK) using Precision Super Glue (Loctite, Germany).

In order to test the variety of different chip designs in this work, a variety of methods were used. There were: double sided adhesives, glue, and ultrasonic welding. For the double-sided adhesives, sheets of double-sided adhesive tape (3M, US) were laser cut to contain the shape of the channel, before the tape was used to stick the 3 layers of the chips (top channel, carrier layer, and bottom channel) together. For the glued devices, the same chip designs were used only this time, a thin layer of Loctite superglue was used to bond the layers of the chip. In some instances, a 500 x 500 μm square channel was included encircling the microfluidic channels on the chips to catch any excess glue and prevent channels from clogging. For the ultrasonically welded devices, the chips were designed with weld seams encircling the channels. Despite the weld seam geometry being optimised in Chapter 3, the seams used here were designed to have 500 x 500 μm triangular profile as it was found that the larger weld seams worked better with the two step welding processes. This process consisted of first welding the carrier layer containing the membrane to the bottom channels, before welding the top channel on to seal the chip entirely. This process is discussed in more detail in section 4.3.2.

For the electrodes in the chip, a variety of different materials and fabrication techniques were considered. Firstly, evaporated gold electrodes were fabricated by laser cutting a mask (in PS foil) that contained holes where the electrodes would be evaporated through. With the mask placed over the chip, a Plassys MEB

550S Electron Beam Evaporator (Plassys, France) was used to deposit 100 nm of gold onto the chips. The masks were then removed leaving only the patterned electrodes. Another electrode material investigated here was conductive nylon tape (Adafruit, US) which was cut to size with a scalpel and then stuck on to the devices. Indium tin oxide coated polyethelyne (ITO PET, Adafruit) was also considered as an electrode material. To fabricate these electrodes, the PET was cut to size with a scalpel and the electrodes were glued to the chips using Loctite super glue. Alongside these, conductive silver paint (RS, UK) was also used to fabricate electrodes. For these, the paint was brushed onto the chips using a fine tipped paint brush before the chips were baked in an oven at 80^{o}C to remove any excess solvents. Finally, 300 µm diameter gold wires (Alfa Aesar, US) were also studied as electrodes. These wire electrodes were either glued in place, or held in place by the weld seams on the chips.

As it was found that the weld seams were damaging some of the electrodes being investigated here, some chips were designed to contain channels to protect the electrodes form the welding processes which were then plugged with glue to seal the chip (either UV curable glue, Loctite, or food grade silicone adhesive (Wacker 120, Wacker, Germany)) as it was found that the Loctite superglue flowed into the chips and blocked the channels. This process is described in more detail in section 4.4.

Troubleshooting on the electrodes was conducted using PBS in a 6 well plate where the electrodes could be isolated from the other components of the chip. Finally, to troubleshoot the ToaC devices, devices were made with the membrane omitted (but still with the carrier layer) such that any effects the membrane was having on the results could be isolated from the results.

4.2.2 – MDCK cell culture and staining

MDCK cells were used for experiments as they are easy to handle and, with a doubling time of 24 hrs, would grow quick enough such that results from the TEER measurements could be obtained quickly. Furthermore, they are commonly used in experiments studying the formation of tight-junctions thus were considered a good model cell for the TEER chips as well as for simple

biocompatibility testing. MDCK cells were cultured and harvested in accordance with the protocol described in section 3.2.4.

To image the cells, phase contrast micrographs were taken using an EVOS FL1 imaging system (Thermofisher) with either 10x, or 20x objectives. With regards to staining, a variety of different stains were used on the MDCK cells throughout this work. During the staining, all reagents were added to the chips by pipetting them in slowly so as not to disturb the layer of cells. Firstly, the Live/dead stain was used as described in section 2.3. To stain the actin cytoskeleton and the nucleus, Actin Actigreen 488 ReadyProbes reagent (Invitrogen) and NucBlue Fixed Cell Stain ReadyProbe (Invitrogen) were used. To apply these stains, cells were washed in PBS before being fixed with 4% paraformaldehyde solution in phosphate buffered saline at 4 °C for 15 min. The cells were washed in PBS again, before the membranes of the cells were permeabilised with a 0.1% Triton X-100 (Sigma Aldrich) in PBS solution for 10 mins at room temperature. The cells were washed again, before a solution containing 2 drops/ml (in PBS) of both the NucBlue and Actin 488 stains was added to the cells for 30 mins at room temperature. The cells were washed with PBS a final time before they were imaged.

In the case of the antibody stains, the cells were washed, fixed and permeabilised as above. Once permeabilised, the cells were then blocked with a solution of 10% goat serum, and 1% bovine serum albumin (BSA) in PBS for 1 hr at room temperature. Cells were stained with ZO-1 antibody in at a ratio of 1:100 in a solution of 1.5% goat serum and 0.1% BSA overnight at 4ºC. After staining, cells were washed in PBS before the secondary antibody was applied (1:500 Anti Rabbit 644, 1:500 DAPI, 1:50 Phalloidin) again in 1.5% goat serum and 0.1% BSA solution for 2 hrs at room temperature. Finally, the cells were rinsed with PBS and imaged.

4.2.3 – TEER measurements

As discussed above, TEER measures the impedance of a layer of cells. To do this, an electrode is placed in the media on either side of cells growing on a membrane and the impedance in recorded (shown in Figure 1.4). In a

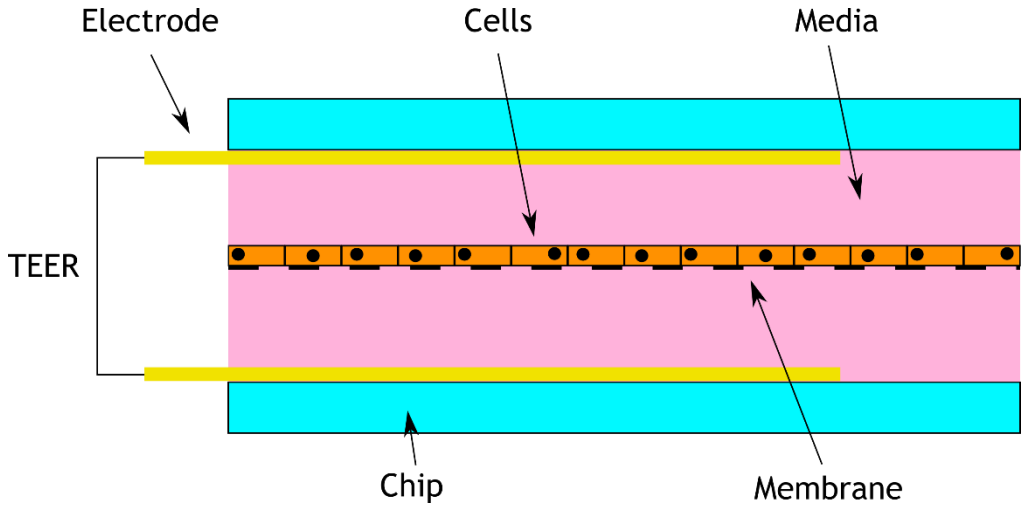

Figure 4.1 – A schematic of a TEER-on-a-chip device. 4.1 shows the chip containing electrodes, media, and cells which all contribute to the impedance of the chip. As the cell populate and cover the membrane, the impedance between the electrodes is increased.

microfluidic TEER-on-a-chip device, the electrodes are incorporated into the chips. A schematic of such a device is shown in Figure 4.1. As the electrolyte, in this case, cell culture media is inert, there is a transport of molecules to the electrodes in what's known as a non-Faradaic (capacitive) process. In a non-Faradaic process, when a DC voltage is applied, charged molecules accumulate at the electrodes and undergo no redox reactions. That is, there is no charge transfer across the electrode-solution interface[233,234].

The DC resistance of such a system can also be estimated using equation 4.1[235]:

$$R = \frac{D}{kA} \tag{4.1}$$

Where R is the DC resistance of the system; D is the distance between the electrodes separated by an electrolyte with a conductivity, k; and A is the effective surface area of the electrode. In the instance of the system described here, D = 0.12 cm, A = 0.28 cm. The conductivity of PBS[236] (used here as a proxy for cell culture media) is ~ 15 mS/cm^2 giving an overall system resistance of ~30 Ω. This value can be used to determine if there are any other impedances that may be present in the system, and would be a useful check to determine if there are no other unexpected large resistances that could impact the TEER measurements. This would have been especially useful when examining the membrane resistance experiments discussed in Section 4.8. However, no DC measurements of the resistance were acquired in this work, so this is discussed

in more detail in the future work section (Section 4.10). A summary of how the TEER measurements of the system is given below.

In the configuration shown in Figure 4.1, the impedance recorded is not just the impedance of the cell layer, but rather the impedance of the electrodes, the electrical contacts, the media, the membrane, and the cells. This impedance is referred to as Z_{Chip}. In order to isolate the impedance of the cell layer, a recording of the impedance on the chips filled with media prior to cell seeding was taken (Z_{Blank}). Thus, the impedance of the cell layer (Z_{Cell}) is given by equation 4.2. [235]

$$Z_{Chip} - Z_{Blank} = Z_{Cell} \tag{4.2}$$

As the impedance of the chips were measured at subsequent time points after seeding, Z_{Blank} was subtracted from every impedance measurement giving a value of Z_{Cell} for every time point. For all experiments here, MDCK cells were used and were seeded at a density of 100,000 cells/cm^2. A high cell density was used so that the cells would quickly form a confluent monolayer on the chips meaning that TEER measurements could be obtained rapidly. The TEER chips were either left for 24 or 72 hrs depending on the experiment.

The impedance measurements were performed using a handheld mini LCR meter (Multicomp Pro, US) which allowed for impedance recordings at 10 frequencies (100, 400, 1k, 4k, 10k, 40k, 50k, 75k, and 100k Hz). As both the resistance (R, the real component of the impedance) and the reactance (X, the imaginary component) were recorded, the impedance (Z) is given in equation 4.3:

$$Z = R + jX \tag{4.3}$$

where j is the imaginary unit. The magnitude of the impedance is shown in equation 4.4:

$$|Z| = \sqrt{R^2 + X^2} \tag{4.4}$$

and the phase of the impedance ($\emptyset$) is shown in equation 4.5:

$$\emptyset = \tan^{-1}\frac{X}{R} \quad (4.5)$$

As the impedances were recorded at a range of frequencies, the magnitude and the phase were calculated at each frequency for each separate chip. Impedance and phase spectra (Bode Plots) were obtained by plotting the calculated impedance magnitudes and phases with respect to frequency.

In most instances in this work, the TEER is expressed as either $|Z_{Cell}|$ at a specific frequency multiplied by the area of the membrane giving a value of $|TEER|$ (Ωcm_2). This whole process is described by Bossink *et al.*[149].

4.3 Incorporation of membranes into injection moulded microfluidic chips

As previously, the translation from PDMS based fabrication to thermoplastic fabrication through injection moulding poses a series of new challenges. Injection moulded devices benefit from higher throughput compared to other fabrication techniques as discussed in section 1.1.3.1 This means that devices can be mass produced and shipped to consumers as and when they required so that researcher need not spend time manufacturing their own devices. This in turn should lead to a greater uptake of microfluidic techniques within the life sciences communities. However, as ToaC devices require multi-layered chips containing electrodes and membranes, manufacturing them in thermoplastic materials presents a series of issues. Broadly speaking, these issues are mainly due to the sealing processes required for thermoplastic device fabrication. As PDMS forms a conformal seal with most materials, a membrane can simply be introduced between the two layers of the chip without any further fabrication steps. As thermoplastics do not form this conformal seal, special consideration must be taken in order to incorporate the membrane into the device. This section details the design and manufacture of an injection moulded microfluidic chip containing a membrane separating two chambers.

4.3.1 Ultrasonic welding of membranes

As discussed in Chapter 2, the bonding and sealing of thermoplastic microfluidic chips presents a challenge in the translation of PDMS prototypes to mass producible devices. As discussed previously, PDMS devices can be sealed purely through relying on the seal formed when two pieces of PDMS are in conformal contact with one another. However, this approach cannot be used for thermoplastic devices they will not form this conformal seal with another surface. As detailed in Chapter 2, ultrasonic welding presents and attractive method of sealing thermoplastic devices in a high throughput manner. However, when ToaC devices are considered, the inclusion of the weld seam required for ultrasonic welding introduces other issues. Figure 4.2A shows a schematic of the assembly of a simple membrane device. For this part, the membrane was simply inserted between the two layers of the chip. During the welding, the weld seams puncture through the membrane and seal to the chip on the other side. However, as can be seen in 4.2B, this process leads to the membrane no longer being flat inside the chip. As the weld seam melt, the polymer redistributes itself and the membrane moves with the melted polymer causing it to compress and wrinkle inside the device. These wrinkles mean that different points of the membrane are at different heights inside the chip and thus will lead to difficulties imaging the chip. Furthermore, the wrinkling means that the flow of media over the cells may not be uniform. That is, the flow is constricted in areas where the membrane is closer to the channel roof, while the media can flow more freely in areas where the membrane is further away. This could potentially lead to areas of the cell culture receiving less nutrients compared to others. Furthermore, this stretching and compressing of the membrane is likely to lead to damage during fabrication and could lead to leaks between the two separated micro-channels. As such, these issues demonstrate the need for methods that allows for the incorporation of membranes into thermoplastic devices in a rapid and roust manner to compliment the injection moulding process.

While thermal bonding is a gentler process the time associated with bonding each part means that many of the benefits gained from a high-throughput manufacture method such as injection moulding are lost. As such, there is a need for a means of sealing the devices around the membranes that are included into the devices without disrupting them.

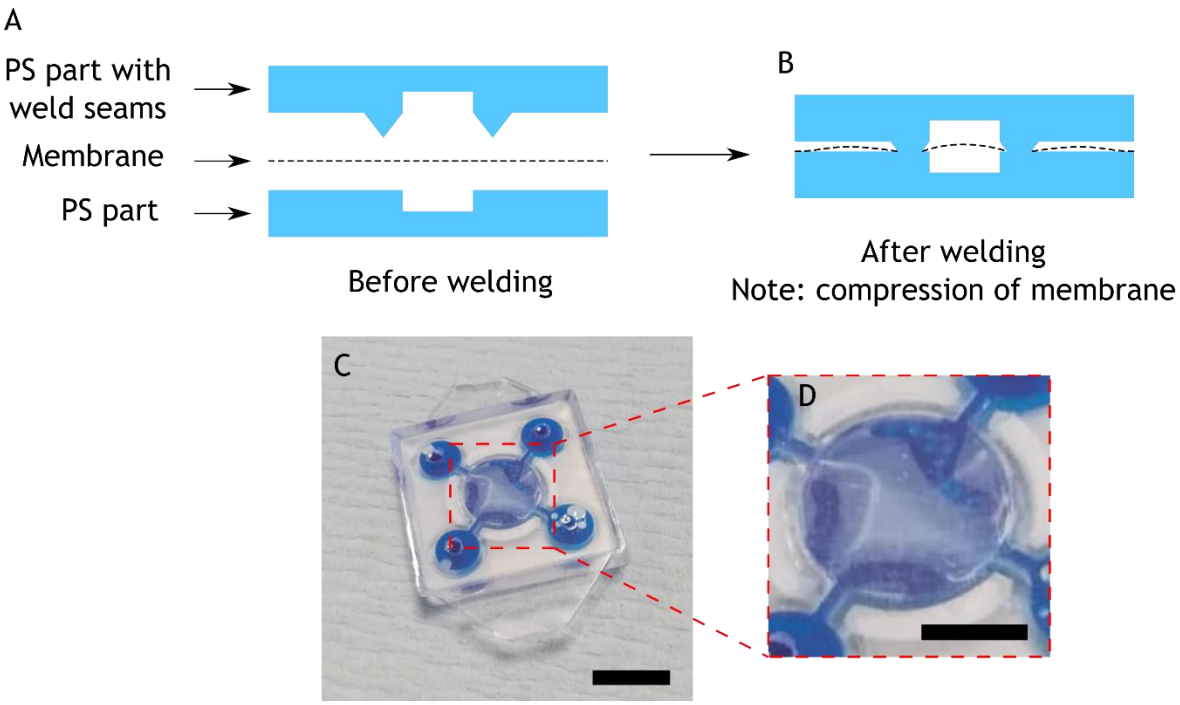

Figure 4.2 – Issues with weld seams and membranes. A shows a schematic of the chip prior to welding while B shows the chip after welding with the compressed membrane. C shows an image of a chip after welding with a compressed and wrinkled membrane. The chip was filled with blue dye to better visualise the membrane. D shows a close up of the chip in C where the compressed membrane can be seen in more detail. Scale bar in C = 10 mm, while D = 5 mm.

4.3.2 Sealing of devices with glue and tape

As discussed above, ultrasonic welding would lead to a wrinkling of the membrane inside a device. As such, alternative sealing methods were sought. It is also worth mentioning that the lamination process outlined in Chapter 2 was not considered as there was a thickness limit on the laminator of 1.2 mm and the multi-layered TEER chips would have exceeded this. Furthermore, it was thought that the un-localised heat of the laminator could have melted and distorted the membranes used.

To address these issues with previously described sealing methods and approach using double sided tape was tested. In the past, double sided tape has been shown to be effective in sealing microfluidic devices manufactured in materials such as PMMA[55]. In this approach, microfluidics channels can be fabricated through a variety of methods such as hot embossing, laser cutting, or micro-milling. A double-sided adhesive tape is then cut with the necessary vias and channels before the whole structure is sandwiched together and pressure is applied to create a good seal. To determine if this method was suitable for

injection moulded ToaC devices, chips were moulded contain the required channels and no other features such as weld seams. Double sided adhesive was then laser cut to contain the vias and the channel layout before the layers were aligned by hand and compressed. A photograph of a chip filled with red and blue food dye is shown in 4.3A. Here it can be seen that although the parts are bonded together, there is not a watertight seal around the channels causing the dye to leak out. Even though this approach had been used previously and with great success to create multi-layered microfluidic devices, it was thought to have failed here as the injection moulded PS parts were not completely flat. In the device reported by Kinahan *et al.*, the layers were formed of laser cut acrylic sheets which have been manufactured to be flat[55]. However, due to the injection moulding process, when the part is released from the mould, it still cools further which can lead to deformation known as warping. Although this warping in negligible and not a concern in most other applications, it can cause issues when sealing microfluidic devices as the two layers naturally want to pull away from each other. It was thought that annealing the assembled device under pressure would help in forming the sealing however this had no effect. As such, other approaches for sealing were considered.

Similar to bonding using adhesive layers, and perhaps the most widely used adhesive bonding technique, glue has been used to seal microfluidic devices[57]. In this method, uncured glues are applied to the device, the device is assembled, and the glue is allowed to cure either though UV curing, or solvent evaporation[54,237]. To test this method, superglue was applied to microfluidic devices and the two sides were held in contact with each other with a membrane separating the two central chambers. However as can be seen in the photograph shown in Figure 4.3B, the chip has failed to seal. Again, this was thought to be due to the inherent curvature of injection moulded PS devices. A channel surrounding the device designed in a bid to contain all the excess glue and prevent clogging of the channels.

Moreover, although tapes and glues have been shown to create sealed microfluidic devices, there are still discussions about the suitability of these approaches for OoaC applications. Namely, both adhesive tapes and glues contain materials which are likely to leach into the cell culture media and harm

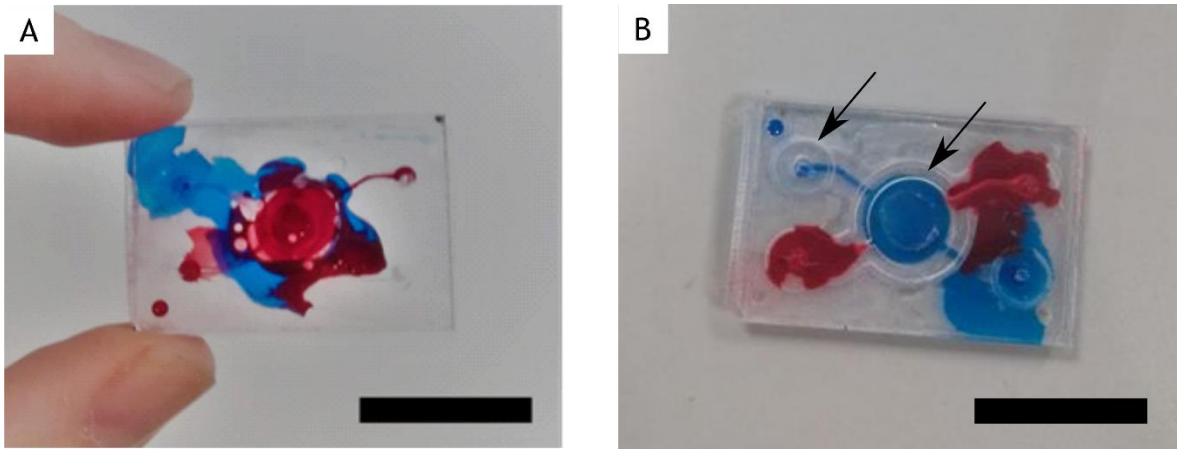

Figure 4.3 – Sealing of microfluidic devices containing membranes with glue and tape. A shows a photograph of a device sealed with double sided tape. Channels have been filled with red and blue food dye (corresponding to the upper and lower channels respectively). B shows a device sealed with glue, with the arrows showing the glue seam designed to prevent issues with clogging. Scale bars = 20 mm.

any cell cultures. Furthermore, the use of tape means that the adhesion of devices is likely to lessen over time causing further issues with the longevity of devices. In addition to this, the requirement for coating in glue or laser cutting adhesive layers increased the complexity and time requirements of the fabrication processes.

Despite that fact that the success of using both double sided adhesive and glue for the sealing of the devices has been documented by Kinahan *et al.*[55] (tape) and Arayanarakool *et al.*[54] (glue), it is thought that both methods failed here due the fact that the injection moulded chips have a small curvature to them. Both the chips described by Kinahan *et al.* and Temiz *et al.* were produced through laser cutting or glass etching which produce much flatter chips which are more suitable to be sealed by these methods.

As both above approaches (tape and glue) had failed to create a sealed device here, the chips were redesigned to allow for membranes to be incorporated into ultrasonically welded devices without the weld seams interfering with the membrane.

4.3.3 Incorporating membranes using a three-layer structure

As discussed above, attempts to seal the devices using tape and glue had proved unsuccessful in crating sealed microfluidic devices containing membranes. As ultrasonic welding had been so successful in creating sealed devices in Chapter one, a protocol was sought that would allow for both the incorporation of a

membrane into the device without the warping issue described in section 4.3.1. As the issues were all caused by direct interaction of the weld seams and membranes, it was thought that by immobilising the membrane onto a PS carrier layer, the bonding could occur between the weld seams and the carrier, while the membrane would be left unaffected by the welding process. A PS carrier was used as it was the same material as the channels. This meant that there were no compatibility issues in ultrasonically welding the PS to other materials. Sackman *et al.* showed how different materials could be welded to one another however, PS only showed good welding compatibility with itself, poly-lactic acid (PLA), and styrene-acrylonitril copolymer (SAN)[238]. Furthermore, PS showed moderate welding compatibility with PET (the membrane material) indicating that a glue-less bonding of the membrane to the carrier layer could be achieved in the future. A schematic of the device with a carrier layer is shown in Figure 4.4A.

Here, a 200 µm thick PS foil was laser cut containing the necessary vias and hole for the membrane to cover. A photograph of this carrier layer is shown in 4.4B. The membrane was then glued to the carrier (Superglue, Loctite, Germany). The carrier was then welded to one half of the device before the second half was sealed in a separate welding process. As the weld seams only interacted with the PS foil, the membrane was not compressed or stretched leading to a flat surface. A photograph of a sealed device filled with red and blue food dye is shown in Figure 4.4C. Here It can be seen that there is no leaking in the device, and the membrane has successfully separated both sides of the device (shown by the separation of the red and blue dyes). Furthermore, by minimising the use of glue and tape, the seal is completely formed from PS minimising the risk of solvents leaching into cell cultures. However, before an attempt was made to incorporate electrodes into the chips, the three-layer membrane chips were first tested for biocompatibility to ensure that cells could grow on the membrane and form a barrier.

4.3.4 Biocompatibility of membranes

As discussed above, it is possible to seal fluidic chips containing membranes using a carrier layer to hold the membrane and protect it from the ultrasonic welding process. However, it was still not known whether cells would readily

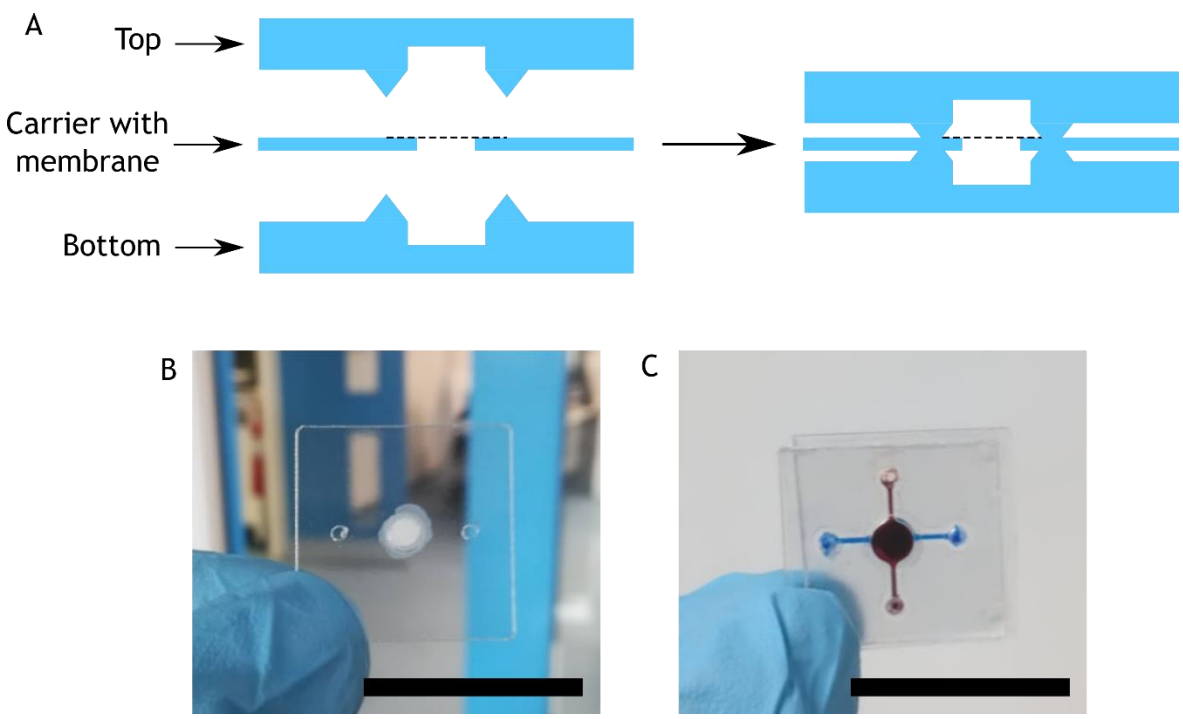

Figure 4.4 - Carrier layer for integration of membrane. A shows a schematic of the device prior to, and after welding. B shows a photography of the carrier layer with a membrane glued to it while C shows a fully assembled device. Red and blue food dye have been added to aid in the visualisation of the channels. Scale bars = 25 mm.

grow on the membrane, or whether the glue used to stick the membrane to the carrier would influence the viability of the cells. As such, MDCK cells were seeded onto the chips and media was flowed through both the top and the bottom channels to determine whether the cells would grow on the membrane. This setup is shown in Figure 4.5A. However, as can be seen in the micrograph shown in 4.5B, after 24 hrs, there were little to no cells found attached to the membranes. As such, a series of test chips were constructed to determine what the cause of the lack of cells was. The first of these chips consisted of cells grown on the carrier layer/membrane without any fluidic channels, to test whether the cells could attach and grow on the membrane and whether the glue had any negative effects on the viability. Next, cells were seeded onto a chip however, the chip had no fluid connectors or media flow to determine whether it was the flow that was detaching the cells from the membrane. Fluorescent micrographs of each of the chips are shown in 4.5C and D.

4.5B shows cells growing on the membrane that had not been assembled into a microfluidic device. The presence of healthy cells on this chip means that the membranes and the glue holding it to the carrier layer are biocompatible and do not negatively affect the health of the cells. 4.5D shows the cells grown on a

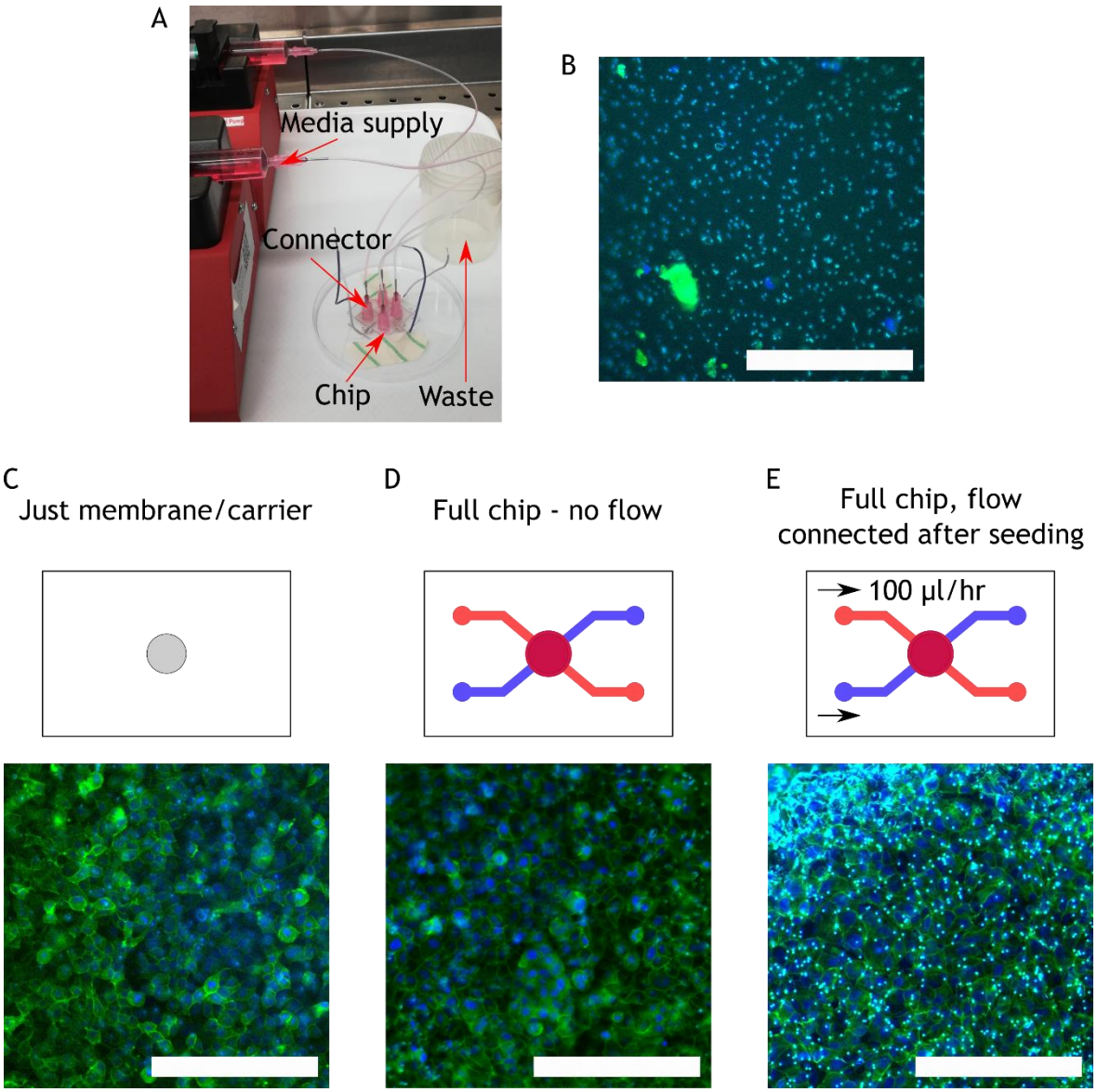

Figure 4.5 – Membrane biocompatibility testing. A shows a photo of the experimental setup showing the media supply, the fluidic connectors and the chip. B shows a fluorescent micrograph of the chip 24 hrs after MDCK cells were seeded and media was flowed through for 24 hrs at a flow rate of 100 µl/hr. C shows a fluorescent micrograph of MDCK cells grown on the membrane/carrier while D shown an image of the cells in a chip with no media flow. Finally, E shows MDCK cells on the membrane in a chip where the cells were seeded prior to the connectors being added. Green indicates the actin, while blue shows the nucleus of the cells. Scale bars = 50 µm.

chip with no flow. Here the cells were simply pipetted into the top chamber and media was pipetted into the bottom. Drops of excess media were placed over both the inlets and the outlets to prevent the chip from drying out due to evaporation in the incubator. Again, the presence of healthy cells on the membrane indicates that the full assembly of the chip was biocompatible and was not influencing the cells. The fact that there are no healthy cells observed in the image in 4.5B however, indicates that the issue with the cell viability must be down to either the flow of media detaching the cells, or the fluidic connectors interfering with the cell seeding. The chips in 4.5B were seeded by

pushing the cells through the fluidic connectors with a syringe while the chips in 4.5D were seeded by pipetting the cells onto the chip. To determine whether the connectors were interfering with the seeding, chips were seeded by pipetting cells into the chips before the fluidic connectors were attached and media was flowed through at a rate of 100 µl/hr in both the top and bottom channels. 4.5E shows fluorescent micrographs of the cells imaged in this chip after 24 hrs. Here, the presence of healthy cells indicates that it was the fluid connectors affecting the seeding.

Considering the above, the chips have been shown to be biocompatible however, while the fluidic connects allow for the flow of media through the chips, they are preventing the cells from being seeded on the membrane. It is thought that the connectors are introducing currents in the media before it reaches the device which are trapping the cells and preventing them from being seeded on the membrane. As such, when flow is required, the cells can be seeded prior to the connectors being attached which allows the cells to attach and spread on the membrane, while still allowing for the flow of fluid.

From this, it has been demonstrated how a chip containing a membrane can be fabricated through injection moulding and ultrasonic welding. It has also been shown that the blunt tipped needle style connects described in Chapter two prevent the seeding of cells, however this issue can be overcome by seeding the cells prior to the connectors being attached. As such, focus was moved to incorporating electrodes into a membrane chip sealed through ultrasonic welding. The following sections details how these chips were designed and tested.

4.4 Incorporation of electrodes into ultrasonically welded thermoplastic chips

As discussed above, it is possible to seal injection moulded thermoplastic fluidic chips containing a membrane using a three-layer construction. When the incorperation of electrodes into the chip is considered however, the weld seams used in this chip configuration pose an issue. Any electrode that is included into a fluidic device needs to be able to traverse the sealing of the device without creating any leaks. In the chips described by Maoz et al.[145], Henry et al.[144], and

van der Helm et al. (2019)[146], evaporated gold electrodes are used. As the channels are made from PDMS, the conformal seal offered by this material means that it is reltively simple to incroperate the electrodes while still maintinging a seal. However, the high energies associated with ultraosinc welding process can lead to damage to electrodes. This is illustraed schematically in Figure 4.6.

4.6 shows how the electrodes on the surface of the device can be damaged by the welding process. For the ultrasonic welding process to work, the weld seams must puncture through the electrodes meaning that they will no longer conduct a current into the devices. When other sealing methods such as laser welding are considered, the same issue persists wherein melting of the plastic is likely to damage electrodes rendering them useless. Thermal bonding on the other hand is a gentler process, however the time associated with bonding each part means that many of the benefits gained from a high-throughput manufacture method such as injection moulding are lost. As such, there is a need for a means of sealing the devices around whichever electrodes that are included without disrupting them.

The follwing sections detail the design of a ToaC device that allows for the incroperation of electrodes into an ultrasonically welded chip. Alsong side this, different elecotrode materials are considered in order to find the best material in terms of assembly time and cost.

4.4.1 Use of channels to protect electrodes from weld seams

Ultrasonic welding proved to be the most robust method for sealing devices. Furthermore, it is possible to both seal a device through welding and incorporate a membrane. As such, an approach that would allow for the incorporation of electrodes into the devices sealed through ultrasonic welding would mean that the a ToaC device could be fabricated with a fabrication process that was both rapid, and did not rely on many materials. To address this, a device was designed that contained channels that would allow for the electrodes to run from the outside of the device into the main culture area. As the electrodes were contained inside channels, they would not be damaged by the welding

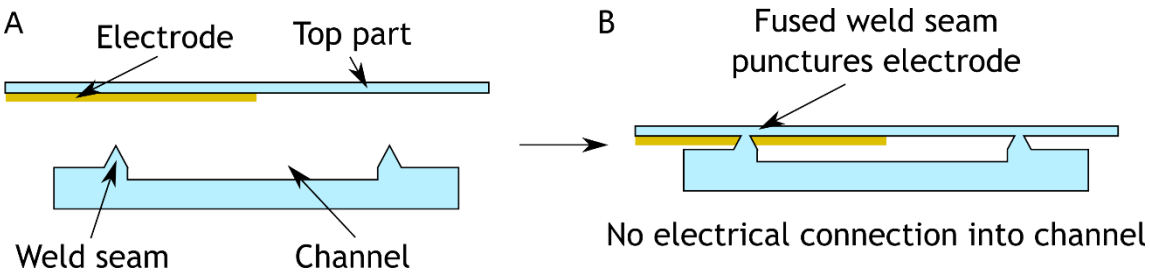

Figure 4.6 – Issues with sealing electrodes with weld seams. A shows a schematic of a device consisting of a moulded channel (blue), and an evaporated gold electrode (yellow) prior to welding. B shows that after welding, the weld seam punctures through the electrode leading to no electrical connection into the channel.

process (just as the fluidic channels were not damaged during welding). However, this also meant that glue would be required to seal the gap left in the device due to these electrode channels. A schematic of one side of such a chip is shown in Figure 4.7A with a close-up of the electrode channel shown in B. The depth of the channels used here for the electrodes were 100 µm while the width was 500 µm. C shows a schematic of the electrode channel both before and after welding and shows how the electrode is protected from the weld seams. D shows an image of an assembled chip complete with the undamaged electrodes (a close-up of which is shown in E). The electrodes were tested for damage by filling the chip with PBS and testing whether an electrical current could be conducted between all the electrode pairs. A small plug of glue was used to seal the small electrodes channels. Despite initial concerns into the use of glue to seal microfluidic devices, there was a precedent for sealing electrodes into TEER-on-a-chip devices using glue with both the devices described by van der Helm *et al.* (2016)[147], and Bossink *et al.*[149] requiring the electrodes to be inserted into the device before the holes were plugged with a small quantity of liquid adhesive. In both instances, no issues associated with channel clogging, or biocompatibility were reported. Furthermore, the design detailed by van der Helm *et al.* (2016), also used horizontal electrodes running into the device similar to the design shown in 4.7.

4.4.2 Comparison of electrode material

As discussed above, a method of including electrodes into ToaC devices has been established. However, for the injection moulded ToaC devices, alternative

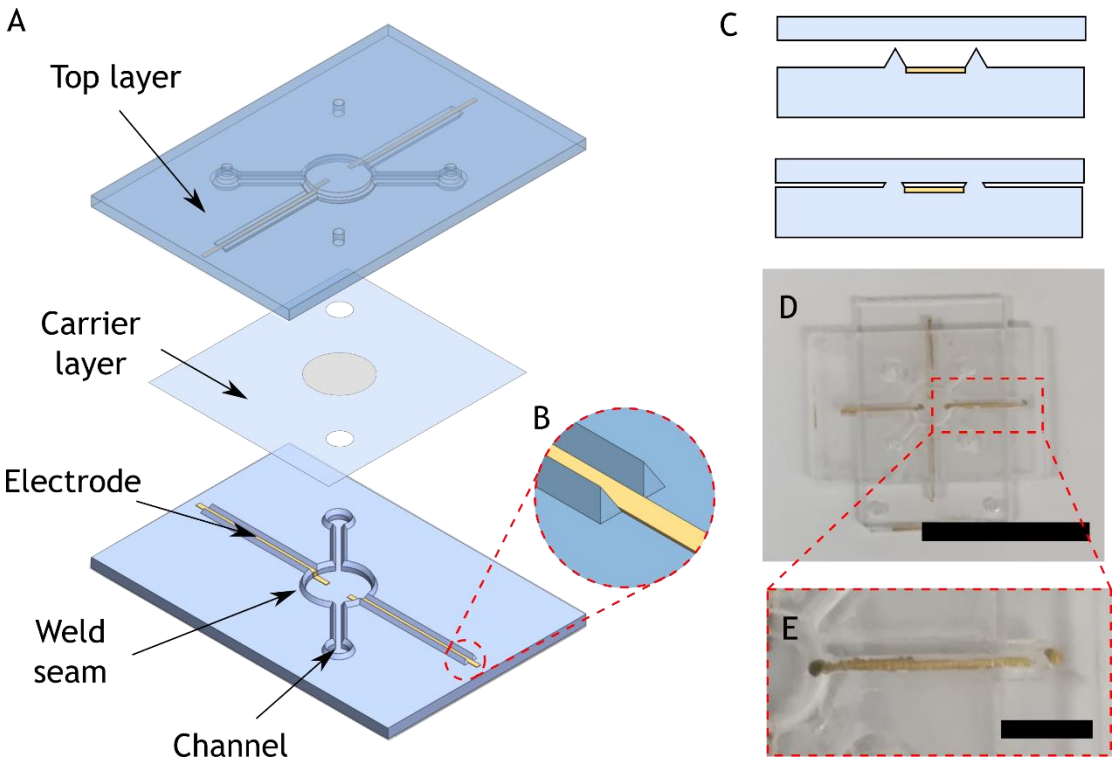

Figure 4.7 – Electrode channels to protect the electrodes during welding. A shows an exploded view of a chip with the weld seams and electrode channels. A close up of the electrode channel is shown in B. C shows a schematic of the electrode channel both before and after welding. The small gap in the channel was sealed with a small quantity of glue. D shows a photograph of an assembled chip with a close-up of an intact electrode shown in E. Scale bars = 25 mm in D and 5 mm in E.

electrode materials and fabrication methods were considered. As mentioned previously, most ToaC devices, and indeed most microfluidic devices with integrated electrodes in general, rely on evaporating gold or platinum onto the substrate using a mask. These materials are used as they are known to be biocompatible while also showing high conductance. This high conductance means that small, thin strips of these metals have a low resistance making them ideal for sensing applications. However, these electrodes are often fabricated by metal evaporation. This process involves placing the chip into a vacuum, whereby a target material is heated by an electron beam causing the metal to evaporate. The metal then cools on contact with the substrate leaving a thin layer of the metal on the surface. The mask is then removed, leaving metal only on the exposed areas of the substrate. This method has been widely used in electronics manufacture to produce electrodes and connections on a wide variety of substrates, and was utilised by Moaz *et al.*[145], Henry *et al*[144], and van der Helm *et al.*(2019)[146], to create the electrodes on the glass substrates used in their devices. However, this fabrication method takes time as each sample needs to be under a vacuum and also requires very expensive equipment to carry out. As such, when the patterning of injection moulded devices is considered,

this approach is too slow and expensive to fit into a mass production protocol. In the devices documented by Bossink *et al.*[149] and van der Helm *et al.* (2016)[147], electrodes were created by inserting 250 µm diameter platinum wire into the devices. Although this approach is entirely clean room free, the platinum wire costs ~ £200 per meter[239] meaning that a device containing four 2 cm electrodes has a cost of £8 per chip on top of all other fabrication methods. This cost was deemed too high and as such, other materials and fabrication methods were considered.

The materials investigated in this work include silver colloidal paint (RS, UK), conducting nylon tape (Adafruit, US), as well as indium tin oxide coated polyethylene (ITO PET, Adafruit, US). As the electrodes will be in contact with cell cultures, the biocompatibility of the electrodes is of the utmost importance when electrode material for a ToaC application is considered. 4.8A shows the micrographs of MDCK cells grown for 3 days in 12 well plates containing either no electrode, the silver paint, the nylon tape and the ITO PET (B – D respectively). After 3 days, the cells were rinsed with PBS to remove any non-adherent cells and the biocompatibility was estimated by counting the number of adherent cells in each field of view. This is shown in 4.8E with the data normalised to the number of cells in the control sample. Finally, 4.8F shows the conductivity of all the materials considered here.

From B and E, it can be concluded that the silver paint was having a negative impact on the health of the cells. In the case of the silver paint, although the paint contains solvents such as ethanol, acetone and ethyl acetate[240], it was thought that baking the paint once it had been applied to the substrate, would remove all the solvents leaving only the silver behind (as per the data sheet[240]). That, along with the fact that silver is regarded as a biocompatible material[241], had led to the belief that the silver paint would be suitable for use in a TEER-on-a-chip device. However, as demonstrated by the images and data presented in 5.8B and E, the silver paint was not suitable for use as electrodes in OoaC applications. In the case of the nylon tape, no details could be found pertaining to the chemical make-up of the conducting element of the tape. However, as demonstrated in 4.8C and E, a component of the tape was having a negative impact on cell health and as such, was eliminated from consideration as a suitable electrode material for ToaC.

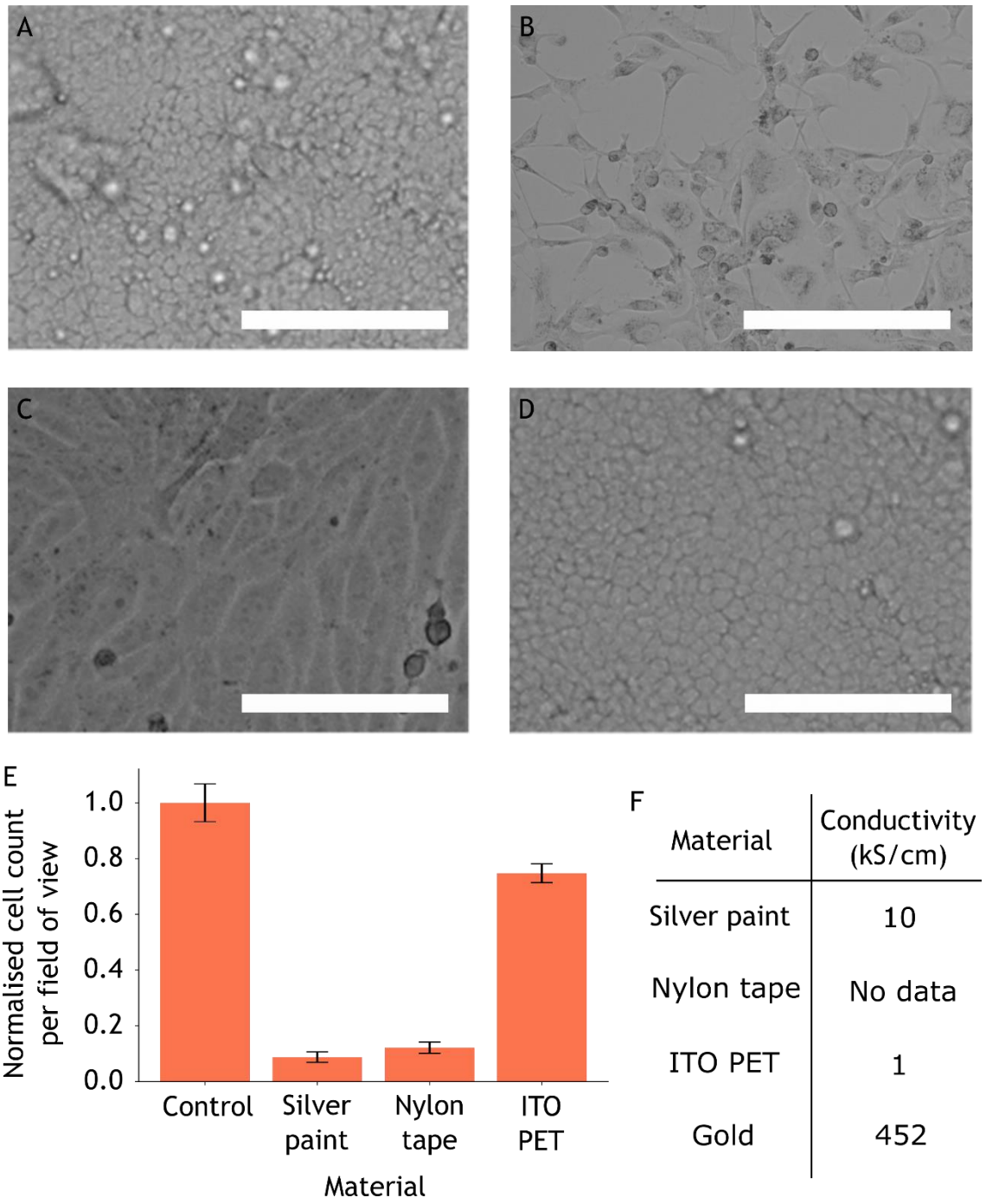

Figure 4.8 – Biocompatibility of electrode materials. A shows a micrograph of cells grown in a 12 well plate with no other material present which acts as a control. B-D shows micrographs of cells grown for 3 days in well plates with conductive silver paint, conductive nylon tape, and ITO coated PET respectively. E shows the number of cells in each field of view for each of the materials with the numbers normalised to the control. F shows a table of the conductivity of the materials used in this project. Data in E = mean ± standard deviation. Scale bars = 50 µm.

The ITO PET has been used as a conductive material in biomedical devices in the past[242]. From 4.8D and E it appeared that the ITO PET did not have a negative effect on cell health. However, in the case of ToaC device where the electrodes need to be thin to fit into the electrode channels, the low conductance of ITO PET meant that it was unable to conduct a current into the chips in an assembled device. With this and the above considerations into silver

paint, and nylon tape in mind, gold wire was selected as the electrode material of choice. Although gold wire has the issues associated with the increased cost, the use of wire means that the electrodes come pre-manufactured and just need to be inserted into the devices after assembly without any complicated fabrication process. As such, it was determined that this outweighed any issues in the cost of the chips. Furthermore, gold is known to be highly conductive as well as having few issues associated with its biocompatibility[241] so was deemed to be the ideal material choice for the TEER electrodes.

4.5 TEER measurements in injection moulded chips

As discussed above, chips with evaporated gold electrodes placed in their own channels proved to be the best option when it came to fabricating ToaC devices. As such, chips were fabricated as described in section 4.4.1 before MDCK cells were seeded onto them, and their impedances were measured every day for 3 days. For the impedance of the cells to be separated from the impedance of the chip, chips were first filled with media that had been allowed to heat up to 37°C and impedances were recorded at a series of frequencies ranging from 100 – 100 kHz. Then the cells were seeded onto the device and the impedance spectra were recorded at 24 hr intervals for 3 days. The reason that the first measurement was done without cells, was so this value could be subtracted from the measured impedances of the cells meaning that only the impedance of the cell layer was considered – not the impedance of the electrodes, the membrane and the media. Full details of this approach to TEER measurement have been described by Bossink *et al.*[149] and detailed in section 4.2.3. Furthermore, care was taken during this step to use media at 37°C as it had been shown in the past that the temperature of the media has a large effect on the impedance of the media, and thus the measured TEER values[243]. Furthermore, the media was changed and the cells were placed back into the incubator for 30 mins prior to each reading to reduce any effect that the changing composition of the media would have on the results. The impedance spectra (Bode plots) for the blank chips and the chips with cells after 3 days is shown in Figure 4.9A, with the TEER measured at 1 kHz for each day shown in 4.9B. Here it can be seen that compared to the impedances of the blank chips at day 0, the impedance of the chips containing MDCK cells does not change significantly, while the impedance

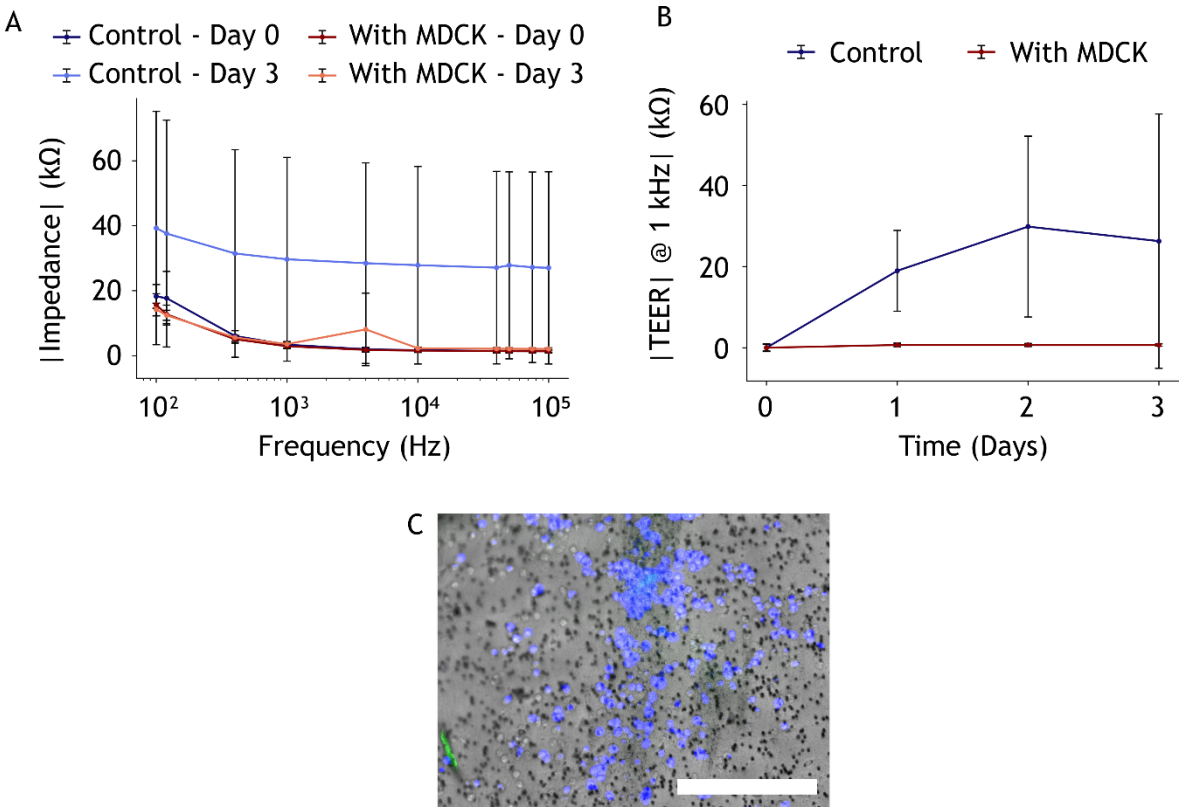

Figure 4.9 – TEER measurements in glue sealed chips. A shows the impedance spectra of the chips with and without cells at day 0 (dark blue and orange respectively) and at day 3 (light blue and orange respectively). B shows the magnitude of the calculated TEER (measured at 1 kHz) for the control (dark blue) and the chips containing MDCK cells (orange). Points = mean ± standard deviation with n = 3. C shows a micrograph of the cells on the membrane after 3 days. The cells have been stained for dapi (blue) to show the nucleus, and actin in green. Scale bar = 100 µm.

of the control chip (no cells) appears to increase. However, this increase in the control chips is highly variable as illustrated by the large error bars, and when the $|TEER|$ @ 1 kHz is considered in 4.9B. After three days, the error is large enough that it overlaps the control values showing an insignificant difference in TEER values. To further investigate why there was no significant increase in TEER after 3 days, the cells were stained for dapi and actin and imaged to see if the chips were having a negative effect on cell health. Figure 4.9C shows the MDCK cells on the chips after 3 days. Comparing the image of the chips in 4.9C with those shown in Figure 4.5, there is no actin network in the cells grown in the TEER chips containing electrodes, while the cells grown on the chips containing just a membrane and no electrodes (Figure 4.5C-E) show a healthier phenotype. As the only differences between the two chips used here are the inclusion of the gold electrodes and the use of glue to seal the electrode channels a study was conducted in order to determine whether the glue was having an impact on the health of the cells.

4.5.1 Biocompatibility of the adhesive

As discussed above, there was something in the chips used for the experiments in section 4.5 that was having a negative impact on the health of the MDCK cells used. As the injection moulded PS channels, the PET membranes, and the gold electrodes had already been shown to not have a large impact on the health of the cells (as discussed in section 4.4.2), it was thought that the glue used to seal the electrode channels was having a toxic effect. The glue used here was thought to be biocompatible as is was based on PDMS which is commonly used in microfluidic applications for the culture of cells. From the glue data sheet[244], it is based on PDMS with an acetoxysilane cross-linker. Furthermore, the adhesive was marketed as "Food safe" which was initially assumed to mean that it would not be toxic to cells. To test the biocompatibility of the glue, well-plates containing a blob of the glue were seeded with MDCK cells, and imaged along with wells not containing any glue. After 3 days, the cells were rinsed with PBS to remove any non-adherent cells, and imaged with an image of the cells grown without the glue shown in Figure 4.10A (control) and B respectively showing the well with the glue. As can be seen here, the cells that had not contacted the glue were healthy and formed the classic cobblestone like structure on the surface of the well plate. However, there were no cells attached to the surface of the wells that contained the glue (4.10B). This clearly indicates, that despite the initial assessment that the glue did not contain any harmful ingredients, there was something in it that had a catastrophic effect on the health of the cells. The relative number of each cells in each frame is shown in the plot in 4.10C. Again, using the relative number of cells per frame as a measure of the biocompatibility, it shows how the glue was having a massive impact on the health of the cells. Although there is evidence in literature of other glues being used for the sealing of electrodes in microfluidics chips (namely the use of Norland Optics UV curable adhesives [147,149]) it was decided that an approach that did not involve the use of adhesives would be beneficial. As discussed previously, including an adhesive into microfluidic fabrication increases the complexity of the assembly process as well as increases the risk of blocking the channels during fabrication. A such, a new approach was needed to fabricate the chips without the requirement of glue to seal the electrode channels.

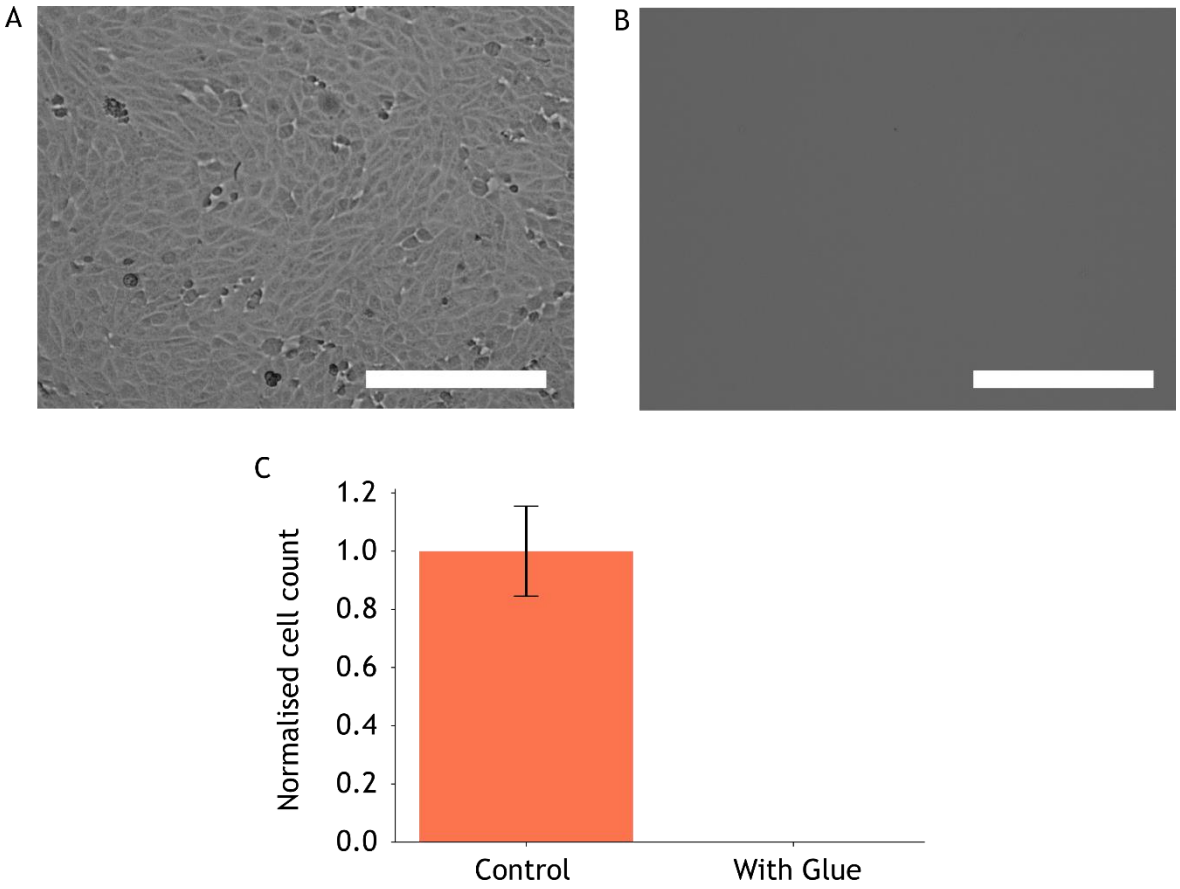

Figure 4.10 – Biocompatibility of the glue. A shows an micrograph of MDCK cells grown in blank wells for 3 days while B shows an image of a well containing the Wacker Food Safe adhesive used to construct the chips. C shows the relative number of cells normalised to the blank wells for both the control and the wells containing the glue. Error bars = mean ± standard deviation with n = 3. Scale bars = 50 µm.

4.6 Incorporation of gold wires into chips directly through weld seams

Based on the discussion above, there is a need for injection moulded TEER chips that do not require additional glue to seal off the electrode channels. In the chips detailed by Bossink *et al.*[149] and van der Helm *et al.*[147], the platinum electrodes were held in place using UV curable adhesive from Norland optics. However, the fabrication of TEER chips could be improved and streamlined if electrodes could be incorporated into the device and sealed without the need for any additional fabrication. Furthermore, by eliminating the glue, all the issues associated by introducing further materials into the chips, such as leaching of uncured glue back into the media, or absorption of small molecules are eliminated. As well as this, and risks associated with the glue clogging the channels would be reduced. As mentioned in section 4.4.2, the standard evaporated gold electrodes can only be included into devices if special channels are made to protect the electrodes form the weld seams that would otherwise

rupture them. However, the sealing of these channels is an issue as it involves the inclusion of glue that complicates the fabrication protocol as well as introduces the issues mentioned above. To combat this, a new method of incorporating gold electrodes into the chips was investigated.

The evaporated gold electrodes discussed in section 4.4.2 consisted of a 500 µm wide, and 100 nm thick layer of gold. During the ultrasonic welding process, it was found that the weld seams simply pierced through this thin layer meaning that no electrical current could be transmitted from the inside of the chip to the outside. It was thought however, that by using gold wires as opposed to evaporated gold, the rounded shape and increased thickness of the wires would make them more likely to survive the welding process as the weld seams would simply melt and flow round the wires. This technique has previously been described by Sackman *et al.*[238] where grooves in the weld seams allowed for the inclusion 50 µm filaments without rupture of the wire. A schematic of a chip with the gold wire electrodes is shown in Figure 4.11A and a photograph of a chip sealed against a blank piece of polystyrene containing a wire electrode running through the weld seam is also shown in 4.11B. Here, the electrode can be seen intact, running from the outside of the chip to the inside, while the food colouring remains inside the channel indicating a water-tight seal. A hole was then punched in the polystyrene film to give access to the portion of the electrode inside the chip. This meant that a multi-meter could be used to confirm whether the electrodes were intact after the welding process. Of the three chips fabricated this way, all showed a resistance of less than 1 Ω. This indicates that the electrodes were intact and should be able to be used for the transmission of current through the chips such that TEER measurements could be taken.

Despite the relative simplicity of the protocol to the incorporation of electrodes into the device, this approach also contains several advantages over the other methods of ToaC manufacture described previously. Firstly, the chips can be fabricated and sealed without the need for glue that could be toxic to the cells. This means that the chip used here are fabricated entirely in polystyrene (with a PETE membrane) without any additional materials. Secondly, by eliminating the step involving gluing the electrodes into place, the fabrication process of the

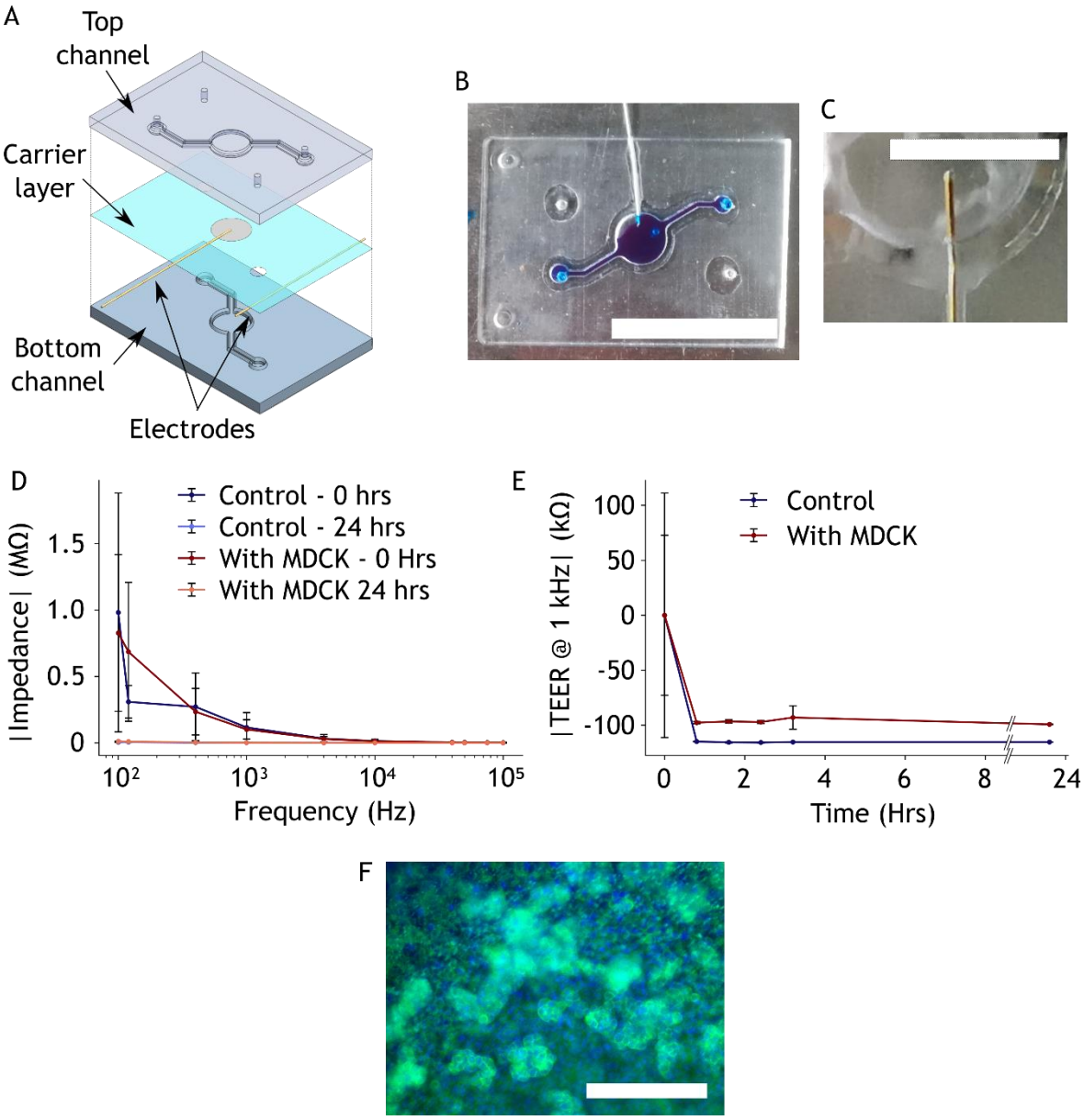

Figure 4.11 – Through-weld seam electrodes and TEER measurements. A shows an exploded schematic of the chips made with the through-weld seam electrodes with the three layers of the device, and the gold wire electrodes incorporated at the welding step. B shows a photograph of a chip with a wire electrode sealed with a PS foil. The channel was filled with blue food colouring to examine for leaks. C shows a close up of the gold wire going through the weld seam showing how the wire remains intact after welding. D shows the impedance spectra of the chips with and without cells at day 0 (dark blue and orange respectively) and at day 3 (light blue and orange respectively). E shows the magnitude of the calculated TEER (measured at 1 kHz) for the control (dark blue) and the chips containing MDCK cells (orange). Points = mean ± standard deviation with n = 3. F shows a micrograph of the cells on the chip after 24 hrs. nucleus = blue (dapi), actin = green. Out of focus areas indicate the 3D structures apparent in the cell layer. Scale bars = 25 mm in B, 5 mm in C and 100 µm in F.

chips can be streamlined. In this approach, the incorporation of the electrodes, and the sealing of the chips can be done in a single step, expediting the chip fabrication process. As such, the manufacture of the chips is more aligned with the injection moulding process meaning that chips could easily be scaled to a mass manufacturing process if required.

With these new ToaC devices with the through-weld seam wire electrodes, the TEER measurements were repeated to see if more meaningful recordings of barrier integrity could be achieved.

4.6.1 TEER measurements in gold wire electrode chips

To record the TEER values from MDCK cells, chips were filled with warm media and the impedance spectra were recorded. Then, half the chips were seeded with MDCK cells, while the others were kept blank. Differing to the previously described TEER experiments, measurements were recorded at 2 hr intervals for 8 hrs, and then a final measurement was taken at 24 hrs. this was due to the fact that when seeded at a high density, MDCK cells had been shown to reach their peak TEER value after less than 24 hours[245]. Again, the impedance spectra recorded on day 0, and the spectra recoded after 24 hrs are shown in Figure 4.11D. Here it can be seen that there is a drop in the impedance of the chips from the first recording made of the blank chips, and the final measurement taken of the chips with and without cells after 24 hrs. This is also shown in the TEER plot in 4.11E where the impedance of the chips drops greatly in the first 2 hrs, and then remains constant for the rest of the experiment. Again, the chips with cells were imaged to ensure check that the cells were healthy, and a micrograph of the cells is shown in 4.11F. This image shows that the cells are not only healthy but have also formed 3D structures on the membrane shown by difference in focus over the image, with the out of focus cells being further away from the membrane than the in-focus ones. This is indicative of a healthy cell population and shows how the biocompatibility of the devices has been improved from the chips discussed in section 5.5.

Despite the apparent health of the cells, the chips were still not able to reliably record the TEER of the MDCK cells. The literature quoted TEER values for MDCK cells are 1500 Ωcm^2 [246] and here we see a decrease of by ~100 kΩ. To investigate this, every aspect of the TEER-on-a-chip devices was scrutinised to see if a solution could be found details of this study are given in the section below.

4.7 Troubleshooting electrodes in TEER-on-a-chip devices

To determine if the electrodes were causing this apparent decrease in the TEER measurements, 3 aspects of the electrodes were considered. These were: 1. The conditioning of electrodes with time, 2. The use of a two-point measurement, versus a four-point measurement, and 3. The effective area of the electrodes. The results of this study are presented in the sections below.

4.7.1 Two-point vs four-point impedance measurements

Despite the differences between TEER chips being laid out in table 4.1, perhaps the largest difference between the two groups of chips is the way in which impedance measurements are taken. In the chips described by Maoz *et al.*[145], Henry *et al.*[144] and van der Helm (2019) *et al.*[146], the chips use a 4 point impedance measurement, while in the chips described by Bossink *et al.*[149], and van der Helm (2016) *et al.*[147], a two-electrode configuration is used. In a two-electrode configuration, each electrode is placed either side of the cell containing membrane, and the same electrodes are used for both the measurement and the current supply. This gives a simple electrode configuration that is capable of measuring the TEER of the cell layers on the membranes. The four-electrode configuration, however, requires two electrodes on either side of the membrane, with one electrode pair supplying the current, and the other performing the measurement. This configuration is shown schematically in Figure 4.12A. in this configuration, the current supply, or force leads create a voltage drop across the target impedance in accordance with Ohm's law[247]. As the measurement electrodes are placed immediately next to the current electrodes, and as such, any measurement taken does not include the impedance of the force leads. Since there is negligible current flow in the measurement electrodes, there is not voltage drop across these either. As such, four-point impedance sensing removes the lead and the contact resistance from the impedance measurement. To investigate the effect of this, a six well-plate was filled with PBS and two electrodes were placed on either side. Impedance spectra were recorded using a four-point measurement, as well as a two-point measurement of the same well. These impedance spectra are shown in Figure 4.12B.

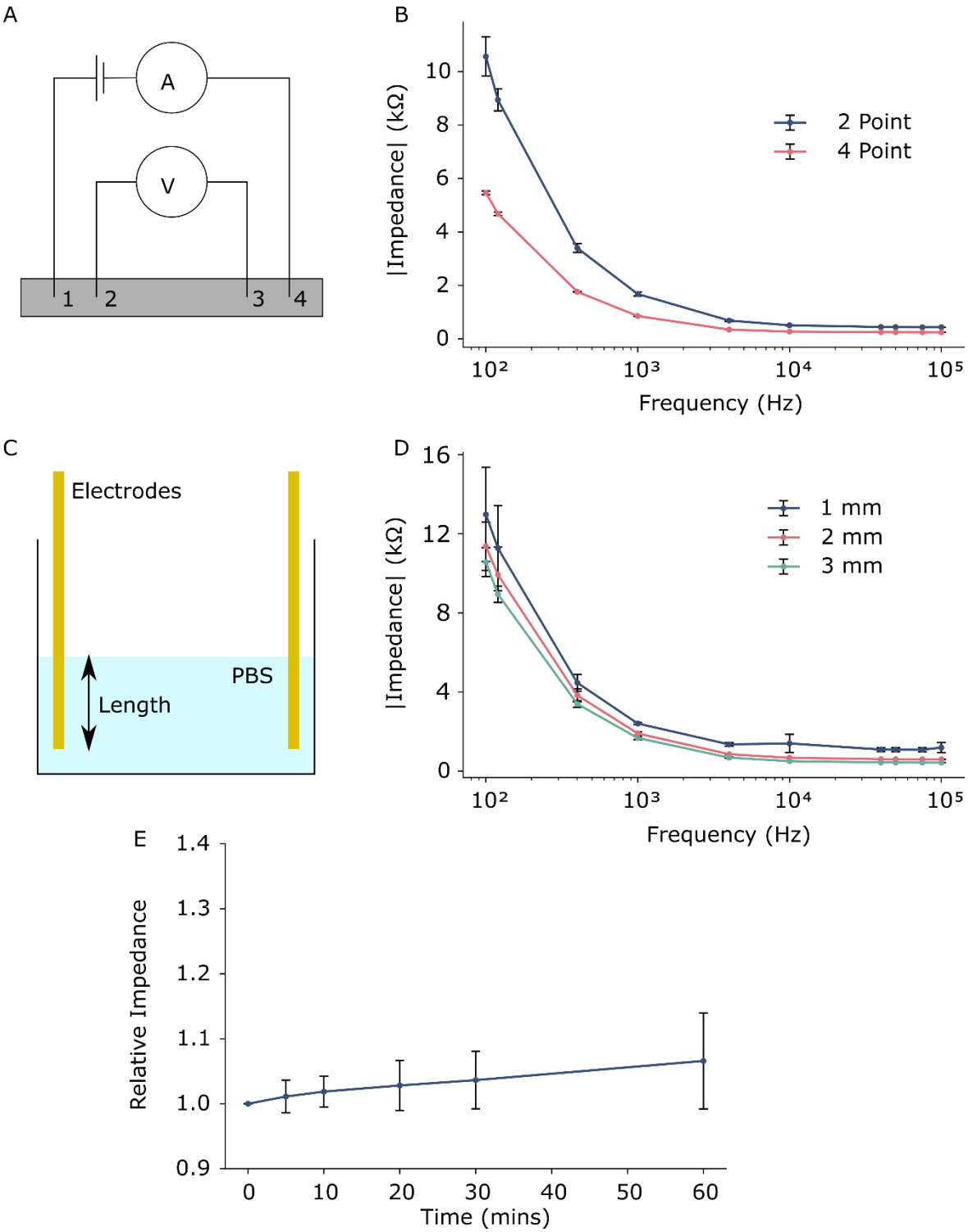

Figure 4.12 – Electrode troubleshooting. A shows a schematic of a four-point impedance measurement with the force leads shown by 1 and 4, with 2 and 3 showing the sense leads. B shows the difference in the measured impedance spectra of a system using a four-point measurement (red) and a two-point measurement (blue). C shows a schematic of the setup used to determine the effect of the effective contact area of the electrodes while D shows the impedance spectra taken with electrodes inserted 1, 2, and 3 mm into the PBS solution (blue, red, and green respectively). Finally, E shows the change in impedance of a 2-point measurement with 3 mm electrodes measured at 1 kHz over the course of 60 mins. Error bars = mean ± standard deviation with n = 3.

In this plot, the four-point measurement gives a lower impedance reading than the two-point measurement, due to the fact that the lead resistance and contact resistance have been eliminated from these measurements. However,

despite the decrease in the impedances measured, it was not thought that the use of a two-point measurement for the previous TEER readings was the cause of contact and lead resistances will cancel out, so will not be present in the calculated TEER values. As such, two-point impedance measurements continued to be used for all future TEER measurements.

4.7.2 Analysis of electrode length

Alongside the configuration of the measurement electrodes, the effective length of the electrodes has also been shown to have an effect on the measured impedance of a system[248]. In most cases, large flat electrodes are preferable as they create a spreading out of the electric field between them, meaning that more of the area between them is probed during the impedance measurement. However, as gold wires were the electrode of choice in this application, large flat geometries could not be realised. As such, the same well plate set up detailed above was used, but this time, impedances were recoded with the electrodes inserted at different lengths into the PBS to simulate a difference in effective area of the electrodes. This setup is shown in the schematic presented in 4.12C with the recorded impedance spectra shown in 4.12D.

From the data presented in 4.10D, it can be concluded that the larger the effective area of the electrodes are, the lower the measured impedance is. However, this change in impedance is even smaller than that switching from a four-point to a two-point measurement so was deemed to not be large enough to mask any change in the TEER measurements. Furthermore, as the electrodes were held in a fixed position inside the chip, the effective area of the electrodes will not change over the course of an experiment. Moreover, the change in the impedance is so small (~2 kΩ for an added 2 mm in length), even if the electrodes were slipping in the device, it would not be enough to cause the large drop in impedance shown in Figure 5.11E. Additionally, this experiment highlights one of the main advantages of TEER-in-a-chip as opposed to well plate systems where the position of the electrodes can change with each measurement, thus altering the measured TEER values. Additionally, as above, the impedances of the blank chips are subtracted from the impedance of the same chips with cells in them. As such, and variation in the contact the contact resistance from chip to chip is eliminated from the final reported TEER values.

4.7.3 Analysis of electrode conditioning in TEER-on-a-chip systems

Electrode size and configuration are not the only electrodes properties that may influence the measurement of TEER, however. As the electrodes are in contact with electrolytic solutions, they may be subject to corrosion, or conditioning. This in turn may lead in an apparent change in the TEER between time points due to a difference in the lead and contact resistances of the electrodes. To investigate this, a well plate was filled with PBS and an electrode was placed either side such that the impedance of the electrodes and PBS could be recorded. For this experiment, a 2-point measurement was taken, with electrodes inserted 3 mm into the media. Impedances were measured at a frequency of 1 kHz at time intervals up to an hour. The reason only an hour was used is that in the TEER measurements shown in 4.11E, the largest change in the impedance happens over this first hour in culture. The relative impedance change of the electrodes and PBS are shown in 4.12E. Here it can be seen that although there is a slight change in the impedance over the course of the hour, it is still within error of the initial impedance. Furthermore, any change in impedance could have been down to a change in concentration of the PBS through evaporation, or a temperature change of the liquid. Again, it became clear that the conditioning of the electrodes was not the primary reason behind the decrease in impedance preventing the TEER from reliably being recorded.

Between the investigation into the electrode configuration, effective area, and the conditioning, it was concluded that it was not an effect of the electrodes causing the massive drop in impedance over the first hours of the TEER measurements. With that in mind, the electrode configuration inside the chips was kept the same, and the membranes were investigated to see if they were influencing the impedance measurements.

4.8 Analysis of the membrane in TEER-on-a-chip systems

As with the electrodes, the membranes used in the chips were investigated to determine what effect, if any, they were having on the measured impedance values. To do this, chips were assembled in the normal way, while chips were also assembled without attaching a membrane to the carrier layer, resulting in

no semi-permeable barrier between the two halves of the chip. Both sets of chips were filled with PBS and for each chip, impedances were recorded every hour. Figure 4.13A and B show schematics of the chips used for this experiment (with and without membranes respectively). While 4.13C and D show the impedance spectra recorded at subsequent time points after adding PBS to the chips. In 4.13C, the impedance of the chips begins high at 0 hrs however, after 2 hrs, the impedance has decreased to a much lower value where it remains stable up until 24 hrs. the chips not containing any membranes showed no change in impedance over the duration of the experiment indicated by the tightly grouped spectra in 4.13D. Furthermore, the impedance of the chips with membranes after 2 hrs settles to the same value of the impedance of chips without membranes.

With this in mind, and re-examining the data from the TEER experiments presented in Figure 4.10, this decrease in impedance of the first 2 hrs of the experiment matches well with the data presented in Figure 4.13. Possible mechanisms for this reduction in TEER are discussed below, as well as solutions to this problem.

A possible mechanism for the decrease in impedance over the first 2 hrs of the experiment, is that it takes time for a fluid to penetrate through the pores of the membrane. When the fluid is first introduced to the chip, air remains in the pores meaning the is no transfer of current through the membrane. Over time, these air pockets are replaced by the media, allowing more current to flow between the two chambers, leading to a decrease in the impedance. However, without a more detailed investigation into the conditioning of the membranes (a study outwith the scope of this thesis), this mechanism remains a hypothesis.

Interestingly, there were no other recorded cases of this decrease in the TEER immediately after introducing media to the chips in any of the other pre-existing ToaC literature. However, all the these included a fibronectin coating step to improve the adhesion of the cells to the PDMS or PETE membranes used. In this process, the chips are filled with a solution containing fibronectin which is then left overnight before the solution is flushed out and the chips are filled with warm media. As such, even if there was in initial decrease in impedance when

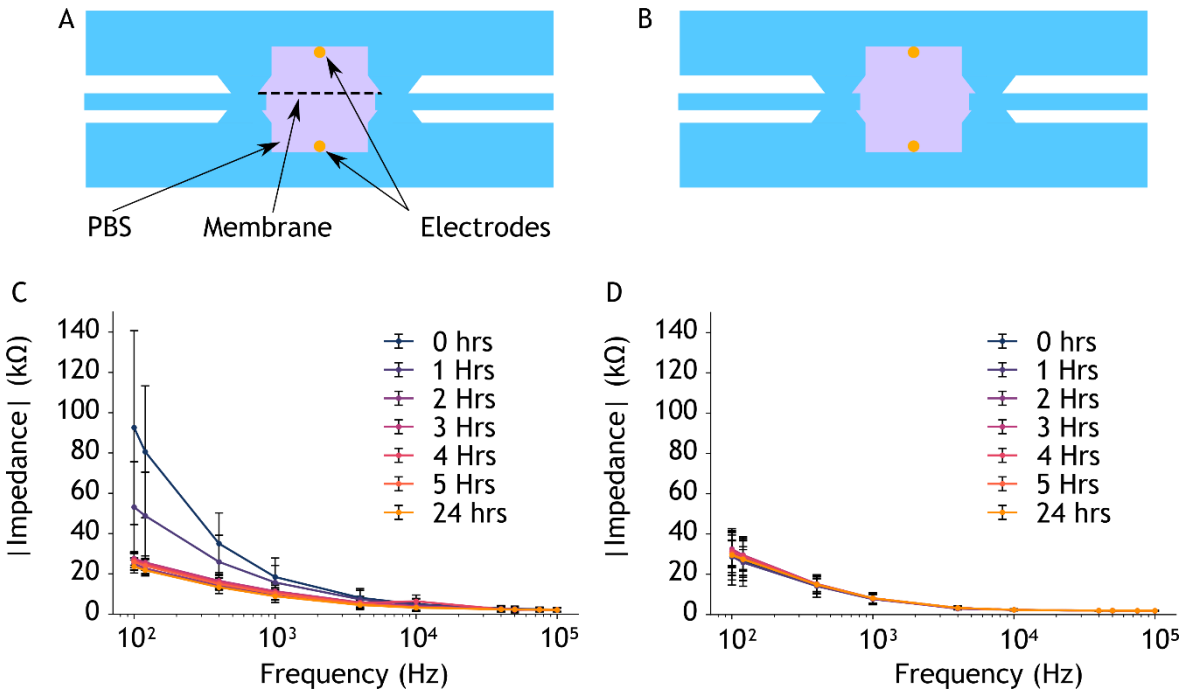

Figure 4.13 – Wetting of the membrane. A shows a cross-sectional schematic of a standard TEER chip with the electrodes (yellow) placed either side of a membrane separating two channels. B shows the same chip, without a membrane. C shows the impedance spectra recorded at different time points for chips shown in A, while D shows the same but for the chips shown in B. Colours in C and D represent the different time points ranging from 0 hrs (blue) through to 24 hrs (yellow). Error bars = mean ± standard deviation with n = 3.

the chips were filled, this would occur during the attachment of fibronectin when no impedance measurement were being taken. Then, by the time any impedances were being recorded, the impedance of the chip would have already settled to a constant value, meaning any initial decrease would go unnoticed. As plasma treatment was used to increase the adhesion of the cells to the PET membranes in this work, no such soaking step was required, meaning that the impedance measurements were taken right after media was introduced to the chips. As such, for future experiments, chips were filled with media, and left in the incubator overnight prior to any impedance recordings being made to allow the impedance to settle.

4.9 TEER measurements in conditioned devices

As discussed in section 4.8, it was thought that the conditioning of the membranes after being subject to a solution for the first time was the cause in the large drop in the measured TEER values over the first couple of hours of an experiment. This large drop was large enough to mask any potentially small changes in the impedance caused by the MDCK cell present in the chip. A such, to mitigate this issue, chips were fabricated and media was introduced to them.

These chips were then left in an incubator overnight before the initial impedance spectra of the chips were measured. Half of the chips were then seeded with MDCK cells while the others were left blank as a control and the impedances were recorded every day for 3 days. The mean impedance spectra for the control and MDCK chips are shown in Figure 4.14A, with the phase shift shown in the lower half of the plot. Again, like the results presented in Figure 4.11, there is a drop in the impedance spectra across the chips from day 0, to day 3 (both for the control, and for the chips with cells). Furthermore, there is no apparent difference in the phase of the chips that contain cells, and those that do not (lower half of 4.14A), with all the phase plots being within error of each other, indicative of no significant difference in them. Typically, in this sort of measurement, as the cell populate the membrane, there is not only an increase in the impedance of the chip, but also a change in the phase[149]. However, as presented in 4.14A, there is no such change in the phase between the control chips and the chips containing cells after 3 days. The phase data is useful here as while an increase in the magnitude of the impedance ($|Z|$) would give an indication of an increase in cell density on the membrane, $|Z|$ does not fully describe the system. As $|Z|$ is composed of two components (the real part or the resistance, Z_R and the imaginary part or the reactance, Z_I. As such, as single value for $|Z|$ could be composed of multiple different combinations of Z_R and Z_I. Thus, a difference in the resistance and reactance values between the experimental chips and the control could be being masked by the change in Z_R and Z_I resulting in similar values of $|Z|$. However, as shown in 4.14A, no such change can be observed between the two chips. This, coupled with the fact that the values of $|Z|$ are similar (top plot in 4.13A) indicates that that the inclusion of cells onto the chips has led to no change in the impedance of the membrane.

Furthermore, in the plot of the calculated TEER (4.14B), we still see a drop of the TEER over the 3 days of the experiment, although this drop is significantly smaller than that seen in the data presented in Figure 5.10 (~2 kΩ with the preconditioned membranes, compared to over 100 kΩ for the non-conditioned chips). As before, the chips were imaged to determine if the cells were still healthy inside them, and this micrograph is shown in 5.13C. It is worth mentioning here however, that for the previous images of cells, they had been stained with just dapi, to image the nucleus, and actin, to serve as a proxy for

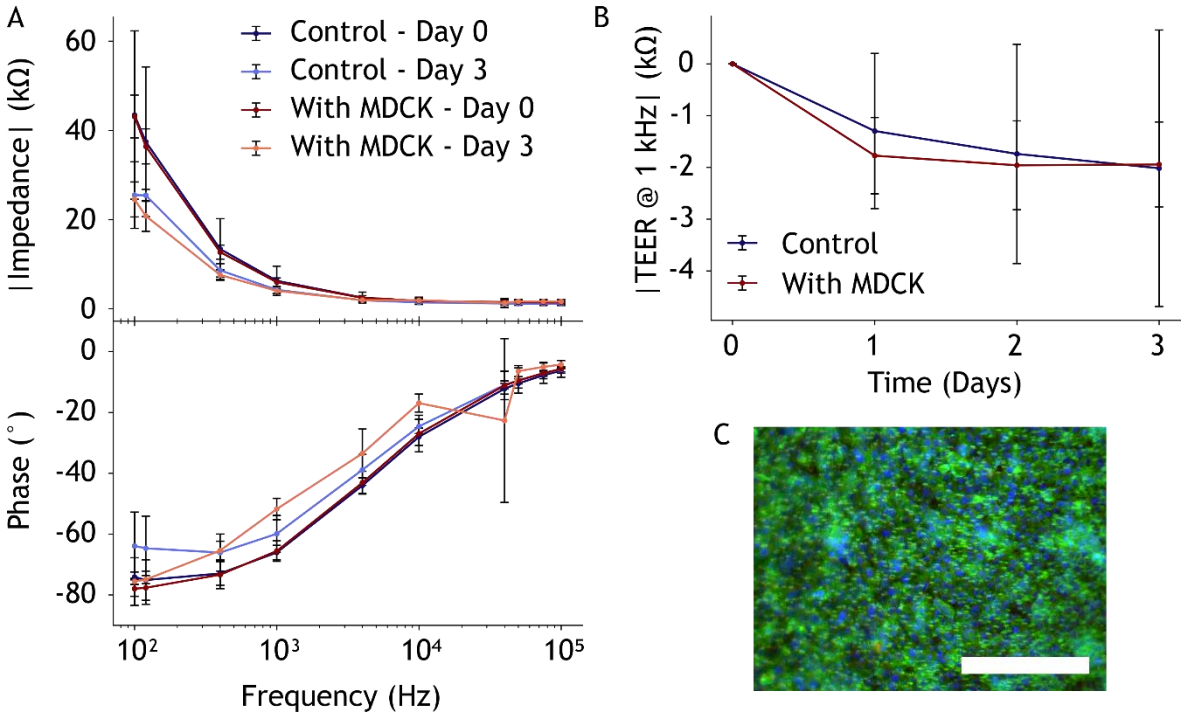

Figure 4.14 – TEER measurements in conditioned chips. A shows a Bode plot of the control chips (dark and light blue for 0 and 3 days respectively), and the MDCK containing chips (dark and light orange for 0 and 3 days respectively), with the upper plot showing the impedance spectra and the lower plot showing the phase of the impedance over the frequency range. B shows the measured TEER over the 3 days of the experiment in both the control chips (no cells, blue), and the chips with MDCK cells (red). C shows a micrograph of the MDCK cells in the chips after 3 days with nucleus = blue, actin = green, and ZO-1 = red. Error bars = mean ± standard deviation. Scale bar = 100 µm.

tight junctions as an abundance of actin at the boundaries between cells is often a good indicator of junction formation. In the image presented in 5.14C however, the cells have been stained for dapi (blue), actin (green), and ZO-1 (red). However, only the actin and dapi channels appear to show any structure within the image with the ZO-1 not showing up near the cell junctions at all. This would indicate that although the cells appeared to be healthy and growing on the chips, they were not perhaps forming the tight junctions that would give rise to the increase in measured impedance, and thus increasing TEER with time. On the other hand, it may be that the stain had simply not worked in this case, and a fault with the chips were still the main cause of the non-reliable TEER measurements.

4.10 Summary, discussion, and conclusions

In this chapter, details on the development of an injection moulded ToaC system have been given. Considerations such as how the chips are sealed compared to existing ToaC devices have been made, as well as an investigation into how the membranes could be reliably incorporated into the chips, without leading to

creases in the membrane that could ultimately affect the cells through changes in flow rate, and nutrient availability. Details on how cells can be seeded into the devices reliably were also investigated.

In previously described devices, electrodes had been held in place using glue and it was thought that a similar approach could be used for these injection moulded chips. However, as described above, the chips did not function as predicted when it came to measuring TEER in MDCK cell layers. The first iterations of the chips relied on having glue to block off the channels made to carry the electrodes into the device, however, it was found that although the glue was supposedly biocompatible, it was in fact killing the cells in the chips, preventing a barrier from being formed. As such, a chip was designed that allowed for the incorporation of gold wire electrodes, through the weld seams, meaning the chip that could be fabricated entirely out of PS and sealed without any additional fabrication steps. This means that the fabrication of the ToaC device aligns well with the injection moulding process detailed in Chapter 3 and allows for the realisation of amass produced ToaC system. Furthermore, by taking PDMS away from the devices, devices can be fabricated, sored, and shipped with ease, meaning that ToaC devices can more readily be put into the hands of researchers without access to cleanroom facilities, or highly skilled expertise. Moreover, by incorporating the electrodes directly into the sealing process, the chips could be fabricated with little additional time (and thus cost) over standard microfluidic chips maintaining the appeal of rapidly fabricated chips through injection moulding from 3D printed masters.

However, even with the issue with the biocompatibility issues of the glue being eliminated, the chips still did not function as they should. To combat this, troubleshooting into the configuration and conditioning of the electrodes was conducted, however, these studies could not pinpoint the cause of the massive reduction in the impedance of the chips during the first 2 hrs of the experiment. When the chips with membranes were compared to chips without however, it became apparent that there was an issue with the wetting of the membranes meaning that the impedance of the chips started out high immediately after a solution was added and dropped to a steady value after 2 hrs. As such, it was determined that this was the main cause of the loss in impedance over the first 2 hrs of the experiment and chips could be conditioned in media overnight

before the impedances were measured to reduce any impact this wetting was having on the recordings of TEER. When impedance measurements were taken, and TEER was calculated there was still an apparent drop in the TEER over the 3 days of the experiment although it was almost two orders of magnitude less that that seen in the unconditioned chips. A set of potential reasons why this may be the case are discussed in the section below.

4.10.1 Possible mechanisms causing the chips to not work that that merit further investigation

As shown in the data presented in section 4.9, the chips still do not perform as they should when it comes to allowing for a robust and reliable measurement of barrier integrity. The configuration, and conditioning of the electrodes and the wetting of the membrane have already been discussed and evaluated with respect to interfering with cell impedance measurements, however, there are still a host of other potential reasons as to why the chips do not work. One such reason in that the area of the membranes may be too large. In the chips presented by Bossink *et al*. the area of the membrane probed by the electrodes is 0.04 cm^2 [149]. This means that the electrodes only probe a small area of the cells meaning that it is unlikely that it becomes more unlikely that the cells wouldn't completely cover the membrane, leading to gaps in the barrier that could leak current and lead to a reduction in the TEER values. The chips used here however, have a membrane area of 0.28 cm^2 as it was thought that a diameter of 6 mm would better mimic a 96 well format and allow for direct comparisons to Transwell systems. This increase of seven times when compared to the chips described by Bossink *et al*. could potential make gaps in the barrier more likely, and thus a reduction in the measured TEER values.

Along-side the membrane area being potentially too large, the area of the electrodes may be too small in relation to the membrane area. A discussed in section 5.6.1, the ideal scenario is to have as large sensing electrodes as possible to spread the electric field out, and probe as large an area of the membrane as possible, without concentrating the current into one small area of the device. As the electrodes here have an area of 63 μm^2 (3 mm length, 200 µm diameter), there may be a large concentration of current between the electrodes that means only a small area of the cells are impacting the TEER measurements.

However, as discussed in section 5.3, wider, fatter electrodes could not be used in the chips with the current design as they would be ruptured by the ultrasonic welding process.

Another possible reason for accurate TEER measurements not being recorded, is that the cells may not be behaving as predicted on the membrane. As discussed in Chapter 1, cells need to first form a confluent layer on a surface, before the tight-junctions are formed. As described in section 4.9, the MDCK cells here were potentially not forming tight junctions within the chips. This could be that there was still a material in the chips that was impacting the metabolism of the cells such that tight junctions were not being formed, or that the micropattern of the membrane pores were influencing the cell morphology. The membranes used in these chips contained 7 µm pores, which is close to the 5 µm pores in the PDMS membrane used by van der Helm (2016)[147], although over an order of magnitude higher than the 0.4 µm pores in the PET membrane used by Maoz *et al.*[145]. This large difference in pore size between the two PET membranes may have had an effect on the cell phenotype as this cellular response to nano- and micro-topography is a well understood phenomenon[249]. Additionally, it could be that the ZO-1 stain used here did not work properly, so further investigation is needed before this can be ruled out as reason for the TEER not being measured accurately. Details on these further investigations are given below.

4.10.2 Recommendations for further work

As mentioned above, there are a plethora of reasons as to why the chips presented here do not give a reliable readout of the TEER of the MDCK cells. However, due to the time constraints of this project, further experiments could not be conducted to improve on the design and functionality of the chips. As such, details of possible experiments have been given to give guidance on any future work that should be conducted in order for fully functioning injection moulded ToaC devices to be realised.

Firstly, the experiment detailed in section 5.8 should be repeated in order to rule out any equipment failures as a cause for the lack of increasing TEER values. Issues with the incubator used to house the cells between measurements may have caused a change in CO_2 or O_2 concentrations in the cell media which

has been shown to impact the formation of tight junctions in cells[130]. A repetition of this experiment would also determine where there was any tight junctions present on the cells inside the chips. It is hypothesised that the stain may not have been applied correctly to the chips shown in Figure 5.13. Typically, when a ZO-1 stain is applied, even if there is not any tight junction visible between the cells, the stain still highlights any ZO-1 protein that is inside the cells however, as shown in Figure 5.13, no such protein is visible here. If the chips are shown to impede the production of tight junctions, then further investigations into the materials, chip geometry, and media supply would need to be conducted to discover the cause of this. In particular, the media supply to the cells could be an issue. As discussed previously, the cells here were cultured statically in order to allow for greater experimental throughput. This is also in line with the protocol detailed by Bossink *et al.*[149] however it may be that the cells are not receiving the adequate nutrition required for tight-junction production. To investigate this, cells should be cultured in chips both with, and without flow to determine if there is any difference in tight junction formation. Flow has been shown in the past to increase the production of tight-junction proteins in cells, however, there have been no documented cases of cells not producing any ZO-1 protein under static culture. Furthermore, the O_2 sensor described in Chapter 4 could be incorporated into the chips in order to rule out the aforementioned effect of hypoxia on barrier formation. Chapter 3 showed how the O_2 concentration inside a PS microfluidic chip dropped when cells were growing and no media was supplied. However, in this instance, media was replaced every day so this was not thought to be an issue. This could be ruled out by measuring the oxygen concentration in the chips to ensure that it remains in a normoxic range for MDCK cells.

However, if a repeat of the experiment in section 4.9 showed that the cells were producing the tight-junctions, then it would be shown that the issue with the chips was down to the measurement of the impedance and not any biological factor.

Secondly, all the electrode and membrane troubleshooting conducted here had been done in PBS as opposed to cell culture media. PBS has been shown to have similar impedance to media, however, the makeup of the two solutions are different, with media having more protein content. The membrane wetting

experiment should be redone using the cell culture media (in the case of MDCK cells, DMEM, FBS, and penicillin streptomycin) to determine whether this would have any different effect on the wetting of the membranes. The wetting of the membranes is likely to be dependent on the internal energy of the fluid and the viscosity which is impacted greatly by the addition of molecules such as proteins and sugars. A quick check for this would be comparing the resistance of a chip filled with PBS to the value calculated from Equation 4.1. If the value is a lot larger than ~30 Ω, then there is another, unaccounted for impedance in the system that would need to be investigated.

If the biological factors and membrane wetting issues described above could be ruled out, chips with geometries like that of the design by Bossink *et al.*[149], Maoz *et al.*[145], and van der Helm *et al.*[146,147] should be constructed (allowing for small variations in design to accommodate for the ultrasonic welding and electrode insertion). By measuring TEER values using chip geometries that have been shown to work, the impact of the geometry of the chip, and the membrane size/electrode area can be potentially ruled out. Furthermore, by using the same chips as described here, but with a variety of membrane areas and pore sizes/densities, the effect of the membrane on the TEER measurements and the MDCK cells can be characterised fully. These experiments concerning the effect of the membrane pores on MDCK cell phenotype should be conducted on membranes in a well plate to isolate the cells from any effect the chips may be having on their behaviour.

4.10.3 Conclusions

In summary, this Chapter details the development of a ToaC device. The experimental results here point to an issue in the chips that could not be identified by the work here. As such, possible hypotheses for the cause of the issue have been discussed as well as details on the future work required to understand the issue better. It is believed that with this work, a fully functioning, injection moulded ToaC system could be achieved paving the way for a host of studies involving barrier integrity and drug delivery. By mass producing such devices, the reliance of open Transwell systems could be reduced, and new OoaC studies could be realised in more physiologically relevant conditions in mass produced chips thus expediting research in this area.

Chapter 5 – Conclusions and future work

5.1 Success in meeting the aims of this thesis

Throughout this thesis, the background and motivations for developing a novel method of producing microfluidic devices by injection moulding has been given. Also described is the work conducted, as well as the analysis of the obtained results with respect to the analysis of the fabrication method (Chapter 2) and the applications of this method in creating an oxygen sensor (Chapter 3) as well as a TEER-on-a-Chip device (Chapter 4). This Chapter gives a discussion of the project as a whole, as well as describing any future directions for the work. To begin with, the aims of the thesis are discussed to evaluate to what extent each aim was met.

5.1.1 Discussion of individual aims

In this section, the aims of the project a reprinted in italics, followed by a discussion.

Develop a platform for the cheap and reliable fabrication of microfluidic devices. This platform should revolve around injection moulding to take advantage of the high throughput capabilities, while also allowing for the fabrication of devices in thermoplastic materials to overcome some of the disadvantages associated with PDMS devices.

Chapter 2 documents the development of a fabrication process consisting of injection moulding from a 3D printed master. This process is capable of faithfully replicating the structures on the 3D printed master provided the desired structures are within the resolution limit of the printer and an appropriate draft angle and feature spacing has been incorporated into the design. This process is reliable and robust with the capability of moulding over 500 identical parts from the same master before it fails. The sealing of the devices through ultrasonic welding and lamination was also discussed showing how the robust seals could be produced by methods complimentary (in terms of timescale) to the high throughput manufacture of injection moulding. Furthermore, by relying on 3D

printing and injection moulding (two fully automated fabrication processes) the person hours required for device fabrication (excluding design) are limited (~2 hrs per production run) reducing the overall cost of fabricating parts when compared to PDMS fabrication that requires costly clean room facilities and a hands-on protocol. Furthermore, the entire process from the design of a device, to biological experiments can be completed within 1 day, rivalling the rapid-prototyping capabilities of processes such as soft lithography.

In addition to the above, the fact that this protocol can be used to fabricate devices out of thermoplastic materials such as PS means that devices more closely resemble tissue culture plastic so it is easier to draw analogues between experiments in well plates, and on chip. This is especially important for the evaluation of OoaC devices.

Finally, by demonstrating the use of one of these devices for culturing liver organoids, it was shown how complex 3D geometries could be easily created and how such devices could be used in the life sciences to enable complex biology.

Taking the above into account, the fabrication platform described here does indeed meet the aim described at the beginning of the project and augments existing manufacturing processes used for microfluidic device fabrication. However, this process is limited by the resolution of the 3D printer and the weld seams required for ultrasonic welding do lead to geometric changes in the channel. Work was done to mitigate these factors, however a full discussion of the further work that could be done is given in section 5.2.

Demonstrate how dissolved oxygen concentration can be controlled in PS microfluidic devices and develop a sensor that gives real-time and spatial information on the distribution of oxygen within a device. This sensor should be able to be rapidly incorporated into a microchannel to align with the high throughput manufacture associated with injection moulding. The performance in terms of sensitivity and the temporal resolution should also be determined.

Chapter 3 documents how the control of oxygen within a PS microfluidic device can be achieved. While the gas permeability of PDMS devices makes it more suitable for cell culture applications, it was thought that the permeability of PS

would mean that the O_2 concentration could be more easily controlled in thermoplastic devices. While issues with the experimental setup and the data gathered meant that no valid conclusions could be drawn from this work, there are many chips described in the literature that are commonly used to increase, and control oxygenation in microfluidic cell culture devices. Furthermore, there is also literature that backs up the idea that a non-gas permeable device may be more suitable for many cell culture applications[217]. Therefore, this aim was not directly achieved by the work presented in this thesis, but a review of the literature surrounding this issue suggests that ample oxygenation can be achieved in PS microfluidic devices and that the oxygenation can be more easily controlled.

With regards to demonstrating an oxygen sensor, the use of PSP meant that both temporal and spatial information of O_2 concentration with PS microfluidic devices could be obtained with reasonable accuracy (~1.3%). While this accuracy is enough for looking at how the oxygen concertation on a device changes over a long timescale, for experiments concerning cell metabolism where the O_2 is measured in the media both before and after it has flowed over a cell culture, this may lead to some errors in calculating the true oxygen consumption of tissues. However, the biocompatibility does mean that the sensor is suitable for biological applications.

Finally, the fact that it is incredibly fast to fabricate the sensors form the PSP means that the manufacture of the sensor aligns well with injection moulding. This means that devices can contain sensors at little extra cost to that of a basic device.

As such, the aims of this Chapter have been met and helps dispel the notion that thermoplastic devices are not suitable for cell culture due to their permeability to gas. That being said, further work is required to fully characterise this. Alongside this, the description of the oxygen sensor does indeed allow for the measurement of both temporal and spatially resolved oxygen data with the performance of the sensor also being discussed. However, despite the rapid fabrication of the sensor, the sensitivity lags behind that of other academic and commercially available devices. Section 5.2 details the works that could be carried out to improve this further.

Demonstrate a barrier on a chip model with integrated TEER measurements for use in modelling epithelial permeability. Again, this chip should be assembled rapidly to align with the injection moulding process. Work on the chip will focus on two areas. First, the assembly of a microfluidic chip including a membrane separating two channels. This assembly should produce a water tight seal while also being quick enough to align with the injection moulding process. Secondly, the electrode material and how the electrodes are incorporated into the device should be investigated to determine the best solution in terms of sealing and electrode performance.

The work relating to this aim is described in Chapter 4. Here, a few designs were tested for incorporating membranes and electrodes into injection moulded microfluidic devices. Membranes were able to be incorporated into devices using a 3-layer structure and sealing through ultrasonic welding. A variety of different electrode materials and designs were also tested with having gold wires running directly through the weld seams proving to be the best option as it meant that devices could be constructed without the use of glue to seal up any other channels. In this regard, the project was successful in creating a device consisting of a membrane separating two flows as well as having electrodes on either side of the membrane. This process was also quick and by having the gold wire electrodes run directly though the weld seams, no additional fabrication steps were required in order to incorporate these features into the device. This aligns well with the high throughout injection moulding processes.

However, despite the fact that all the aspects of the device had been shown to work individually, when TEER measurements were attempted on MDCK cells, it was clear that there was something in the chips causing a decrease in the resistance with time instead of the expected increase. Troubleshooting on both the electrodes and the membranes highlighted that the impedance of the membrane drops rapidly in the 2 hrs after the introduction of fluid, however, when devices were conditioned overnight prior to the 1st measurements, an increase in the TEER could not be observed. This was despite the fact that the device was densely populated with MDCK cells. Details on the work required to fully troubleshoot this problem have already been discussed in Chapter 4 while section 5.2 looks ahead to the research that could be enabled with such devices.

With the above in mind, it has to be said that this aim was not met. While devices containing electrodes and membranes were fabricated, the fact that they could not be used be used for modelling epithelial permeability (or indeed any biological TEER measurement) means that the devices created simply did not function as intended. As previously mentioned, the steps required to fix this are given in Chapter 4.

5.1.2 Discussion of project as a whole

While there was mixed success in meeting the individual aims of the project, there are some successes to be found while analysing the project as a whole. That is, the project describes processes by which complex microfluidic devices can be fabricated. The devices can consist of complex 3D geometry, incorporate different fluidic features such as semi permeable membranes, and include in-built sensing capabilities for the real-time monitoring of biological systems. Furthermore, if such a complex device was fabricated by other means, the time and cost required would likely be much larger than that those described here. Small batches of the TEER-on-a-chip device (10-20 chips) could still be designed, fabricated, assembled and tested all within one working day meaning the theoretical turnaround time for experimentation is now limited by the biology. Furthermore, by having such a quick, high throughput fabrication processes that is capable of making devices in PS, the reliance of PDMS in life-science research can be reduced as well as having devices made in materials that are so well understood in biological research. That being said, there are still many areas that could be investigated to build in the work presented here and these are discussed in the subsequent sections.

5.2 Suggestions for future work

The preceding chapters in this thesis cover the work already conducted to meet the aims of the project. This section however covers the experiments that could be completed in the future to build off this work and expand the capabilities of the processes described here. The following sections describe the further work relating to each Chapter and aim before the final section details the future work that could be in incorporating all aspects of the work shown here.

5.2.1 Improvements to the fabrication process of the basic chips

As mentioned in Chapter 2, the limitations of the fabrication process in terms of resolution are limited by the 3D printer used to create the master. That is, the injection moulding process seems to faithfully replicate the structures, and smaller features have been fabricated through injection moulding using other masters for years. It follows then, that using a higher resolution 3D printer should allow for all the benefits of the protocol described here (rapid manufacture and complex 3D geometry) while also allowing the production of features over a wider range of dimensions. Since the experimental work presented here was conducted, new 3D printers, such as the MicroArch series from Boston Micro Fabrication[250] are quoted to have a minimum feature size of 2 µm which is much smaller than the 140 µm laser spot size on the FormLabs printers used here. Furthermore, BMF's HTL resin shows similar material properties to that of the FormLabs clear resin indicating it's suitability for injection moulding applications[251].

In addition to improving the fabrication of the master, the moulding of the devices could also be optimised to reduce the time needed to cool each part and increase the throughput of the fabrication while maintaining high part quality. The current protocol for moulding includes two cooling steps. A first one for 35 s before the tool is opened slightly and then a secondary 10 s cooling. This was done to ensure that the parts cooled entirely in the mould before ejection to prevent the parts from warping however, cooling times of 5 s have been used for injection moulding of micro- and nano-structures in the past[252] so an optimisation of the process could theoretically improve the throughput by about 3 – 4 times.

Finally, the fabrication process could also benefit from sealing that has much less of an impact on the geometry of the channels. The welding processes here was limited by the fact that ultrasonic welding requires energy directors that add additional height to the channels. By using a higher resolution printer, these energy directors could be made smaller leading to less added height. Also, by incorporating a tongue and groove design, the additional height could be eliminated entirely. This would require a higher resolution printer in order to

make the tongue and grooves with a high enough tolerance to ensure complete sealing.

5.2.2 Future research in to oxygen control and further development of the PSP based oxygen sensor

With regards to the control of O_2 within the microfluidic devices, some work was conducted to show how the dissolved oxygen concentration could be better controlled in PS devices compared to PDMS. However, the work presented here was fairly limited in scope, so more experiments are required in order to show this fully. This could incorporate a control loop whereby the reading from an O_2 sensor inside the chips is used to increase or decrease the flow of media coming from the pumps. Using a Y channel similar to that shown in Chapter 3, hypoxic media could be mixed with hyperoxic media at a ratio of different flow rates such that the O_2 concentration inside the chip could be controlled accurately over time. For this to work however, different sensing hardware would need to be used as the setup used in Chapter 3 would not fit in an incubator. Such a setup would have to consist of a power supply and a light source capable of emitting 405 nm light. The reading of the emission of the PSP would either require a means of measuring light specifically at 650 nm wavelengths, however small inexpensive circuit boards such as that from SparkFun allow for the measurement of light intensity at 450, 500, 550, 570, 600 and 650 nm while still costing less than $30[253]. Some control software would also be required but could be run on a raspberry pi, or Arduino hardware to send commands to the pumps to increase or decrease the flow rate. Something like this could be built with a footprint smaller than a typical syringe pump making it suitable for use in most incubators. This would also allow for experiments that would require good temporal control over the O_2 concentration such as studying ischemia, or modelling adipose tissue.

Finally, the work presented on the oxygen sensor consists of a proof-of-concept of a sensor that can be fabricated rapidly while allowing for the temporal and spatial measurement of O_2 concentration. However, the sensor could likely be improved with some more work into the fabrication process. In this work, the PSP was simply sprayed onto the devices which lead to a grain like texture formed of all the individual droplets. By stamping the PSP onto the devices, a

much more uniform layer of paint could be deposited thus improving the appearance, and likely the performance of the paint. Furthermore, a stamping process would also like control the thickness of the PSP better leading to less part-to-part variability.

5.2.3 Future directions on TEER-on-a-chip research

With regards to the TEER-on-a-chip work, the obvious area for further work is to simply spend more time understanding the system such that the issues surrounding measuring TEER can be fixed. The process by which this should be studied is given in Chapter 4 with an emphasis on studying the individual aspects of the chip to understand what may be causing a reduction in the measured TEER. Once this work has been conducted and if the device has been shown to work properly, then there is scope for a range of different physiological systems that can be studied. In chapters 1 and 4, the gastro-intestinal tract was mentioned as an area of interest as all orally ingested drugs are required to cross this barrier. Some studies have shown how permeation enhancers can temporarily disrupt the barrier function to allow for the passage of compounds into the blood stream. These compounds work in two main ways. Paracellular enhances work by disrupting the cell tight junctions (or the resistive element of the TEER) while transcellular enhancers disrupt the plasma membrane of cells (or the capacitive element of TEER)[124]. As such, a Nyquist plot of a system with a paracellular enhancer should look different from one with a transcellular enhancer. Analysis like this could give a better understanding on how these drugs work and give an indication of their efficacy prior to clinical trials. In addition to this, a PS ToaC device would be the first of its kind and allow for the study of barrier integrity on chip without the drawbacks of PDMS (mainly small molecule absorption). Such as system would be not just limited to the gastro-intestinal tract and could be utilised to provide accurate models of other cellular barriers such as the lungs, and the blood-brain barrier.

5.2.4 Outlook on all aspects

As mentioned in the preceding sections, there is still plenty of scope for further work surrounding all of the individual aspects of this work. However, as with the

aims, when the project as a whole is considered there are a wide range of studies made possible by work presented here.

Firstly, the work here describes two different sensors (a basic electrode for measuring current flow, and an oxygen sensor based on fluorescence quenching). Not presented here, but as shown in Convery *et al*. 2021, the microfluidic devices are also compatible with injection moulded plasmonic sensor arrays[254]. This means that, between the fluorescent sensor, the electronic sensor and a plasmonic sensor, a wide range of sensing technologies have been shown to be compatible with the injection moulded devices. As such, efforts to incorporate new sensors such as glucose, insulin, albumin etc. would allow for a suite of devices with sensing capabilities for OoaC applications. This would allow for the study of many parameters within a single system enabling researchers the tools required to study physiological systems in greater depth than seen before.

Secondly, Chapter 2 and Chapter 4 show how devices can be made with varying degrees of complexity with regards to geometry. The liver organoid-on-a-chip device presented in Chapter 2, as well as the weld seam work shows how 3D geometries can easily be incorporated into the devices, while Chapter 4 details how multilayer devices can be assembled. This means that for devices designed in the future need not be limited to simple, monolithic shapes as complex architectures that more closely resemble human physiology could be created with ease. This becomes more powerful when body-on-a-chip devices are considered. While human-on-a-chip systems have been hypothesised and to some extent demonstrated[255], the ability to create complicated geometries would allow for the creation of integrated organ-on-a-chip devices. Such a device could consist of an oxygen gradient over some liver organoids to mimic zonation sitting downstream of a gastro-intestinal barrier. Here, real time changes in the TEER as a result of permeation enhancers could be measured as well as what the real-time effects on the target compounds on the liver are (measured by studying the albumin secretion). Furthermore, it is not unreasonable that all the above functions could be fabricated on a single chip with modularity and customisability happening at the design lever where different organ modules could be compiled together, before a master is printed, and the device fabricated. This would allow researchers to focus on the applications of the chips, instead of the manufacture. Finally, by fabricating in a material such as

PS, devices can easily be shared around the work simply by packaging and posting meaning that devices can be evaluated in different labs, with different users.

5.3 Summary

Reviews in the field of microfluidics have highlighted the inherent drawbacks of device fabricated with PDMS[22]. The processes developed in this project go some way to providing an alternative approach to microfluidic device fabrication that doesn't compromise on the rapid prototyping capabilities, but also allows for the creation of devices in a more industrially representative fabrication method and materials.

This thesis has presented a new fabrication technology as well as demonstrated two applications. This addresses several needs of microfluidic device fabrication as well as expands the existing toolbox of injection moulding techniques which could lend itself to prototype manufacture in areas outside of biological and chemical sciences. Indeed, since the work on this project was completed, FormLabs have create their own injection moulding resins for the sole purpose of creating master moulds for prototype parts[256]. However, the process described in this thesis goes above and beyond what is capable with this new method in terms of compatibility with an industrial injection moulding machine, and higher resolution of parts by using the clear resin. Moreover, this work enables cutting edge biological research into the rapidly expanding fields of microfluidics and more specifically, organ-on-a-chip. The processes described here look forward to future applications an up-scaling through the fact that they are high throughput by design. This is aided in the fact that they are realised through simple fabrication processes that require little expertise or dexterity to carry out properly. As such, these processes show novel means of creating functional microfluidic chips that help bridge the gap between prototype development, and mass manufacture.

References

1. Convery, N. & Gadegaard, N. 30 years of microfluidics. *Micro and Nano Engineering* **2**, 76–91 (2019).

2. Tabelling, P. *Introduction to Microfluidics*. (Oxford Press, 2005).

3. Reynolds, O. An Experimental Investigation of the Circumstances Which Determine Whether the Motion of Water Shall Be Direct or Sinuous, and of the Law of Resistance in Parallel Channels. *Philos. Trans. R. Soc. London* **174**, 935–982 (1883).

4. Shang, L., Cheng, Y. & Zhao, Y. Emerging Droplet Microfluidics. *Chem. Rev.* **117**, 7964–8040 (2017).

5. Heller, A. & Feldman, B. Electrochemical glucose sensors and their applications in diabetes management. *Chemical Reviews* **108**, 2482–2505 (2008).

6. Hu, J. *et al.* Advances in paper-based point-of-care diagnostics. *Biosensors and Bioelectronics* **54**, 585–597 (2014).

7. Zhou, Y., Wu, Y., Ding, L., Huang, X. & Xiong, Y. Point-of-care COVID-19 diagnostics powered by lateral flow assay. *TrAC - Trends Anal. Chem.* **145**, 116452 (2021).

8. Martinez, A. W., Phillips, S. T., Butte, M. J. & Whitesides, G. M. Patterned paper as a platform for inexpensive, low-volume, portable bioassays. *Angew. Chemie - Int. Ed.* **46**, 1318–1320 (2007).

9. Manz, A., Widmers, H. M. & Graber, N. Miniaturized total chemical analysis systems: A novel concept for chemical sensing. *Sensors Actuators B Chem.* **1**, 244–248 (1990).

10. Qin, D. *et al.* Microfabrication, Microstructures and Microsystems. in *Microsystem Technology in Chemistry and Life Sciences* (eds. Manz, A. & Becker, H.) 1–20 (Springer, 1999).

11. Lorenz, H. *et al.* High-aspect-ratio, ultrathick, negative-tone near-UV photoresist and its applications for MEMS. *Sensors Actuators, A Phys.* **64**, 33–39 (1998).

12. Sato, H., Matsumura, H., Keino, S. & Shoji, S. An all SU-8 microfluidic chip with built-in 3D fine microstructures. *J. Micromechanics Microengineering* **16**, 2318–2322 (2006).

13. McDonald, J. C. *et al.* Fabrication of microfluidic systems in poly(dimethylsiloxane). *Electrophoresis* **21**, 27–40 (2000).

14. McDonald, J. C. & Whitesides, G. M. Poly(dimethylsiloxane) as a material for fabricating microfluidic devices. *Acc. Chem. Res.* **35**, 491–499 (2002).

15. Unger, M. A., Chou, H.-P., Thorsen, T., Scherer, A. & Quake, S. R. Monolithic Microfabricated Valves and Pumps by Multilayer Soft Lithography. *Science*. **288**, 113–116 (2000).

16. Bernard, A., Michel, B. & Delamarche, E. Micromosaic immunoassays. *Anal. Chem*. **73**, 8–12 (2001).

17. Chou, H.-P., Spence, C., Scherer, A. & Quake, S. A microfabricated device for sizing and sorting DNA molecules. *Proc. Natl. Acad. Sci.* **96**, 11–13 (1999).

18. Ismagilov, R. F., Ng, J. M. K., Kenis, P. J. A. & Whitesides, G. M. Microfluidic arrays of fluid-fluid diffusional contacts as detection elements and combinatorial tools. *Anal. Chem.* **73**, 5207–5213 (2001).

19. DeBusschere, B. D. & Kovacs, G. T. A. Portable cell-based biosensor system using integrated CMOS cell-cartridges. *Biosens. Bioelectron.* **16**, 543–556 (2001).

20. Sia, S. K. & Whitesides, G. M. Microfluidic devices fabricated in poly(dimethylsiloxane) for biological studies. *Electrophoresis* **24**, 3563–3576 (2003).

21. Xia, Y. & Whitesides, G. M. Soft Lithography. *Angew. Chemie Int. Ed.* **37**, 550–575 (1998).

22. Berthier, E., Young, E. W. K. & Beebe, D. Engineers are from PDMS-land,

biologists are from polystyrenia. *Lab on a Chip* **12**, 1224–1237 (2012).

23. van Meer, B. J. *et al.* Small molecule absorption by PDMS in the context of drug response bioassays. *Biochem. Biophys. Res. Commun.* **482**, 323–328 (2017).

24. Toepke, M. W. & Beebe, D. J. PDMS absorption of small molecules and consequences in microfluidic applications. *Lab on a Chip* **6**, 1484–1486 (2006).

25. Gewandter, J. S., Staversky, R. J. & O'Reilly, M. A. Hyperoxia augments ER-stress-induced cell death independent of BiP loss. *Free Radic. Biol. Med.* **47**, 1742–1752 (2009).

26. Gervais, T., El-Ali, J., Günther, A. & Jensen, K. F. Flow-induced deformation of shallow microfluidic channels. *Lab Chip* **6**, 500–507 (2006).

27. Regehr, K. J. *et al.* Biological implications of polydimethylsiloxane-based microfluidic cell culture. *Lab on a Chip* **9**, 2132–2139 (2009).

28. Eddington, D. T., Puccinelli, J. P. & Beebe, D. J. Thermal aging and reduced hydrophobic recovery of polydimethylsiloxane. *Sensors Actuators, B Chem.* **114**, 170–172 (2006).

29. Callister, W. D. & Rethwisch, D. G. *Materials in Science and Engineering: An Introduction*. (John Wiley and Sons, 2000).

30. Wang, Z., Volinsky, A. A. & Gallant, N. D. Crosslinking effect on polydimethylsiloxane elastic modulus measured by custom-built compression instrument. *J. Appl. Polym. Sci.* **131**, 41050 (2014).

31. Hyatt, J. S. & Hyatt, J. W. improvement in Process and Apparatus for Manufacturing Pyroxyline,. (1872).

32. Insights, F. B. *Injection Molded Plastics Market Size, Share & COVID-19 Impact Analysis, By Resin Polypropylene (PP), Acrylonitrile butadiene styrene (ABS), High-density polyethylene (HDPE), Polystyrene (PS), and*

Others), By Application (Automotive, Packaging, Building &. (2022).

33. Matschuk, M. & Larsen, N. B. Injection molding of high aspect ratio sub-100 nm nanostructures. *J. Micromechanics Microengineering* **23**, 25003–10 (2013).

34. Polychronopoulos, N. D. & Vlachopoulos, J. *Polymer Processing and Rheology*. (Springer, 2019). doi:https://doi.org/10.1007/978-3-319-95987-0

35. Yu, L., Koh, C. G., James Lee, L., Koelling, K. W. & Madou, M. J. Experimental investigation and numerical simulation of injection molding with micro-features. *Polym. Eng. Sci.* **42**, 871–888 (2002).

36. Becker, H. & Heim, U. Hot embossing as a method for the fabrication of polymer high aspect ratio structures. *Sensors Actuators A Phys.* **83**, 130–135 (2000).

37. Giboz, J., Copponnex, T. & Mélé, P. Microinjection molding of thermoplastic polymers: A review. *J. Micromechanics Microengineering* **17**, 96 (2007).

38. Gadegaard, N., Mosler, S. & Larsen, N. B. Biomimetic polymer nanostructures by injection molding. *Macromol. Mater. Eng.* **288**, 76–83 (2003).

39. Macintyre, D. & Thoms, S. The Fabrication of High Resolution Features By Mould Injection. *Science*. **42**, 211–214 (1998).

40. Yoon, S. *et al.* Evaluation of novel tooling for nanoscale injection molding. in *Proceedings of SPIE* 107 (2005). doi:10.1117/12.599959

41. Zhao, J. *et al.* Development of Rapid Manufacturing Technology of Polymer Microfluidic Devices By Micro Moulding Using Silicon Mould Inserts. in *Proceedings of the 6th International Conference on Nanochannels, Microchannels, and Minichannels, Pts a and B* 1187–1194 (2008). doi:10.1115/ICNMM2008-62232

42. Yoon, S.-H., Palanisamy, P., Padmanabha, P., Mead, J. L. & Barry, C. M. F. Comparison of Tooling Materials in Injection Molding of Microscale Features. *Vol. 12 Micro Nano Syst. Parts A B* **2009**, 545–552 (2010).

43. Hansen, T. S., Selmeczi, D. & Larsen, N. B. Fast prototyping of injection molded polymer microfluidic chips. *J. Micromechanics Microengineering* **20**, 1 (2010).

44. Park, S. H., Lee, W. I., Moon, S. N., Yoo, Y. E. & Cho, Y. H. Injection molding micro patterns with high aspect ratio using a polymeric flexible stamper. *Express Polym. Lett.* **5**, 950–958 (2011).

45. Zhang, N., Byrne, C. J., Browne, D. J. & Gilchrist, M. D. Towards nano-injection molding. *Mater. Today* **15**, 216–221 (2012).

46. Stormonth-Darling, J. M. & Gadegaard, N. Injection moulding difficult nanopatterns with hybrid polymer inlays. *Macromol. Mater. Eng.* **297**, 1075–1080 (2012).

47. Ramos, B. & Choquette, S. Embossable Grating Couplers for Planar Waveguid Optical Sensors. *Anal. Chem.* **68**, 1245 (1996).

48. Chou, S. Y., Krauss, P. R. & Renstrom, P. J. Imprint of sub-25 nm vias and trenches in polymers. *Appl. Phys. Lett.* **67**, 3114 (1995).

49. Heckele, M. & Schomburg, W. K. Review on micro molding of thermoplastic polymers. *Journal of Micromechanics and Microengineering* **14**, 1–14 (2004).

50. Lin, T. Y., Do, T., Kwon, P. & Lillehoj, P. B. 3D printed metal molds for hot embossing plastic microfluidic devices. *Lab Chip* **17**, 241–247 (2017).

51. Esch, M. B., Kapur, S., Irizarry, G. & Genova, V. Influence of master fabrication techniques on the characteristics of embossed microfluidic channels. *Lab Chip* **3**, 121–127 (2003).

52. Miserere, S. *et al.* Fabrication of thermoplastics chips through lamination

based techniques. *Lab Chip* **12**, 1849–1856 (2012).

53. Kricka, L. J. *et al.* Fabrication of plastic microchips by hot embossing. *Lab Chip* **2**, 1–4 (2002).

54. Arayanarakool, R., Le Gac, S. & Van Den Berg, A. Low-temperature, simple and fast integration technique of microfluidic chips by using a UV-curable adhesive. *Lab Chip* **10**, 2115–2121 (2010).

55. Kinahan, D. J. *et al.* Xurography actuated valving for centrifugal flow control. *Lab Chip* **16**, 3454–3459 (2016).

56. Kratz, S. R. A. *et al.* Characterization of four functional biocompatible pressure-sensitive adhesives for rapid prototyping of cell-based lab-on-a-chip and organ-on-a-chip systems. *Sci. Rep.* **9**, 9287 (2019).

57. Temiz, Y., Lovchik, R. D., Kaigala, G. V. & Delamarche, E. Lab-on-a-chip devices: How to close and plug the lab? *Microelectronic Engineering* **132**, 156–175 (2015).

58. Mair, D. A. *et al.* Room-temperature bonding for plastic high-pressure microfluidic chips. *Anal. Chem.* **79**, 5097–5102 (2007).

59. Ng, S. H. *et al.* Thermally activated solvent bonding of polymers. *Microsyst. Technol.* **14**, 753–759 (2008).

60. Shah, J. J. *et al.* Capillarity induced solvent-actuated bonding of polymeric microfluidic devices. *Anal. Chem.* **78**, 3348–3353 (2006).

61. Kelly, R. T., Pan, T. & Woolley, A. T. Phase-changing sacrificial materials for solvent bonding of high-performance polymeric capillary electrophoresis microchips. *Anal. Chem.* **77**, 3536–3541 (2005).

62. Bhattacharyya, A. & Klapperich, C. M. Mechanical and chemical analysis of plasma and ultraviolet-ozone surface treatments for thermal bonding of polymeric microfluidic devices. *Lab Chip* **7**, 876–882 (2007).

63. Tsao, C. W., Hromada, L., Liu, J., Kumar, P. & DeVoe, D. L. Low temperature bonding of PMMA and COC microfluidic substrates using UV/ozone surface treatment. *Lab Chip* **7**, 499–505 (2007).

64. Cho, K. *et al.* Effects of photoirradiation in UV and VUV regions during plasma exposure to polymers. *Thin Solid Films* **519**, 6810–6814 (2011).

65. Matteucci, M. *et al.* Fabrication and characterization of injection molded multi level nano and microfluidic systems. *Microelectron. Eng.* **111**, 294–298 (2013).

66. Truckenmüller, R., Ahrens, R., Cheng, Y., Fischer, G. & Saile, V. An ultrasonic welding based process for building up a new class of inert fluidic microsensors and -actuators from polymers. *Sensors Actuators, A Phys.* **132**, 385–392 (2006).

67. Kistrup, K., Poulsen, C. E., Hansen, M. F. & Wolff, A. Ultrasonic welding for fast bonding of self-aligned structures in lab-on-a-chip systems. *Lab Chip* **15**, 1998–2001 (2015).

68. Scannell, J. W., Blanckley, A., Boldon, H. & Warrington, B. *Diagnosing the decline in pharmaceutical R&D efficiency*. *Nature Publishing Group* (2012). doi:10.1038/nrd3681

69. Suckow, M. A. & Stewart, K. L. *Principles of Animal Research for Graduate and Undergraduate Students*. (Elsevier Inc., 2017).

70. Shanks, N., Greek, R. & Greek, J. Are animal models predictive for humans? *Philos. Ethics, Humanit. Med.* **4**, (2009).

71. Reardon, S. 'Organs-on-chips' go mainstream. *Nature* **523**, 266 (2015).

72. Bhise, N. S., Ribas, J., Manoharan, V., Shrike, Y. & Polini, A. Organ-on-a-chip platforms for studying drug delivery systems. *J. Control. Release* **190**, 82–93 (2014).

73. Russell, W. M. S. & Burch, R. L. *The principles of humane experimental*

techniquee. (Methuen and Co, 1959).

74. Bhatia, S. N. & Ingber, D. E. Microfluidic organs-on-chips. *Nat. Biotechnol.* **32**, 760–772 (2014).

75. Grosberg, A. *et al.* Muscle on a chip: In vitro contractility assays for smooth and striated muscle. *J. Pharmacol. Toxicol. Methods* **65**, 126–135 (2012).

76. Park, S. H. *et al.* Chip-Based Comparison of the Osteogenesis of Human Bone Marrow- and Adipose Tissue-Derived Mesenchymal Stem Cells under Mechanical Stimulation. *PLoS One* **7**, (2012).

77. Liu, M.-C. *et al.* Electrofluidic pressure sensor embedded microfluidic device: a study of endothelial cells under hydrostatic pressure and shear stress combinations. *Lab Chip* **13**, 1743 (2013).

78. Huh, D. *et al.* Reconstituting organ-level lung functions on a Chip. *Science.* **328**, 1662–1668 (2010).

79. Villenave, R. *et al.* Human gut-on-a-chip supports polarized infection of coxsackie B1 virus in vitro. *PLoS One* **12**, 1–17 (2017).

80. Scott, A. *et al.* A microfluidic microelectrode array for simultaneous electrophysiology, chemical stimulation, and imaging of brain slices. *Lab Chip* **13**, 527–535 (2013).

81. Agarwal, A., Goss, J. A., Cho, A., McCain, M. L. & Parker, K. K. Microfluidic heart on a chip for higher throughput pharmacological studies. *Lab Chip* **13**, 3599 (2013).

82. Rogal, J., Probst, C. & Loskill, P. Integration concepts for multi-organ chips: how to maintain flexibility. *Futur. Sci. OA* **3**, FSO180 (2017).

83. Huh, D., Hamilton, G. A. & Ingber, D. E. From 3D cell culture to organs-on-chips. *Trends in Cell Biology* **21**, 745–754 (2011).

84. Roy, S. *et al.* Oxygen sensing by primary cardiac fibroblasts: A key role of p21Waf1/Cip1/Sdi1. *Circ. Res.* **92**, 264–271 (2003).

85. Semenza, G. L. HIF-1, O2, and the 3 PHDs: How animal cells signal hypoxia to the nucleus. *Cell* **107**, 1–3 (2001).

86. Roy, P., Baskaran, H., Tilles, A. W., Yarmush, M. L. & Toner, M. Analysis of oxygen transport to hepatocytes in a flat-plate microchannel bioreactor. *Ann. Biomed. Eng.* **29**, 947–955 (2001).

87. Kietzmann, T. Metabolic zonation of the liver: The oxygen gradient revisited. *Redox Biology* **11**, 622–630 (2017).

88. Allen, J. W., Khetani, S. R. & Bhatia, S. N. In vitro zonation and toxicity in a hepatocyte bioreactor. *Toxicol. Sci.* **84**, 110–119 (2005).

89. Allen, J. W. & Bhatia, S. N. Formation of steady-state oxygen gradients in vitro: Application to liver zonation. *Biotechnol. Bioeng.* **82**, 253–262 (2003).

90. Lee-Montiel, F. T. *et al.* Control of oxygen tension recapitulates zone-specific functions in human liver microphysiology systems. *Exp. Biol. Med.* **242**, 1617–1632 (2017).

91. Tomlinson, L. *et al.* In vitro Liver Zonation of Primary Rat Hepatocytes. *Front. Bioeng. Biotechnol.* **7**, 17 (2019).

92. Tonon, F. *et al.* In vitro metabolic zonation through oxygen gradient on a chip. *Sci. Rep.* **9**, (2019).

93. Sato, A., Kadokura, K., Uchida, H. & Tsukada, K. An in vitro hepatic zonation model with a continuous oxygen gradient in a microdevice. *Biochem. Biophys. Res. Commun.* **453**, 767–771 (2014).

94. Kang, Y. B. A., Eo, J., Mert, S., Yarmush, M. L. & Usta, O. B. Metabolic Patterning on a Chip: Towards in vitro Liver Zonation of Primary Rat and Human Hepatocytes. *Sci. Rep.* **8**, (2018).

95. Bulutoglu, B. *et al.* A microfluidic patterned model of non-alcoholic fatty liver disease: Applications to disease progression and zonation. *Lab Chip* **19**, 3022–3031 (2019).

96. Nock, V., Blaikie, R. J. & David, T. Patterning, integration and characterisation of polymer optical oxygen sensors for microfluidic devices. *Lab Chip* **8**, 1300–1307 (2008).

97. Karasinski, J. *et al.* Detection and identification of bacteria using antibiotic susceptibility and a multi-array electrochemical sensor with pattern recognition. *Biosens. Bioelectron.* **22**, 2643–2649 (2007).

98. Akyilmaz, E., Erdoğan, A., Öztürk, R. & Yaşa, I. Sensitive determination of l-lysine with a new amperometric microbial biosensor based on Saccharomyces cerevisiae yeast cells. *Biosens. Bioelectron.* **22**, 1055–1060 (2007).

99. Wu, C. C. *et al.* Microfluidic chip integrated with amperometric detector array for in situ estimating oxygen consumption characteristics of single bovine embryos. *Sensors Actuators, B Chem.* **125**, 680–687 (2007).

100. Papkovsky, D. B., Ponomarev, G. V., Trettnak, W. & O'Leary, P. Phosphorescent Complexes of Porphyrin Ketones: Optical Properties and Application to Oxygen Sensing. *Anal. Chem.* **67**, 4112–4117 (1995).

101. Amao, Y. Probes and Polymers for Optical Sensing of Oxygen. *Microchimica Acta* **143**, 1–12 (2003).

102. Carraway, E. R., Demas, J. N. & DeGraff, B. A. Luminescence Quenching Mechanism for Microheterogeneous Systems. *Anal. Chem.* **63**, 332–336 (1991).

103. Fischkoff, S. & Vanderkooi, J. M. Oxygen diffusion in biological and artificial membranes determined by the fluorochrome pyrene. *J. Gen. Physiol.* **65**, 663–676 (1975).

104. Alderman, J. *et al.* A low-volume platform for cell-respirometric screening

based on quenched-luminescence oxygen sensing. in *Biosensors and Bioelectronics* **19**, 1529–1535 (Elsevier, 2004).

105. Sud, D. *et al.* Optical imaging in microfluidic bioreactors enables oxygen monitoring for continuous cell culture. *J. Biomed. Opt.* **11**, 050504 (2006).

106. O'Mahony, F. C. *et al.* Optical oxygen microrespirometry as a platform for environmental toxicology and animal model studies. *Environ. Sci. Technol.* **39**, 5010–5014 (2005).

107. Chang-Yen, D. A. & Gale, B. K. An integrated optical oxygen sensor fabricated using rapid-prototyping techniques. *Lab Chip* **3**, 297–301 (2003).

108. Vollmer, A. P., Probstein, R. F., Gilbert, R. & Thorsen, T. Development of an integrated microfluidic platform for dynamic oxygen sensing and delivery in a flowing medium. *Lab Chip* **5**, 1059–1066 (2005).

109. Xiong, X., Xiao, D. & Choi, M. M. F. Dissolved oxygen sensor based on fluorescence quenching of oxygen-sensitive ruthenium complex immobilized on silica-Ni-P composite coating. *Sensors Actuators, B Chem.* **117**, 172–176 (2006).

110. Lee, S., Ibey, B. L., Coté, G. L. & Pishko, M. V. Measurement of pH and dissolved oxygen within cell culture media using a hydrogel microarray sensor. *Sensors Actuators, B Chem.* **128**, 388–398 (2008).

111. Wang, X. D. & Wolfbeis, O. S. Optical methods for sensing and imaging oxygen: Materials, spectroscopies and applications. *Chem. Soc. Rev.* **43**, 3666–3761 (2014).

112. Mills, A. Optical Oxygen. *Platin. Met. Rev* **41**, 115–127 (1997).

113. Quaranta, M., Borisov, S. M. & Klimant, I. Indicators for optical oxygen sensors. *Bioanal. Rev.* **4**, 115–157 (2012).

114. Wolfbeis, O. S. Luminescent sensing and imaging of oxygen: Fierce competition to the Clark electrode. *BioEssays* **37**, 921–928 (2015).

115. Ungerböck, B., Charwat, V., Ertl, P. & Mayr, T. Microfluidic oxygen imaging using integrated optical sensor layers and a color camera. *Lab Chip* **13**, 1593–1601 (2013).

116. Qiu, W. & Nagl, S. Automated Miniaturized Digital Microfluidic Antimicrobial Susceptibility Test Using a Chip-Integrated Optical Oxygen Sensor. *ACS Sensors* **6**, 1147–1156 (2021).

117. Penso, C. M. *et al.* PtOEP–PDMS-based optical oxygen sensor. *Sensors* **21**, (2021).

118. Lasave, L. C., Borisov, S. M., Ehgartner, J. & Mayr, T. Quick and simple integration of optical oxygen sensors into glass-based microfluidic devices. *RSC Adv.* **5**, 70808–70816 (2015).

119. Hedaya, M. A. *Basic Pharmacokinetics*. (Taylor & Francis, 2012).

120. Abbott, N. J., Rönnbäck, L. & Hansson, E. Astrocyte-endothelial interactions at the blood-brain barrier. *Nature Reviews Neuroscience* **7**, 41–53 (2006).

121. Cho, C. W. *et al.* Ultrasound-induced mild hyperthermia as a novel approach to increase drug uptake in brain microvessel endothelial cells. *Pharm. Res.* **19**, 1123–1129 (2002).

122. Rapoport, S. I. Osmotic opening of the blood-brain barrier: Principles, mechanism, and therapeutic applications. *Cellular and Molecular Neurobiology* **20**, 217–230 (2000).

123. Schirmacher, A. *et al.* Electromagnetic fields (1.8 GHz) increase the permeability to sucrose of the blood - Brain barrier in vitro. *Bioelectromagnetics* **21**, 338–345 (2000).

124. Maher, S., Brayden, D. J., Casettari, L. & Illum, L. Application of permeation enhancers in oral delivery of macromolecules: An update. *Pharmaceutics* **11**, 41 (2019).

125. Eichner, M., Protze, J., Piontek, A., Krause, G. & Piontek, J. Targeting and alteration of tight junctions by bacteria and their virulence factors such as Clostridium perfringens enterotoxin. *Pflugers Archiv European Journal of Physiology* **469**, 77–90 (2017).

126. Chuang, E. Y. *et al.* Calcium depletion-mediated protease inhibition and apical-junctional- complex disassembly via an EGTA-conjugated carrier for oral insulin delivery. *J. Control. Release* **169**, 296–305 (2013).

127. Zupančič, O. & Bernkop-Schnürch, A. Lipophilic peptide character – What oral barriers fear the most. *Journal of Controlled Release* **255**, 242–257 (2017).

128. Maher, S. *et al.* Effects of surfactant-based permeation enhancers on mannitol permeability, histology, and electrogenic ion transport responses in excised rat colonic mucosae. *Int. J. Pharm.* **539**, 11–22 (2018).

129. Perinelli, D. R. *et al.* Correlation among chemical structure, surface properties and cytotoxicity of N-acyl alanine and serine surfactants. *Eur. J. Pharm. Biopharm.* **109**, 93–102 (2016).

130. Deli, M. A., Ábrahám, C. S., Kataoka, Y. & Niwa, M. Permeability studies on in vitro blood-brain barrier models: Physiology, pathology, and pharmacology. *Cellular and Molecular Neurobiology* **25**, 59–127 (2005).

131. Abdullahi, W., Tripathi, D. & Ronaldson, P. T. Blood-brain barrier dysfunction in ischemic stroke: Targeting tight junctions and transporters for vascular protection. *Am. J. Physiol. - Cell Physiol.* **315**, C343–C356 (2018).

132. Bäsler, K. *et al.* The role of tight junctions in skin barrier function and dermal absorption. *J. Control. Release* **242**, 105–118 (2016).

133. Matter, K. & Balda, M. S. Functional analysis of tight junctions. *Methods* **30**, 228–234 (2003).

134. Lohmann, C., Hüwel, S. & Galla, H. J. Predicting blood-brain barrier

permeability of drugs: Evaluation of different in vitro assays. *J. Drug Target.* **10**, 263–276 (2002).

135. Bowman, P. D., Ennis, S. R., Rarey, K. E., Lorris Betz, A. & Goldstein, G. W. Brain microvessel endothelial cells in tissue culture: A model for study of blood-brain barrier permeability. *Ann. Neurol.* **14**, 396–402 (1983).

136. Horibe, Y., Hosoya, K. I., Kim, K. J., Ogiso, T. & Lee, V. H. L. Polar solute transport across the pigmented rabbit conjunctiva: Size dependence and the influence of 8-bromo cyclic adenosine monophosphate. *Pharm. Res.* **14**, 1246–1251 (1997).

137. Duffy, S. L. & Murphy, J. T. Colorimetric assay to quantify macromolecule diffusion across endothelial monolayers. *Biotechniques* **31**, 495–501 (2001).

138. Benson, K., Cramer, S. & Galla, H.-J. Impedance-based cell monitoring: barrier properties and beyond. *Fluids Barriers CNS 2013 101* **10**, 1–11 (2013).

139. World Precision Intruments. Epithelial Volt/Ohm (TEER) Meter 3. Available at: https://www.wpiinc.com/evom3-epithelial-volt-ohm-teer-meter-3. (Accessed: 21st July 2021)

140. WPI. EVOM2. (2022). Available at: https://www.wpi-europe.com/products/cell-and-tissue/teer-measurement/evom2.aspx.

141. Jovov, B., Wills, N. K. & Lewis, S. A. A spectroscopic method for assessing confluence of epithelial cell cultures. *Am. J. Physiol. - Cell Physiol.* **261**, (1991).

142. Booth, R. & Kim, H. Characterization of a microfluidic in vitro model of the blood-brain barrier (μBBB). *Lab Chip* **12**, 1784–1792 (2012).

143. Asif, A., Kim, K. H., Jabbar, F., Kim, S. & Choi, K. H. Real-time sensors for live monitoring of disease and drug analysis in microfluidic model of proximal tubule. *Microfluid. Nanofluidics* **24**, 1–10 (2020).

144. Henry, O. Y. F. *et al.* Organs-on-chips with integrated electrodes for trans-epithelial electrical resistance (TEER) measurements of human epithelial barrier function. *Lab Chip* **17**, 2264–2271 (2017).

145. Maoz, B. M. *et al.* Organs-on-Chips with combined multi-electrode array and transepithelial electrical resistance measurement capabilities. *Lab Chip* **17**, 2294–2302 (2017).

146. van der Helm, M. W. *et al.* Non-invasive sensing of transepithelial barrier function and tissue differentiation in organs-on-chips using impedance spectroscopy. *Lab Chip* **19**, 452–463 (2019).

147. van der Helm, M. W. *et al.* Direct quantification of transendothelial electrical resistance in organs-on-chips. *Biosens. Bioelectron.* **85**, 924–929 (2016).

148. Walter, F. R. *et al.* A versatile lab-on-a-chip tool for modeling biological barriers. *Sensors Actuators, B Chem.* **222**, 1209–1219 (2016).

149. Bossink, E. G. B. M., Zakharova, M., De Bruijn, D. S., Odijk, M. & Segerink, L. I. Measuring barrier function in organ-on-chips with cleanroom-free integration of multiplexable electrodes. *Lab Chip* **21**, 2040–2049 (2021).

150. Galla, H. -J. *et al.* The blood-brain barrier in vitro: regulation, maintainance and quantification of the barrier properties by impedance pectroscopy. in *Horizons in neuroscience research* (eds. Costa, A. & Villalba, E.) 1–14 (Nova, 2011).

151. Hoheisel, D. *et al.* Hydrocortisone reinforces the blood-brain barrier properties in a serum free cell culture system. *Biochem. Biophys. Res. Commun.* **244**, 312–316 (1998).

152. Wegener, J., Abrams, D., Willenbrink, W., Galla, H. J. & Janshoff, A. Automated multi-well device to measure transepithelial electrical resistances under physiological conditions. *Biotechniques* **37**, 590–597 (2004).

153. Weidenfeller, C., Schrot, S., Zozulya, A. & Galla, H. J. Murine brain capillary endothelial cells exhibit improved barrier properties under the influence of hydrocortisone. *Brain Res.* **1053**, 162–174 (2005).

154. Kröll, S. *et al.* Control of the blood-brain barrier by glucocorticoids and the cells of the neurovascular unit. *Ann. N. Y. Acad. Sci.* **1165**, 228–239 (2009).

155. Keese, C. R., Wegener, J., Walker, S. R. & Giaever, I. Electrical wound-healing assay for cells in vitro. *Proc. Natl. Acad. Sci. U. S. A.* **101**, 1554–1559 (2004).

156. Von Wedel-Parlow, M. *et al.* Neutrophils cross the BBB primarily on transcellular pathways: An in vitro study. *Brain Res.* **1367**, 62–76 (2011).

157. Wedel-Parlow, M. von & Galla, H.-J. A microscopic in vitro study of neutrophil diapedesis across the blood-brain barrier. in *MICROSCOPY: SCIENCE, TECHNOLOGY, APPLICATIONS AND EDUCATION Contents Vol. 2* 1161–1167 (2010).

158. Beebe, D. J., Mensing, G. A. & Walker, G. M. Physics and Applications of Microfluidics in Biology. *Annu. Rev. Biomed. Eng.* **4**, 261–286 (2002).

159. Whitesides, G. M. The origins and the future of microfluidics. *Nature* **442**, 368–373 (2006).

160. Manfrinato, V. R. *et al.* Resolution limits of electron-beam lithography toward the atomic scale. *Nano Lett.* **13**, 1555–1558 (2013).

161. Terry, S. C., Herman, J. H. & Angell, J. B. A gas chromatographic air analyzer fabricated on a silicon wafer. *IEEE Trans. Electron Devices* **26**, 1880–1886 (1979).

162. Datta, M. Fabrication of an Array of Precision Nozzles by Through-Mask Electrochemical Micromachining. *J. Electrochem. Soc.* **142**, 3801–3805 (1995).

163. Aghvami, S. A. *et al.* Rapid prototyping of cyclic olefin copolymer (COC) microfluidic devices. *Sensors Actuators, B Chem.* **247**, 940–949 (2017).

164. Chen, C. S. *et al.* Shrinky-Dink microfluidics: 3D polystyrene chips. *Lab Chip* **8**, 622–624 (2008).

165. Matellan, C. & Del Río Hernández, A. E. Cost-effective rapid prototyping and assembly of poly(methyl methacrylate) microfluidic devices. *Sci. Rep.* **8**, (2018).

166. Selzer, D., Spiegel, B. & Kind, M. A Generic Polycarbonate Based Microfluidic Tool to Study Crystal Nucleation in Microdroplets. *J. Cryst. Process Technol.* **08**, 1–17 (2018).

167. Paoli, R. *et al.* Rapid Manufacturing of Multilayered Microfluidic Devices for Organ on a Chip Applications. *Sensors 2021, Vol. 21, Page 1382* **21**, 1382 (2021).

168. Cheng, J. Y., Wei, C. W., Hsu, K. H. & Young, T. H. Direct-write laser micromachining and universal surface modification of PMMA for device development. *Sensors Actuators, B Chem.* **99**, 186–196 (2004).

169. Formlabs. *Material data sheet - standard.* (2017).

170. Formlabs. *Material data sheet - high temp.* (2018).

171. Telecka, A. *et al.* Mapping the transition to superwetting state for nanotextured surfaces templated from block-copolymer self-assembly. *Nanoscale* **10**, 20652–20663 (2018).

172. Meincken, M., Berhane, T. A. & Mallon, P. E. Tracking the hydrophobicity recovery of PDMS compounds using the adhesive force determined by AFM force distance measurements. *Polymer (Guildf).* **46**, 203–208 (2005).

173. Bodas, D. & Khan-Malek, C. Hydrophilization and hydrophobic recovery of PDMS by oxygen plasma and chemical treatment-An SEM investigation. *Sensors Actuators, B Chem.* **123**, 368–373 (2007).

174. Prysiazhnyi, V., Zaporojchenko, V., Kersten, H. & Černák, M. Influence of humidity on atmospheric pressure air plasma treatment of aluminium surfaces. *Appl. Surf. Sci.* **258**, 5467–5471 (2012).

175. Harrison, S. *et al.* Scalable production of tissue-like vascularised liver organoids from human PSCs. *bioRxiv* (2020). doi:https://doi.org/10.1101/2020.12.02.406835

176. Siller, R., Greenhough, S., Naumovska, E. & Sullivan, G. J. Small-molecule-driven hepatocyte differentiation of human pluripotent stem cells. *Stem Cell Reports* **4**, 939–952 (2015).

177. Symes, M. D. *et al.* Integrated 3D-printed reactionware for chemical synthesis and analysis. *Nat. Chem.* **4**, 349–354 (2012).

178. Formlabs. Clear Resin SDS. (2016).

179. Świercz, R. & Oniszczuk-Świercz, D. Experimental Investigation of Surface Layer Properties of High Thermal Conductivity Tool Steel after Electrical Discharge Machining. *Metals (Basel).* **7**, 550 (2017).

180. Terada, Y., Ohkubo, K., Mohri, T. & Suzuki, T. Thermal conductivity in nickel solid solutions. *J. Appl. Phys.* **81**, 2263–2268 (1997).

181. Kelava, L. *et al.* Stereolithography 3D Printing of a Heat Exchanger for Advanced Temperature Control in Wire Myography. *Polym. 2022, Vol. 14, Page 471* **14**, 471 (2022).

182. Majewski, C. & Hopkinson, N. Reducing ejection forces for parts moulded into direct metal laser sintered tools. *Int. J. Adv. Manuf. Technol.* **24**, 16–23 (2004).

183. Lancaster, M. A. & Knoblich, J. A. Organogenesis in a dish: Modeling development and disease using organoid technologies. *Science.* **345**, (2014).

184. Yin, X. *et al.* Engineering Stem Cell Organoids. *Cell Stem Cell* **18**, 25–38

(2016).

185. Clevers, H. Modeling Development and Disease with Organoids. *Cell* **165**, 1586–1597 (2016).

186. Saini, A. Cell Stem Cell Profile Cystic Fibrosis Patients Benefit from Mini Guts. *Cell Stem Cell* **19**, 425–427 (2016).

187. Hockemeyer, D. & Jaenisch, R. Cell Stem Cell Review Induced Pluripotent Stem Cells Meet Genome Editing. *Stem Cell* **18**, 573–586 (2016).

188. Spence, J. R. *et al.* Directed differentiation of human pluripotent stem cells into intestinal tissue in vitro. *Nature* **470**, 105–110 (2011).

189. Lancaster, M. A. *et al.* Cerebral organoids model human brain development and microcephaly. *Nature* **501**, 373–379 (2013).

190. Takasato, M. *et al.* Directing human embryonic stem cell differentiation towards a renal lineage generates a self-organizing kidney. *Nat. Cell Biol.* **16**, 118–126 (2014).

191. Takebe, T. *et al.* Vascularized and functional human liver from an iPSC-derived organ bud transplant. *Nature* **499**, 481–484 (2013).

192. Eiraku, M. *et al.* Self-organizing optic-cup morphogenesis in three-dimensional culture. *Nature* **472**, 51–58 (2011).

193. Zbinden, A. *et al.* Non-invasive marker-independent high content analysis of a microphysiological human pancreas-on-a-chip model. *Matrix Biol.* **85-86**, 205–220 (2020).

194. Achberger, K. *et al.* Merging organoid and organ-on-a-chip technology to generate complex multi-layer tissue models in a human retina-on-a-chip platform. *Elife* **8**, (2019).

195. van Wenum, M. *et al.* Oxygen drives hepatocyte differentiation and phenotype stability in liver cell lines. *J. Cell Commun. Signal.* **12**, 575–588

(2018).

196. Dabaghi, M. *et al.* An ultra-thin highly flexible microfluidic device for blood oxygenation. *Lab Chip* **18**, 3780–3789 (2018).

197. Presens. Oxygen Sensor Foil SG-RPSu4. Available at: https://www.presens.de/products/detail/oxygen-sensor-foil-sf-rpsu4. (Accessed: 8th November 2021)

198. ISSI. *Safety Data Sheet ISSI UniCoat Pressure Sensitive Paint (UNC-12).* (2018).

199. Kundu, P. K. & Cohen, I. M. *Fluid Mechanics*. (2016).

200. Ochs, C. J., Kasuya, J., Pavesi, A. & Kamm, R. D. Oxygen levels in thermoplastic microfluidic devices during cell culture. *Lab Chip* **14**, 459–462 (2014).

201. Menezes, P. D., Gadegaard, N., Natal Jorge, R. M. & Pinto, S. I. S. Modelling human liver microphysiology on a chip through a finite element based design approach. *Int. j. numer. method. biomed. eng.* **37**, (2021).

202. Shiku, H. *et al.* Oxygen permeability of surface-modified poly(dimethylsiloxane) characterized by scanning electrochemical microscopy. *Chem. Lett.* **35**, 234–235 (2006).

203. Niles, W. D. & Coassin, P. J. Cyclic Olefin Polymers: Innovative Materials for High-Density Multiwell Plates. *Assay Drug Dev. Technol.* **6**, 577–590 (2008).

204. Wenger, R., Kurtcuoglu, V., Scholz, C., Marti, H. & Hoogewijs, D. Frequently asked questions in hypoxia research. *Hypoxia* 35 (2015). doi:10.2147/hp.s92198

205. Leclerc, E., Sakai, Y. & Fujii, T. Microfluidic PDMS (Polydimethylsiloxane) bioreactor for large-scale culture of hepatocytes. *Biotechnol. Prog.* **20**, 750–755 (2004).

206. Higgins, J. M., Eddington, D. T., Bhatia, S. N. & Mahadevan, L. Sickle cell vasoocclusion and rescue in a microfluidic device. *Proc. Natl. Acad. Sci. U. S. A.* **104**, 20496–20500 (2007).

207. Lachaux, J. *et al.* A compact integrated microfluidic oxygenator with high gas exchange efficiency and compatibility for long-lasting endothelialization. *Lab Chip* **21**, 4791–4804 (2021).

208. Femmer, T., Eggersdorfer, M. L., Kuehne, A. J. C. & Wessling, M. Efficient gas-liquid contact using microfluidic membrane devices with staggered herringbone mixers. *Lab Chip* **15**, 3132–3137 (2015).

209. Lo, J. F., Sinkala, E. & Eddington, D. T. Oxygen gradients for open well cellular cultures via microfluidic substrates. *Lab Chip* **10**, 2394–2401 (2010).

210. Adler, M., Polinkovsky, M., Gutierrez, E. & Groisman, A. Generation of oxygen gradients with arbitrary shapes in a microfluidic device. *Lab Chip* **10**, 388–391 (2010).

211. Lam, R. H. W., Kim, M. C. & Thorsen, T. Culturing aerobic and anaerobic bacteria and mammalian cells with a microfluidic differential oxygenator. *Anal. Chem.* **81**, 5918–5924 (2009).

212. Polinkovsky, M., Gutierrez, E., Levchenko, A. & Groisman, A. Fine temporal control of the medium gas content and acidity and on-chip generation of series of oxygen concentrations for cell cultures. *Lab Chip* **9**, 1073–1084 (2009).

213. Ameri, A. R., Imanparast, A., Passandideh-Fard, M. & Mousavi Shaegh, S. A. A whole-thermoplastic microfluidic chip with integrated on-chip micropump, bioreactor and oxygenator for cell culture applications. *Anal. Chim. Acta* **1221**, 340093 (2022).

214. Barsukova, A. D. Integrated Microfluidic Culture Media Oxygenator for Organ-on-a-Chip Applications. (2022).

215. Sønstevold, L., Czerkies, M., Escobedo-Cousin, E., Blonski, S. & Vereshchagina, E. Application of Polymethylpentene, an Oxygen Permeable Thermoplastic, for Long-Term on-a-Chip Cell Culture and Organ-on-a-Chip Devices. *Micromachines* **14**, (2023).

216. Park, J., Bansal, T., Pinelis, M. & Maharbiz, M. M. A microsystem for sensing and patterning oxidative microgradients during cell culture. *Lab Chip* **6**, 611–622 (2006).

217. Bussooa, A. *et al.* Real-time monitoring of oxygen levels within thermoplastic Organ-on-Chip devices. *Biosens. Bioelectron. X* **11**, 4–11 (2022).

218. Liu, H. *et al.* Heart-on-a-Chip Model with Integrated Extra- And Intracellular Bioelectronics for Monitoring Cardiac Electrophysiology under Acute Hypoxia. *Nano Lett.* **20**, 2585–2593 (2020).

219. Suga, H. *et al.* Adipose tissue remodeling under ischemia: Death of adipocytes and activation of stem/ progenitor cells. *Plast. Reconstr. Surg.* **126**, 1911–1923 (2010).

220. Gregory, J. W., Asai, K., Kameda, M., Liu, T. & Sullivan, J. P. A review of pressure-sensitive paint for high-speed and unsteady aerodynamics. *Proc. Inst. Mech. Eng. Part G J. Aerosp. Eng.* **222**, 249–290 (2008).

221. Lee, S. K. & Okura, I. Photostable Optical Oxygen Sensing Material: Platinum Tetrakis(pentafluorophenyl)porphyrin Immobilized in Polystyrene. *Anal. Commun.* **34**, 185–188 (1997).

222. ISSI. *UniCoat Pressure Sesitive Paint Data Sheet*.

223. Fan, Y., Li, H., Yi, Y. & Foulds, I. G. PMMA to Polystyrene bonding for polymer based microfluidic systems. *Microsyst. Technol.* **20**, 59–64 (2014).

224. Stern, O. & Volmer, M. Uber di abklingungszeit der fluoreszenz. *Phys. Zeitschr.* **183**, 188 (1919).

225. Nock, V. Control and measurement of oxygen in microfluidic bioreactors. (University of Canterbury, 2009).

226. Kumar, A. & Whitesides, G. M. Features of gold having micrometer to centimeter dimensions can be formed through a combination of stamping with an elastomeric stamp and an alkanethiol 'ink' followed by chemical etching. *Appl. Phys. Lett.* **63**, 2002–2004 (1993).

227. Ghosh, P., Lackowski, W. M. & Crooks, R. M. Two new approaches for patterning polymer films using templates prepared by microcontact printing. *Macromolecules* **34**, 1230–1236 (2001).

228. Burnham, A. K. Use and misuse of logistic equations for modeling chemical kinetics. *J. Therm. Anal. Calorim.* **127**, 1107–1116 (2017).

229. Meyer, T. N., Schwesinger, C., Ye, J., Denker, B. M. & Nigam, S. K. Reassembly of the Tight Junction after Oxidative Stress Depends on Tyrosine Kinase Activity. *J. Biol. Chem.* **276**, 22048–22055 (2001).

230. Omar Zaki, S. S., Kanesan, L., Leong, M. Y. D. & Vidyadaran, S. The influence of serum-supplemented culture media in a transwell migration assay. *Cell Biol. Int.* **43**, 1201–1204 (2019).

231. Bluhmki, T. *et al.* Development of a miniaturized 96-Transwell air–liquid interface human small airway epithelial model. *Sci. Rep.* **10**, (2020).

232. Wolff, A., Antfolk, M., Brodin, B. & Tenje, M. In Vitro Blood-Brain Barrier Models - An Overview of Established Models and New Microfluidic Approaches. *J. Pharm. Sci.* **104**, 2727–2746 (2015).

233. Biesheuvel, P. M., Porada, S. & Dykstra, J. E. The difference between Faradaic and non-Faradaic electrode processes. *arXiv* 1–16 (2018).

234. Bard, A. J. & Faulkner, L. R. *Electrochemical Methods: Fundamentals and Applications*. (Wiley, 2000).

235. Su, L., Liao, X. & Huang, Z. A theoretical study on resistance of

electrolytic solution : Measurement of electrolytic conductivity. *Results Phys.* **13**, 102274 (2019).

236. UFC-Bio. 1X PBS (Phosphate Buffered Saline) - 500 mL. Available at: https://ufcbio.com/products/1x-pbs-phosphate-buffered-saline#:~:text=PBS is non-toxic to mammalian cells and isotonic.&text=Specifications%3A,)%3A 13.5-17.0 mS%2Fcm. (Accessed: 4th February 2024)

237. Bartolo, D., Degré, G., Nghe, P. & Studer, V. Microfluidic stickers. *Lab Chip* **8**, 274–279 (2008).

238. Sackmann, J. *et al.* Review on ultrasonic fabrication of polymer micro devices. *Ultrasonics* **56**, 189–200 (2015).

239. Aesar, A. 45093 Platinum wire, 0.25mm (0.010in) dia, 99.9% (metals basis). Available at: https://www.alfa.com/en/catalog/045093/.

240. RS. *Safety Data Sheet, RS Pro Silver Conductive Paint*. (2020).

241. Manam, N. S. *et al.* Study of corrosion in biocompatible metals for implants: A review. *Journal of Alloys and Compounds* **701**, 698–715 (2017).

242. Chiou, P. Y., Ohta, A. T. & Wu, M. C. Massively parallel manipulation of single cells and microparticles using optical images. *Nature* **436**, 370–372 (2005).

243. Blume, L. F., Denker, M., Gieseler, F. & Kunze, T. Temperature corrected transepithelial electrical resistance (TEER) measurement to quantify rapid changes in paracellular permeability. *Pharmazie* **65**, 19–24 (2010).

244. Wacker. *WACKER 120 Food Contact Safety Data Sheet*. (2019).

245. Biophysics, A. *TEER 24 Data Sheet*.

246. Srinivasan, B. *et al.* TEER Measurement Techniques for In Vitro Barrier Model Systems. *Journal of Laboratory Automation* **20**, 107–126 (2015).

247. Miccoli, I., Edler, F., Pfnür, H. & Tegenkamp, C. The 100th anniversary of the four-point probe technique: The role of probe geometries in isotropic and anisotropic systems. *Journal of Physics Condensed Matter* **27**, 223201 (2015).

248. Vanýsek, P. Impact of electrode geometry, depth of immersion, and size on impedance measurements. *Can. J. Chem.* **75**, 1635–1642 (1997).

249. Dalby, M. J. *et al.* The control of human mesenchymal cell differentiation using nanoscale symmetry and disorder. *Nat. Mater.* **6**, 997–1003 (2007).

250. BMF. 2µm Series Printers. Available at: https://bmf3d.com/2µm-series-3d-printers/. (Accessed: 30th October 2022)

251. BMF. *HTL Resin Datasheet*.

252. John Moir Stormonth-Darling, B. Fabrication of difficult nanostructures by injection moulding. (2013).

253. SparkFun. SparkFun Spectral Sensor Breakout - AS7262 Visible (Qwiic). Available at: https://www.sparkfun.com/products/14347. (Accessed: 30th October 2022)

254. Convery, N. *et al.* 3D Printed Tooling for Injection Molded Microfluidics. *Macromol. Mater. Eng.* **306**, 2100464 (2021).

255. Maschmeyer, I. *et al.* A four-organ-chip for interconnected long-term co-culture of human intestine, liver, skin and kidney equivalents. *Lab Chip* **15**, 2688–2699 (2015).

256. FormLabs. Low-Volume Rapid Injection Molding With 3D Printed Molds. Available at: https://3d.formlabs.com/injection-molding/. (Accessed: 30th October 2022)